

**Finite element and durability modelling of  
roller shells and shafts.  
(Project - JCU6S)**

by  
S.I.Anderson and J.G.Loughran  
Department of Mechanical Engineering  
James Cook University of North Queensland

May 1998



## EXECUTIVE SUMMARY

The technology that has been adopted by the Australian raw sugar industry for roller shells and shafts has evolved over the past 40 years. Apart from Crawford's theoretical calculations on shell design and Cullen's factory experiments on operational stress states in roller shafts, little has been done to address the current problems associated with up to 10 mill roller failures each year. Ultrasonic testing of shafts has been used as a means of identifying problem shafts for many years. However, despite this, cracked rollers still prevail. The problem is exacerbated when one considers the operational costs associated with the removal of problem rollers during continuous crushing or an unplanned shutdown due to a roller failure.

This project has utilised finite element analysis to investigate the complex stress state that occurs in mill rollers during crushing. Predictions coupled with factory observations indicate key problem areas that must be addressed to reduce the occurrence of fatigue related damage to mill rollers. The report addresses these issues specifically through:

1. Detailed analysis of the complex stress state in an existing mill roller. Interference fits, nominal roll and torsional loads were applied and resulting stresses were investigated. The effect of roll lift and associated misalignment loads on roller stress was also analysed;
2. Analysis of ten alternative roller designs was undertaken. Variations in geometry, shell material and attachment methods were investigated. The resulting stress states in the critical fillet and shell-end regions highlight specific problems with existing designs. An alternative design is presented which should have a substantially improved durability; and
3. Durability modelling of the existing roller design. A simple model to evaluate the structural integrity of a cracked mill roller is presented and then verified using finite element methods. The model is user-friendly and can be used by factory engineers to assess the likelihood of catastrophic failure of a cracked roller shaft under known loading conditions. A case study predicting the critical crack depth and crack propagation rate for a candidate shaft material is presented.



## CONTENTS

<b>1.0</b>	<b>Introduction</b>	1-1
1.1	Components of a mill set	1-2
1.1.1	General milling system	1-2
1.1.2	Steel shaft and cast iron shell	1-4
1.1.3	Mill cheeks and brass bearings	1-5
1.1.4	Tailbar and couplings	1-6
1.1.5	Pinion gears	1-8
1.2	Materials and manufacturing methods	1-9
1.2.1	Shaft and shell material properties	1-9
1.2.2	Production of forged steel shaft	1-9
1.2.3	Production of cast iron shell	1-11
1.2.4	Reconditioning of shaft and shell	1-11
1.3	Roller failures	1-13
1.3.1	Factory experience	1-13
1.3.2	Preventative maintenance techniques	1-14
1.4	Current practice	1-18
1.4.1	Roller geometry	1-18
1.4.2	Load statistics	1-18
1.5	Bearing and lubrication technology - past and present	1-19
1.5.1	Brass bearings	1-19
1.5.2	Roller bearings	1-20
1.6	Design of roller shells	1-22
1.6.1	Shrink fit stress in roller shell	1-22
1.6.2	Maximum transmittable torque	1-24
1.6.3	Division of roller torque	1-25
1.6.4	Axial stress in shell due to roller loading	1-26
1.6.5	Discussion	1-26
1.7	Experiments on mill rollers	1-27
1.7.1	Experimental detail	1-27
1.7.2	Pintle-end stress	1-28
1.7.3	Drive-end stress	1-29
1.7.4	Drive-end torque	1-30
1.7.5	Discussion	1-31

1.8	Roll load estimations	1-32
1.8.1	Roll pressure loading	1-32
1.8.2	Roll torque loading	1-34
1.8.3	Tailbar misalignment and associated loading	1-36
1.9	Application of finite element modelling to roller design	1-38
1.9.1	Simplified modelling of mill roller	1-38
1.9.2	Modelling of roller shaft transition fillets	1-39
1.9.3	Durability modelling of mill rollers	1-41
1.9.4	Discussion	1-42
1.10	Objectives of finite element modelling	1-43
<b>2.0</b>	<b>Finite element modelling - existing roller design and practice</b>	<b>2-1</b>
2.1	Interference fit - 2D finite element modelling	2-3
2.1.1	Preliminary modelling and results	2-3
2.1.2	Final modelling and results	2-13
2.1.3	Effect of shell parameters on roller stress	2-19
2.1.4	Discussion	2-21
2.2	Operational stress prediction - 3D finite element modelling	2-22
2.2.1	Model parameters and techniques	2-23
2.2.2	Roll load, torque transmission and interference fit results	2-28
2.2.3	Tailbar misalignment / roll lift and bearing restraint effects	2-40
2.2.4	Review of critical regions and associated stress states	2-51
<b>3.0</b>	<b>Alternative designs</b>	<b>3-1</b>
3.1	Physical and economic design considerations	3-2
3.1.1	Mill roller economics	3-2
3.1.2	Geometry restraints	3-5
3.1.3	Materials and manufacturing procedure	3-5
3.2	Conceptual designs	3-6
3.2.1	Shell design and attachment alternatives	3-6
3.2.2	Shaft design alternatives	3-8
3.3	FEA of alternative roller designs	3-10
3.3.1	Alternative designs and associated results	3-10
3.3.2	Discussion	3-50
3.4	Alternative design summary	

<b>4.0</b>	<b>Durability modelling</b>	4-1
4.1	Fracture mechanics theory	4-2
	4.1.1 Stress intensity theory	4-2
	4.1.2 Crack propagation theory	4-8
4.2	Stress intensity prediction - 3D finite element modelling	4-12
	4.2.1 Model parameters and techniques	4-12
	4.2.2 Discussion	4-17
4.3	Evaluation of a cracked mill roller	4-18
	4.3.1 Case study	4-18
	4.2.2 Discussion	4-21
4.4	Durability modelling summary	4-22
<b>5.0</b>	<b>Conclusions and recommendations</b>	5-1
	<b>References</b>	R-1
	<b>Appendices</b>	A-1
A.1	Mill roller geometry	A-1
A.2	Mill brass geometry	A-5
A.3	Roll load calculations	A-7
A.4	Misalignment load calculations	A-15
A.5	Roller stress calculations	A-17



# *Chapter 1*

*Introduction*



## 1.0 Introduction

Each year the Australian raw sugar industry faces downtime and loss in production due to the failure of typically 10 - 12 roller shells and shafts. These failures are generally catastrophic often resulting in consequential damage to ancillary equipment such as mill cheeks, pinions, gearing and tailbars. Some mills utilise ultra-sonic inspection of roller shafts to detect cracks. When a cracked shaft is observed, loads are either reduced to hopefully ensure safe operation or the shaft is immediately taken out of service. The total cost of these failures and decisions can be estimated to be about 1.5 million dollars per year.

As conventional design methods are not readily applicable to the optimal design of roller shells and shafts, engineers often rely on experience and codes of practice. Modern finite element methods and durability analysis can be used to fine tune the design of roller shells and shafts which are subjected to complex loading conditions.

There is a need to investigate the stresses in existing rollers under operating conditions. An excellent experimental investigation was undertaken over 29 years ago (Cullen, 1968). However, experimental investigations of this type are extremely difficult and time consuming and are therefore limited in scope. No subsequent experimental investigations have been carried out. The problem can be economically addressed using modern computational tools. Complete three dimensional finite element models of roller shells and shafts would highlight critical regions, enable configurations of alternative geometry and materials to be explored, and provide insight into crack initiation when linked to durability modelling. The link to durability modelling and hence condition monitoring in terms of frequency of inspection might also be exploited.

The general aim of this project was to apply finite element methods to analyse the stress state in roller shells and shafts and to explore alternative geometry and materials. In addition, durability modelling of roller shafts to extend life and improve condition monitoring procedures was undertaken.

In short, finite element models of the roller shells and shafts will be used to:

1. Enable a better understanding of the stress states resulting from operating conditions;
2. Consider alternative geometry and materials which result in lower operating stresses but are still plausible from an engineering and economic standpoint;
3. Investigate the fatigue resistance of shafts; and
4. Investigate strategies for reducing the whole of life costs of roller shells and shafts.

## 1.1 Components of a mill set

This chapter is directed towards readers who are unfamiliar with the components, design, use and evolution of the crushing units used in all Australian sugar factories. Chapter 1.1 describes the components which make up a mill set.

### 1.1.1 General milling system

Mechanically harvested sugar cane is transported to the sugar factories either by road or rail. Upon arrival, the sugar cane in billet form is prepared for further processing via high speed hammer mills which reduce the cane to a fine fibrous state. This cane fibre can then be processed in either of two ways, crushing or diffusion. Crushing, the most common method of juice extraction in Australia, involves the cane fibre being fed through a series of milling units. Each unit contains three feeding rollers and three main rollers which basically squeeze the juice from the cane fibre (bagasse) under high pressure. To achieve satisfactory juice extraction, commonly 96 - 98 per cent, a milling train would require between four and six milling units in series. The extracted juice is processed into raw sugar and the bagasse is used as a fuel source for factory operation and generation of power for export.

The simplistic design and process of the three roller mill has virtually remained unchanged during the last century. However, innovations over the past 30 years have been introduced to improve the performance of the three roller mill in both efficiency and capacity. Such improvements include better cane preparation, introduction of feed rollers, innovative hydraulic loading devices and more powerful prime movers [Anand, 1983]. Figure 1.1 depicts the typical layout for a milling train.

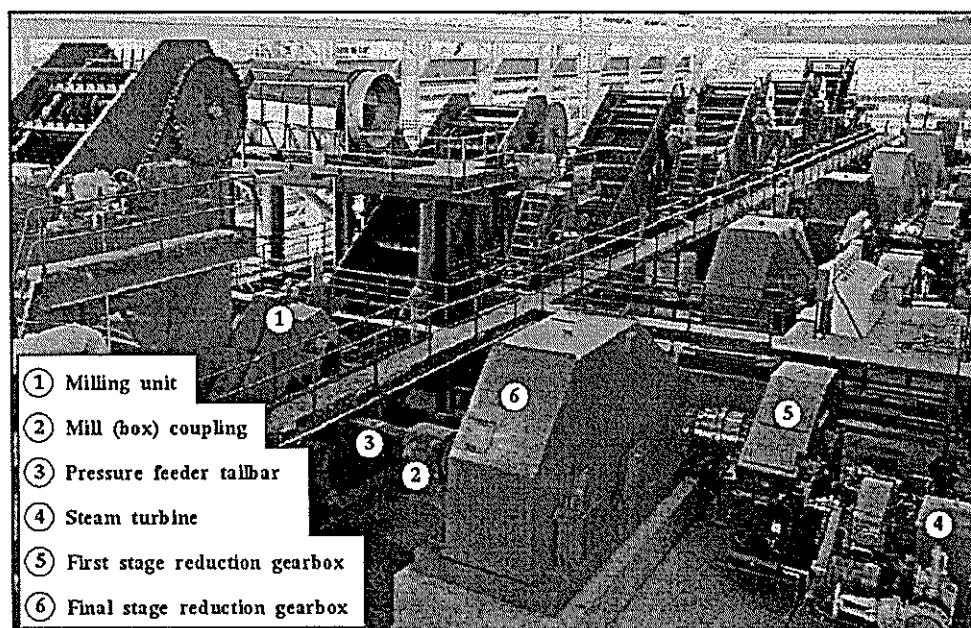


Figure 1.1 Typical milling train.

Engineers have experimented with the design of the standard three roller mill in an attempt to improve its performance and the life of components. Clarke (1958) discusses some of these designs. Figure 1.2 shows a typical mill set ready for installation. Figure 1.3 illustrates the general flow of prepared cane through a six roller mill.

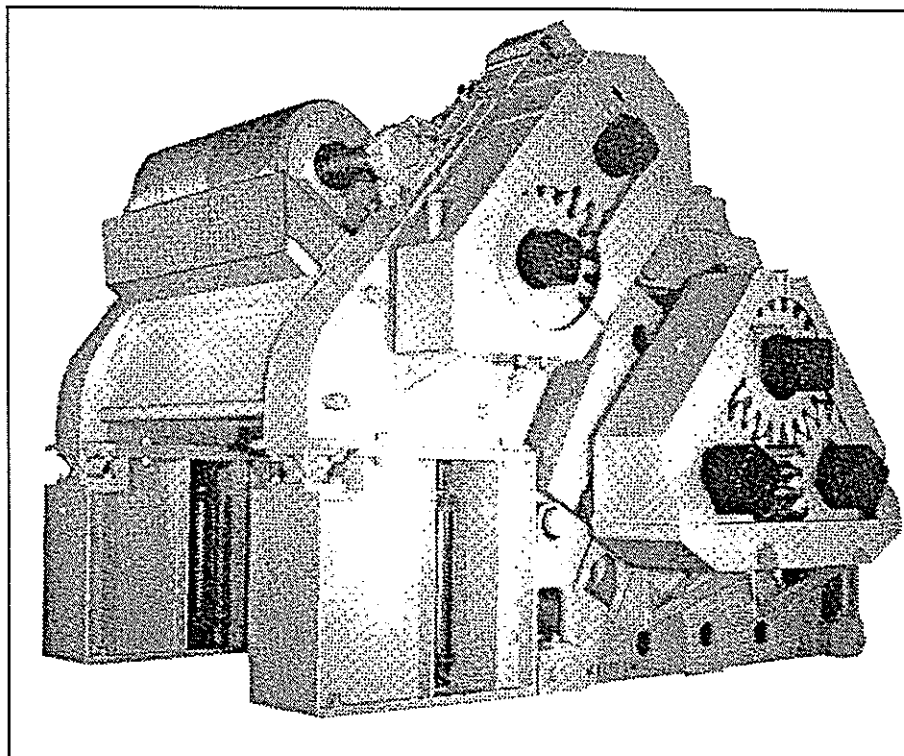


Figure 1.2 Six roller mill set.

Current mill designs incorporate hydraulically loaded floating top rollers (Scriven, 1962) in combination with fixed or free feed-and-delivery rollers. Various other designs such as self-setting mills and inverted mills are being used in some factories around the world. Interestingly, the majority of mill sets incorporating three main rollers still exploit the isosceles triangle arrangement. The addition of pressure feed rollers to mill sets has dramatically improved the feeding characteristics of such mills.

Power has historically been supplied to the mill sets via steam powered turbines in combination with cumbersome gear arrangements. In recent years the need for better drive control and increased crushing rates has seen the introduction of hydraulic drives which attach directly to the mill rollers and hence avoid the need for gearing (Shield and Cant, 1995).

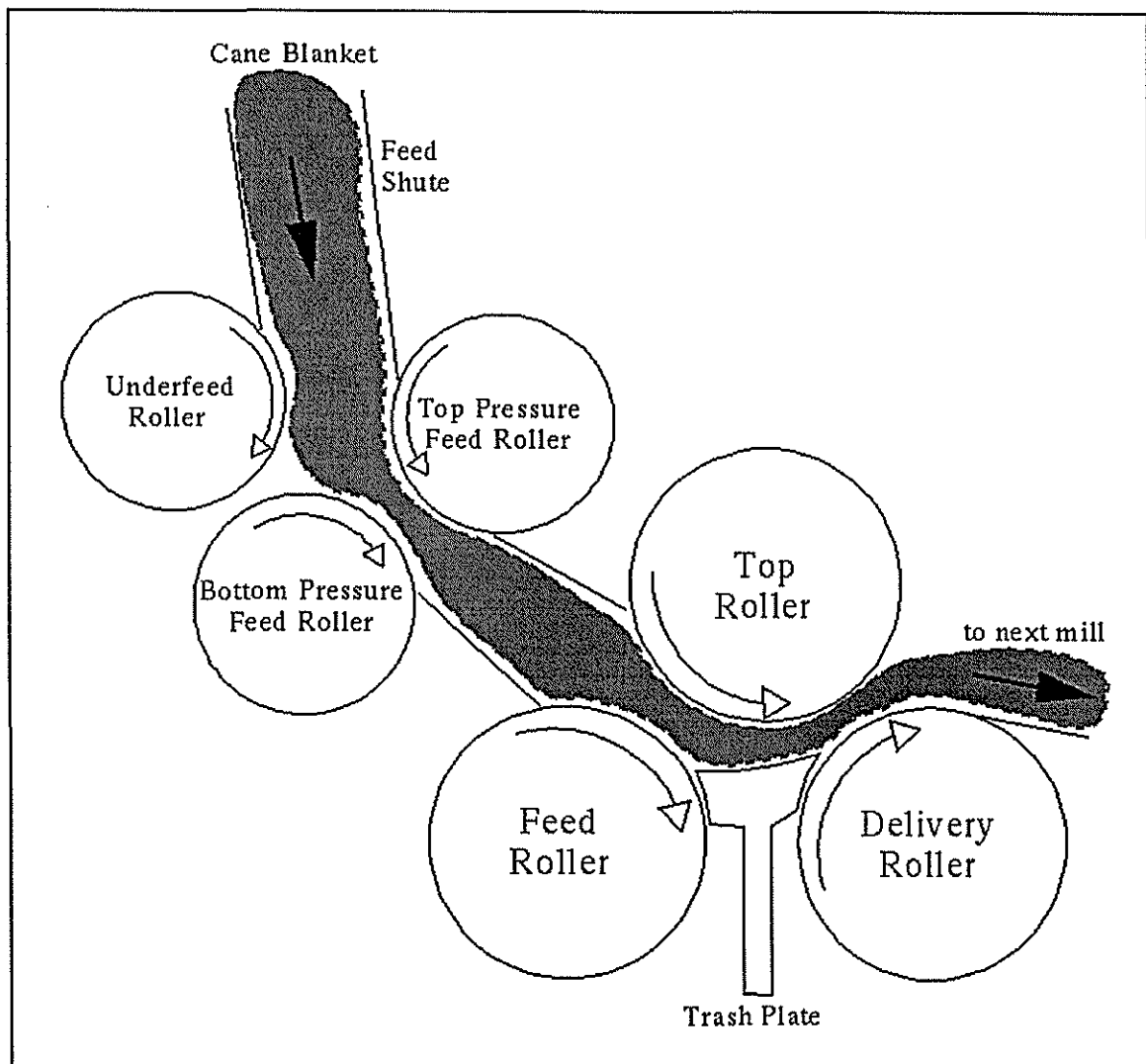


Figure 1.3 Schematic of six roller mill and path of cane blanket.

### 1.1.2 Steel shaft and cast iron shell

A roller comprises of a forged steel shaft with a cast iron shell. The grooved shell is shrunk onto the shaft. The length to diameter ratio for the roller shell is approximately two which is standard throughout the Australian sugar industry with the most common shell length used being seven foot (2.13 m). Figure 1.4 displays a roller highlighting the major sections.

The materials and production methods for the roller shaft and shell are described in Chapter 1.2.

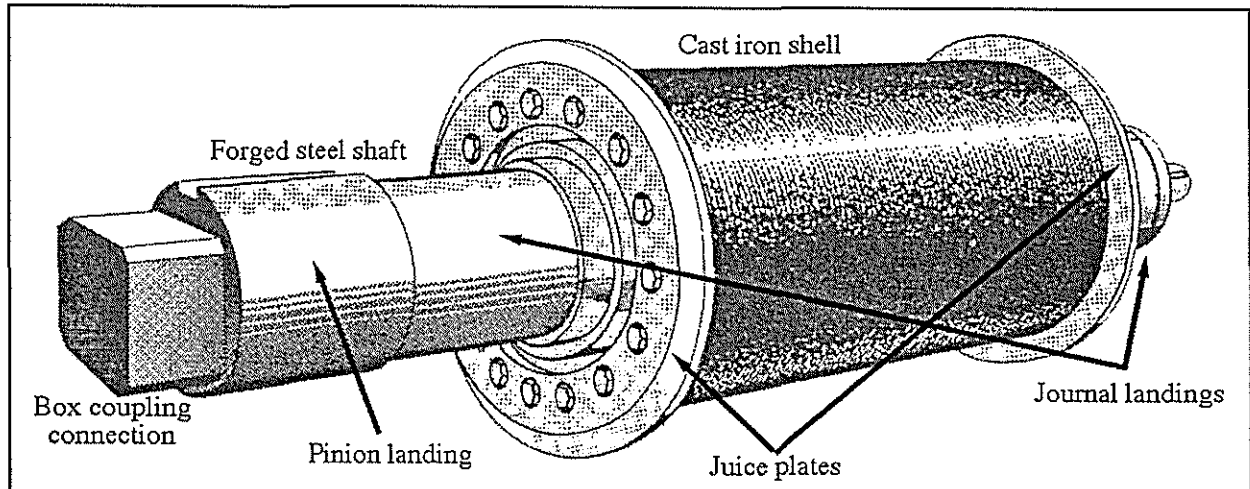


Figure 1.4 Roller shell and shaft.

### 1.1.3 Mill cheeks and brass bearings

Mill cheeks are the large side frames of a mill set which house the bearings for the three main rollers and the hydraulic loading rams. Their design is of importance for both adequate strength during operation and also ease of roller removal during maintenance work. Mill cheeks are either cast steel or fabricated from steel plate and later machined to accept the bearing components. Figure 1.5 shows the location of the mill cheeks in relation to other components.

Historically, journal bearings have been used for supporting mill rollers. Roller bearings were introduced into the Australian industry in the late 1970s but were not generally accepted due to the high costs involved. Water cooled brass bearings are mounted in the mill cheeks, mechanically lubricated and loaded via spherical seats (supposedly to account for shaft misalignment). Additional seals are added to the bearing to stop the ingress of juice contaminating the lubrication. Brass bearings are subject to sizeable roll loads and thrust forces and consequently experience considerable wear during the crushing season. As a result, brass bearings require replacement after several seasons if lubrication is inadequate or operating conditions are extreme.

Chapter 1.5 discusses the influence of brass and roller bearings on induced loads.

### 1.1.4 Tailbar and couplings

Top rollers are generally driven by square section tailbars and box couplings unless hydraulic drives are being used as the prime movers. Power and Clarke (1977) suggest that the reason for the continued use of the tailbar system is due to its simplistic and economic design. Figure 1.5 illustrates the positioning of the tailbar in relation to the mill set. Although the tailbar design is adequate for torque transmission to the rollers, undesirable thrust and radial forces can be developed when top roller shaft and gear shaft move out of alignment. This misalignment is a result of the floating top roller and does cause considerable wear and reduction in life to the tailbar and box coupling (Mosert, 1969). Figure 1.6 shows two typical wear problems experienced through box coupling use resulting from roller misalignment induced forces.

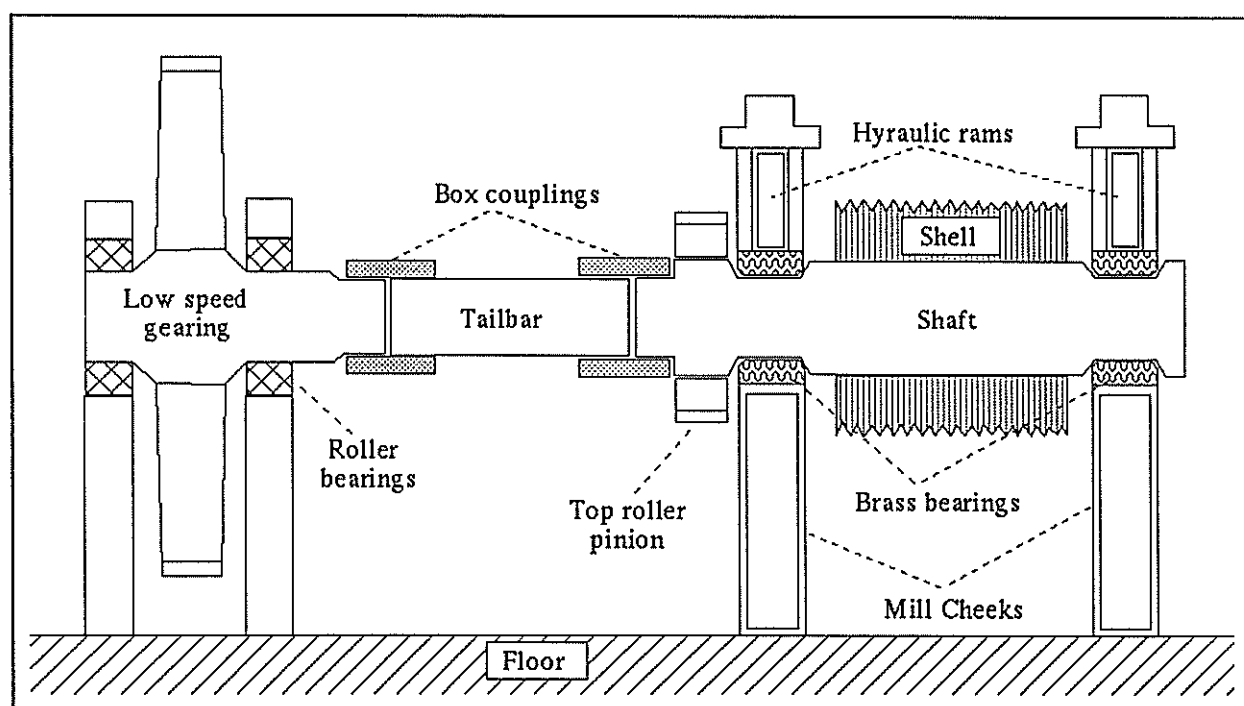


Figure 1.5 Schematic showing top roller and tailbar positioning. –

Clarke (1977) suggests a number of alternate coupling designs to reduce the undesirable thrust forces generated. Although the alternatives to the box coupling are feasible there would still remain the problem of successful lubrication. Tosio (1988) discusses the South African multi-misalignment coupling which eliminates thrust loads. This coupling, shown schematically in Figure 1.7 incorporates torque transmission through a wire rope arrangement. Further claimed benefits of this coupling include: lower shaft loading and wear; reduced maintenance costs because the coupling doesn't require lubrication; minimal damage to shaft squares and reduced gearing problems. However, these couplings are physically large and may not be practical for retrofitting to some existing milling installations.

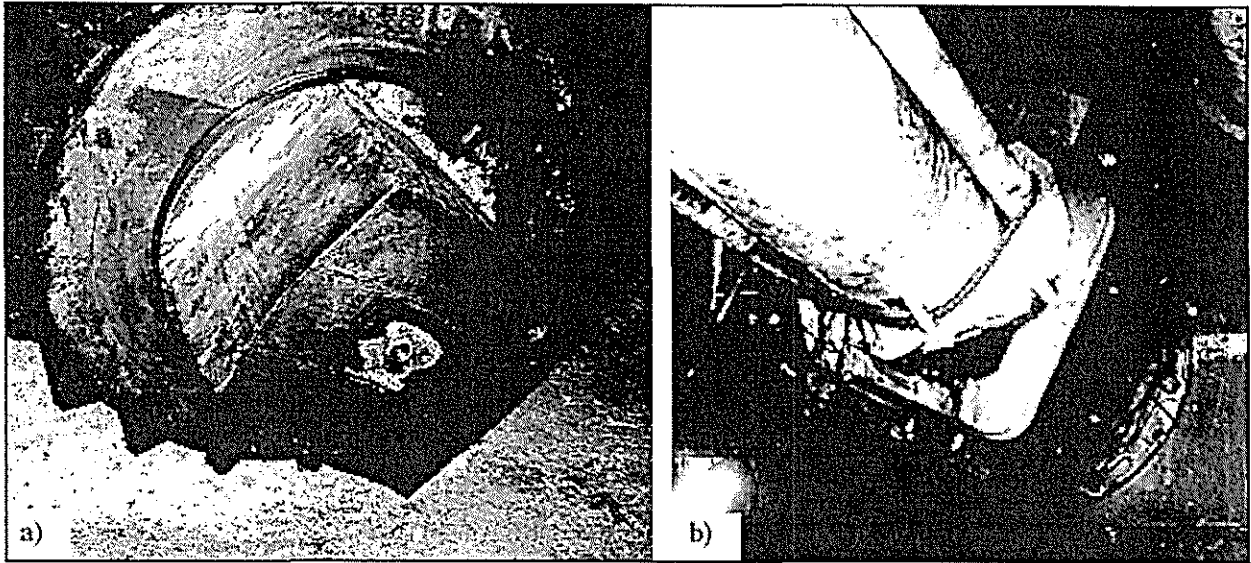


Figure 1.6 a) Plastic deformation and wear on shaft square. b) Extreme wear on tailbar square.

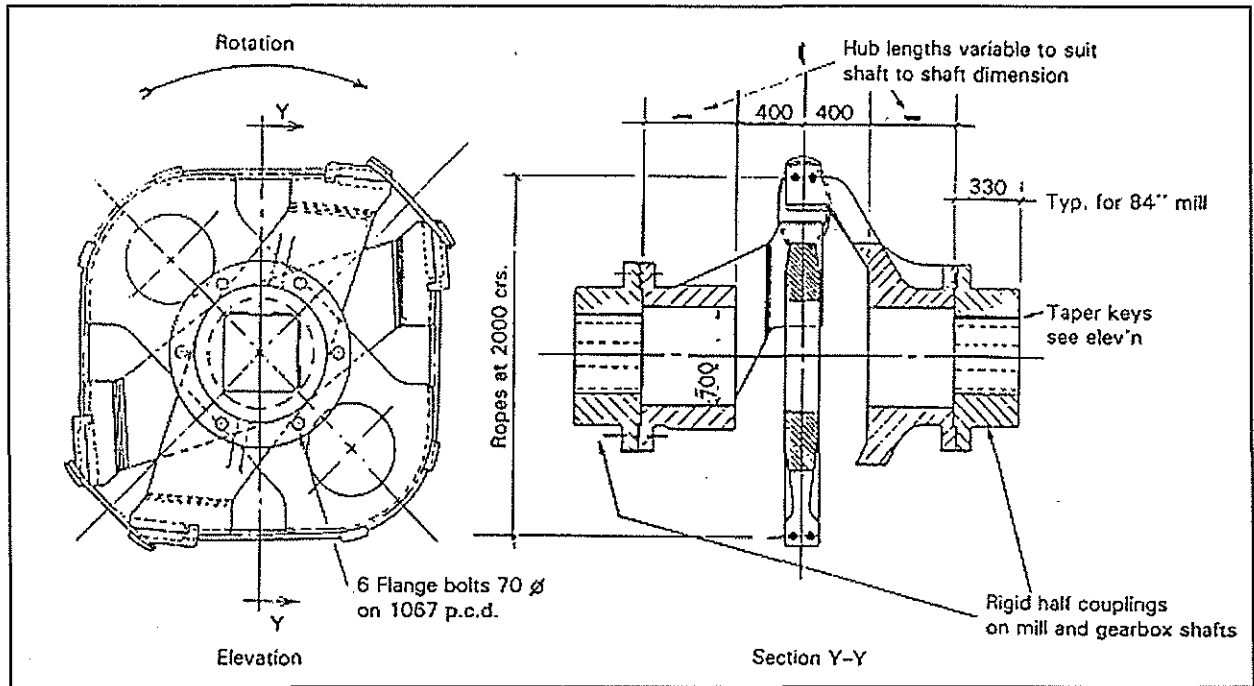


Figure 1.7 Schematic of wire driven multi-misalignment coupling. (after Tosio, 1988)

### 1.1.5 Pinion gears

Torque is transmitted to the top roller via the tailbar. Approximately one half of this torque is diverted to the feed and delivery rollers via external pinions keyed to their respective shafts. The top roller pinion teeth undergo high load cycles whilst transmitting torque to both side rollers (Clarke, 1981). Mill pinions are lubricated in one of two ways: encased in an oil bath (see Figures 1.2 and 1.8) or by spraying solvent based lubricants directly onto the teeth. However, misalignment in the hydraulically loaded rollers alters the contacting characteristics of the mating pinions resulting in increased uneven tooth loading. These high loads restrict effective lubrication and tooth wear increases dramatically. Typically mill pinions have 18 to 20 teeth. This small number of teeth (longer tooth form) is attractive as regards to flexibility in mill settings, however, torque transmission to the mill rollers becomes jerky as reported by Cullen (1968).

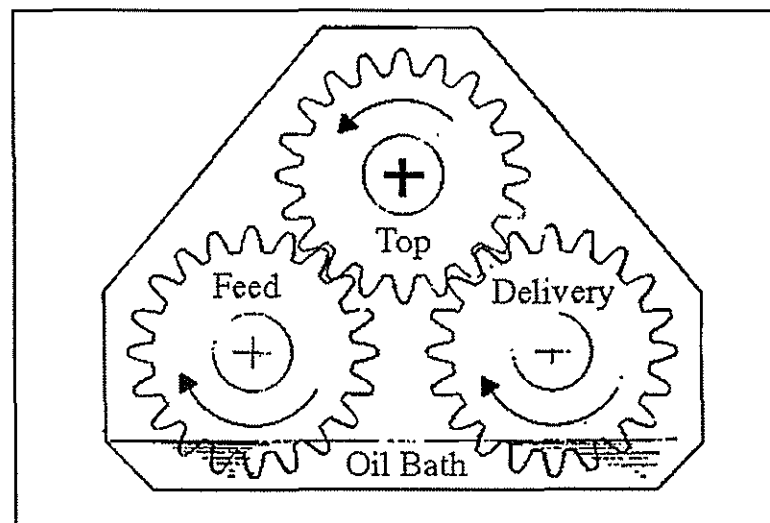


Figure 1.8 Interaction of roller pinions. (after Clarke, 1981)

Tyzack (1977) found that roller pinions are overloaded and that uneven roll lift was the major contributor to excessive flank wear and high tooth bending stresses which resulted in premature gear failure through tooth fracture as seen in Figure 1.9. Gatley and Pierce (1979) discuss additional hydraulic equipment which can be fitted to existing mill sets to avoid uneven roll lift.

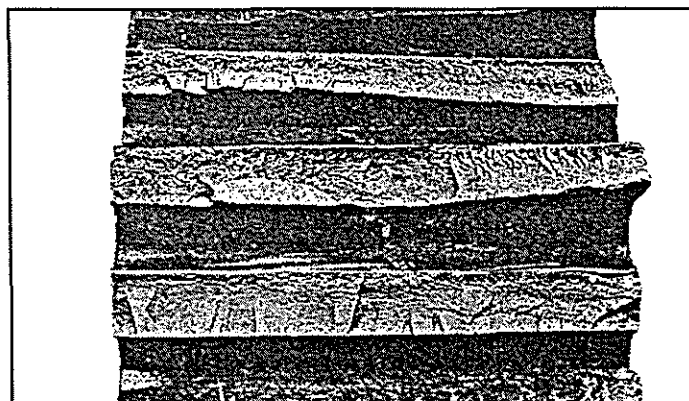


Figure 1.9 Fractured pinion teeth.

## 1.2 Materials and manufacturing methods

This section covers the materials used in roller shell and shafts and manufacturing techniques.

### 1.2.1 Shaft and shell material properties

Modern mill rollers consist of a grey cast iron shell which is shrunk onto a forged steel shaft. The roller shafts are forged from low carbon, alloy steel similar to that of mild steel (Tyzack and Gatley, 1980). The majority of roller shells consist of a steel like matrix which contains a high percentage of free carbon, graphite, and a low percentage of combined carbon (Crawford, 1970). The physical properties of both shaft and shell materials vary with composition and manufacturing methods. The elastic properties used in the finite element modelling in this report are listed below. Any changes from these properties will be noted.

Shell - Modulus of elasticity = 120 GPa  
Poisson's ratio = 0.26  
Ultimate strength = 150 MPa

Shaft - Modulus of elasticity = 207 GPa  
Poisson's ratio = 0.29  
Yield stress = 250 MPa  
Ultimate strength = 450 MPa

### 1.2.2 Production of forged steel shaft

Kirkness (1965 and 1977) reported on developments in sugar mill shaft production. The increasing demands for higher mill throughputs and efficiency has seen improvements in the manufacturing sector. Larger mills with improved shaft designs have resulted.

Electric furnaces have all but phased out the open hearth process in shaft production over the last 30 years. The reason being that electric furnaces can achieve a very close control over chemical composition in the shaft steels at all stages of the refining process.

The production of a shaft begins in the furnace where suitable steel scrap is melted. The molten metal (melt) at approximately 1600 °C then undergoes the first stages of refining. Oxygen is injected into the metal where it reacts with silicon, manganese, phosphorous and sulphur to form oxides which in turn form a slag which is removed from the metal. This oxygen technique produces precise carbon levels, good mixing of the melt and also removes impurities such as those previously mentioned along with harmful gases such as hydrogen and nitrogen. Following the oxygen process, the melt is then deoxidised to ensure good steel quality.

At this stage the composition of the melt is analysed and alloys are added as needed. Vacuum degassing of the melt follows where undesirable gases are removed. The melt is then ready for casting. Bottom or direct pouring techniques are used to fill the heavy cast iron moulds. The ingots are generally three times the cross section of the final shaft. The forging process reduces the ingot down to the required size. Forging occurs in large presses where the steel castings, reheated up to 1300 °C, are gradually reduced to the required size ready for final machining. The end result of the forging process is increased strength properties in the axial direction due to effective grain lengthening.

Heat treatment of the rough shaft form such as normalizing and tempering follow the hot forging process. Correct heat treatment procedures are required to avoid detrimental residual stresses and poor grain structure in the forging. In addition, heat treatment procedures directly affect the physical properties of the roller.

Inspection of the forging locates surface defects which are removed before final machining. Small samples from the forging are taken and tested for physical properties and chemical composition. Ultrasonic testing is commonly performed before and after machining the shaft so as to detect any internal defects or discontinuities. Satisfactory forgings are machined to the final design on numerically or computer numerically controlled (NC or CNC) lathes so that fine tolerances can be achieved (Figure 1.10). Other processes and machining techniques which improve the fatigue strength of shafts will be discussed in Chapter 1.3.2.

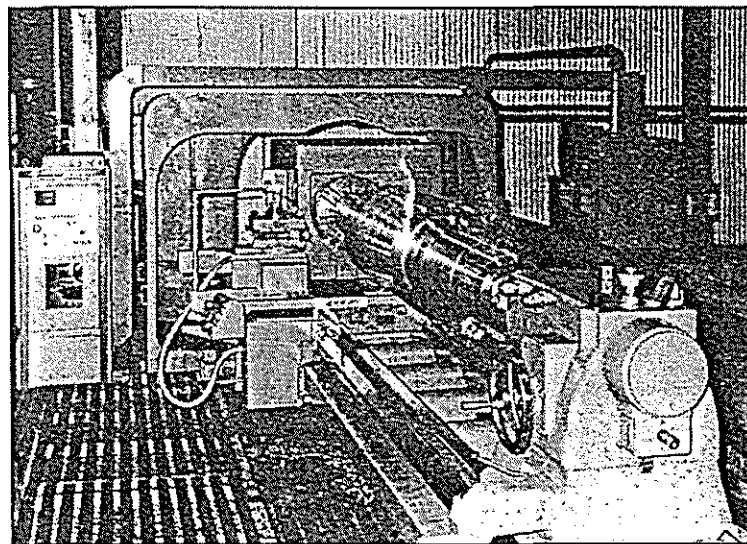


Figure 1.10 Machining of roller shaft using CNC lathe. (after Kirkness, 1977)

### 1.2.3 Production of cast iron shell

Successful mill operation is highly dependant on adequate mill feeding. For this reason the surface condition of the roller shell is of importance to the mill engineer. To refurbish worn shells, surface roughening (welding process) of the groove tips and flanks may be required several times a week. In addition to surface roughening, abrasion from dirt in the bagasse, chemical erosion from sugar juice products and periodic machining to maintain groove profiles has limited the operational life of the roller shell. Top roller shells typically last three to four seasons at which point the diameter has been reduced by approximately 10 per cent and is considered unsuitable for further use. Occassionly, however, mills report roll diameter losses of up to 120 mm in one season (Private communication with Mr. D. Steveson, South Johnston Mill, 1995). Old shells are removed, remelted as a feed stock at the foundry and new shells are fitted to existing shafts and returned to the mill.

Shells have historically been made of low strength cast iron. The desired properties of the final shell material include, resistance to wear and polishing, suitable strength and good machineability and weldability. Being of a large section, the shell casting requires careful attention to prevent undue porosity and shrinkage cavities. Once the casting has cooled at the correct rate, it is machined ready for the reshelling of a shaft. Precise machining of the internal through hole is critical to ensure an adequate shrink fit onto the shaft to avoid shell slippage in service.

### 1.2.4 Reconditioning of shaft and shell

Reshelling of shaft was once considered undesirable and the entire roller shell and shaft would be discarded (George and Reid, 1951). Due to modern developments in shaft design and manufacturing processes, shafts can now be reshelled numerous times. During the reshelling process other repairs such as rebuilding of badly worn shaft journals is possible using modern welding techniques and machining. Figure 1.11 shows a shaft journal being repaired.

Papers have been published regarding arc welding cast iron rollers (Coates, 1947; Thistlethwaite, 1949; Cessford, 1956 and Loughran and Henderson, 1992). The selection of groove profile and size has also been a topic for debate. Figure 1.12 shows the standard V-shaped grooving with additional chevron grooves machined axially along the shell. Chevron grooves are produced with automated grinding machines as in Figure 1.13.

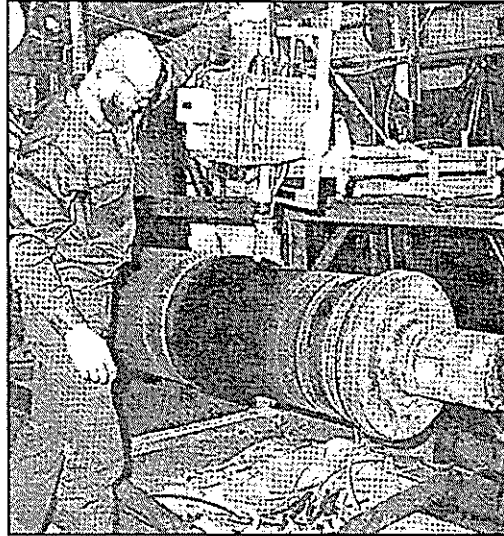


Figure 1.11 Worn roller journal being reclaimed by a specialised welding machine.

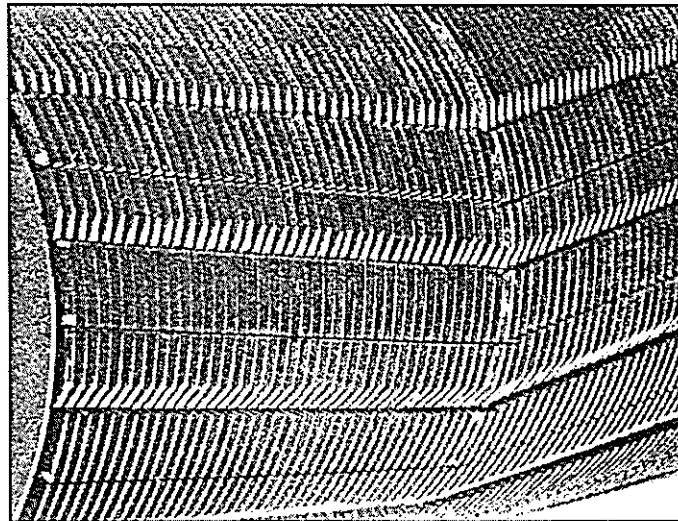


Figure 1.12 Grooving patterns used on roller shells to aid mill feeding.

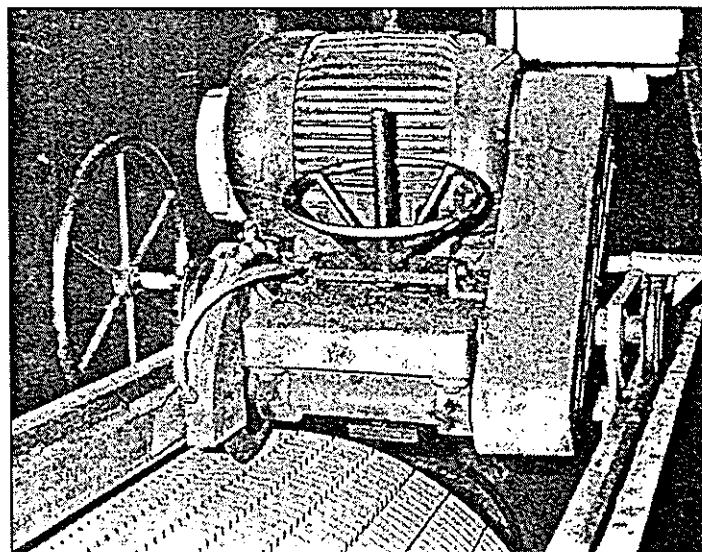


Figure 1.13 Grinding machine producing axial grooves.

### **1.3 Roller failures**

Component failure can occur via various modes such as wear, surface fatigue, plastic flow or breakage. Each type of failure mode has a distinguishable cause and possible remedy. Fatigue failure is the most common and unpredictable of all failure types. For this reason research has gone into understanding the mechanisms involved with metal fatigue. Many texts are available on the subject. Put simply, fatigue failure occurs in two distinct stages. Firstly a small crack is initiated (shear and slip process), generally at the surface of the component under stress fluctuations. This crack then propagates under repeated stress loadings until the remaining cross section of the component is unable to transmit the load whereupon sudden failure occurs.

Most steels have a fatigue strength (endurance) limit which is approximately one half of the ultimate strength value in the absence of stress concentrations. Generally, if the operating stresses are below the endurance limit the component should have infinite life. However, the endurance limit of most steels is further reduced in the presence of stress concentrations and more so in corrosive environments (Pattenden and Walker, 1980). Several papers regarding fatigue failure and its effect on various sugar mill components have been published (Williams, 1931; Rhydderch, 1934; Dalziel, 1953; Shann, 1959 and Tyzack and Gatley, 1980). These papers state the important role that satisfactory design, material, heat treatment, machining and operation techniques play in regard to reducing the number of fracture type failures. Methods being used to increase the life of components susceptible to fatigue are discussed in Chapter 1.3.2.

#### **1.3.1 Factory experience**

Economically, roller shafts are expensive to purchase and more so if they should fail in service. Unexpected or premature failure of a shaft due to poor design, overload or faulty material structure can cause expensive unplanned shutdowns and losses in mill extraction whilst a replacement is found. The introduction of regular shaft inspections using ultrasonic flaw detection techniques has been accredited with reducing the number of unexpected shaft failures (discussed in Chapter 1.3.2).

Top roller shafts are subject to the greatest stress as they transmit the full torsional load from the prime mover and crushing load from the feed and delivery rollers and the trashplate. Consequently one would expect a higher percentage of top rollers to fail than feed or delivery rollers. However, history does not support this theory. George and Reid (1951) suggest that this is probably due to top rollers being occasionally interchanged with feed or delivery rollers in the attempt to lengthen shell life.

The most common regions for shaft failure are at the tailbar connection fillet, the drive and pintle-end inside journal fillets and the region just under the shell landing. The location of failure

is dependant on several factors, namely: the general design of the roller, operating conditions and loads; material properties; location of manufacturing defects; roller / tailbar alignment and maintenance procedures. Reid (1988) investigated 93 roller failures over an eight year period in South African factories. Figure 1.14 highlights the critical regions with the associated percentage of failures found during the survey. Reid's conclusions were:

- top rollers accounted for 66 % of the total failures;
- the drive-end inboard fillet and shell-end regions were the most common failure positions;
- the average age of a shaft which fails in service is 5.6 seasons;
- all fracture surfaces exhibited stable crack propagation patterns;
- direction of fractured surfaces indicate bending stresses to be dominant in the fatigue process;
- evidence suggests the initial stress raisers for crack initiation were fretting and pitting corrosion, surface defects including welding inclusions, deep machining marks, poor blending between fillet radius and journal, and operational wear grooves at or close to the fillet.

Figure 1.15 shows a roller just prior to reinstallation in an Australian factory. Critical characteristics from a fatigue standpoint are:

1. The scoring marks on the journal and fillet are basically high stress concentrations that render the large fillet radius redundant; and
2. The unplanned gap between shell and shaft (small metal rule inserted) will promote juice related corrosion and reduce the effective length of shaft supported by the shell, thus resulting in higher bending stresses in critical regions on the shaft.

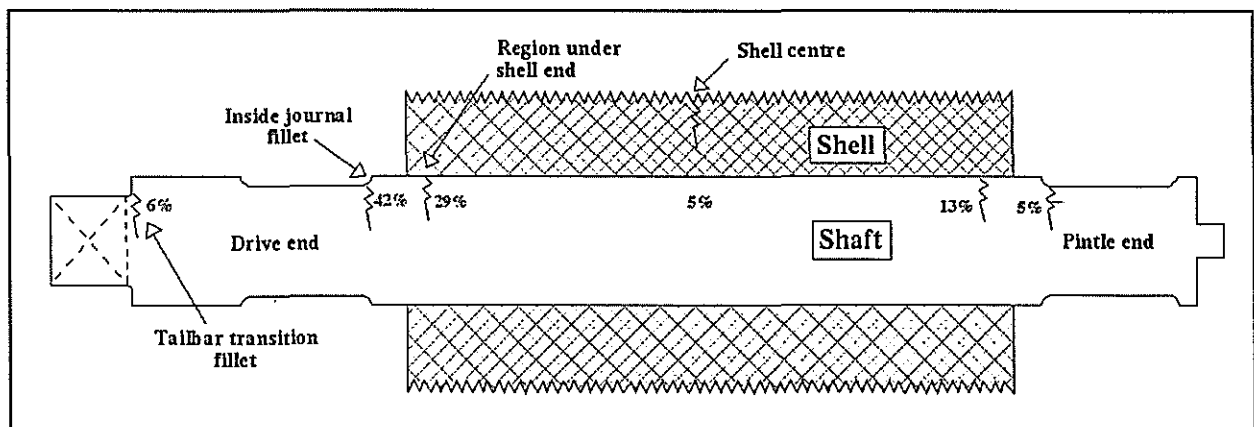


Figure 1.14 Critical regions in a roller shell and shaft.

Little has been published on the exact number of shaft failures experienced by the Australian sugar industry. However, there have been and still are sufficient shaft failures to warrant the current investigation. Apart from the lack of precise details of shaft failures, the general consensus is that both the inside journal fillets and regions just under the shell on the shaft landing are the most common regions of failure. Roll loads and uneven roll lift, torque transmission and shrink fit conditions contribute to the complex stress state in these locations. Figure 1.16 shows a shaft

which failed under the shell region at the drive-end in a corrosive environment. Figure 1.17 shows a shaft failure at the drive-end inboard fillet region due to rotational bending stresses at a stress concentration location.

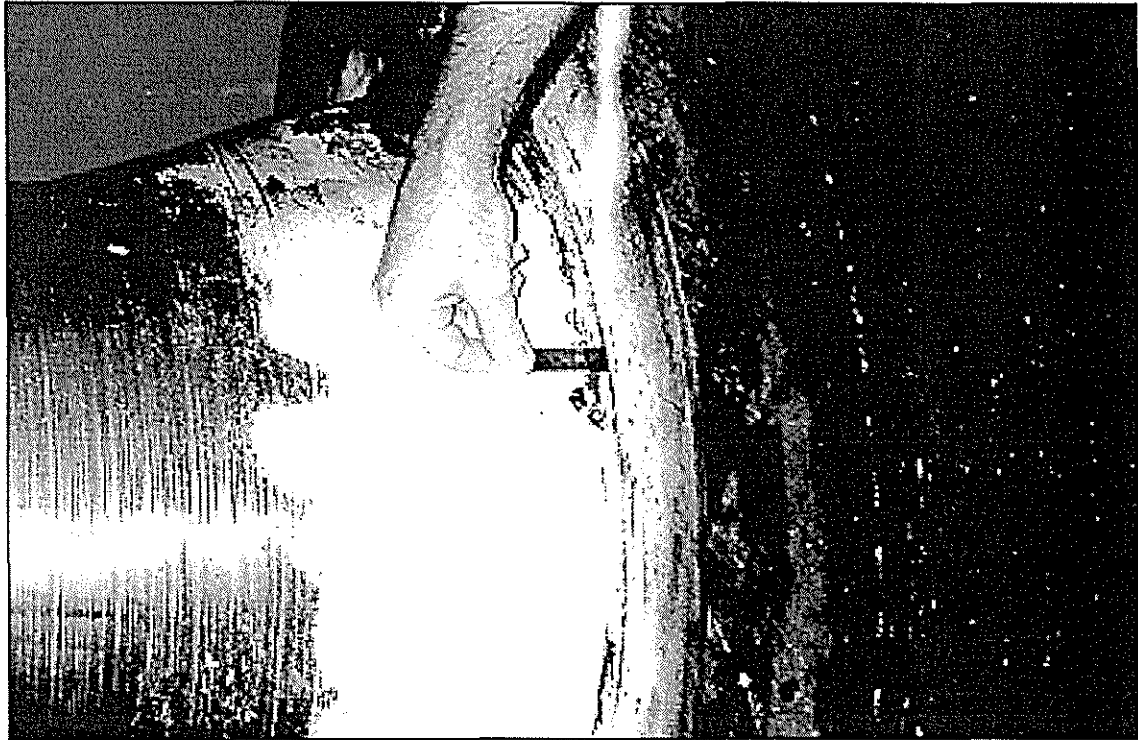


Figure 1.15 Shaft with score marks on fillet and unintended gap under shell end.

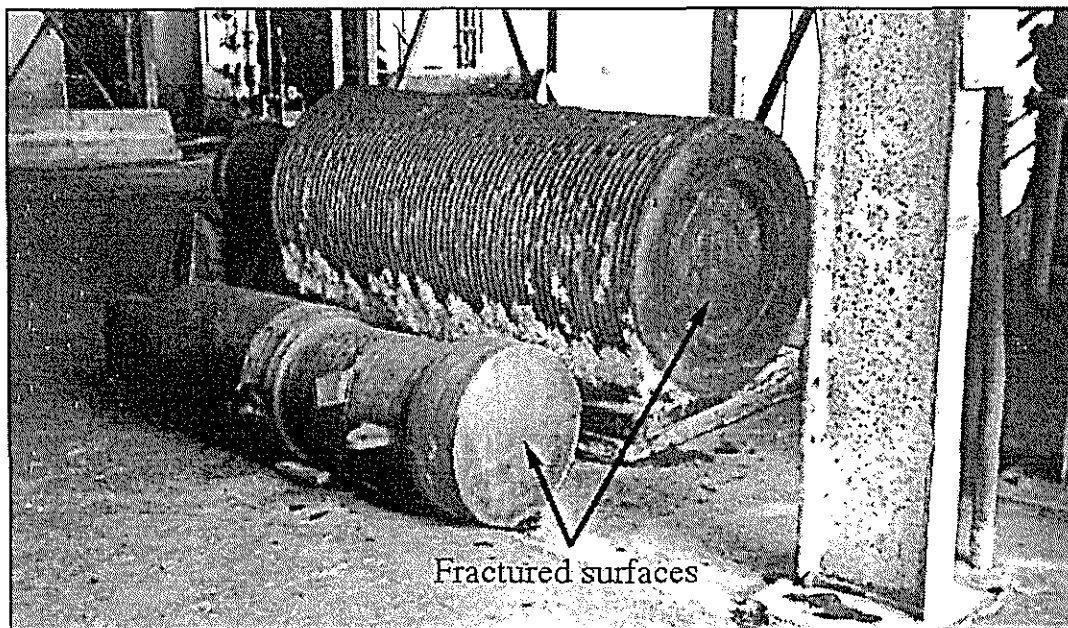


Figure 1.16 Broken shaft sections highlighting corroded fracture surfaces.

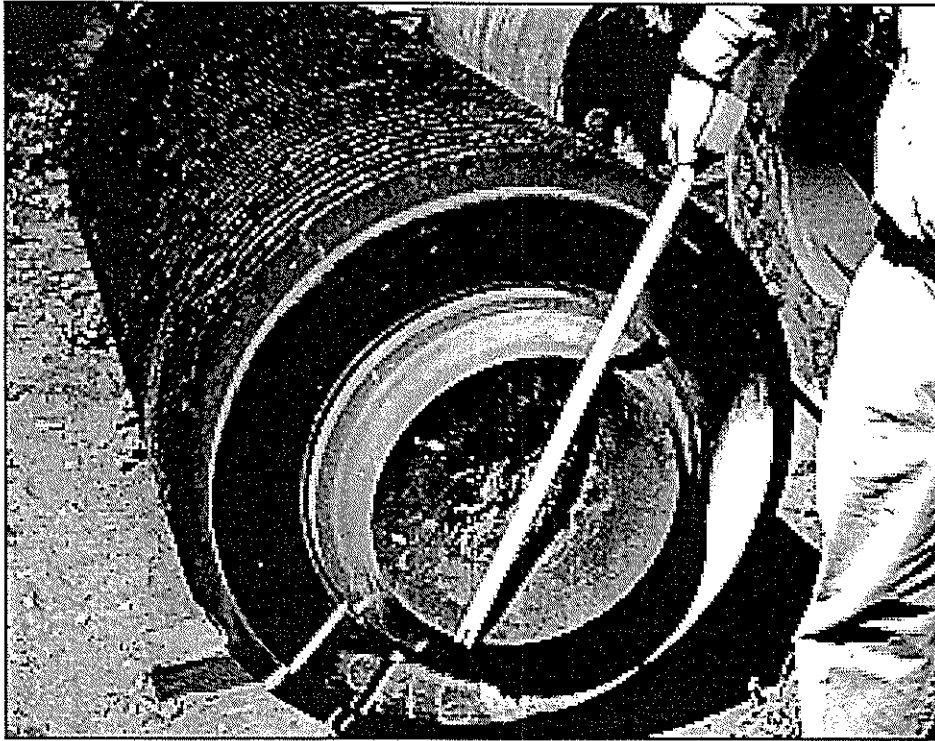


Figure 1.17 Typical fracture surface in fillet region.

### 1.3.2 Preventative maintenance techniques

Correct shaft design, attention to loading / environmental conditions and the introduction of ultrasonic inspection are reported to have seen a marked reduction in unexpected shaft failures. Ultrasonic testing in locating fatigue cracks in roller shafts began in the 1960s. Hill and McGinn (1965) reported on the inspection of 436 rollers over a two year period. During this time, 43 faults (crack-like flaws and inclusions) were verified in which 6 led to shaft failure. Today the ultrasonic inspection of roller shafts, described by Dillion and Millett (1984), has proven to be a useful preventative maintenance technique. The detection and monitoring of faults in shafts through routine inspections has aided in decisions regarding the use of fatigued shafts.

Reducing operating stresses in shafts would theoretically lower the risk of failure. This can be achieved by lowering operating loads and by good design practice and manufacturing techniques. Reducing stress concentration points on a roller shaft will lower the expected stresses in a roller experiencing similar loads. Suitably sized journal fillets are commonly used to lessen the stress experienced in the critical region of a shaft (Ritchie, 1994). Another less obvious stress raiser on a shaft is at end of the shrink fit zone. Crawford (1970) highlighted the sharp increase in gripping pressure at the end of the shrink fit zone. This situation was believed to be reduced with a suitable taper towards the end of the shell.

Operating conditions also affect stresses in a roller shaft. Uneven roll lift was shown to induce considerable stresses in a shaft due to bending moments created by misalignment with the tailbar

(Cullen, 1968). Improved coupling design which allows roll lifts without inducing undesirable forces on the shaft would increase roller life (Tosio, 1988). Clearly start-up torques and excessive roll loads are detrimental to the shaft. Mill operators should avoid placing the rollers under unnecessary loads. The use of a hydraulic drive would avoid tailbar induced forces as the drive is attached directly to the shaft and is free to move with the shaft. Hydraulic drives also result in improved control of torque application (smooth start-ups and stops with negligible rotary inertia) which is an obvious benefit to the shaft (Jorgensen et al, 1986). However, the fitment of a hydraulic drive introduces compressive stresses to the shaft-end due to the taper-lock fit.

A clean environment is crucial to the survival of a roller shaft as corrosion fatigue can become a serious problem. Corrosion fatigue is similar to the normal fatigue process although the process is hastened when in combination with corrosive attack. Dalziel (1953) explains how the fatigue limit of all metals is reduced by corrosion, and in the case of ferrous metals no true fatigue limit is observed. Corrosion of the shaft in the presence of sugar juice forms small oxide pits which are basically stress concentrations. These pits soon form small cracks which then propagate into the shaft under the fatigue process leading to eventual shaft failure. Skimming the shafts before reshearing to remove corrosion on the shell landing is recommended.

Prevention of corrosion fatigue in roller shafts is required to ensure satisfactory shaft life. Tyzack and Gatley (1980) proposed several measures to avoid such problems. All suggestions revolve around keeping the corrosive juice away from the stressed region of the roller shaft. Protective coatings of tar epoxy and paints, urethane and glass reinforced plastics have been used with some success. Nitrided steels have shown a high resistance to corrosion fatigue but this has not been proven in sugar factories. Metal sleeves sealed by o-rings have provided adequate corrosion protection in some sugar factories by separating the juice from the shaft.

The final method to improve the life of a roller shaft involves smarter manufacturing techniques applied to the roller shaft before it is placed or returned to service. Residual compressive stresses in the surface of a shaft generally improves the roller's fatigue properties. These compressive residual stresses effectively reduce the size of the cyclic tensile stress developed by rotational bending loads and as such decrease the chance of crack initiation. Residual compressive stresses can be introduced into the surface of the shaft by various methods including: shot peening; cold rolling and nitriding. Residual tensile stresses, detrimental to fatigue resistance of steel components, are usually a result of poor heat treatment. Surface finish has a marked effect on the fatigue resistance of steel components. The benefits of good surface finish and surface treatment were investigated by Loughran et al. (1995) using computer based fatigue modelling techniques.

## **1.4 Current practice**

The need for higher mill throughput and extraction efficiency has seen the introduction of continuous crushing and improved cane feeding and general mill control. Although mill loads have remained relatively constant over the last 50 years, both cane blanket thickness and rotational speed, hence the number of load cycles experienced by mill rollers has increased. Therefore, sugar factories are implementing larger mill sets in order to successfully process the increasing crop sizes. To improve the extraction efficiency of new mills, variations in design are being trialled. Self-setting mills, floating rollers, hydraulic drives, roller bearings and other smaller design changes are now scattered throughout the industry. This move away from the standard mill size and operating conditions makes the task of selecting a roller design and associated nominal operating loads (representative for the industry) to use in finite element modelling more complex. However, the effect of varying certain design parameters, operating conditions and associated loads on shaft stress will be investigated in Chapters 2 and 3.

### **1.4.1 Roller geometry**

The main defining parameter for a mill roller shaft is the shell's length. General information relating to roller sizes and their usage throughout the industry was obtained from the '1984 BSES Plant Data' annual report. This document is constructed from a yearly survey of all participating factories. It contains details such as roller size, work openings, trash plate positioning, hydraulic loads, fibre rates, drive power and speed and other operating parameters which were typical values for the crushing season. In 1984, 33 sugar factories supplied data for the annual survey. As the highest loaded roller is usually the top roller in the first mill set, efforts were concentrated on analysing survey details relating to this mill set.

The most common shell length used in number one mills in Australian factories in 1984 was seven feet (2.13 m). Lengths ranged from six to nine feet (1.83 to 2.74 m). -

### **1.4.2 Load statistics**

The '1984 BSES Plant Data' was also used to acquire an estimate of typical roll loads and power usage by number one mill sets. This information is used in the finite element modelling. Of the factories with hydraulically loaded top rollers, the typical top roll load was 67 tonnes per foot (2.15 MN/m) of shell's length. Top roll loads varied from 36.9 to 112 tonnes / foot (1.18 to 3.60 MN/m). Typical torque loading on the top rollers was not available.

## 1.5 Bearing and lubrication technology - past and present

Lubrication is an important aspect for mill set operation. Traditionally, journal bearings were used extensively throughout the industry until 1974 when the first roller bearing equipped mill commenced operation in Australia. However, the initial cost associated with roller bearings and modifications required to retro-fit them to existing mill sets has limited their general acceptance throughout the industry. The major advancements in bearing / lubrication technology has been in lubrication products and their application. Scott (1986) proposed a method for developing an effective lubrication system which limits wear and associated problems. Figure 1.18 shows the interaction of the various contributors towards a successful lubrication system.

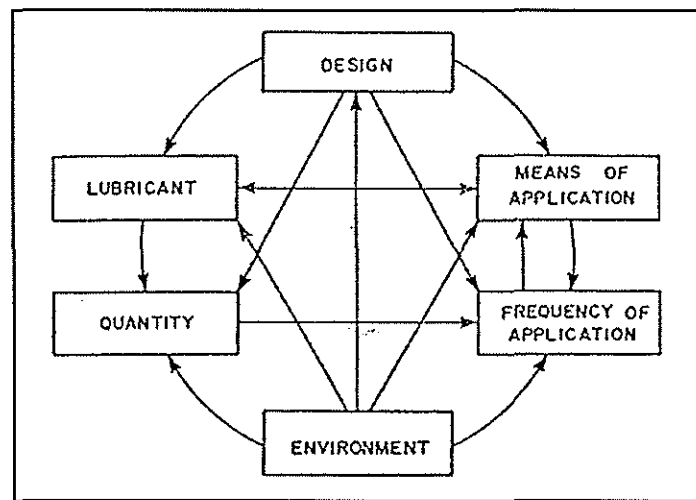


Figure 1.18 Lubrication as a system. (after Scott, 1986)

As lubrication is not anticipated to be a crucial issue to the result of this investigation, no attempt will be made to describe the lubrication process in detail. The following sections will briefly summarise the use of brass journals and roller bearings in the Australian sugar industry.

### 1.5.1 Brass bearings

A journal bearing consists of three principal elements; the journal (rotating shaft), bearing (supports and locates journal) and a desirable thin film of lubricant which separates the journal and bearing thus reducing wear and friction. Figure 1.19 shows the cross section of a typical journal bearing showing the expected pressure pattern. Note, the gap between the journal and bearing is exaggerated and is realistically no more than 0.5 mm for a standard roller.

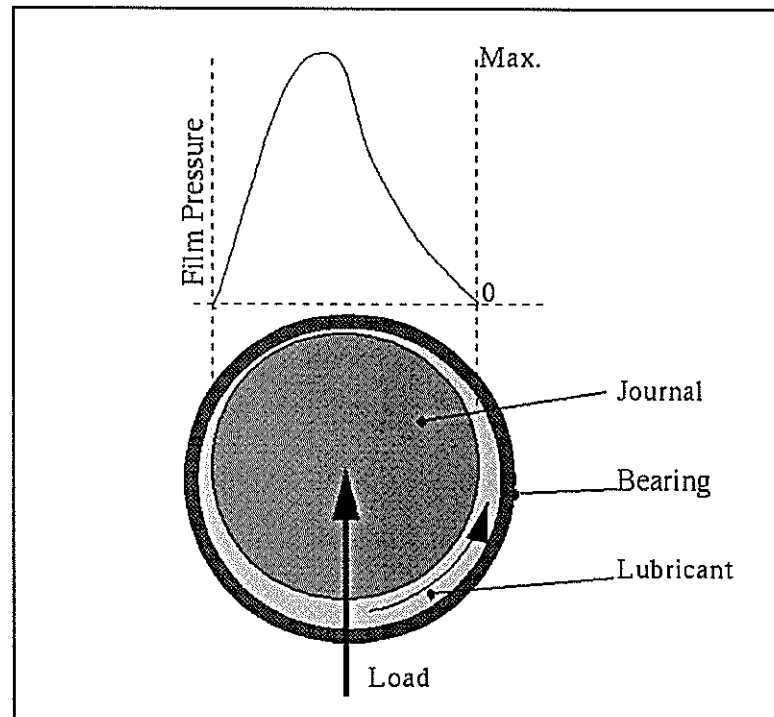


Figure 1.19 Typical journal bearing cross section.

Low surface speeds, shaft misalignment and deflection, high loads and unsuitable lubrication often result in the breakdown of the thin film required for optimal bearing operation. When this occurs, boundary lubrication dominates and wear of the bearing and shaft increases markedly (Brown, 1949). Several improvements in the lubrication process have been accompanied by extended bearing life. Semi-solid mixtures of oil and lime soaps and bituminous greases applied by screw-guns in the 1930s have been replaced by high viscosity refined oil based lubricants applied by advanced mechanical lubricators. Tyson et al (1991) report on the successful trials of solid film lubricant. Reduction in lubricant use and the apparent increase in brass life resulted.

In conclusion, effective brass bearing lubrication and extended life are possible. A combination of properly machined surfaces, efficient application (positive mechanical feed at the correct time via well positioned feed grooves) of the lubricant most suited to the specific loading conditions and the elimination of contaminants from the lubricant would ensure reduced costs and maintenance of journal bearings.

### 1.5.2 Roller bearings

As previously mentioned, roller bearings were introduced to the Australian sugar industry in the 1970s. However, Pihl (1954) reported on the use of roller bearings overseas to the Queensland Society of Sugar Cane Technologists and suggested several economic advantages of roller bearings in sugar factories. Reduced frictional resistance with an associated saving of up to 40 per cent in mill power would allow smaller gearing and prime movers to be used. Reduced friction when using roller bearings would also result in smoother mill start-ups and the elimination of

journal wear. Other benefits such as lower maintenance costs and reduced lubrication requirements are typical for roller bearing usage.

Macey and McGinn (1975) reviewed the performance of the spherical roller bearing trialled at Pleystowe mill in 1974 and compared the mill torque requirements with that of standard brass bearing mills at Farleigh and Marian for similar milling conditions. The roller bearing mill resulted in 25 per cent lower mill torque. Figure 1.20 depicts the workings of a typical spherical roller.

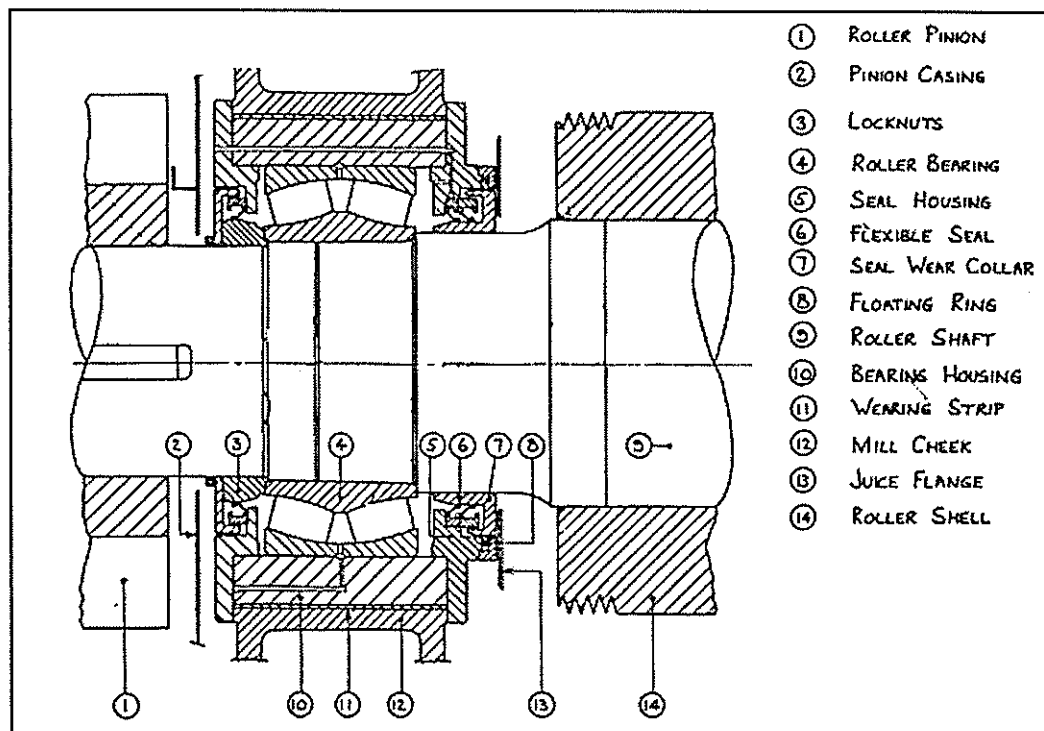


Figure 1.20 Spherical roller bearing. (after Jacklin, 1975)

Unexpected roller bearing failures prompted an investigation a few seasons after introduction into the Australian sugar industry. A survey of failed and damaged roller bearings was carried out to shed light on the situation. The expected life span of roller bearings was 20 years. McGinn and Mason (1982) reported that approximately two thirds of the failed bearings were located on the top roller which suggested that high bearing loads were a factor in the early failure. Juice ingress was very common which led to corrosion of the bearing surface and a reduction in lubrication quality. It was then suggested that bearing failure could be minimised by:

1. Use of adequately sized bearings to account for all loads experienced by the bearings;
2. Use of suitable grease lubricants with anti-corrosive additives;
3. Use of adequate bearing seals to exclude the contaminating juice; and
4. Correct mounting and maintenance procedures.

## 1.6 Design of roller shells

Crawford (1970) presented known theories for shell shrink (interference) fits with regard to stresses induced and also shrink fits required to ensure desired mill roller operation. He stated that the essential requirement of the shrink fit was to ensure that the friction between the shaft and shell was sufficient to transmit the torque necessary for crushing, including transient torque peaks and the reduction in transmittable torque due to roller wear. Crawford, using simple interference fit theory, calculated the tensile hoop stresses, compressive radial stresses and axial stresses induced in the shell. The relationships between material parameters and shell geometry on induced shell stress and transmittable torque were plotted.

The results from established theories of compound cylinders for shrink fit stress calculations were made using the following assumptions:

1. During assembly (cooling), the shell and shaft lengths remain equal once contact is made;
2. The shaft remains virtually at ambient temperature until securely gripped by shell;
3. Shell temperatures are uniform over their lengths during assembly;
4. Surface finishes for the shaft and shell landings are constant; and
5. The shaft and shell bore are circular without taper.

### 1.6.1 Shrink fit stress in roller shell

Before assembly of the shell onto the shaft, the shaft's landing diameter,  $D_2$ , exceeds the shell bore by a diametral interference,  $\delta$ .  $\delta$  is often quoted in terms of its ratio to the shaft landing diameter (interference factor,  $k$ ), i.e.

$$k = \frac{\delta}{D_2} \quad (1.1)$$

After the shell is shrunk onto the shaft during assembly, and assuming ideal conditions, there exists a radial pressure,  $P_i$ , between the shaft and shell. The expansion of the inner shell bore and contraction of the outer shaft landing sum to equal the original interference,  $\delta$ . The radial pressure,  $P_i$ , is given by

$$P_i = \frac{k E_1 E_2}{E_2 \left( \frac{1 + \left( \frac{D_2}{D_1} \right)^2}{1 - \left( \frac{D_2}{D_1} \right)^2} + \nu_1 \right) + E_1 (1 - \nu_2)} \quad (1.2)$$

where  $D_1$  is the effective outside shell diameter (taken at bottom of grooves);  
 $E_1$  is the elastic modulus for the shell material;

$\nu_1$  is the Poisson's ratio for the shell material;  
 $E_2$  is the elastic modulus for the shaft material; and  
 $\nu_2$  is the Poisson's ratio for the shaft material.

Assuming ideal plane strain conditions in the shell (feasible at central plane), tensile hoop stresses, compressive radial stresses and axial stresses are developed from the interference fit as explained in Figure 1.21.

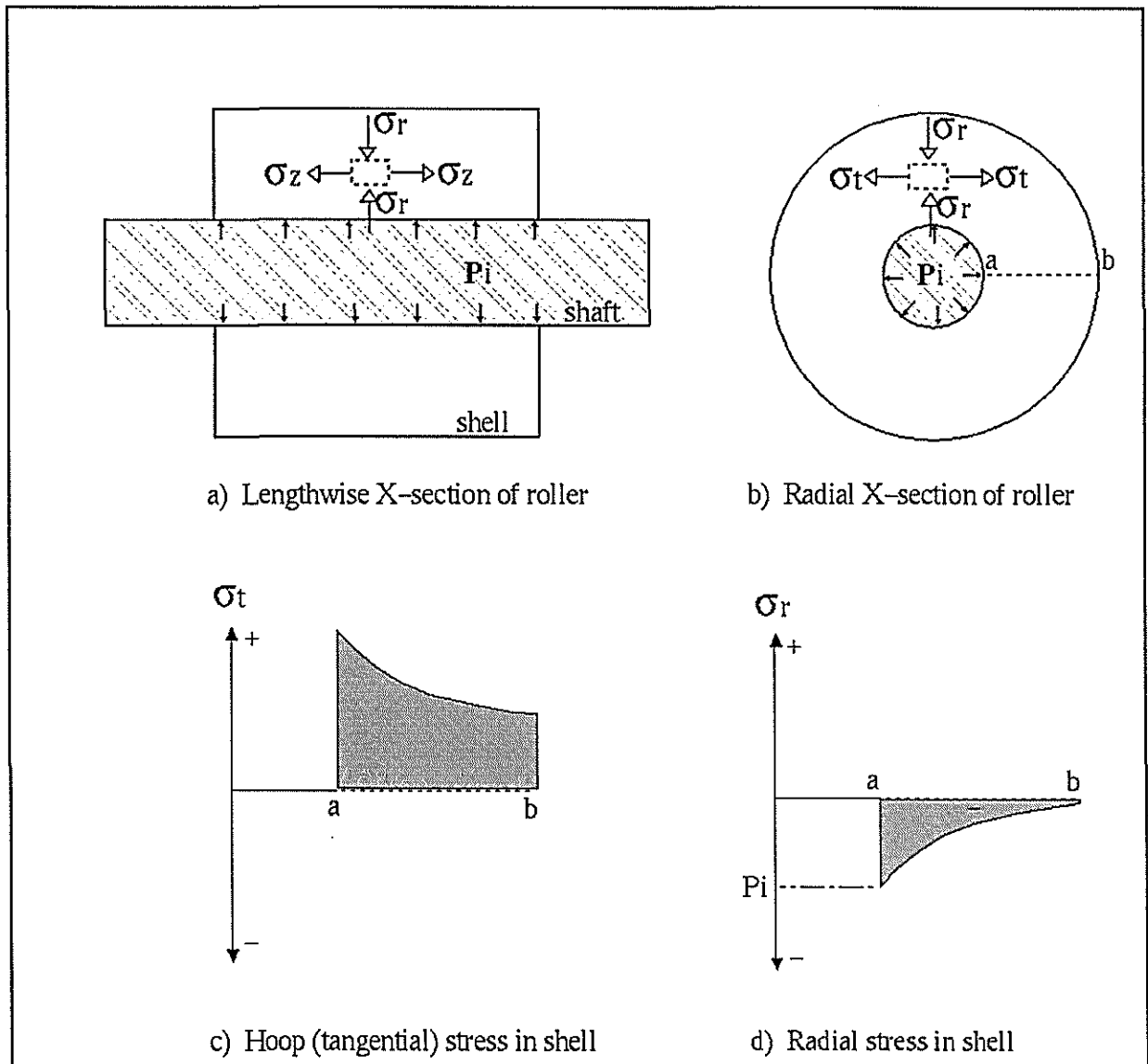


Figure 1.21 Stresses induced in shell by interference fit.

At any shell diameter,  $d$ , the shrink fit stress can be estimated by:

$$\text{Radial stress } (\sigma_r): \quad \sigma_r = -P_i \frac{D_2^2}{D_1^2 - D_2^2} \left( 1 - \frac{D_1^2}{d^2} \right) \quad (1.3)$$

$$\text{Tangential (hoop) stress } (\sigma_t): \quad \sigma_t = P_i \frac{D_2^2}{D_1^2 - D_2^2} \left( 1 + \frac{D_1^2}{d^2} \right) \quad (1.4)$$

and from theory

$$\text{Axial stress } (\sigma_z): \quad \sigma_z = \nu_1 (\sigma_r + \sigma_t) \quad (1.5)$$

Further consideration of equations 1.3 and 1.4 show that the highest radial and hoop stress in the shell occur at the inner surface as illustrated in Figure 1.21. Crawford suggested that under factory conditions the projecting shaft-ends resist compression and hence result in an increased (but unquantified) pressure in this region (Figure 1.22). This increase in stress is studied through finite element analysis (Chapter 2).

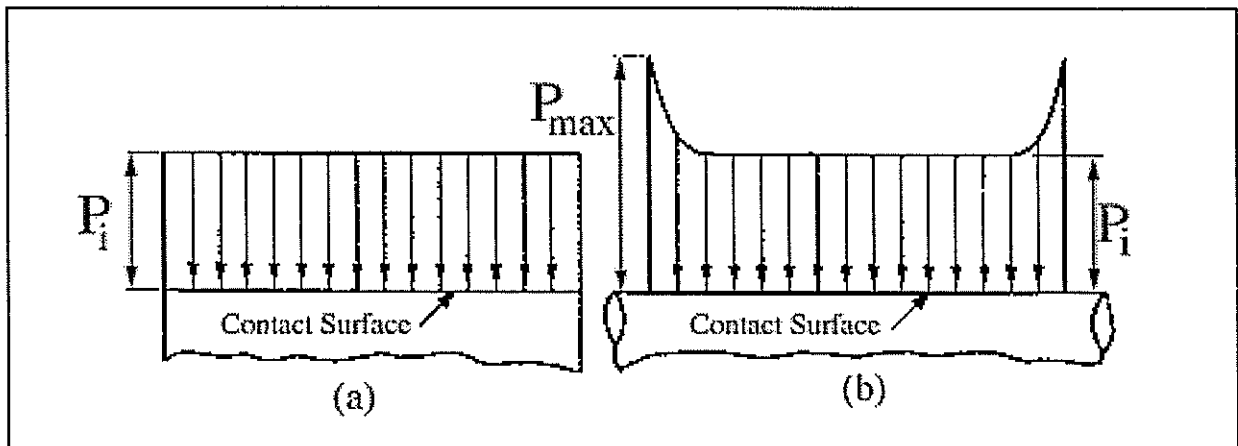


Figure 1.22 Shrinkage pressure. a) ideal b) real (after Crawford, 1970)

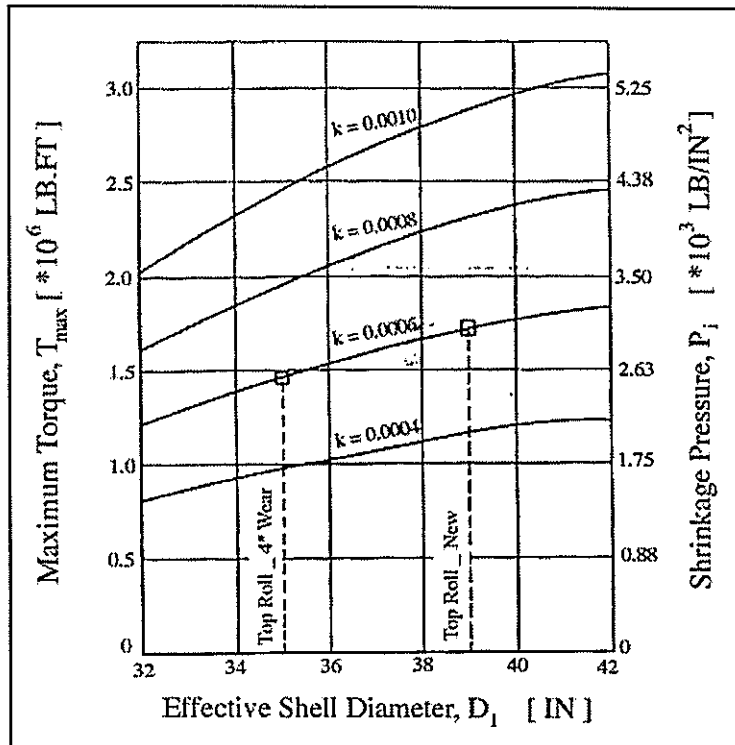
### 1.6.2 Maximum transmittable torque

The torque capacity,  $T_{\max}$ , of a roller utilising a shrink fit in place of keys, depends on the total force of limiting friction which is dependent on the surface area of landing, the pressure due to the shrink fit and the coefficient of limiting friction,  $\mu$ , as determined by:

$$T_{\max} = \frac{P_i \pi D_2^2 L \mu}{2} \quad (1.6)$$

where  $L$  is the length of shell under interference.

Equation 1.6 underestimates the maximum transmittable torque possible for a given interference fit as it does not take into account the pressure increase at the shell-ends. Crawford illustrated the maximum torque and shrinkage pressure in relation to various outer shell diameters and interference factors (Figure 1.23).



$$D_1 = 42 \text{ [in]} \quad (1.066 \text{ m})$$

$$D_2 = 23 \text{ [in]} \quad (0.584 \text{ m})$$

$$E_1 = 13.2 \cdot 10^6 \text{ [lb / in}^2\text{]} \\ (90.1 \text{ GPa})$$

$$E_2 = 30.0 \cdot 10^6 \text{ [lb / in}^2\text{]} \\ (206.7 \text{ GPa})$$

$$\nu_1 = 0.24$$

$$\nu_2 = 0.28$$

$$L = 82.5 \text{ [in]} \quad (2.096 \text{ m})$$

$$\mu = 0.1$$

Figure 1.23 Maximum torque transmission  
(after Crawford, 1970)

### 1.6.3 Division of roller torque

Crawford discusses the division of the output gearbox torque,  $T$ , between the pressure feed and main rollers. He concluded that a feasible breakup of gearbox torque between the rollers was:

$$\text{Pressure feed roller} = 0.0955 T (= 0.25 T / (2 \text{ feed rollers} * 1.31 \text{ gear reduction}));$$

$$\text{Feed roller} = 0.075 T;$$

$$\text{Delivery roller} = 0.3 T;$$

$$\text{Top roller} = 0.375 T.$$

This torque division was deemed necessary to find which roller's interference factor was most critical when effective shell diameters were considered. Crawford identified the top roller interference factor as the most critical.

#### 1.6.4 Axial stress in shell due to roller loading

Crawford estimated the maximum axial shell stress due to roll loads. The assumption that the roller is a simply-supported beam at the bearing centres and the loading is uniform over the shell length was used. The cyclic axial (bending) stress,  $\sigma_1$ , at the effective shell diameter (neglecting the groove stress concentration) is shown in equation 1.7.

$$\sigma_1 = \pm \frac{32}{\pi} \frac{M \frac{E_1}{E_2} D_1}{\left( \frac{E_1}{E_2} (D_1^4 - D_2^4) + D_2^4 \right)} \quad (1.7)$$

where M is the maximum bending moment.

Crawford also stated that the total axial stress at the effective shell diameter is a combination of the cycling stress,  $\sigma_1$  (roll loading and revolution), and the constant stress,  $\sigma_z$  (shrink fit). Therefore, every half revolution of the roller under load, the stress at the axial-centre location of the effective shell diameter surface would fluctuate from  $|\sigma_1| + \sigma_z$  (maximum), to  $-|\sigma_1| + \sigma_z$  (minimum).

#### 1.6.5 Discussion

Using structural mechanics, Crawford predicted the expected stress in a roller shell and explored the effect of roller geometry and material properties on stress. The interference factor for a roller (new or worn) should be sufficient to transmit torque values possibly 3 times larger (start-ups and mill stalls) than the average operating torque values. He concluded by saying that roll loading should be kept at a feasible minimum to lower the cyclic bending stress in the shell and shaft.

Although Crawford's work shed light on the shrink-fit induced stress state in the shell, there are some underlying limitations to his findings. They include:

- for the maximum transmittable torque predictions, no allowance was made for effect of roll loading and the associated change in the shell / shaft interface pressure distribution;
- no mention was made of the stress induced in the shaft from the shrink fit, especially at the region just under the shell-ends where shafts frequently break; and
- the effect of roll load on the interface pressure and associated stress state at the shell-ends was not considered.

## 1.7 Experiments on mill rollers

Cullen (1968) presented results from an extensive experiment to quantify stress in a roller shaft under various operating loads. Initially, a mathematical approach was considered. However, the mathematical assumptions required to account for the distribution of bearing loads, the effect of a rigid tailbar and roll load and lift on roller stress were deemed suspect. It was therefore decided that proper assessment of operating stress in a roller was only possible through experimentation. This quantitative evaluation of shaft stress was complicated by several factors:

1. The bending stress is dependent on the effective lever arm of the bearing reaction which was shown to vary with differing roll lifts;
2. The applied load for hydraulically loaded mills is known with some accuracy but the friction on the brass guides can only be assumed;
3. The rigid coupling connecting the shaft to the prime mover has a restraining effect on the floating roller which varies with drive and pintle lift and angular position of coupling;
4. Although the stress concentration factor at the fillet root decreases with increase in fillet radius, there is a limit to fillet size as larger fillets result in smaller shaft diameters remote from the effective bearing action-line and hence stress increases; and
5. The stress concentration effect at the end of the shell was not considered.

### 1.7.1 Experimental detail

The roller used for the experiment was the top roller of the final mill at Marian sugar factory. The shell length was 78 inches (1.981 m) and the effective shell diameter was 36 inches (0.914 m). Strain gauges were positioned on the shaft so that the bending and shear stress at both the drive and pintle-end and the torsional shear stress at the drive-end could be measured independently. A total of five stress data recordings were made for all combinations of set drive loads (226, 213, 200, 187 and 173 ton) with pintle loads set at a constant value (0, 18, 37 and 55 ton) less than the drive load. From the appropriate bending and shear stress, the effective lever arm and fillet bending stress were calculated for both pintle and drive-ends (Figures 1.24 through 1.27). The nominal lever arm for the roller was 10 inches (0.254 m, one half the journal length).

### 1.7.2 Pintle-end stress

Figure 1.24 shows that the measured pintle bending stress is higher than the theoretical value, calculated from pintle load and effective lever arm (distance from fillet to centre of load application in bearing) assumed to be at the centre. This can be explained by roll lift (higher on the pintle-end as drive-end movement is restricted by coupling interaction and higher hydraulic loads) and the associated increase in effective lever arm due to the slope of the shaft. Figure 1.25 shows the relationship between pintle lever arm and pintle load. The effective pintle lever arm appears independent of drive load.

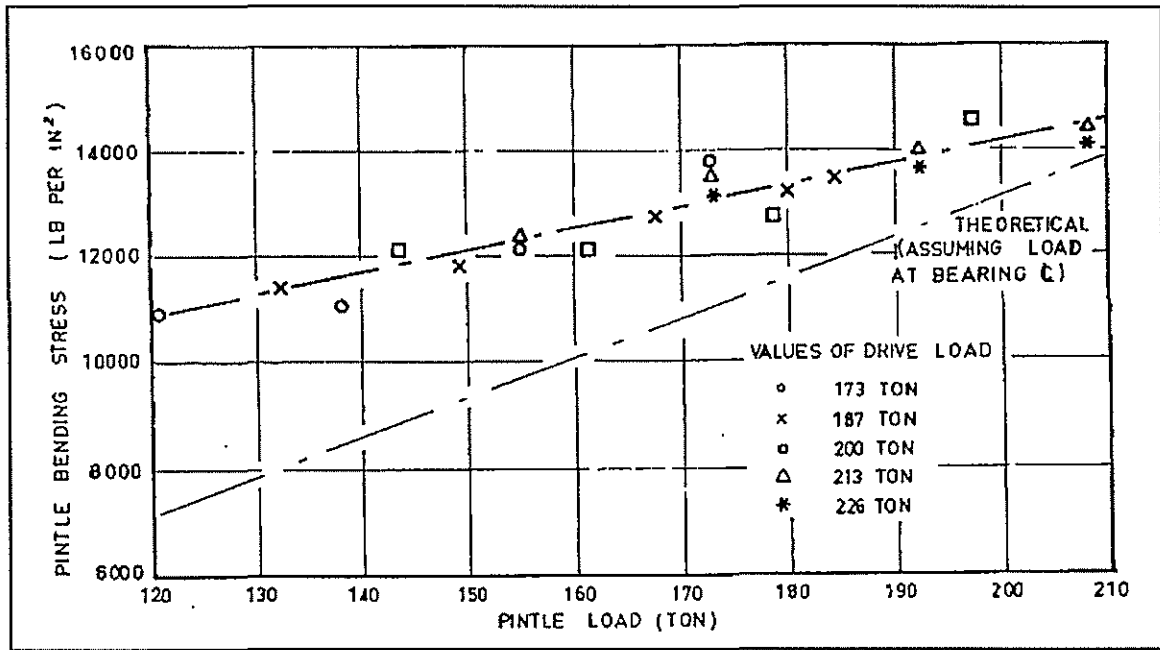


Figure 1.24 Pintle bending stress as a function of pintle load. (after Cullen, 1968)

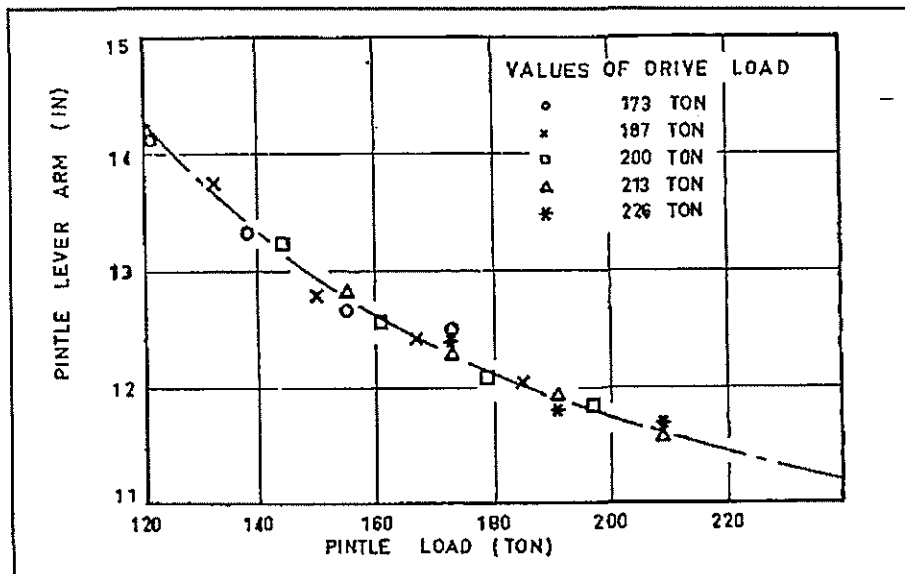


Figure 1.25 Pintle lever arm as a function of pintle load. (after Cullen, 1968)

### 1.7.3 Drive-end stress

Figure 1.26 shows the measured drive bending stress. Note, the theoretical stress is higher than the measured value. This again can be explained by roll lift (higher on the pintle-end for all loading conditions trialed) and the associated decrease in effective lever arm due to the slope of the shaft. The effective drive lever arm (distance from inside fillet to line of force action due to the hydraulic load, pinion reaction and tailbar reaction) is almost independant of drive load but dependant on the difference between drive and pintle loads (Figure 1.27).

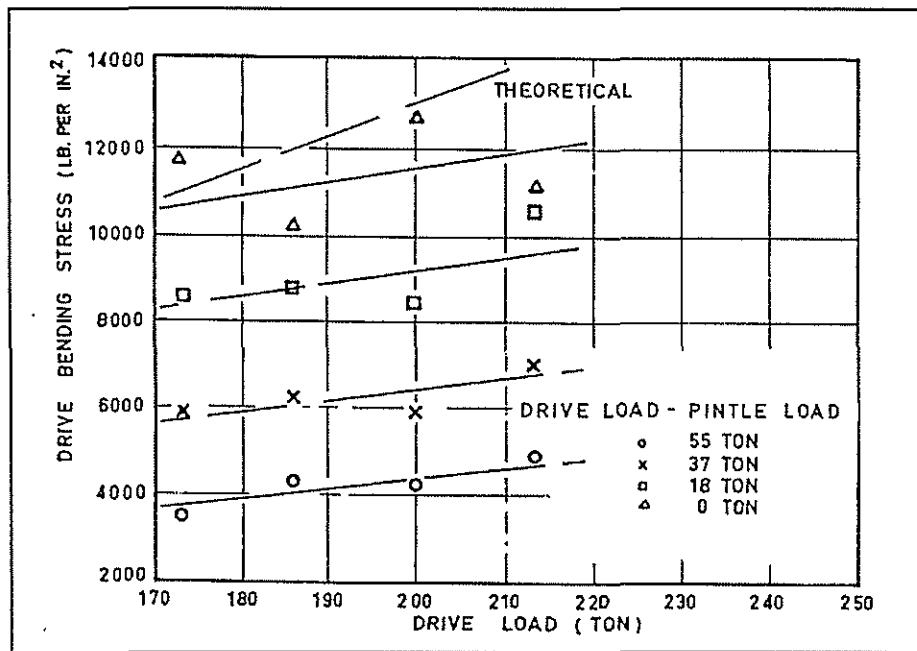


Figure 1.26 Drive bending stress as a function of drive load. (after Cullen, 1968)

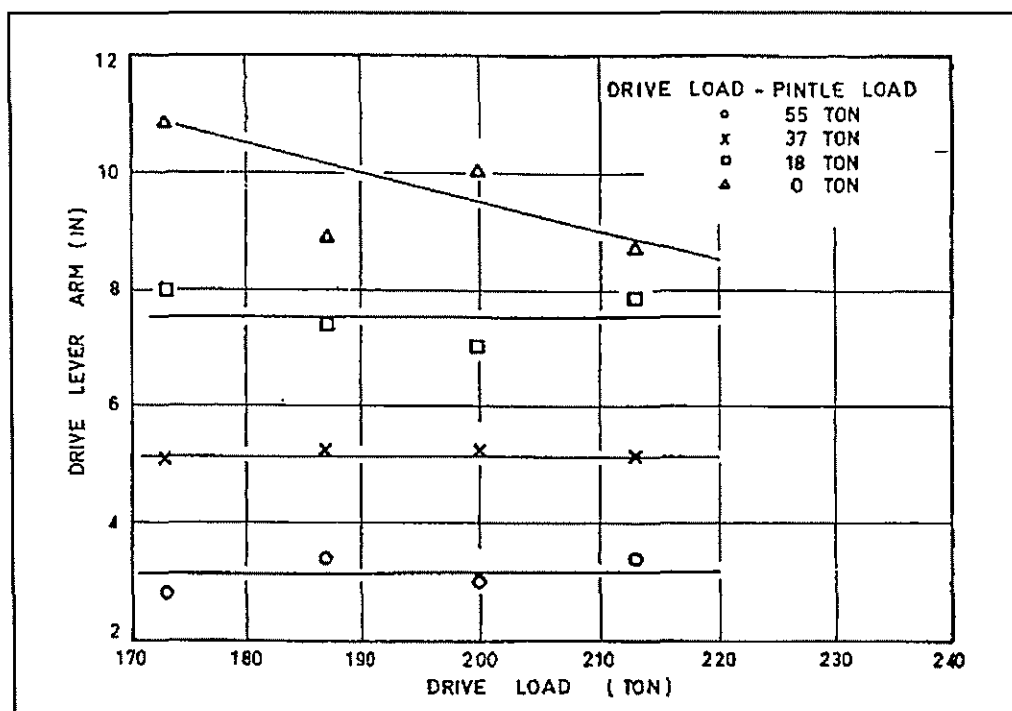


Figure 1.27 Drive lever arm as a function of drive load. (after Cullen, 1968)

Figure 1.28 shows the resulting vertical position of the shaft during experimentation. When the difference between drive and pintle loads is significant, the shaft tends to slope up towards the pintle-end causing the hydraulic load to move its point of application towards the inside fillet on the drive-end which effectively reduces the lever arm (Figure 1.28D). As the difference in loads reduces, the shaft levels out and the additional bending moment from the cantilever-like tailbar is reduced (Figure 1.28A).

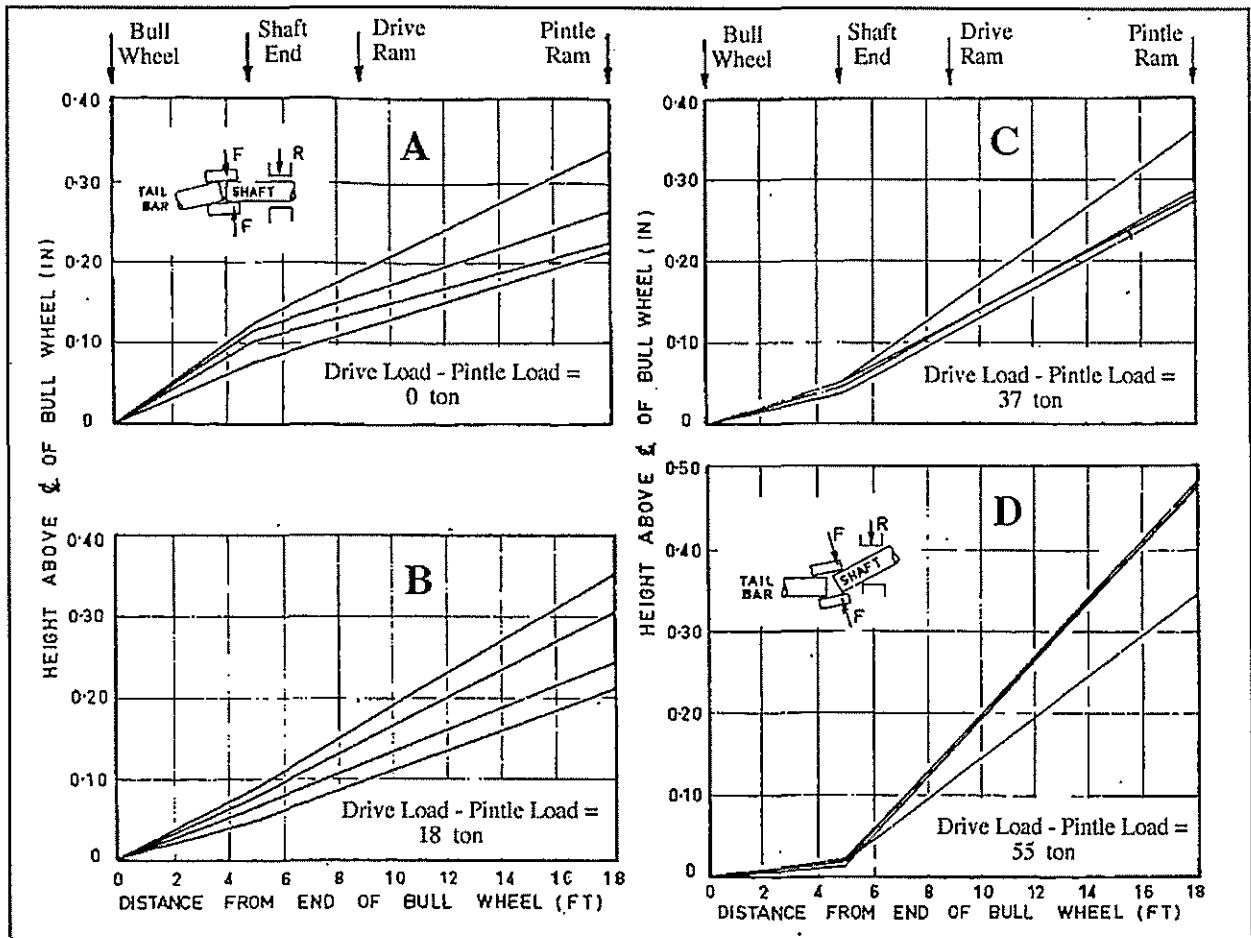


Figure 1.28 Vertical alignment of shaft during experimentation. (after Cullen, 1968)

#### 1.7.4 Drive-end torque

Torsional stress was recorded for several experimental runs with different combinations of drive and pintle loads. The most interesting result from the torque history was 18 fluctuations per shaft revolution. These fluctuations were approximately 30 per cent of the average torque value for reasonably low roll loads. The fluctuations were a direct result of the 18 tooth pinions contacting at non-optimal positions. The torque stress was found to have a definite relationship to load and the turbine chest pressure as well as the average roll lift. Multiple linear regression was used to quantify the relationship between torque (or shear stress) to roll load and lift (equations 1.8 and 1.9). These equations pertain specifically to Cullen's experimental mill set and should not be used in general shaft design.

$$T = 3.73 L + 835 h - 369 \quad (1.8)$$

$$S = 9.70 L + 2170 h - 960 \quad (1.9)$$

where

T = torque (ton in)

L = top roll load (ton)

h = average lift (in)

S = shear stress (lb/in<sup>2</sup>)

### 1.7.5 Discussion

Cullen devised suitable roller design philosophies from the stress levels measured during experimentation. For the drive-end journal design, Cullen suggests that the theoretical bending stress based on the load acting at the bearing centre, a safety factor of 1.4 to account for stress deviation experienced during testing and a torque load number of 0.085 are appropriate. For the pintle-end design, Cullen suggests that the theoretical bending stress based on the load acting two inches outside the bearing centre, the pintle torque is negligible and a safety factor of 1.3 will suffice. Cullen made mention of the endurance limit of shaft steels which was chosen at 45 per cent of the material's tensile strength.

Cullen concluded his work by suggesting several plausible methods for improving shaft life. He suggested that shaft stresses could be reduced by minimising operating loads and limiting shaft and tailbar misalignment. Experimental results indicated that the drive-end bending stress was a maximum when the roller sloped downwards with respect to the tailbar. Setting the centre of the drive-end down 1/8 inch from the centre of the bull wheel and the pintle-end up slightly above the bull wheel's centre line would improve this scenario. Brasses which align with the shaft journal would also be beneficial.

Cullen also mentioned that increasing shaft strength would improve the endurance limit. However, using a costly alloy steel with associated higher notch sensitivity would appear to offer no real advantage over existing shaft materials. Surface treatments including shot peening can improve the endurance limit by introducing compressive stresses into the highly stressed regions.

With regards to the geometric design of a mill roller, Cullen suggested larger fillets would result in decreased stress concentrations. Replacing the mill (box) coupling with a coupling which can transmit torque loads without imposing bending moments onto the shaft would eliminate shaft alignment problems.

## 1.8 Roll load estimations

Research into the effect of milling conditions on roll, torque and tailbar loads has continued since the 1960's. The mechanics of crushing bagasse is complex and has led to the formation of empirical approximations for determining roll loads with reasonable accuracy.

### 1.8.1 Roll pressure loading

Holt (1963) presented an empirical distribution for bagasse being processed between two rollers (Figure 1.29). Holt made the assumption that the distribution could be replaced by three piecewise functions.

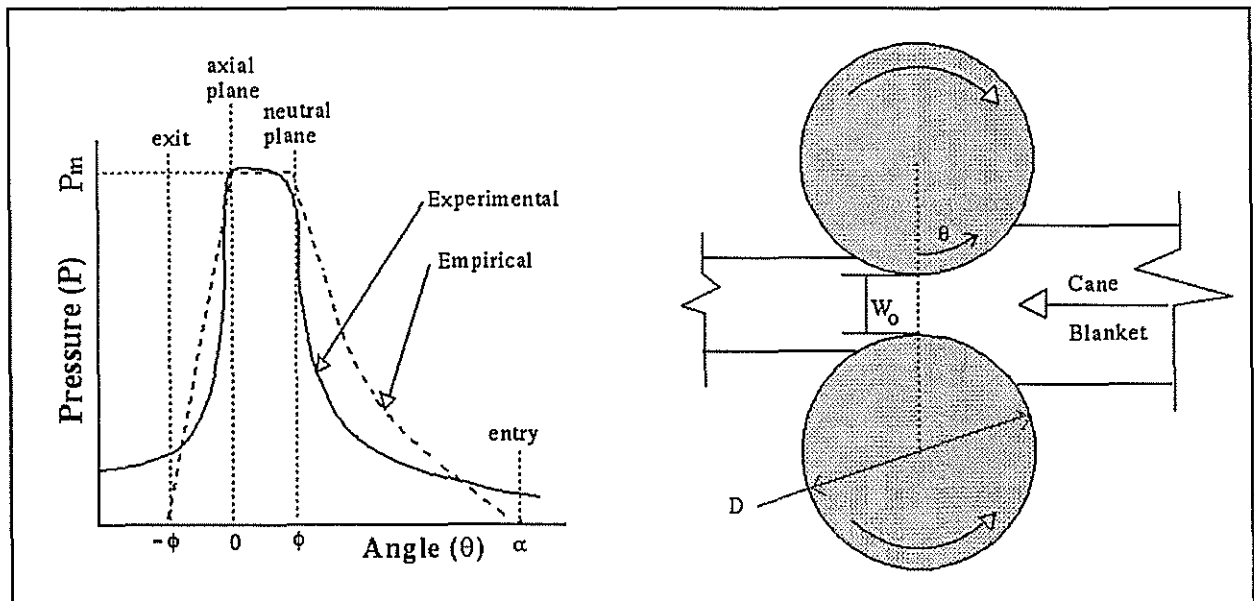


Figure 1.29 Experimental and empirical curves for pressure distribution.

A. Entry to neutral plane (parabolic form).

$$P = \frac{P_m}{(\alpha - \phi)^2} (\alpha - \theta)^2 \quad (1.10)$$

where  $\phi$  is angular position of neutral plane (Equation 1.11);  
 $\alpha$  is angular position of entry plane (Equation 1.12); and  
 $P_m$  is maximum pressure (Equation 1.13).

$$\cos(\phi) = 0.5 \left( 1 + \frac{W_o}{D} \right) + \left[ 0.25 \left( 1 + \frac{W_o}{D} \right)^2 - k \left( \frac{W_o}{D} \right) \right]^{0.5} \quad (1.11)$$

$$\cos(\alpha) = 0.5 \left( 1 + \frac{W_o}{D} \right) + \left[ 0.25 \left( 1 + \frac{W_o}{D} \right)^2 - \frac{q}{d_a S D} \right]^{0.5} \quad (1.12)$$

where  $W_o$  is work opening for roller set;  
 $D$  is average roller diameter;  
 $q$  is crushing rate per foot width of roller;  
 $d_a$  is density of feed material;  
 $S$  is roller surface speed (mm/s); and  
 $k$  is reabsorption factor ( $\approx 1.14$ ).

Solomon (1967) proposed that

$$P_m = 5.11 C_o - 0.00916 S - 3.72 \quad [\text{MPa}] \quad (1.13)$$

where  $C_o$  is overall compression ratio (ratio of no-void volume of prepared cane to escribed volume)

B. Neutral plane to axial plane (constant form).

$$P = P_m \quad (1.14)$$

C. Axial plane to exit. (linear form).

$$P = P_m \left( \frac{\theta}{\phi} + 1 \right) \quad (1.15)$$

Figure 1.30B illustrates the total pressure distribution acting on the top roller. Russell (1968) presented his findings relating to estimation of roll loads. He proposed the following relationship to estimate the total roll load for particular mill settings (Equation 1.16).

$$R_x = P_R L D (C_F - 0.1) \quad (1.16)$$

where  $P_R$  is proportionality factor ( $\approx 6.21$  MPa for no.1 mill set);  
 $L$  is the shell length; and  
 $C_F$  is filling ratio ( $\approx 0.1 C_o$  for 13.7% fibre fraction, Equation 1.17).

$$C_F = \frac{\gamma}{1530} = \frac{TCH F_f / (3.6 L W_o S)}{1530} \quad (1.17)$$

where  $\gamma$  is the compaction;

The denominator (1530) is the value for fibre density [kg / m<sup>3</sup>];  
 TCH is tonnage of cane crushed per hour; and  
 F<sub>f</sub> is fibre fraction.

In the case of a three roller mill, the top roller experiences normal and frictional loads from the trash plate, feed and delivery rollers. The normal loads are illustrated in Figure 1.30A.

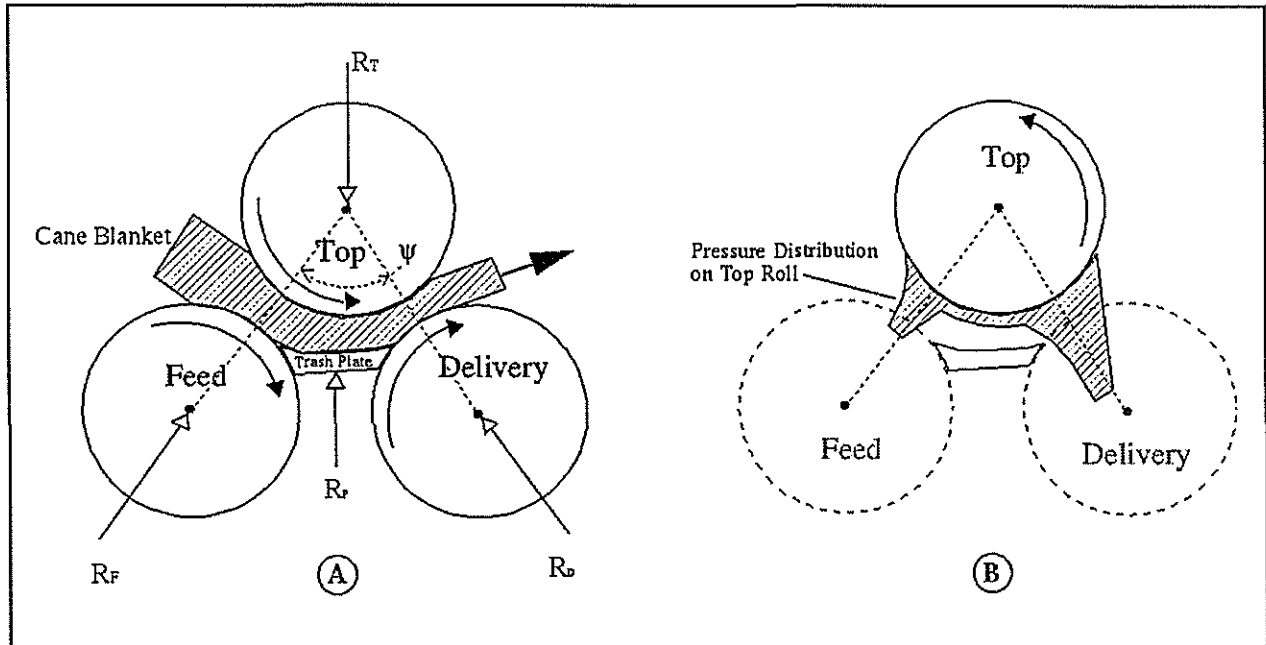


Figure 1.30 A) Normal load system. B). Combined top roll empirical pressure distribution.

Russell and Murry (1968) discussed the relationship to estimate the top roll load incorporating a factor, *m*, to account for the trash plate load (Equation 1.18).

$$m R_T = (R_F + R_D) \cos\left(\frac{\psi}{2}\right) \quad (1.18)$$

where  $R_T$  is top roll load;  
 $R_F$  is feed roll load;  
 $R_D$  is delivery roll load;  
 $\psi$  is apical angle for mill set (typically 72° to 74°); and  
*m* is a constant ( $\approx 0.9$ ), meaning 10 per cent of the top roll load is from the trash plate.

### 1.8.2 Roll torque loading

Murry (1960) postulated that roller torque was proportional to roll load and can be expressed using a torque load number,  $N_x$  (Equation 1.19) which was later derived from extensive experimental data by Munro (1964). The torque,  $G_x$ , utilised between two rollers is given in

Equation 1.20. The torque required to move the cane blanket over the trash plate,  $G_p$ , is approximated by Equation 1.21.

$$N_x = \left( \frac{P_N}{D} \right) \left( \frac{W_{ox}}{D} \right)^{0.5} C_{Fx}^{0.21} \quad (1.19)$$

where  $x$  (subscript) represents a particular roll nip and  
 $P_N$  is the proportionality factor ( $\approx 0.656m$ , for mill set number 1).

$$G_x = N_x R_x D \quad (1.20)$$

$$G_p = \mu (1 - m) R_T \left( \frac{D}{2} + W_{op} \right) \quad (1.21)$$

where  $\mu$  is friction coefficient ( $\approx 0.3$ ); and  
 $W_{op}$  is work opening for trash plate.

The total or drive torque,  $G_T$ , required for mill operation (neglecting brass friction and pressure feed roller torque) is the summation of the torque absorbed by the feed nip,  $G_F$ , the delivery nip,  $G_D$ , and by the trash plate,  $G_p$ . With regard to the top roller, the torque transmission is illustrated in Figure 1.31. The simplified breakdown of torsional loads on the top roller is approximated by Equations 1.22 through 1.24.

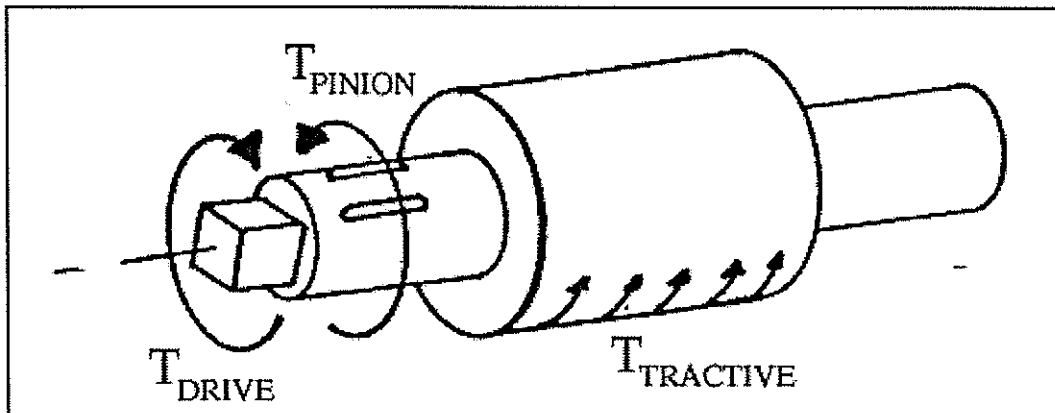


Figure 1.31 Torsional balance on top roller. (after Refalo, 1993)

$$T_{DRIVE} = G_T = G_F + G_p + G_D \quad (1.22)$$

$$T_{PINION} = \frac{G_F}{2} + \frac{G_D}{2} \quad (1.23)$$

$$T_{TRACTION} = \frac{G_F}{2} + \frac{G_D}{2} + G_p \quad (1.24)$$

### 1.8.3 Tailbar misalignment and associated loading

Box (mill) couplings are the most common coupling type used in Australian sugar factories due mainly to their simplistic design and low cost, even though they produce undesirable forces that effect the gear box and top roller. These additional forces generated at a box coupling include; radial and axial forces and bending moments, are developed when there is misalignment between the final gearing shaft and roller shaft. Mosert (1969) and Okamura et al (1972) estimated tailbar induced forces theoretically. Okamura conducted several experiments on a scaled down model of a typical coupling used in the sugar industry to validate the theoretical results. The experiments were conducted under various operating conditions with varying rotational speed, torque transmission, lubrication and distances between shaft centres. Figure 1.32 illustrates the free body diagram used by Okamura to develop equations 1.25 through 1.27.

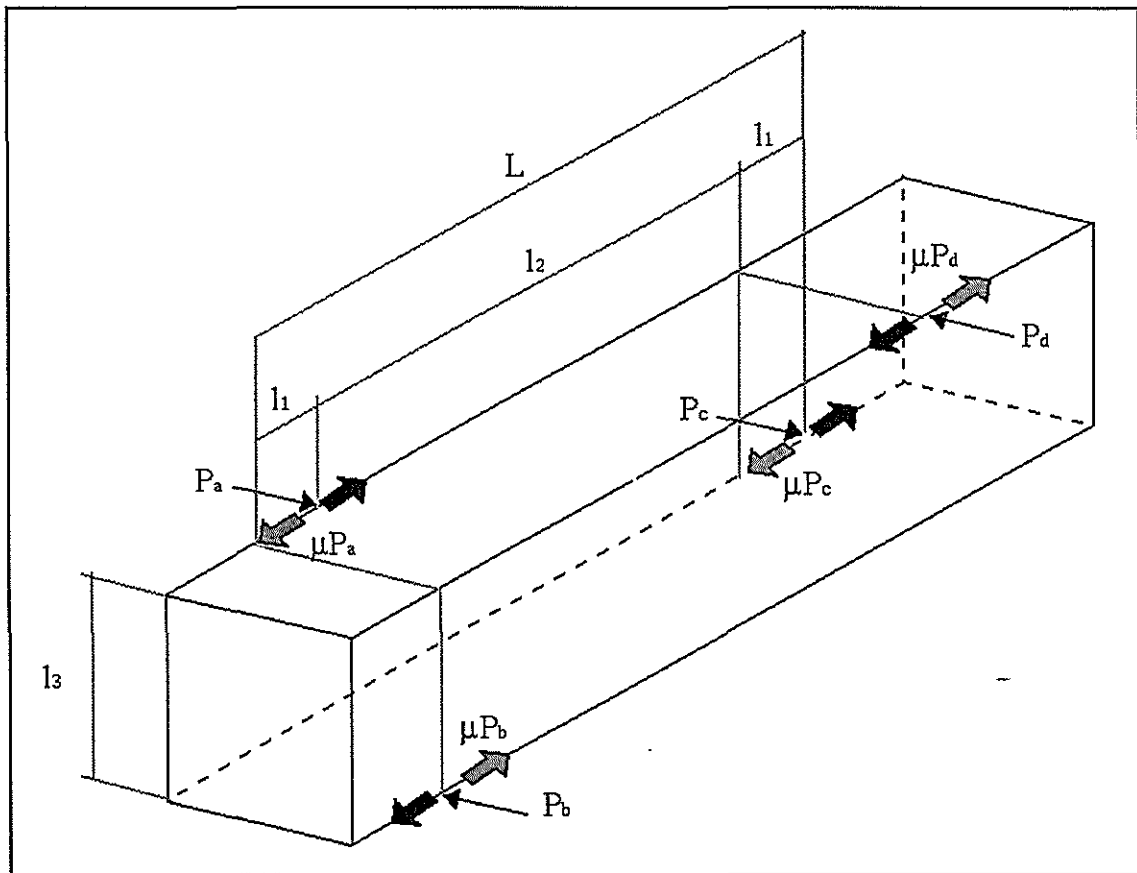


Figure 1.32 Free body diagram of tailbar. (after Okamura, 1972)

#### Radial force

$$F_r = P_a - P_b = \frac{4}{l_3} \left( \frac{l_1 \pm \mu l_3}{L + l_2} \right) T \quad (1.25)$$

Thrust force

$$F_t = \mu(P_a - P_b) = \frac{4}{l_3} \mu \left( \frac{l_1 \pm \mu l_3}{L + l_2} \right) T \quad (1.26)$$

Bending moment

$$\begin{aligned} M_c &= \left[ \left( \frac{l_1}{2}(P_a + P_b) + \frac{l_3}{2}\mu(P_a + P_b) \right)^2 + \left( \frac{l_3}{2}\mu(P_a + P_b) \right)^2 \right]^{0.5} \\ &= \frac{T}{l_3} \sqrt{(l_1 + \mu l_3)^2 + (\mu l_3)^2} \end{aligned} \quad (1.27)$$

where  $l_1$  is axial distance between two contact points;  
 $l_2$  is axial distance between two inner contacting points;  
 $l_3$  is square shaft width or pad width;  
 $L$  is effective length of square shaft; and  
 $T$  is transmitting torque.

Okamura's experimental results compared favourably with theoretical predictions. Experiments verified that the averaged additional forces were proportional to the transmitting torque. The variability of results were explained by the uncertainty of contact point locations which fluctuate during shaft rotation. As the difference between shaft heights was increased so did the measured forces. Interestingly, the radial force direction changes with positive and negative roll lifts. When the roller is higher than the gear shaft (positive lift), a downward radial force is exerted on the roller and vice versa. The addition of lubricant to the contacting surfaces lowered the forces generated. Okamura also trialed various coupling shapes and clearances between the coupling box and shaft and concluded that these had little effect on the extra forces. -

Okamura suggested that equations 1.25 through 1.27 would provide feasible design force values for a coupling. From his experience he implied that 0.3 was suitable for the coefficient of friction for coupling surfaces although it would vary with operating conditions. Based on experimental results, equation 1.28 provides an approximation for  $l_1$ , incorporating the length of the coupling box,  $l_{cb}$ , and roll lift,  $h$ .

$$l_1 = 6.5 \frac{h}{L} l_{cb} \quad (1.28)$$

## 1.9 Application of finite element modelling to roller design

This section summarises past finite element modelling of mill rollers to predict stress states and durability.

### 1.9.1 Simplified modelling of mill roller

Refalo (1993) investigated the operating stresses in a mill roller using finite element methods. The objective was to develop and analyse a detailed linear, three dimensional (3D) finite element model of a mill roller with realistic loads applied. Loads used were applied as mathematical fields based on Murry and Holt's empirical models (Chapter 1.8). Shrink-fit related stresses were validated using Crawford's work (Chapter 1.6).

Computing limitations at the time of Refalo's analyses restricted the mesh size of the finite element models which consequencely led to some inaccuracy in stress results. In addition, contact algorithms were unavailable, so a thermal analolgy was used to model the shrink fit of the shell onto the shaft. This involved the physical joining of the shell to the shaft which itself introduces inaccuracies in load sharing between the two. Suitable temperature differences were applied between the shell and shaft to simulate an interference fit.

Refalo's 3D models were constructed by revolving 2D quadrilateral elements about the shaft axis into 3D six node wedge and eight node brick elements. Figure 1.33 shows the mesh density of the 2D elements prior to revolution for Refalo's most detailed roller model. Tailbar and pinion loads were applied at the corresponding locations on the cylindrical shaft-end, roll loads were applied to the shell using a mathematical pressure distribution and boundary restraints were positioned on both bearing landings. On close inspection, Refalo's application of boundary restraints appear unsuitable as torque transmission is over restrained, resulting in unrealistic journal stress predictions.

Refalo concluded that the element size used throughout his work was too large to ensure confidence in the results. Although accuracy of stress results was hindered by computational power and software, the first insight into the complex stress states experienced by a roller was achieved. Refalo made several suggestions for future modelling of mill rollers, namely:

1. There is a need to investigate tapered shaft landing-ends or stress relieving grooves near the shell-end which may reduce shell-end stress due to the interference fit;
2. There is a need to examine the effect of material properties on operational stress;
3. There is a need to analyse the effect of grooves on shell life;
4. The 'PFATIGUE' software should be used to estimate shaft life for various surface finishes (Chapter 1.8.3);
5. The effect of shell failure on shaft stress should be assessed; and

6. Isoparametric elements should be used in place of less accurate linear based elements to reduce error in stress results, particularly in close proximity to the shaft fillet and shell-end regions.

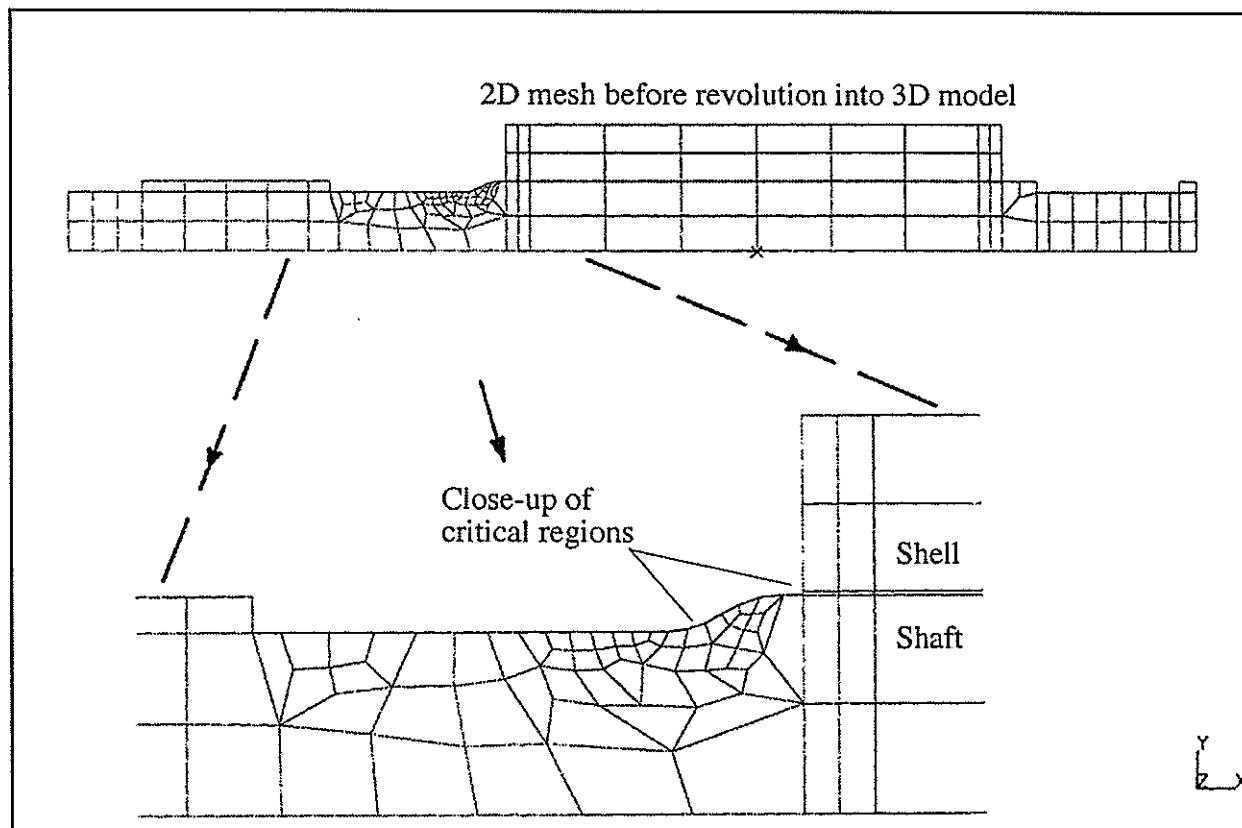


Figure 1.33 Element density on cross section of roller model. (after Refalo, 1993)

### 1.9.2 Modelling of roller shaft transition fillets

Ritchie (1994) continued the investigation of operating stresses in a mill roller using finite element methods. The objective was to explore in detail the roller shaft transition fillet. The investigation was directed at finding the cause of Refalo's inconclusive stress concentration results at the shaft fillet regions. Fatigue modelling of mill rollers was also undertaken to evaluate the application of durability analysis to locate possible design flaws in existing rollers and to explore the sensitivity of the roller's expected operating life to surface finishes and loading conditions.

Ritchie investigated the use of finite elements methods for analysing stress concentrations. Results were obtained for a stepped round shaft model with a shoulder fillet loaded in tension, bending and torsion. For each model, the finite element mesh was refined in the critical region, and stress concentrations were calculated from the analyses and compared graphically with theoretical values (Figure 1.34).

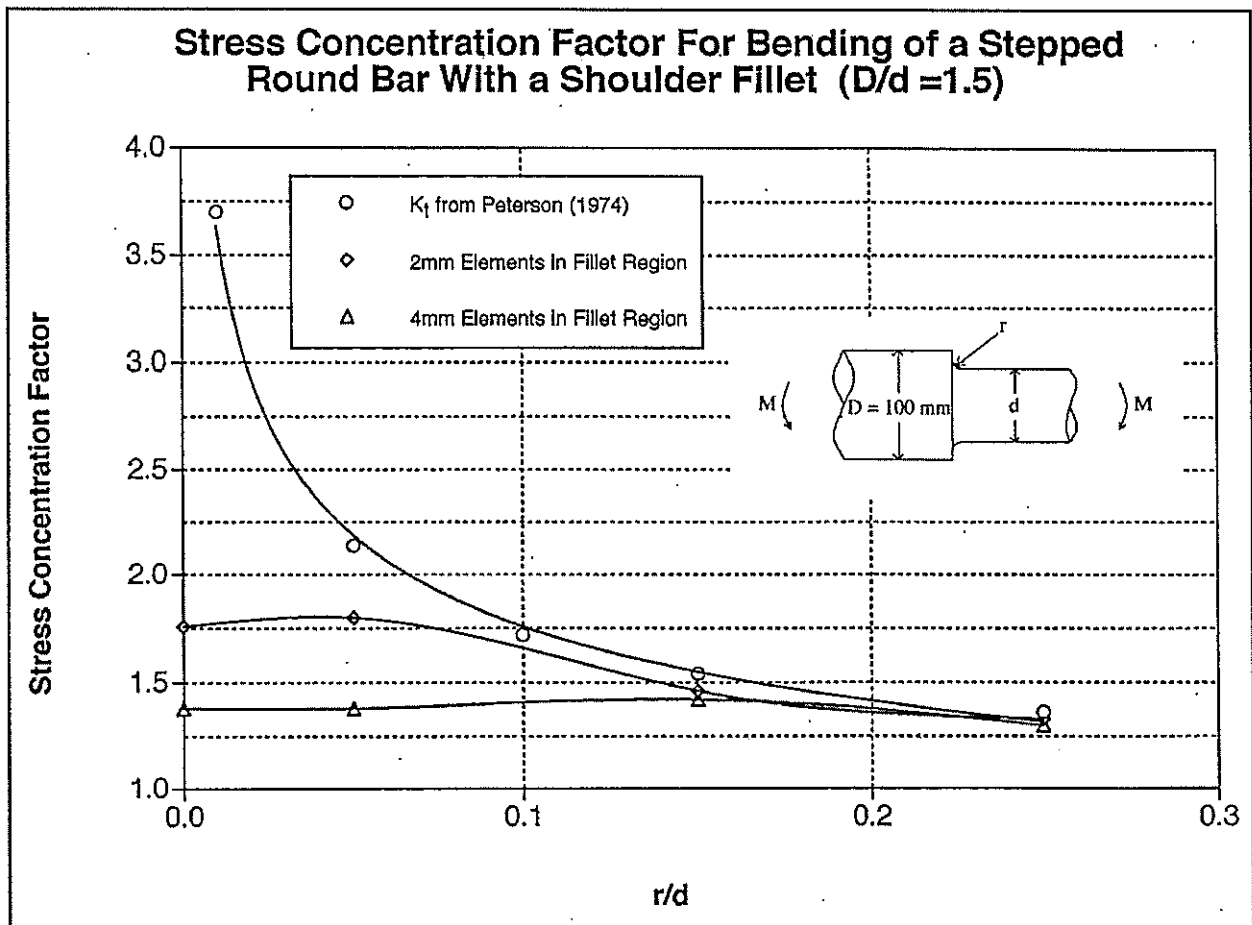


Figure 1.34 Comparison of theoretical and finite element based stress concentration factors for a stepped roller experiencing a bending moment. (after Ritchie, 1994)

Ritchie then modelled the 2.1 m roller investigated by Refalo. An improved method of restraint application was adopted to overcome the limitations of Refalo's modelling. However, like Refalo, Ritchie also used a thermal analogy to apply the shrink fit. The final model used in static and fatigue modelling is shown in Figure 1.35. Note the placement of roll loads and bearing restraints. As contact modelling was unavailable, Ritchie attempted to simulate the pressure distribution in the centre of a bearing by restraining a smaller area of the bearing whilst allowing rotation for torque transmission. Nodal forces were applied tangentially to the appropriate regions to account for the drive, pinion and shell tractive torque loads. Loads used were, drive torque (1.2 MNm), pinion reaction torque (0.53 MNm), shell tractive torque (0.67 Mnm) and roll load (2.14 MN/m or 66.4 tonne/ft). The resulting Von Mises stress in the 25 mm fillet region was approximately 150 MPa compared to 278 MPa from Refalo's result. The contrast in results can be explained by the differing use of bearing restraints between models. Refalo's stress results are clearly suspect in this region as they are beyond the yielding limit for shaft steels (approx. 250 MPa).

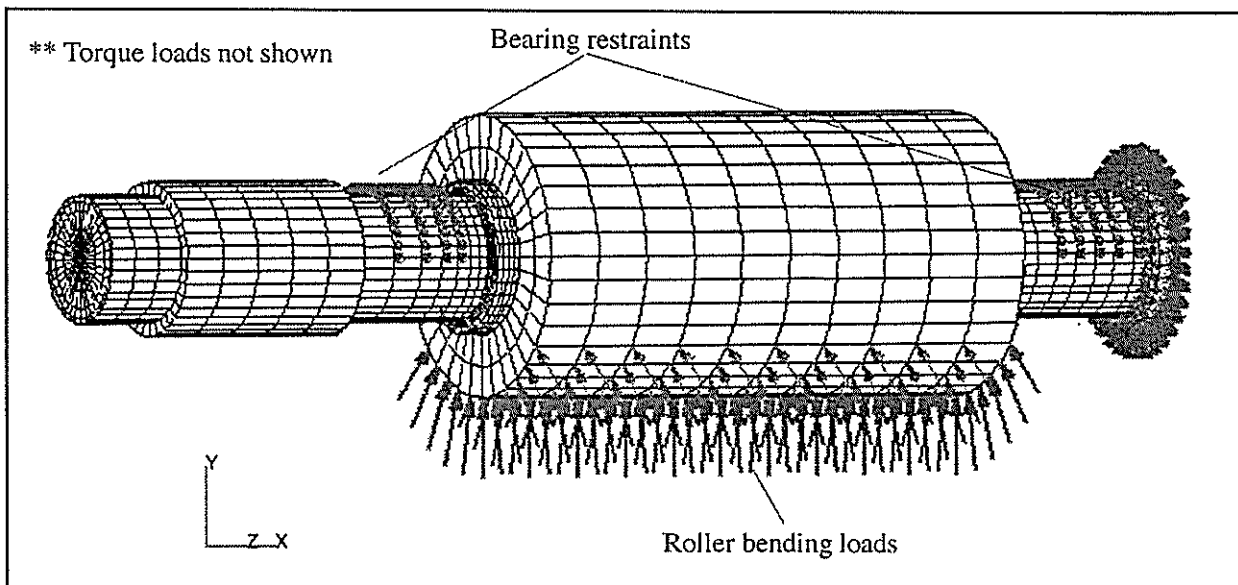


Figure 1.35 Three dimensional model showing roll loads and bearing restraints. (after Ritchie, 1994)

### 1.9.3 Durability modelling of mill rollers

Durability assessment of a roller has been attempted in the form of a series of crack initiation exercises (Ritchie, 1994 and Loughran *et. al.*, 1995). To simulate a rotating roller under load (6 rpm), cyclic roll loads were applied to a stationary model in addition to constant torque loading. This simplified modelling approach was adopted to reduce computational time during fatigue prediction analyses. Approximate crack initiation results (life estimation neglecting crack propagation time) for a roller shaft made of SAE1030\_85A\_HR under an increased roll load (88.3 tonne/ft or 2.83 MN/m) for various surface finishes is shown in Table 1.1. In this case the crack initiation point was on the shaft at the shell-end region. No crack initiation resulted from a roll load of 66.4 tonne/ft (2.13 MN/m).

Table 1.1 Life estimates for roller shaft for varying surface finishes. (after Ritchie, 1994)

Surface Finish	Life Estimation (crushing days)
Polished	1698
Ground	951
Good Machined	625
Averaged Machined	411
Poor Machined	301
Hot Rolled	255
Forged	89
Cast	82
Water Corroded	117
Seawater Corroded	39

The current method adopted by the Australian sugar industry for determining maximum allowable roll load per unit shell length,  $R$ , (equation 1.29) was derived by assuming that the roller is simply supported at the bearing centres. Equation 1.29 is based on the S-N approach for determining component life. Assumptions involved with equation 1.29 include:

1. Shaft failure will occur in the fillet region and not under the shell-end;
2. The shaft is free from cracks developed during previous operation;
3. There is no residual stress (from heat treatment and interference fit) in the fillet region;
4. The effect of torsional shear stress is negligible;
5. There are no tailbar misalignment forces transferred to the shaft;
6. The centre of bearing pressure is known; and
7. The effect of shaft size, surface finish and corrosion effects on the endurance limit is known.

$$R = \frac{\sigma \pi D_b^3}{16 L L_f K_f S_f} \quad (1.29)$$

where  $L$  = Shell length,  
 $L_f$  = Distance from bearing centre to inner drive-end fillet radius,  
 $K_f$  = Fillet stress concentration factor,  
 $S_f$  = Service factor ( $\approx$  safety factor)  
 $\sigma$  = Allowable fatigue limit stress, and  
 $D_b$  = Bearing landing diameter.

As mentioned, equation 1.29 neglects shear stresses induced by torque transmission. Ritchie questioned this assumption and via several basic calculations found that the Von Mises stress in the fillet region increases by approximately 20 to 30 per cent when shear stresses are coupled with bending stress.

#### 1.9.4 Discussion

Refalo and Ritchie have presented a feasible modelling strategy for use on mill rollers. Ritchie suggested an appropriate element size to reduce modelling errors in critical regions. Initial fatigue modelling highlighted two sensitive regions on the shaft for crack initiation to occur, i.e. the drive-side inboard fillet and shell-end regions. Durability analysis provided information regarding the importance of adequate surface finish and the detrimental effect of corrosive sugar juice on the predicted operating life of a roller shaft. Suggestions regarding the use of finer mesh densities in the fillet region and improved modelling of the bearing / shaft interaction were made.

### 1.10 Objectives of finite element modelling

Reviewing the literature regarding mill roller design and operation has aided in setting achievable milestones for this investigation. They involve the use of finite element (FE) modelling to:

1. Evaluate stress states in roller shell and shafts;
2. Explore the feasibility of alternative designs for mill rollers; and
3. Investigate the fatigue resistance of the mill roller under varying conditions.

Asymmetrical loading of the roller shaft dictates that three dimensional (3D) modelling will be required. Torque, tailbar and roll load effects on the roller necessitate 3D analysis. However, 2D axisymmetric modelling of the interference (shrink) fit stress will suffice for assessing the effect of varying interference tolerances on roller stress. PATRAN and ABAQUS (standard) computer codes are used for the investigation.

In Chapter 2, the work by Refalo (1993) and Ritchie (1994) is furthered with the aid of 3D contact modelling so that the complex interactions between shell and shaft and shaft and bearings can be scrutinised. could be reproduced using finite element modelling. Comparisons between modelling results and past experimental findings (Cullen,1968 and Crawford, 1970) were made whenever possible. A better understanding of the complex stress states in rollers should result.

In Chapter 3, highly stressed regions from the initial FE modelling will undergo design changes and re-analysis in the attempt to lower operating stress and the risk of fatigue failure. Alternative geometry and materials will be investigated. Plausible design changes from an engineering and economic standpoint will be discussed.

In Chapter 4, work relating to critical crack sizes in the fillet region and shell-end region of a roller shaft will be reported. A better understanding of the critical crack sizes to improve condition monitoring and operating techniques when dealing with fatigued roller shafts should result.

# *Chapter 2*

*Finite element modelling –  
existing roller design and practice*

## **2.0 Finite element modelling - existing roller design and practice**

This chapter reviews the finite element modelling (FEM) of a mill roller and discusses the results. FEM was utilised to better understand the stress states in a mill roller during normal factory operation. Finite element analysis (FEA) has several advantages over existing experimentation and design procedures which are generally expensive and time consuming. FEA can result in stress and deflection predictions for design changes to a component with sufficient accuracy, in a fraction of the time and effort, as compared to multiple prototyping and experimentation or photoelastic testing.

Although FEA is beneficial to designers, experience is necessary when interpreting results as solutions are to some degree blurred by boundary restraints and load application. The FEA process itself does induce small errors as material properties and behaviour are assumed and loads and boundary restraints are applied to best duplicate anticipated operating conditions. Resulting stress values and deflections should be checked by hand calculations or compared to past experimental results where possible to exclude the possibility of errors in modelling.

Modelling in this investigation has concentrated on the stress states in the vicinity of the inboard journal fillets and regions under the shell-ends. The literature review highlighted that the majority of roller failures occur at these locations. Failures do occur in other regions on a mill roller, such as the outside centre of the shell, the tailbar fillet region and pinion landing keyway. However, as these failures are relatively uncommon, only the critical regions were finely meshed to obtain the stress states resulting from a variety of loading scenarios. Applied roll loads are based on empirical equations (Chapter 1.8).

Several 2D axisymmetric models were analysed to assess the induced stress states resulting from various interference fits for different shell diameters (worn shells), shell material properties and shaft designs. These results were compared to theoretical values and predictions made by Crawford (1970). 3D modelling followed to evaluate stress states induced by roll loads, torque transmission, bearing contacts, tailbar loads and misalignment, interference fits and combinations of the above. Where feasible, theoretical calculations and comparisons with experimental results (Cullen, 1968) were made.

This modelling has demonstrated several improvements on previous applications of FEA to mill roller designs (Refalo, 1993 and Ritchie, 1994). The major advancement has been the ability to model the shell / shaft contact whereas previous investigations had the shell physically joined to the shaft with temperature differences applied to each to simulate the interference fit. The effect of this will be discussed in Chapter 2.2. The ability to model contact between two 3D deformable bodies also permitted the shaft / bearing interaction to be assessed without a prior knowledge of contact patterns. Previously (Refalo, 1993 and Ritchie, 1994), shafts were restrained in locations

assumed to be contacting with the journal bearings. With increased computing power, finer mesh densities were used in critical shaft regions to further improve modelling accuracy.

Figure 2.1 shows schematically the software used in this investigation.

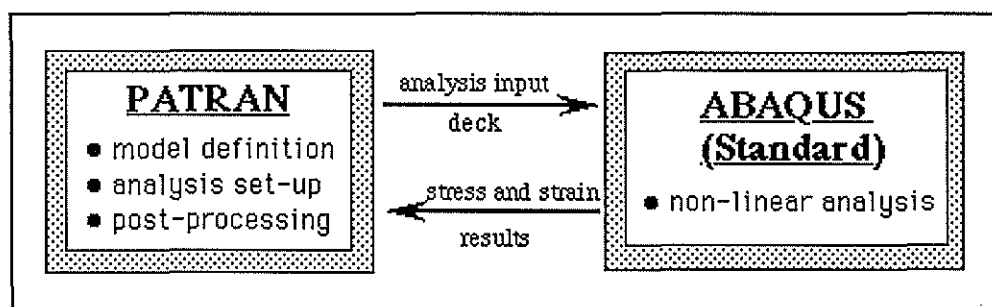


Figure 2.1 Interaction of software packages. (after Anderson, 1995)

PATRAN (P3), a finite element code, was used to create the mill roller models. Loads, boundary restraints and material properties were then assigned, after which input decks (model definitions) were produced for analysis. Some modifications to the input decks were required to specify contact surface pairs. ABAQUS (standard), a versatile and robust non-linear solution code, was used to solve the input decks. Stress and deflection results were then read back into PATRAN for post processing.

## **2.1 Interference fit - 2D finite element modelling**

Interference (shrink) fits to secure shells onto shafts were adopted by the sugar industry approximately forty years ago to replace the key design. Interference fits have several distinct advantages over key designs, namely: the shell puts the shaft under compression; the shell transfers a greater portion of the bending moment away from the shaft; and the stress concentration due to the key way is removed, all of which improve the expected life of the shaft.

The essential requirement of an interference fit is that the friction between shaft and shell be sufficient to transmit the maximum torque expected for crushing, remembering the shell diameter will reduce from operational wear. The stress developed in a shell which has been shrunk onto a shaft can be approximated using the theory described in Chapter 1.6. Such theory is currently used in mill roller design. However, designers are still unsure of the stress states in the shell and shaft near the end of the interference zone (shell-end). The size of the anticipated stress concentration effect in this zone is unknown. To relieve this stress concentration, designers have trialled tapered shaft profiles at the end of the shell landing. FEA was undertaken to explore various interference geometry and to better understand interference fits and associated stress states.

### **2.1.1 Preliminary modelling and results**

Initial FE models to evaluate interference fit stress states were undertaken on a six foot (1.830 m) top roller (see Appendix A1 for detailed drawing). This preliminary modelling was necessary to develop satisfactory analysis techniques, such as suitable mesh density, restraint application and procedure for resolving the initial overclosure. Changes in stress states due to decreasing shell diameter and differing interference factors were investigated. An additional model without the tapered shaft-end design was analysed for comparison.

During reshelling, shafts are commonly machined to remove any signs of corrosion. This process also removes the tapered geometry on the shaft, therefore returning the shell landing back to the parallel design after the first reshell. Final interference fit modelling (Chapter 2.1.2) was performed on a seven foot roller (most common shell length in Australian factories) with a parallel shell landing (Appendix A1). Associated sensitivity analyses can be found in Chapter 2.1.3.

Figure 2.2 shows the typical mesh arrangement used for modelling the interference fit for the six foot roller. Roller symmetry allowed 2D axisymmetric modelling of one half of a roller.

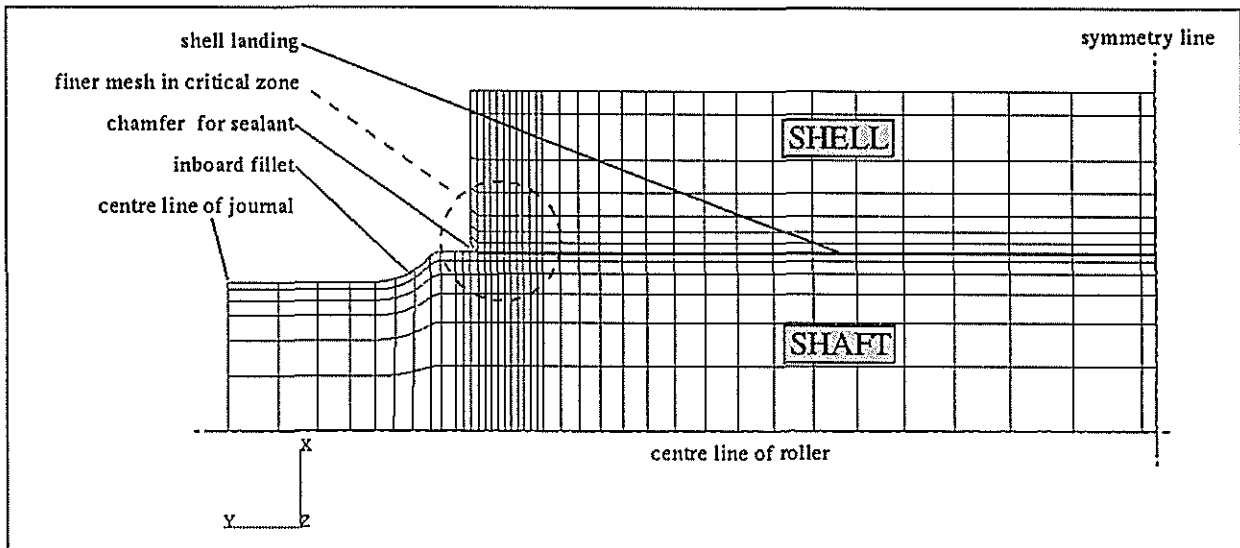


Figure 2.2 Typical 2D axisymmetric model layout for 6 foot roller interference fit analysis.

Contact modelling involved defining two surfaces, one on each of the contacting bodies (ie. shaft and shell). During analysis, the ABAQUS code continually ensures that nodes on the 'slave' surface (shell bore) do not penetrate through the 'master' surface (shaft).

Two methods were trialed for resolving the initial overclosure between the shaft and shell. The first method utilised the 'contact interference' option in the ABAQUS code. In this situation, the ABAQUS code alleviates the pre-calculated overclosure for each 'slave' node over a specified time. The second method involved heating the shell at a uniform rate until the inner shell surface (slave) cleared the shaft surface (master), followed by uniform cooling of the shell back to its initial temperature, whereupon the shell squeezes down onto the shaft. The resulting stress states from the two methods differed by relatively small shear stress ( $< 5$  MPa) developed at the contacting surfaces. The second method (heating and cooling of the shell) was adopted for this investigation as it was intuitively more realistic and closely followed the assumptions made by Crawford (Chapter 1.6) for calculating the interference fit stress.

The following parameters were used for the modelling (Model A), unless otherwise stated:

$D_1$ (effective shell diameter)	= 915 mm	$D_2$ (shaft landing diameter)	= 483 mm
$E_1$ (elastic modulus for shell)	= 120 GPa	$E_2$ (elastic modulus for shaft)	= 207 GPa
$\nu_1$ (Poisson's ratio for shell)	= 0.26	$\nu_2$ (Poisson's ratio for shaft)	= 0.30
inboard fillet radius	= 100 mm	bearing landing diameter	= 400 mm
$k$ (interference factor)	= 0.0007	and $\mu$ (coefficient of friction)	= 0.10

Figure 2.3 illustrates the shell-end region of the two shaft designs modelled. The shell and shaft are displayed overlapped to highlight the initial overclosures of the interference geometry. Although machining inaccuracies are common in roller manufacture which would result in slight variations in stress states predicted, the shell bore and shaft were considered concentric for modelling purposes.

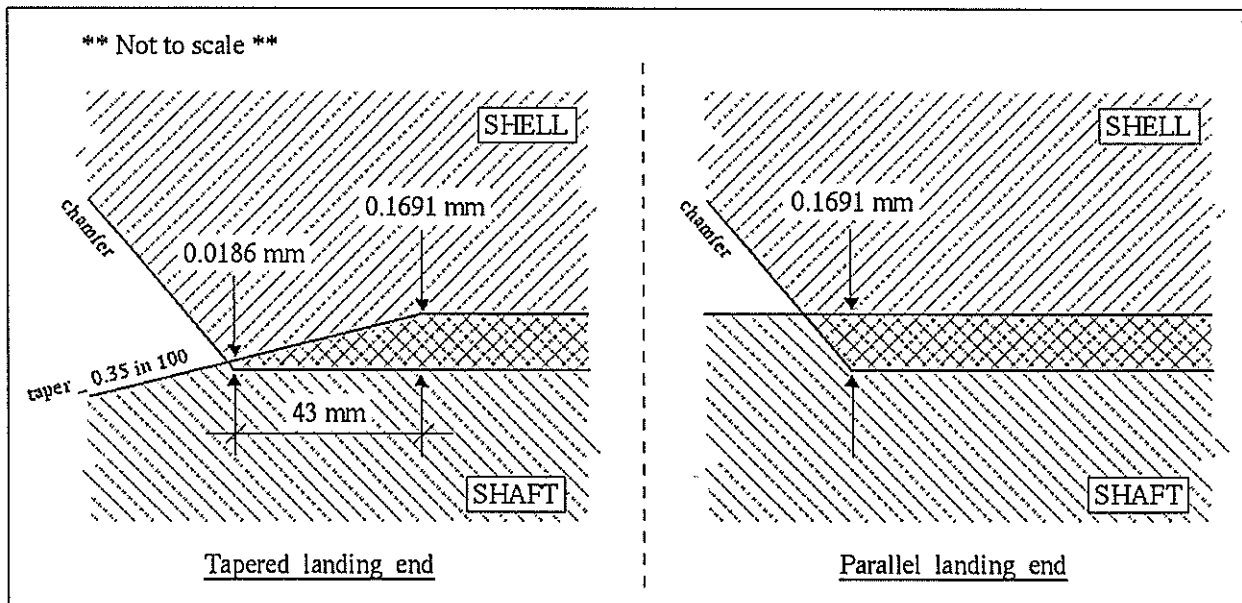


Figure 2.3 Close-up views of initial overclosure (shell-end) of 6 foot roller geometries modelled.

By definition, the effective shell diameter is taken between the tooth profile centres. The effective shell diameter was taken to the tooth tips to simplify the preliminary modelling. The results relate to the tapered shaft landing design for the six foot roller. Figures 2.4 through 2.10 show the results of the interference model A analysed.

Note, that the induced axial stress state displayed in Figure 2.7 does not include the stress concentration effect of the grooves, as these were suppressed. However, the affected region would intuitively be in close proximity to the outer shell surface and not in the critical area at the shaft / shell junction.

Model variations involving different interference factors and effective shell diameters were analysed. A model containing a finer mesh arrangement in the tapered-end region of the shaft (Figure 2.11) and a model containing a parallel landing-end in place of the tapered geometry (Figure 2.3) were also analysed. Both models were based on the original parameters used in 'Model A'. The radial stress states for these two analyses are displayed in Figures 2.12 and 2.13 respectively. Table 2.1 lists the results for the interference modelling of the six foot roller.

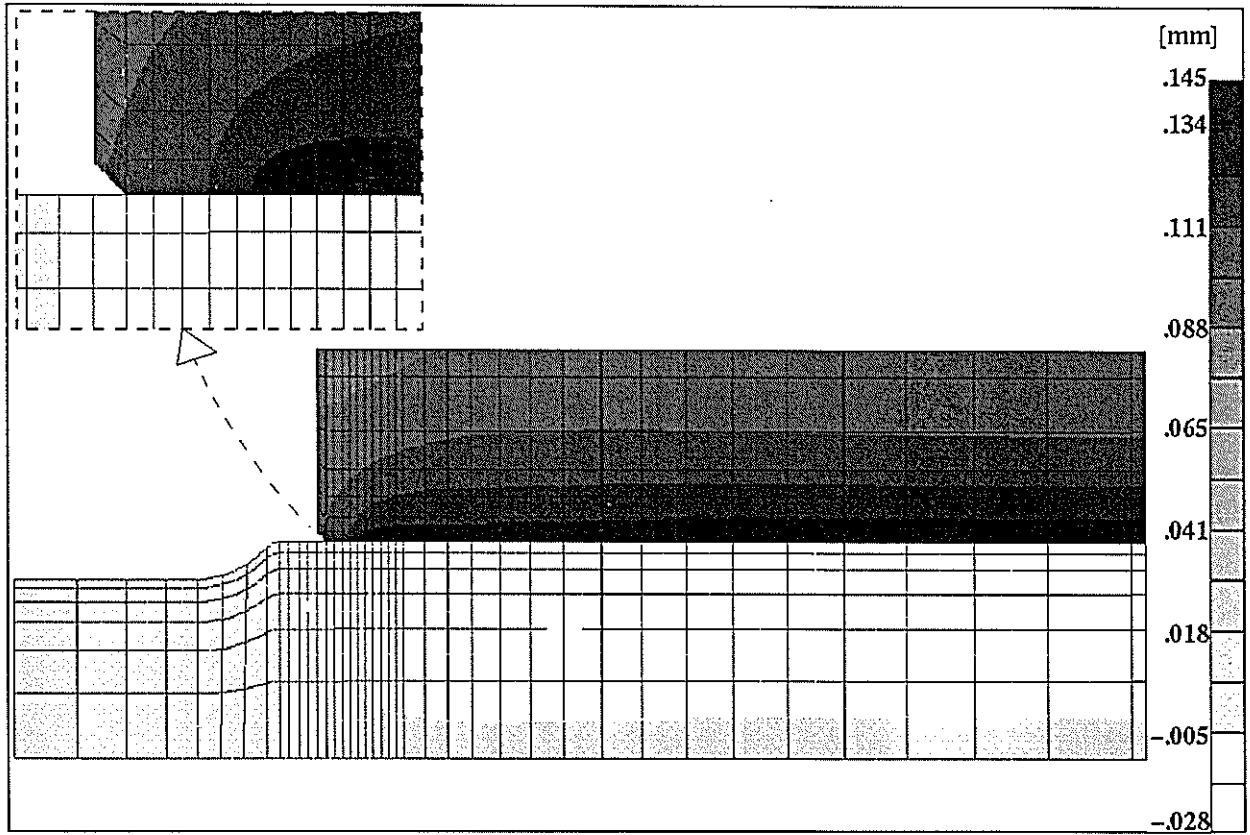


Figure 2.4 Radial displacement plot for interference model A.

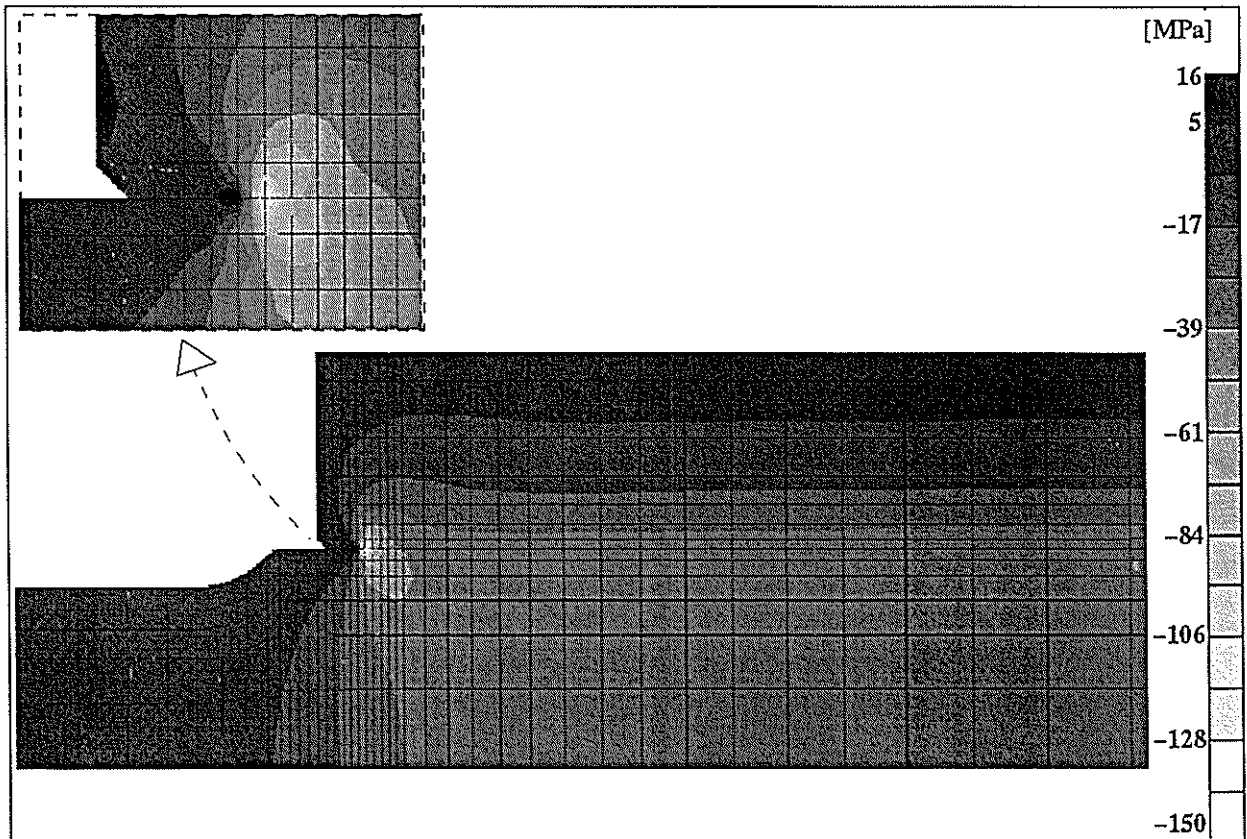


Figure 2.5 Radial stress plot for interference model A.

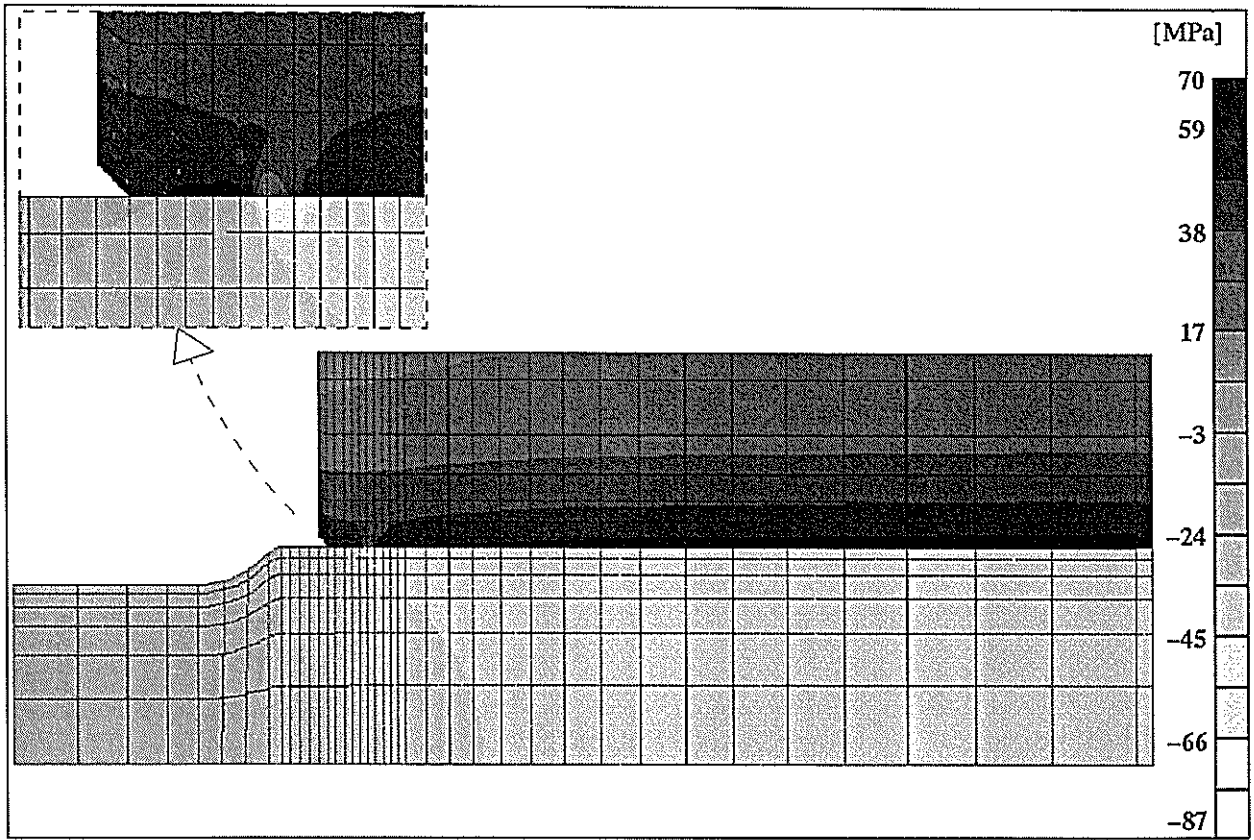


Figure 2.6 Hoop stress plot for interference model A.

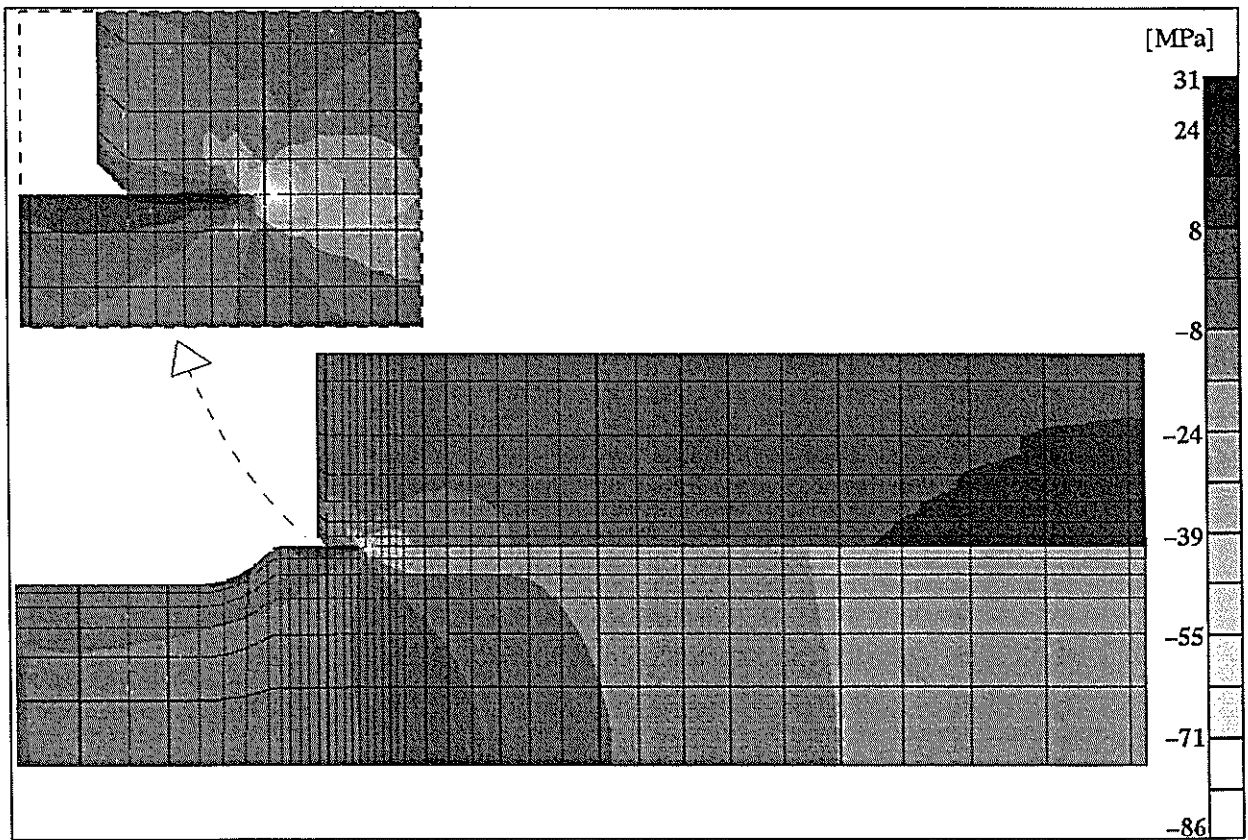


Figure 2.7 Axial stress plot for interference model A.

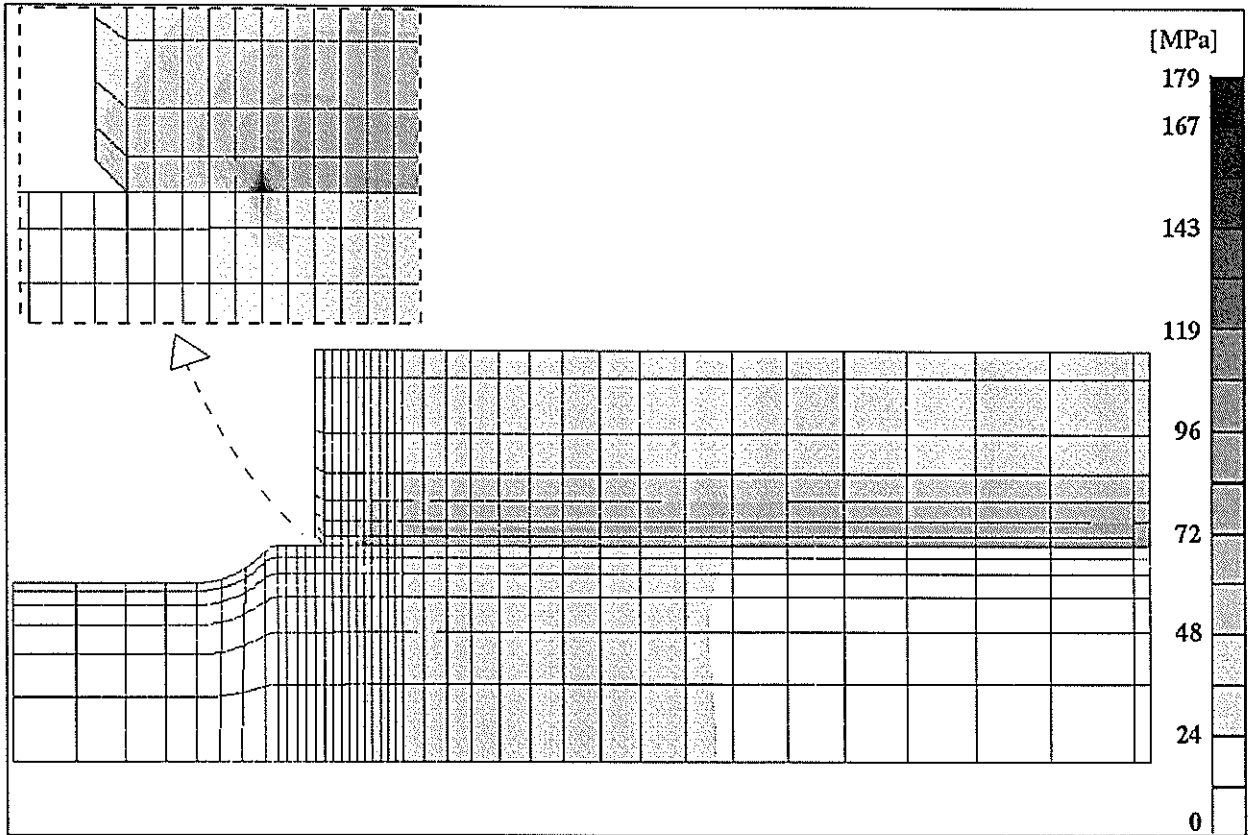


Figure 2.8 Von Mises stress plot for interference model A.

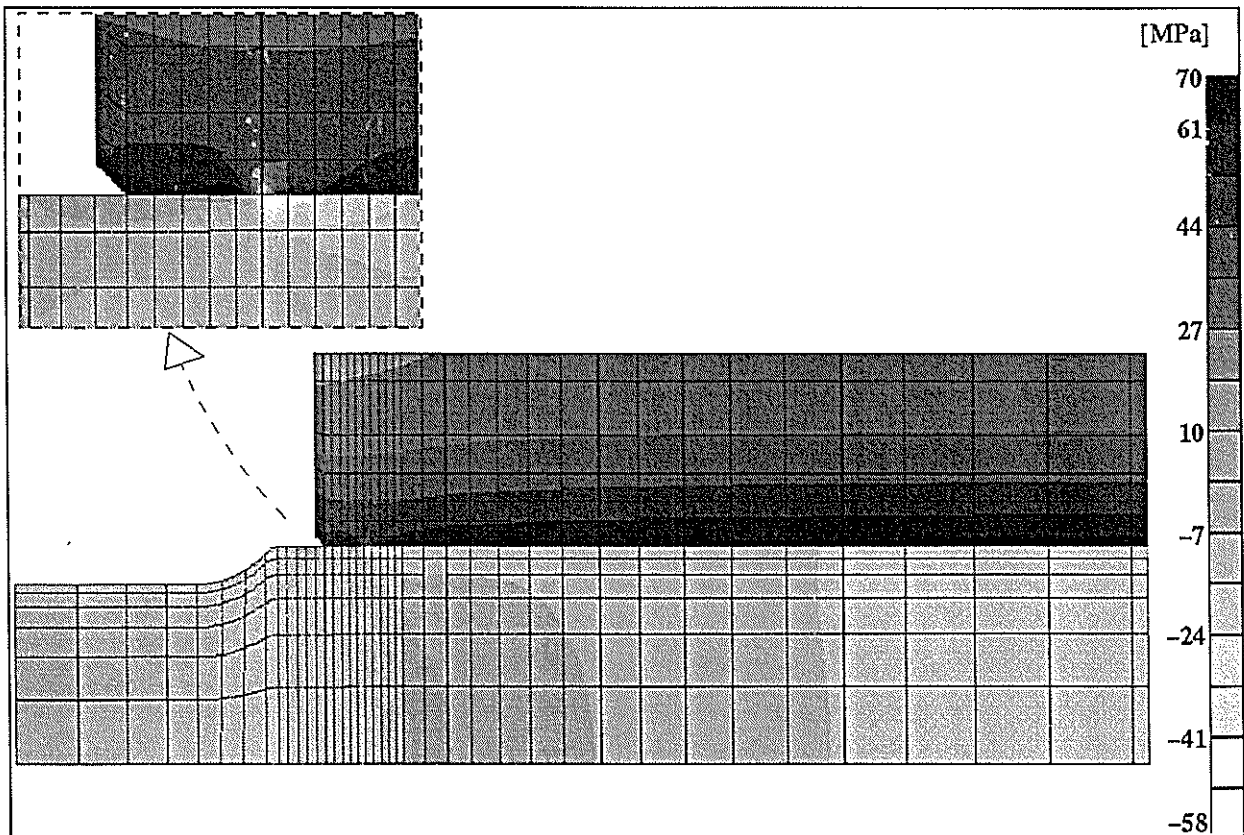


Figure 2.9 Major Principal stress plot for interference model A.

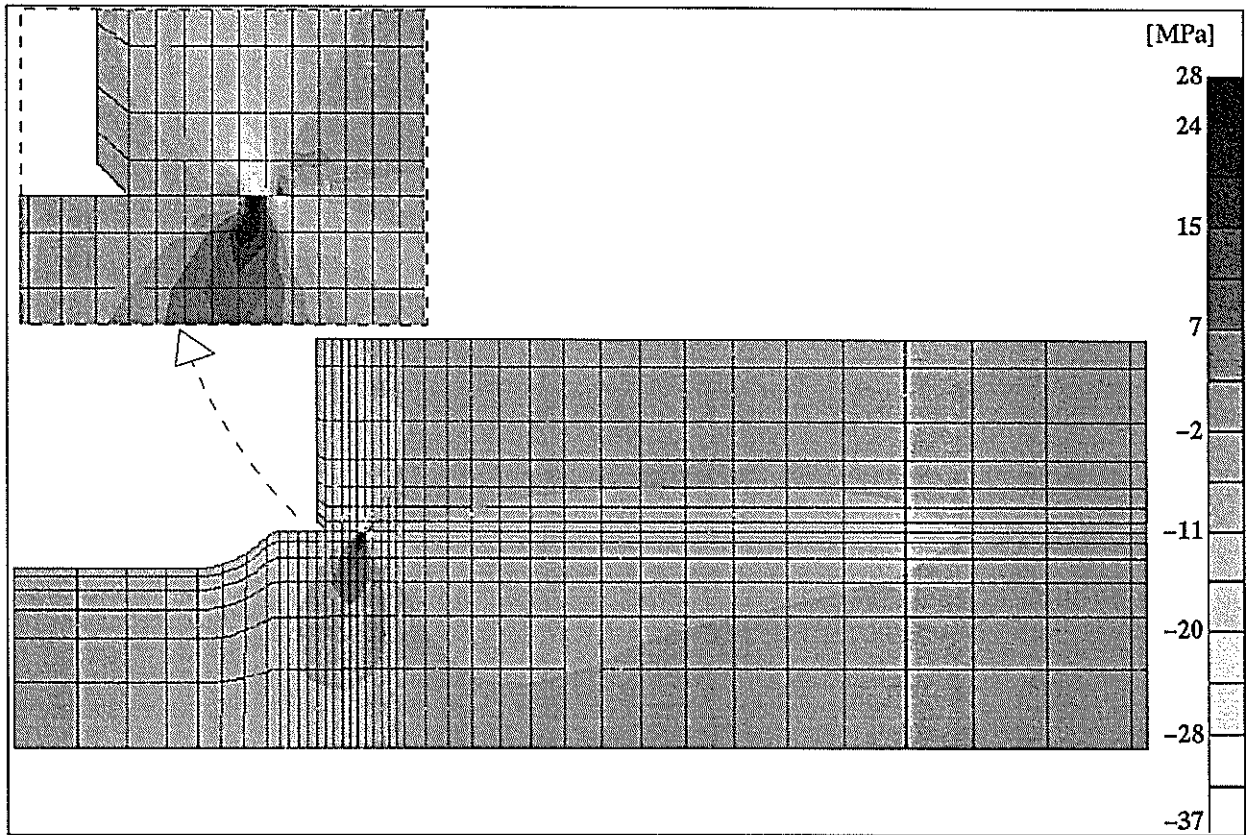


Figure 2.10 Planar shear stress plot for interference model A.

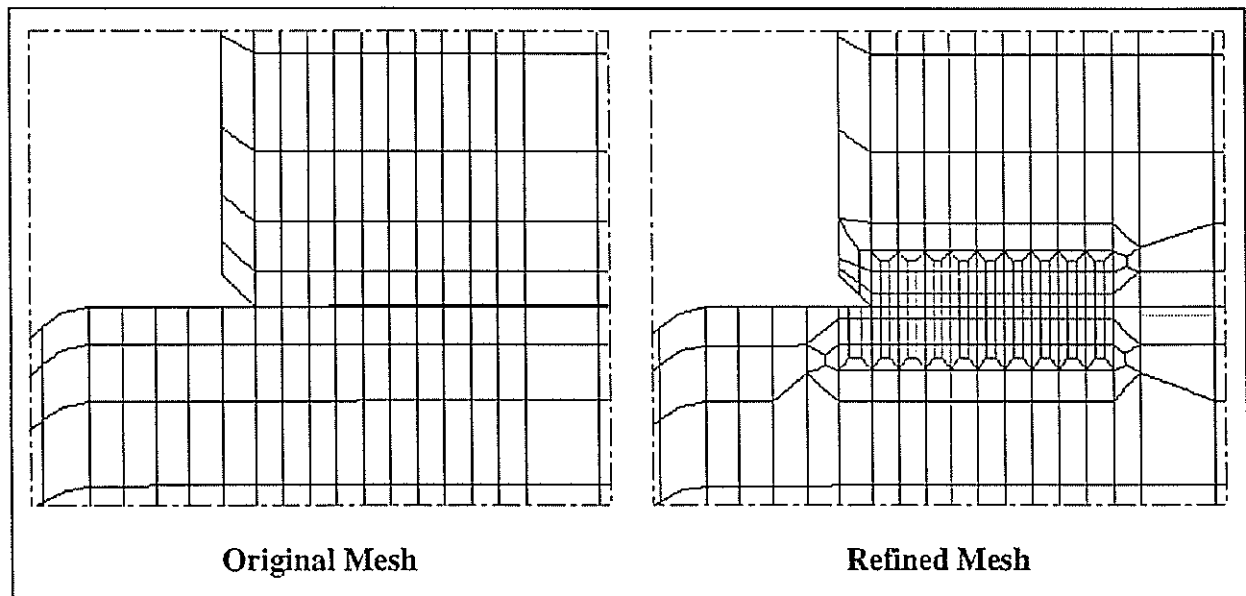


Figure 2.11 Close-up of shell-end region detailing mesh refinement at critical region.

Typical element size in the critical zone for the original mesh model was 11.3 mm by 8.6 mm as compared to 4.5 mm by 2.9 mm for the refined mesh model.

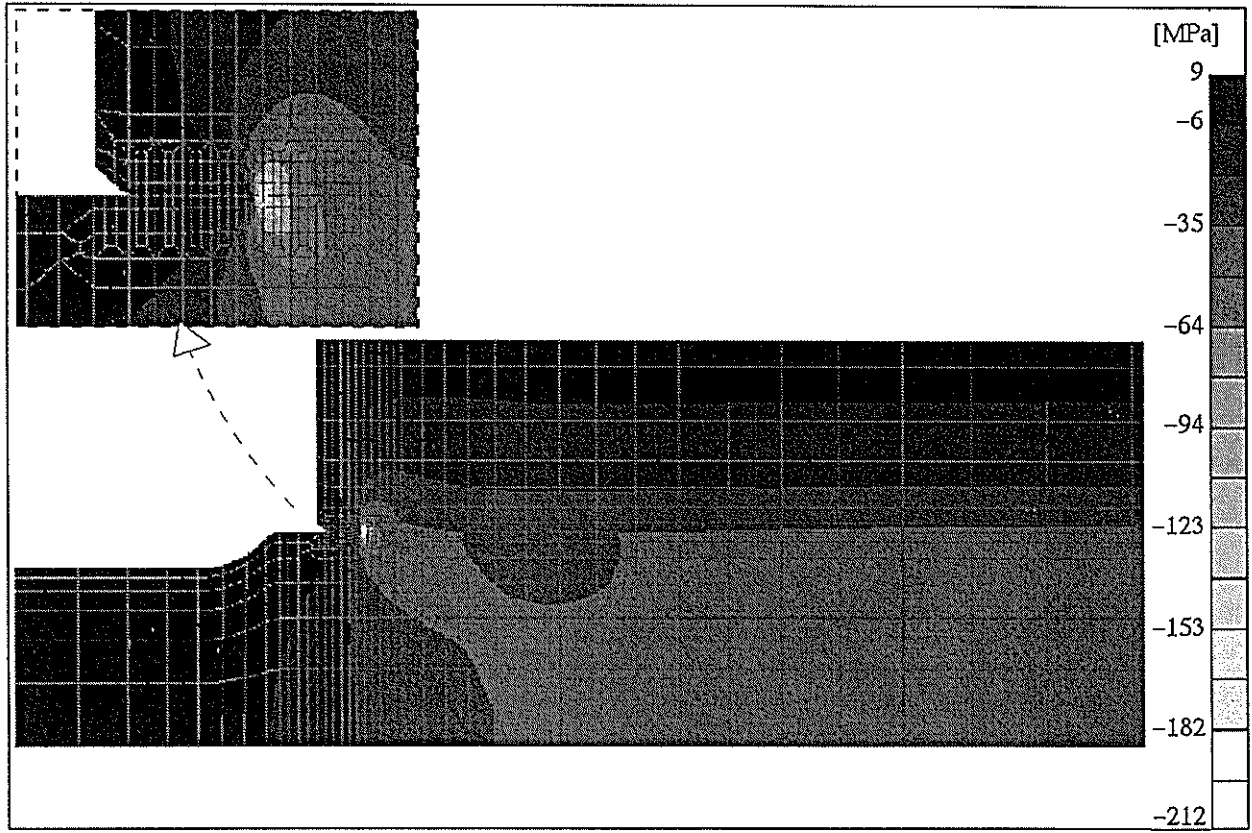


Figure 2.12 Radial stress plot for interference model A with refined mesh.

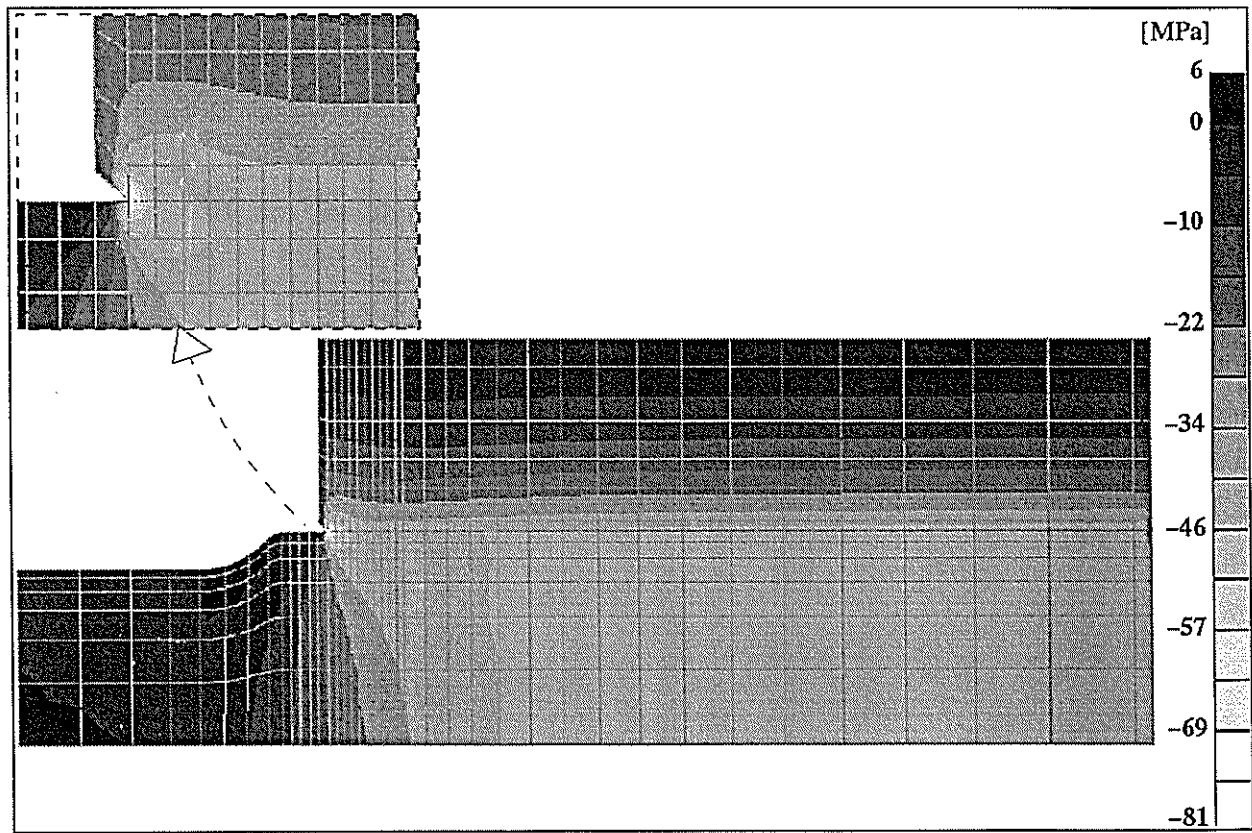


Figure 2.13 Radial stress plot for interference model A with parallel fit and original mesh.

Table 2.1 Interference fit modelling results for the six foot roller

Model Description	Interference Factor, k	Shell Diameter D <sub>1</sub> [mm]	Maximum Von Mises Stress [MPa]	Radial Stress* [MPa]		Hoop Stress* [MPa]		Major Shaft Stress [MPa] Landing, Fillet
				Exp., Theor.	Compressive	Exp., Theor.	Tensile	
original mesh + tapered landing	0.0007	915	179	36.9, 34.5	150	64.6, 61.1	69.5	32.8, 13.7
original mesh + tapered landing	0.0007	853	175	34.5, 32.2	145	66.2, 62.6	70.0	31.1, 12.9
original mesh + tapered landing	0.0005	915	129	26.2, 24.6	108	45.9, 43.6	49.8	23.5, 9.8
original mesh + tapered landing	0.0005	853	126	24.5, 23.0	104	47.0, 44.7	50.1	22.3, 9.2
original mesh + parallel landing	0.0007	915	121	37.1, 34.5	81	64.6, 61.1	69.0	20.6, 14.0
refined mesh + tapered landing	0.0007	915	190	37.0, 34.5	207	64.5, 61.1	70.2	36.3, 13.6

\* Experimental stress values were taken at the shell's contacting surface close to the centre line of the shell so as to avoid boundary and end effects

\*\* Major principal stress induced in the shaft was extracted at two critical regions, the inboard fillet and the area just outside the contacting zone

Preliminary modelling of the six foot roller provided insight into the stress states associated with interference fits. Several major findings resulted, including:

1. The effect of mesh size on stress results;
2. The inadequacies of the tapered shaft-end design;
3. The stress induced in the shaft fillet and shell-end region; and
4. The general effect of shell design parameters on the hoop and radial stress values.

Results displayed in Table 2.1 highlight many characteristics of interference fits used in roller design. The increase in stress where the shell-end contacts the shaft was evident for all analyses. This end-effect mentioned by Crawford (1970) is best illustrated in Figure 2.13 (radial stress or pressure) where the stress contour lines raise up at the shell-end indicating a sudden rise in stress. Unfortunately, the stress concentration effect at the end of the interference fit was not finalised during modelling as mesh refinement induced a comparatively large increase in stress values compared to that obtained from the original mesh. It is believed that this sudden change in geometry at the shell-end or shaft-taper caused a singularity in modelling which cannot be rectified with mesh refinement. Fortunately, the effected area of increased stress is refined to the location of last contact between shaft and shell. Stress remote from this location remained unaffected by mesh refinement suggesting that the mesh density used in the majority of the 2D models was adequate for analysing interference fit stress. The stress concentration effect at the shell-end was predicted to be approximately two for a parallel interference fit. Hence it is suggested that the mesh size chosen for future modelling of the shell-end should be such that the induced radial stress be approximately twice the theoretical value for a particular interference design.

Stress states analysed for the tapered shaft geometry highlighted inadequacies in this design technique. Results indicated that the final point of contact between the shaft and shell was at the beginning of the shaft's taper. Hence the taper was too steep to account for shell deflection and would effectively reduce the supporting length of the shell on the shaft, leading to an increase in shaft bending stress at the shell-end. Figure 2.3 indicates that the initial overclosure of the shell and shaft is 0.0186 mm at the shell-end for the tapered design. This value corresponds to an interference factor of 0.0007 (maximum). For the minimum interference factor, 0.0005, there would be an initial clearance between shell-end and shaft. A resulting gap between shell-end and shaft after assembly would effectively reduce the strength of the roller design and allow juice ingress if not adequately sealed.

Stress induced in a shell by the interference fit was as expected for all combinations of effective shell diameters and interference factors analysed. Small differences between the theoretical (Crawford, 1970) and experimental (FEA) values for both radial and hoop stresses were encountered (see Table 2.1). Anticipated stress increases at the shell-end were supported by the FEA results.

Little was known about the stress induced in the shaft from the interference fit prior to this investigation, especially in the region external to the contacting surfaces. As expected, the compressive radial stress in the shaft below the contacting surface was similar to the interference pressure at the landing. Of major interest was the induced tensile stress in the fillet region of the shaft and the area just outside the contacting zone. All FE models revealed that interference fits developed stress in these critical regions. This additional shaft stress is not considered in current shaft design, especially shaft sizing to avoid fatigue failure. This tensile stress is comparatively small and unfluctuating, however, it would effectively reduce the allowable roll loads determined by the endurance limit for the shaft. Table 2.1 shows that these stress values vary between 9 and 14 MPa for the fillet region and between 20 and 36 MPa for the landing zone

### 2.1.2 Final modelling and results

A seven foot roller was chosen to finalise the interference modelling. Figure 2.14 shows the mesh used for modelling. The roller's symmetry regarding geometry and interference loads allowed for 2D axisymmetric analyses. To aid with sensitivity analyses for varying shell geometry (Chapter 2.1.3), a removeable row of elements over the region occupied by the roller grooves was created as shown.

The following parameters were used for the modelling unless otherwise stated:

$D_1$ (effective shell diameter)	= 920 mm	;	$D_2$ (shaft landing diameter)	= 510 mm
$E_1$ (elastic modulus for shell)	= 120 GPa	;	$E_2$ (elastic modulus for shaft)	= 207 GPa
$\nu_1$ (Poisson's ratio for shell)	= 0.26	;	$\nu_2$ (Poisson's ratio for shaft)	= 0.30
k (interference factor)	= 0.0007	;	$\mu$ (coefficient of friction)	= 0.10
inboard fillet radius	= 75 mm	;	and bearing landing diameter	= 457-mm

The effective shell diameter was taken between the tooth profile roots for the modelling of the seven foot roller. The stress concentration effect of the tooth profiles was not included in the analyses.

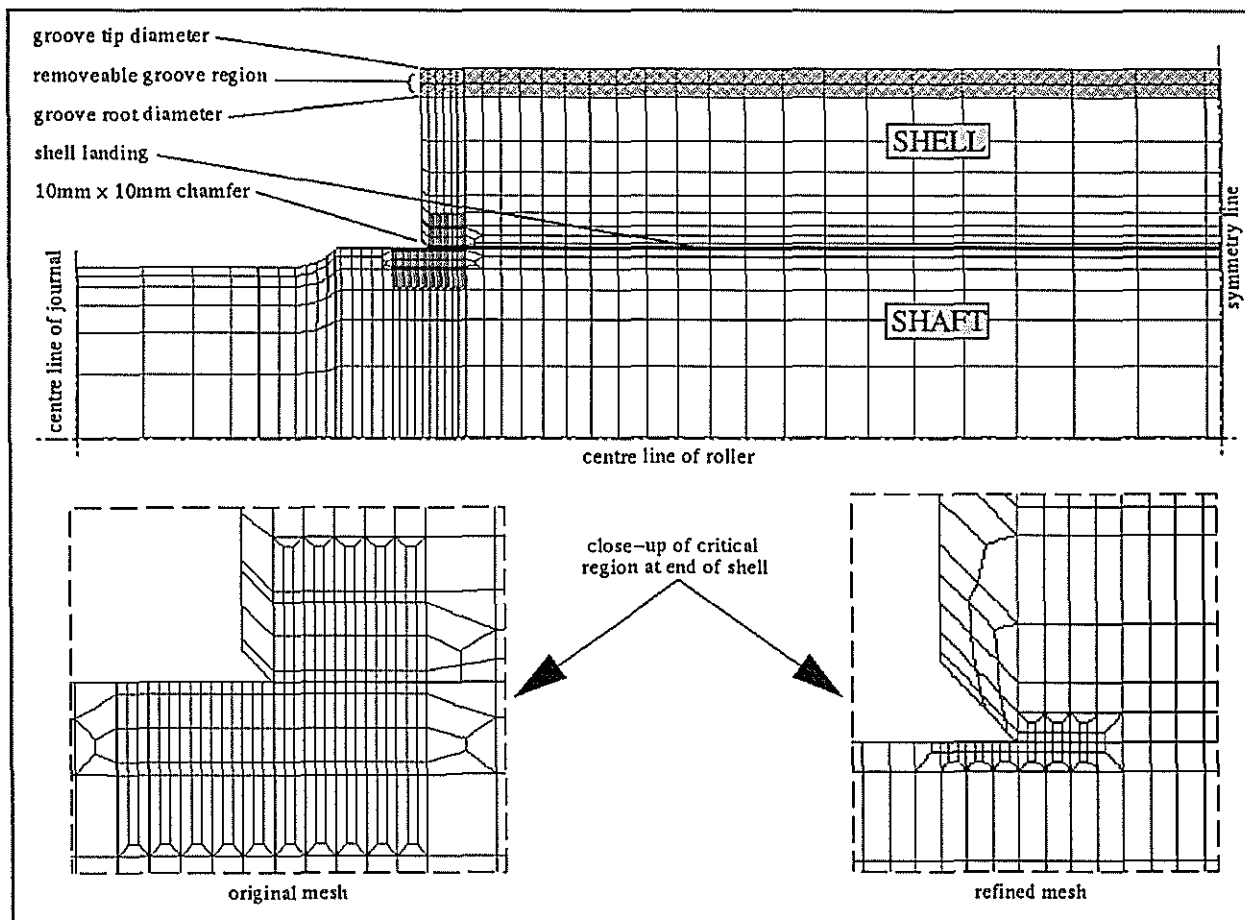


Figure 2.14 2D axisymmetric model of 7 foot roller for interference fit analysis showing various mesh densities trialled in shell-end region.

The modelling procedures used in Chapter 2.1.1 were applied to the seven foot roller models. Figures 2.15 through 2.21 show the results of the original mesh interference model. Figures 2.22 and 2.23 show the results of the refined mesh model. The element size used in the critical shell-end region in the original mesh model was approximately 3 mm square as compared to 1mm square for the refined mesh model.

Modelling of the seven foot roller confirmed the findings made during the six foot roller analyses. Discussion of the seven foot roller results and a summary of the interference fit induced stress states (Table 2.2) can be found in Chapter 2.1.3.

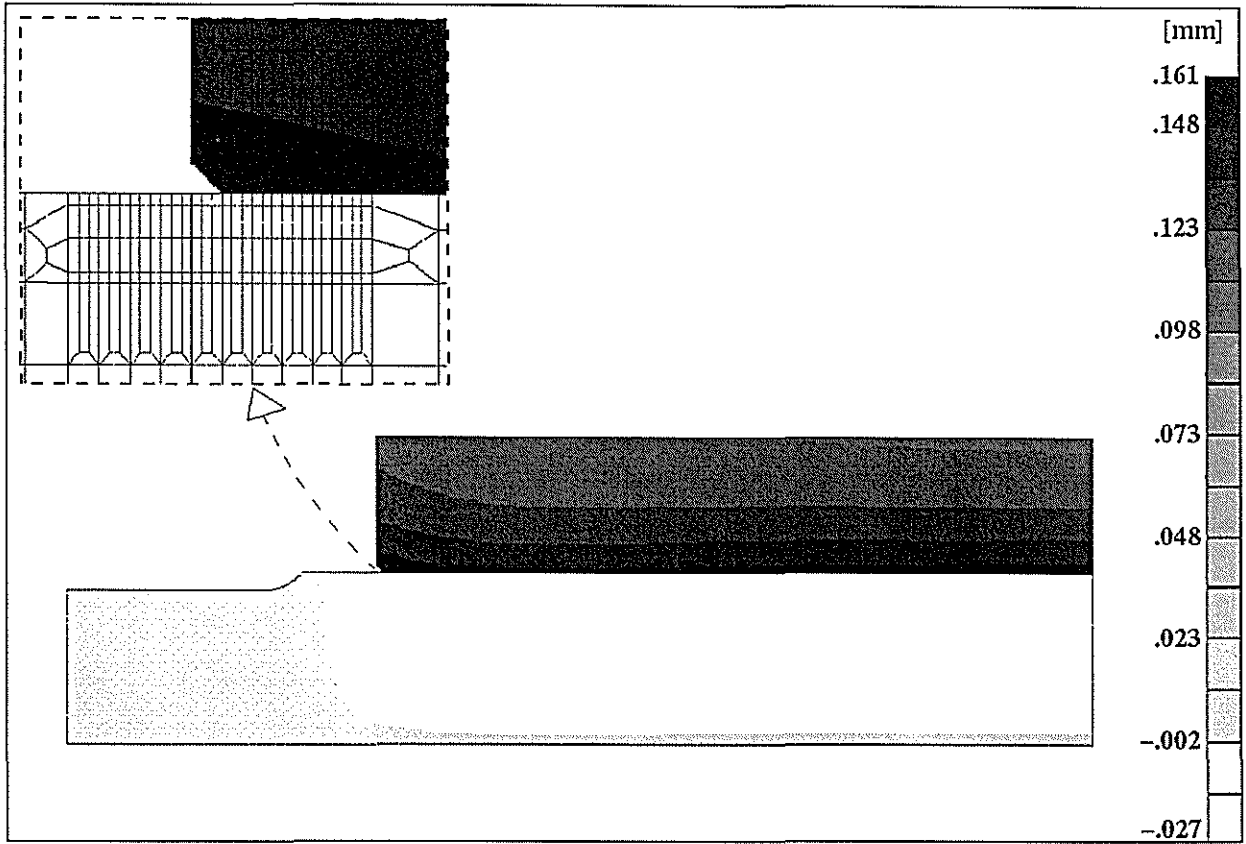


Figure 2.15 Radial displacement plot for original mesh interference model.

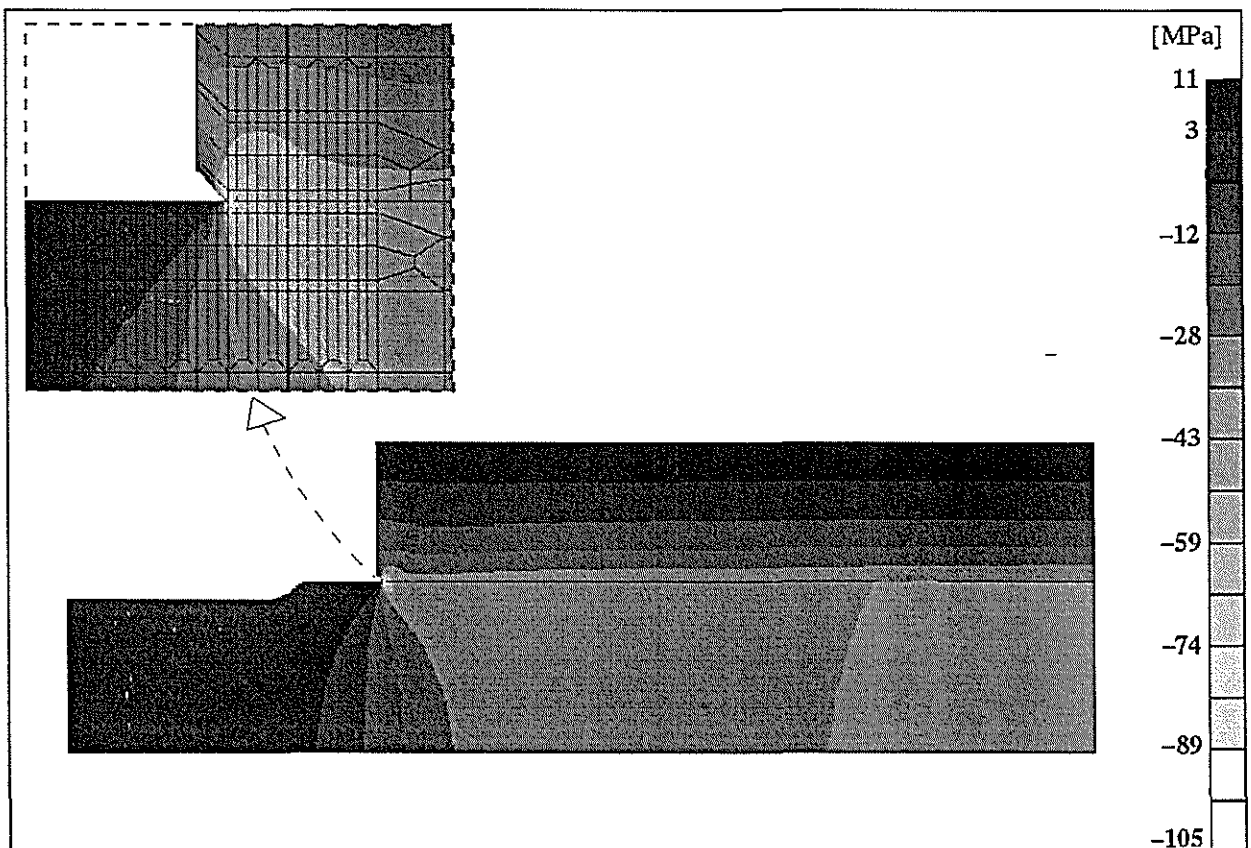


Figure 2.16 Radial stress plot for original mesh interference model.

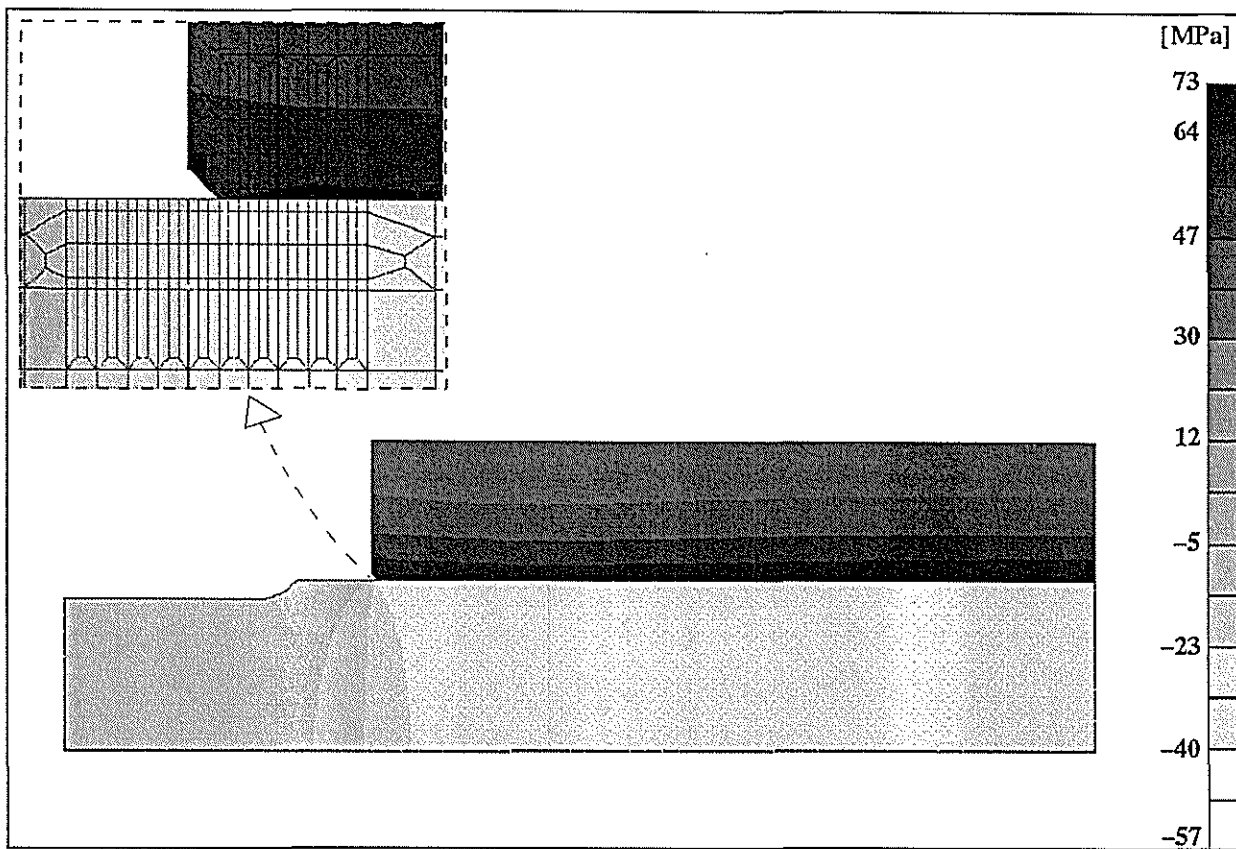


Figure 2.17 Hoop stress plot for original mesh interference model.

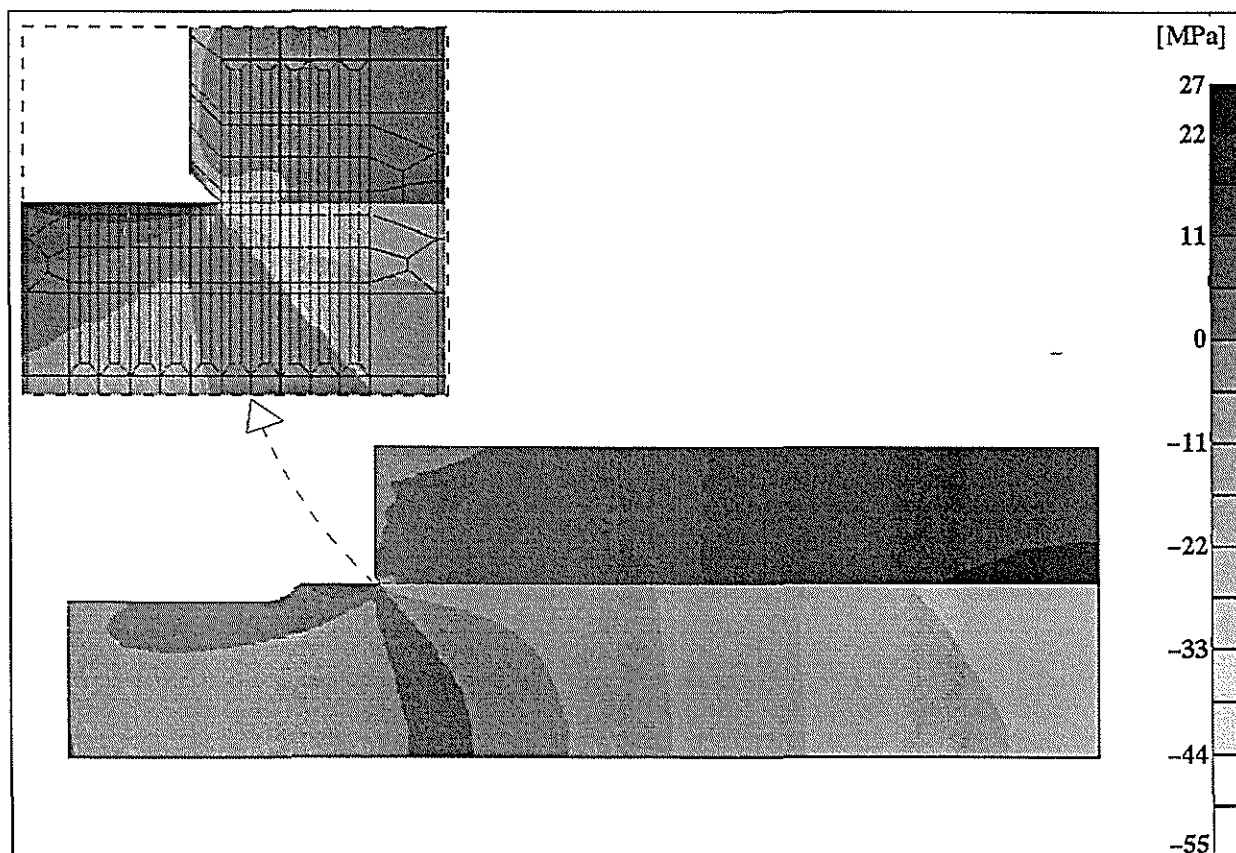


Figure 2.18 Axial stress plot for original mesh interference model.

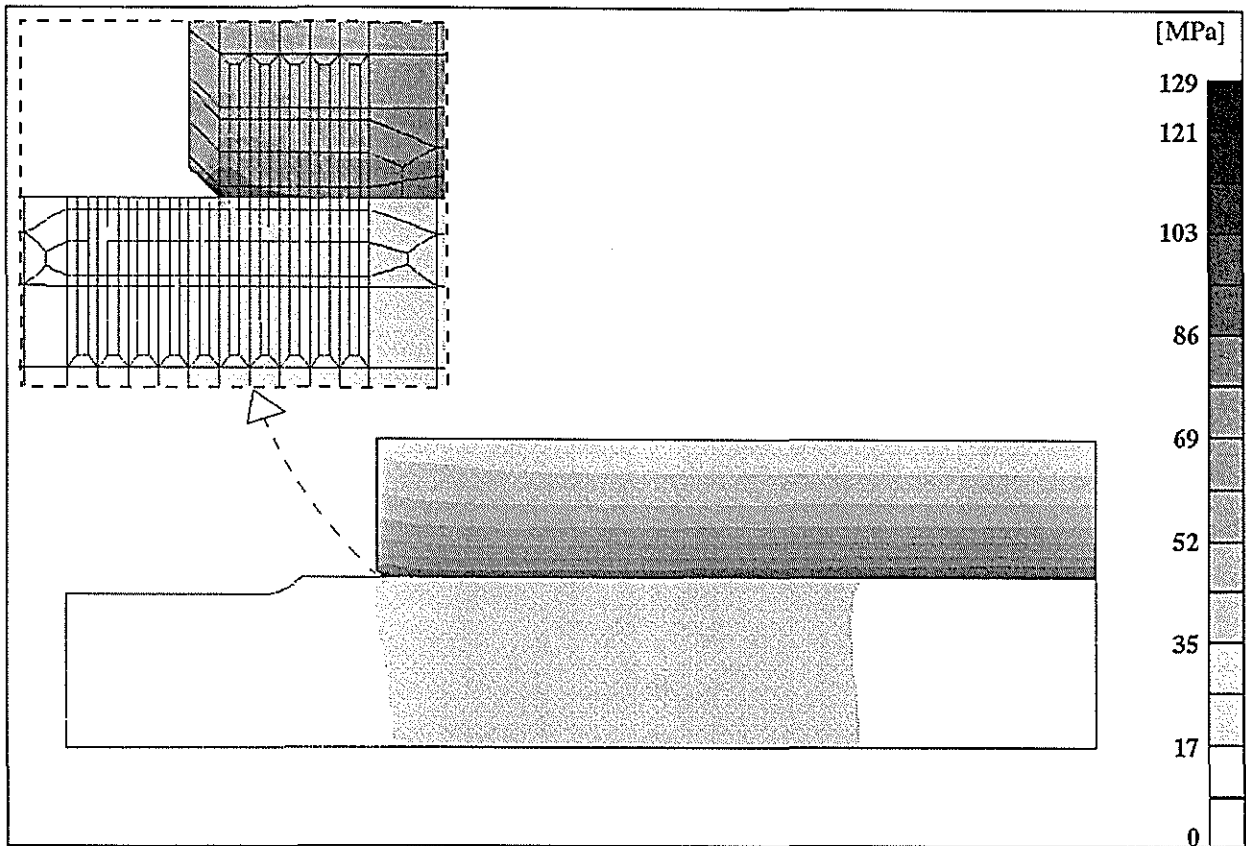


Figure 2.19 Von Mises stress plot for original mesh interference model.

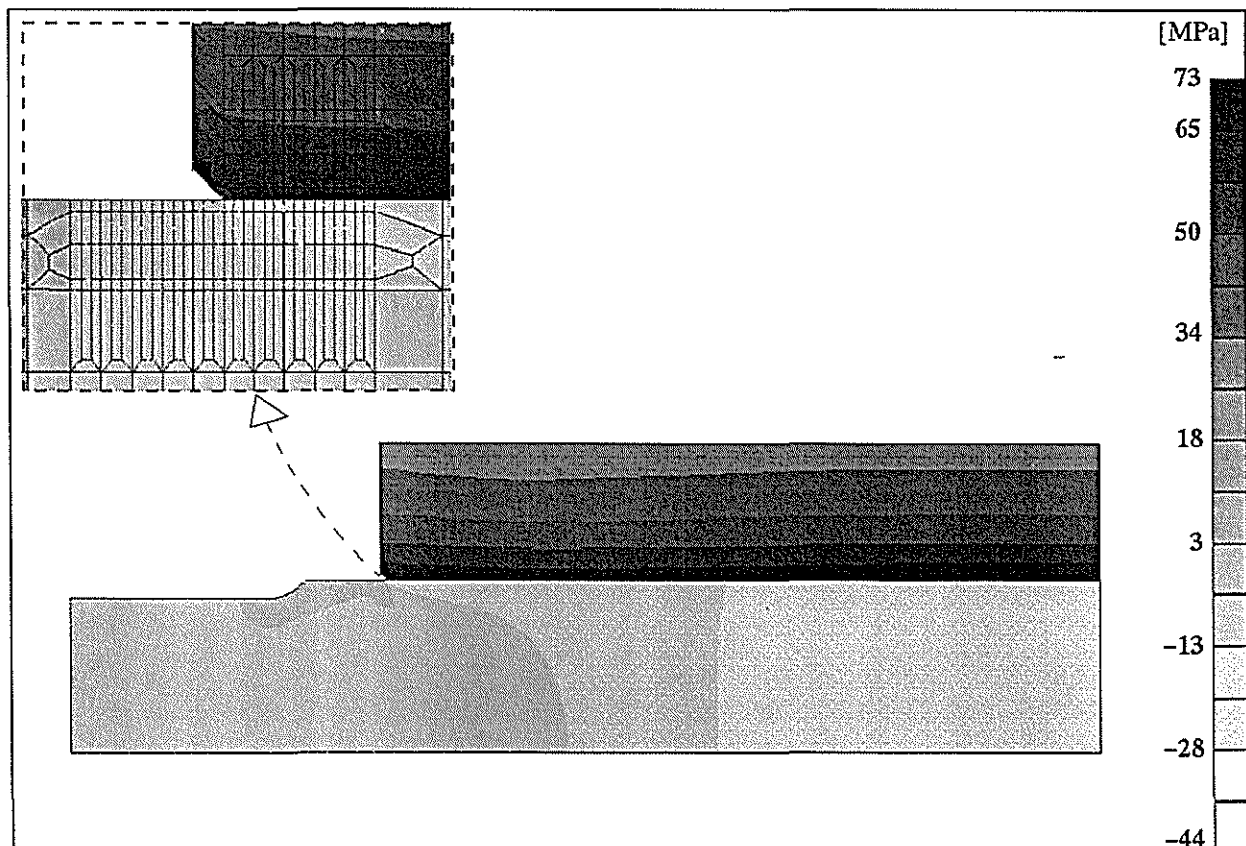


Figure 2.20 Major principal stress plot for original mesh interference model.

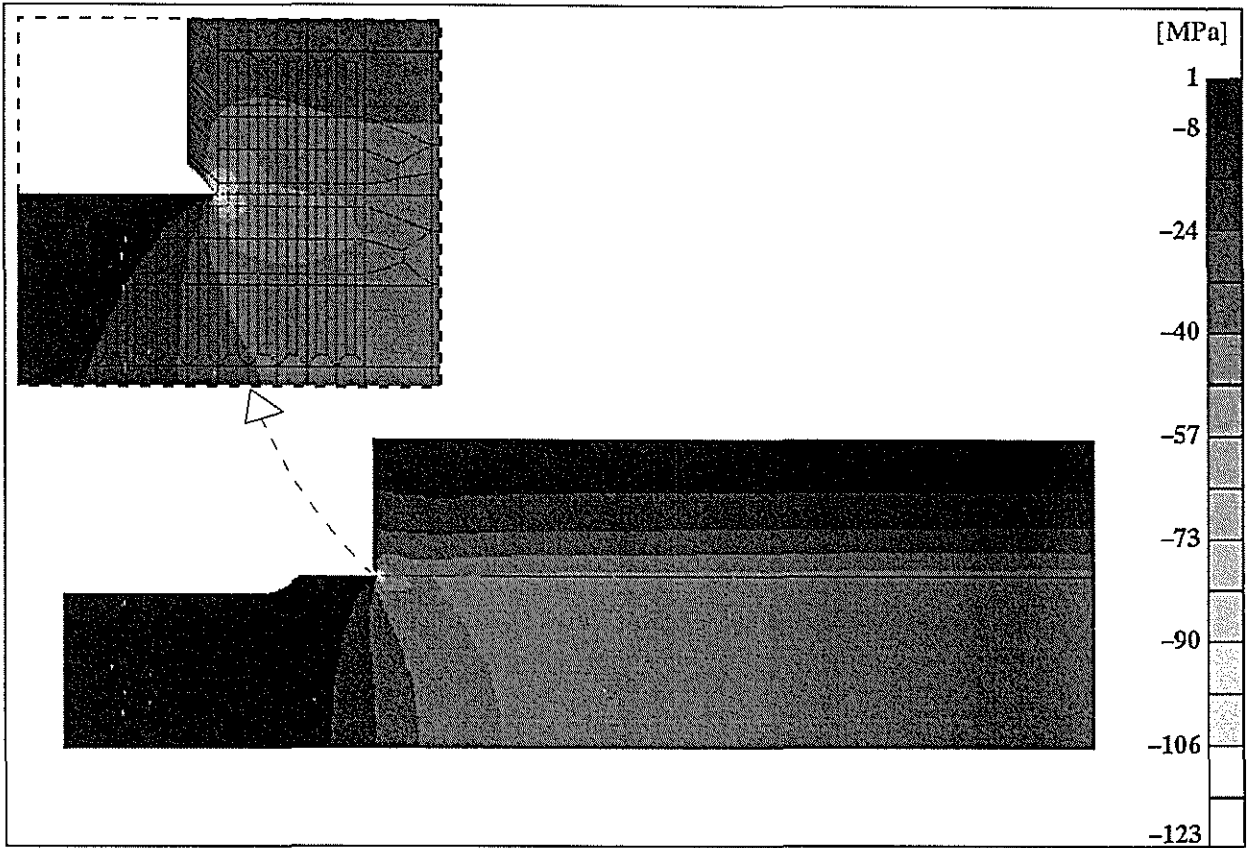


Figure 2.21 Minor principal plot for original mesh interference model.

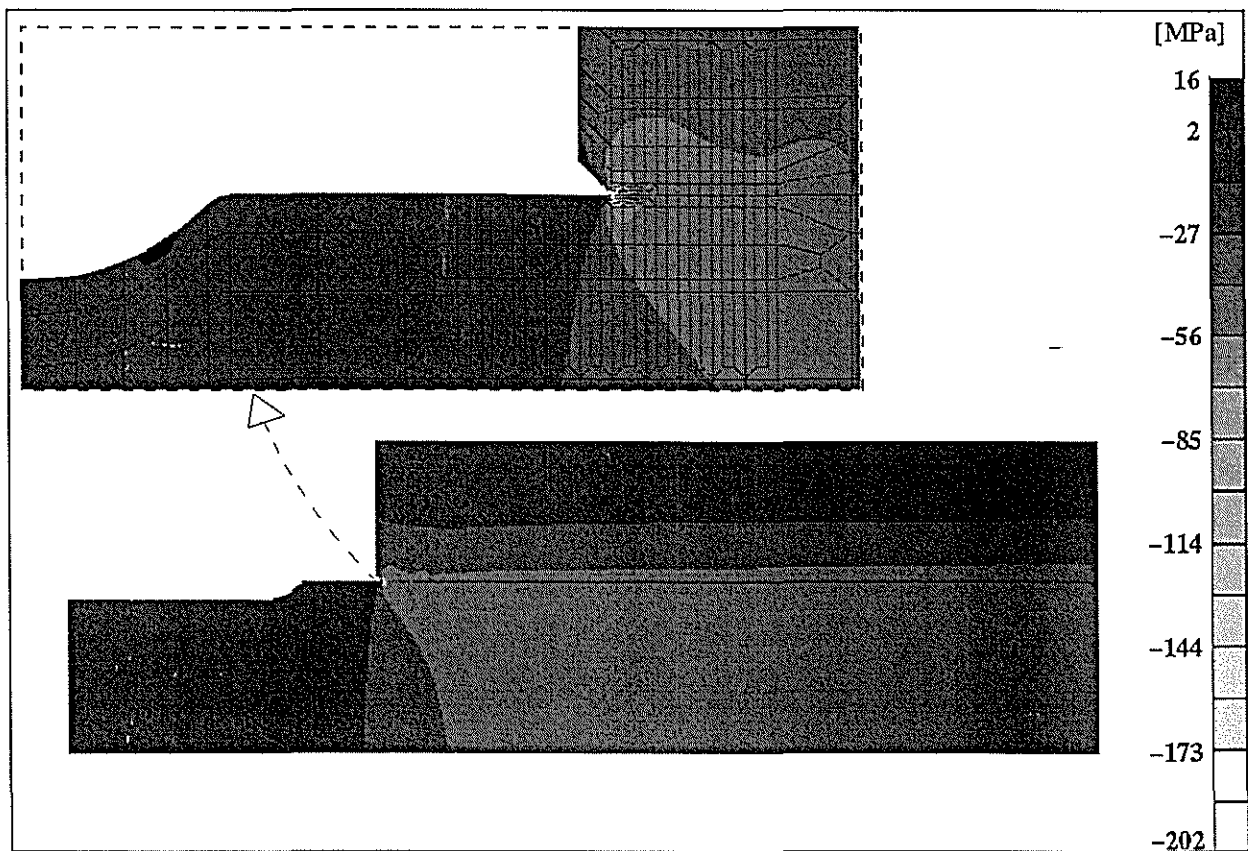


Figure 2.22 Radial stress plot for refined mesh interference model.

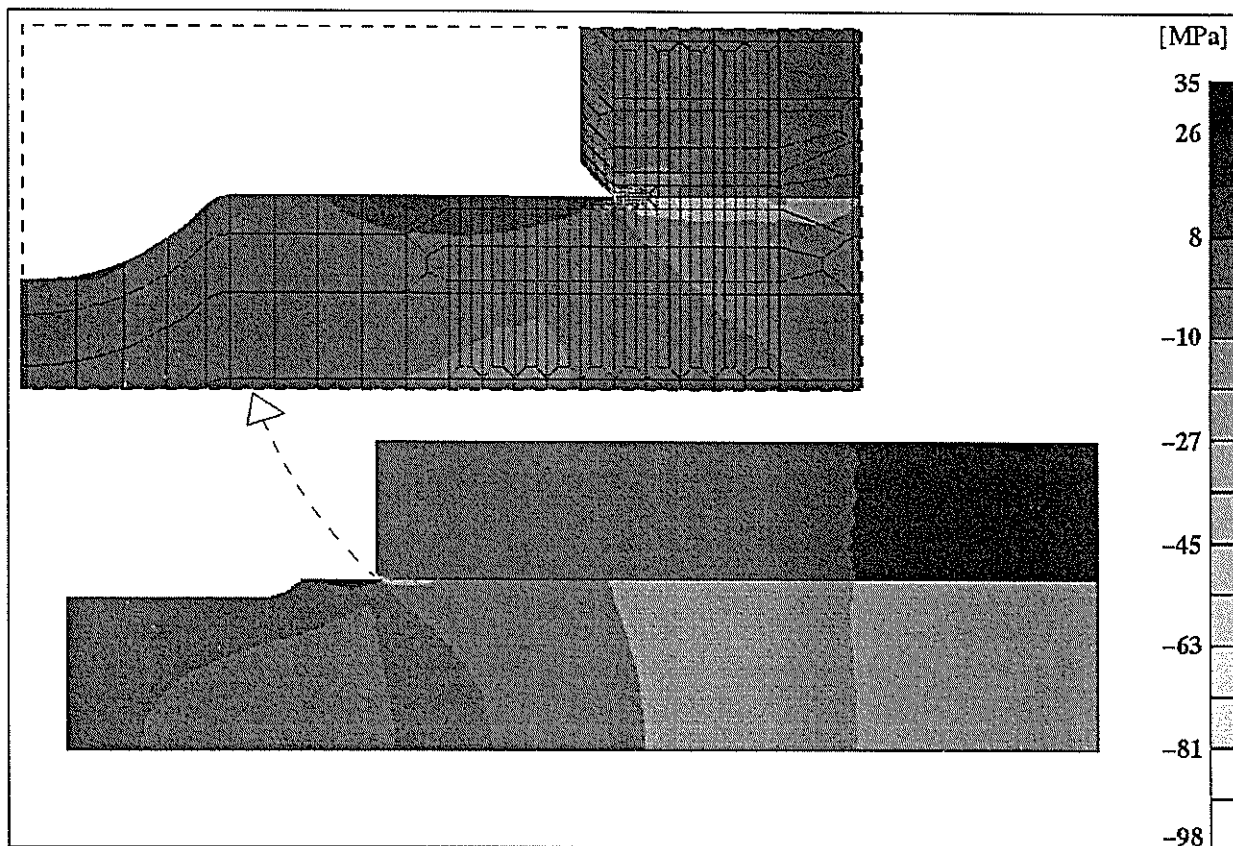


Figure 2.23 Axial stress plot for refined mesh interference model.

### 2.1.3 Effect of shell parameters on roller stress

Modelling of the seven foot roller reinforced the major findings resulting from the interference analysis of the six foot roller. In particular, the results indicate:

1. The high stress experienced at the shell-end;
2. The tensile stress developed in the fillet and landing area near the shell-end; and
3. The effect of shell design parameters on the hoop and radial stress.

A stress concentration factor for the gripping pressure in the shell-end region was not achievable due to the modelling singularity. Refined models revealed that the high stress (>2 times the theoretical radial stress) was restricted to within 5 mm of the shell's last point of contact with the shaft.

Various interference factors and effective shell diameters were combined with 2 different shell materials to provide an insight into their effect on roller stress induced by interference fits. The results of the analyses are summarised in Table 2.2 and discussed in Chapter 2.1.4.

Table 2.2 Interference fit modelling results for the seven foot roller

Mesh Description	Interference Factor, k	Shell Diameter $D_1$ [mm]	Maximum Von Mises Stress [MPa]	Radial Stress <sup>A</sup> [MPa]		Hoop Stress <sup>A</sup> [MPa]		Maximum Hoop Stress [MPa]	Major Shaft <sup>B</sup> Stress [MPa] Landing, Fillet
				Exp., Theor.	Compressive	Exp., Theor.	Tensile		
original <sup>C</sup>	0.0007	920	140	32.8, 32.9		62.0, 62.1		66.7	22.9, 10.3
original	0.0007	920	129	36.1, 32.9		66.7, 62.1		72.8	28.2, 10.3
original <sup>D</sup>	0.0007	920	119	38.7, 32.9		70.8, 62.1		74.4	33.6, 10.3
original	0.0007	1000	134	39.0, 35.5		64.8, 60.4		72.3	30.3, 11.1
original	0.0005	920	93	25.6, 23.5		47.5, 44.4		52.2	20.3, 7.4
original	0.0005	1000	97	27.6, 25.3		46.2, 43.1		51.8	21.8, 8.0
refined	0.0007	920	211	36.2, 32.9		66.8, 62.1		70.1	38.4, 10.3
original <sup>E</sup>	0.0007	920	98	28.2, 25.7		52.0, 48.5		55.8	21.6, 8.0
original <sup>E</sup>	0.0005	920	71	20.0, 18.4		37.1, 34.6		40.1	15.5, 5.8

<sup>A</sup> experimental stress values were taken at the shell's contacting surface close to the centre line of the shell so as to avoid boundary and end effects

<sup>B</sup> major principal stress induced in the shaft were extracted at two critical regions, the inboard fillet and the area just outside the contacting zone

<sup>C</sup> the coefficient of friction,  $\mu$  is set at 0

<sup>D</sup> the coefficient of friction,  $\mu$  is set at 0.2

<sup>E</sup> these models utilised a different shell material with an elastic modulus,  $E_1$  set at 90 GPa and Poisson's ratio,  $\nu_1$  set at 0.24

### 2.1.4 Discussion

Several major findings resulted from the interference modelling. They were:

1. High stress is developed in the shell-end region, however, this high stress is confined to a relatively small area.
2. Radial and hoop stress from the modelling compared well with the theoretical approximations. Axial stress was as expected, although the 2D theoretical simplifications of the complex 3D situation of the shell / shaft interaction were not used for comparison.
3. Hoop stress increased with decreasing shell diameter and / or increasing interference factor and / or increasing elastic modulus. Radial stress (gripping pressure) increased with increasing shell diameter and / or increasing interference factor and / or increasing elastic modulus.
4. Tensile stress is developed in the shaft at the inboard fillet region and area prior to the shell-end. Although this stress is relatively small (10 to 30 MPa), it will have some lowering effect on the allowable roll loads (equation 1.29).
5. Both theoretical and modelling results indicate that the interference factors currently used for existing shell designs are over conservative when considering the gripping pressure required to avoid shell slippage. If accurate concentric machining of the shell bore was guaranteed, then lower interference factors should be considered to reduce the stress levels.
6. An increase in the friction coefficient between shaft and shell resulted in an increase in hoop stress, average radial stress and axial stress and a reduction in maximum radial stress in the shaft prior to the shell-end.
7. 2D analysis highlighted deficiencies in the current tapered shaft landing design.
8. The reported axial stress at the outside surface of the shell does not include the effect of the grooving. Suitable calculations to allow for the stress concentration of the grooves should be used when considering the shell stress resulting from the interference fit and roll loads.
9. The modelling technique for interference fits has provided feasible stress results for the current roller designs. However, alternative designs including thin outer shells would require combined thermal and mechanical modelling (discussed by Crawford, 1970) to accurately model the induced axial stress.
10. Element sizes used in the 2D modelling provided feasible results excluding the shell-end region. 3D modelling should involve fine mesh in the highly stressed regions of the roller to keep model sizes manageable without sacrificing accuracy.

## **2.2 Operational stress prediction - 3D finite element modelling**

3D modelling of the seven foot mill roller was required due to the asymmetric loading conditions. The main objective of the 3D modelling was to gain an improved understanding of the stress states experienced in a roller for a range of operational conditions. Only after this objective is achieved can analysis of suitable design alternatives and durability investigations be attempted.

Modelling techniques used during this investigation differ and improve on those used in the previous FEA work by Refalo and Ritchie. Previous FEA of mill rollers involved the shell being physically attached to the shaft with a temperature difference applied to simulate the interference fit. This technique provided feasible stress states in the centre of the roller. However, stress states at the shell-end regions were erroneous, as normal and shear load transfer between shell and shaft was direct (independent of friction coefficient) and didn't allow for the possibility of shell-end separation. Recent improvements in the analysis package, ABAQUS, has allowed 3D contact modelling of the brass / shaft and shell / shaft interactions which eliminates the need for suspect boundary restraints. Increased mesh refinement in critical regions was also possible with the upgrading in computing capability.

Historically, mill roller design was achieved using standard beam theory for compound cylinders. However, several unknowns and complexities become apparent especially when floating top rollers are considered. Cullen's experimental findings (Chapter 1.7) uncovered several factors which complicate stress prediction for a roller shaft. These include:

1. Roll lift and associated coupling loads;
2. The ability of the brass bearings to align with the deflected shaft;
3. Uneven cane blanket thickness and resulting pressure loading distribution on roller;
4. Pinion reaction; and
5. The hydraulic loading transferred to the shaft.

Modelling of the final seven foot roller was achieved in two stages. 'Stage 1' considered the roller being in perfect alignment with the gear axis. The brass bearings were allowed to align with shaft deflection. 'Stage 2' analyses involved misalignment loads, roll lifts and non-aligning bearings. Chapter 3 reviews several alternative roller designs involving different materials and geometry.

### 2.2.1 Model parameters and techniques

A complete 3D model (Figure 2.24) of a seven foot roller (details in Appendix A1) was constructed using the PATRAN code. Solution decks containing model information such as mesh details, material properties, contact surface definitions, loading and boundary restraint information were developed using PATRAN, modified and then solved with ABAQUS. Details of the brass geometry used are located in Appendix A2. The final roller model contained 18064 eight-node linear brick elements and 22535 nodes. Eight-node elements were chosen for this analysis so as 3D contact could be utilised. Multi-point constraints (MPCs) were also used to simplify brass movement and to account for tailbar misalignment (Chapter 2.2.3). Roller features in relatively non-critical regions including the tailbar fillet, pinion keyway and shell grooves were suppressed to simplify modelling and analysis.

The following parameters were used for the modelling unless otherwise stated:

$D_1$ (shell diameter *)	= 920 mm	$D_2$ (shaft landing diameter)	= 510 mm
$E_1$ (elastic modulus for shell)	= 120 GPa	$E_2$ (elastic modulus for shaft)	= 207 GPa
$\nu_1$ (Poisson's ratio for shell)	= 0.26	$\nu_2$ (Poisson's ratio for shaft)	= 0.29
$k$ (interference factor)	= 0.0007	$\mu$ (coefficient of friction)	= 0.10
shell landing diameter	= 510 mm	journal diameter	= 457.2 mm
journal length	= 572 mm	bearing centres	= 3048 mm
inboard fillet radius	= 75 mm	shell length	= 2138 mm
internal brass diameter	= 457.7 mm		

\* Shell diameter was taken as tooth root diameter. This is considered more realistic when considering future tooth wear and the overall tooth contribution to the shell's section modulus.

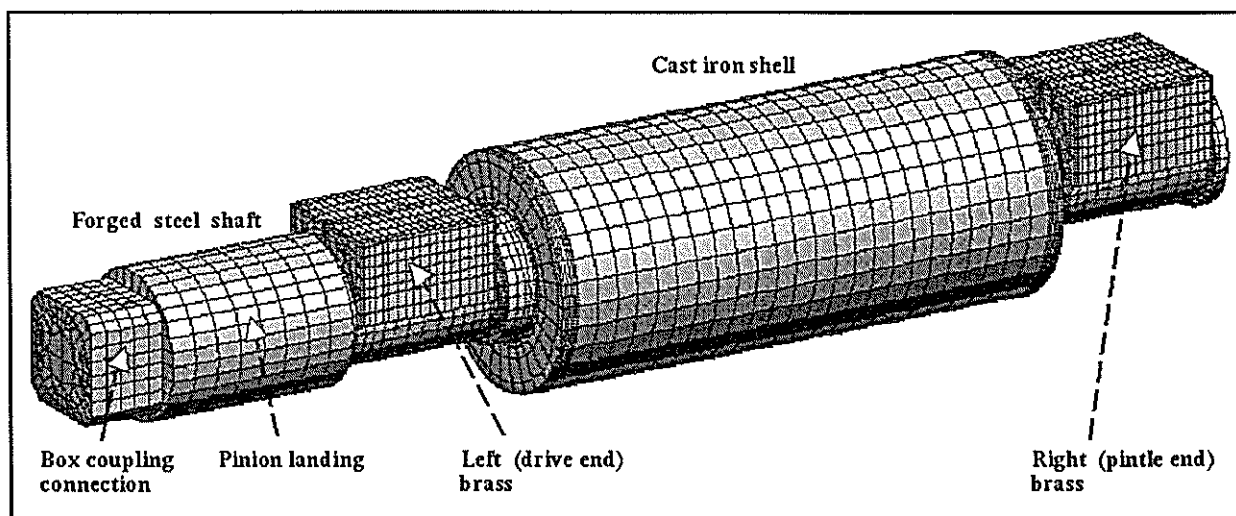


Figure 2.24 3D finite element model of the seven foot top roller.

The circumference of the roller was divided into 32 segments as a compromise between estimated computational time and mesh density in critical regions. This subdivision simplified model construction, load application and the transition to the square tailbar section. It was not possible to reproduce the mesh size used in the 2D interference fit analyses so some modelling error was expected in the 3D analysis. Figure 2.25 shows the typical mesh arrangement used on the sectioned roller. Note the increase in element density towards the fillet and shell-end regions.

Roll bending and torsional loads were approximated using the '1984 BSES Plant Data' and the empirical relationships discussed in Chapter 1.8. Appendix A3 contains the calculations for the roll bending pressures for the trash plate, feed and delivery nips and the torsional loads for the tailbar, pinion and shell. The resultant roll load used was approximately 69.8 ton / ft angled 11.6° from the vertical towards the feed roller. Note that roll load calculations did not include the brass (bearing) and mill cheek interaction forces. Further, the top roller brass guides were assumed to be vertical. However, torque loading does account for the brass / journal friction. The associated tailbar torque loading was approximately 931 kNm shared between the pinion (363 kNm), shell (448 kNm) and the friction allowance for the brasses (120 kNm).

Figure 2.26 illustrates the applied pressure distribution. Note the relative pressure level difference between the feed nip, trash plate and delivery nip which results in the non-vertical roll load. Figure 2.27 illustrates the torsional load distribution. The inclusion of the pinion reaction loads can also be seen.

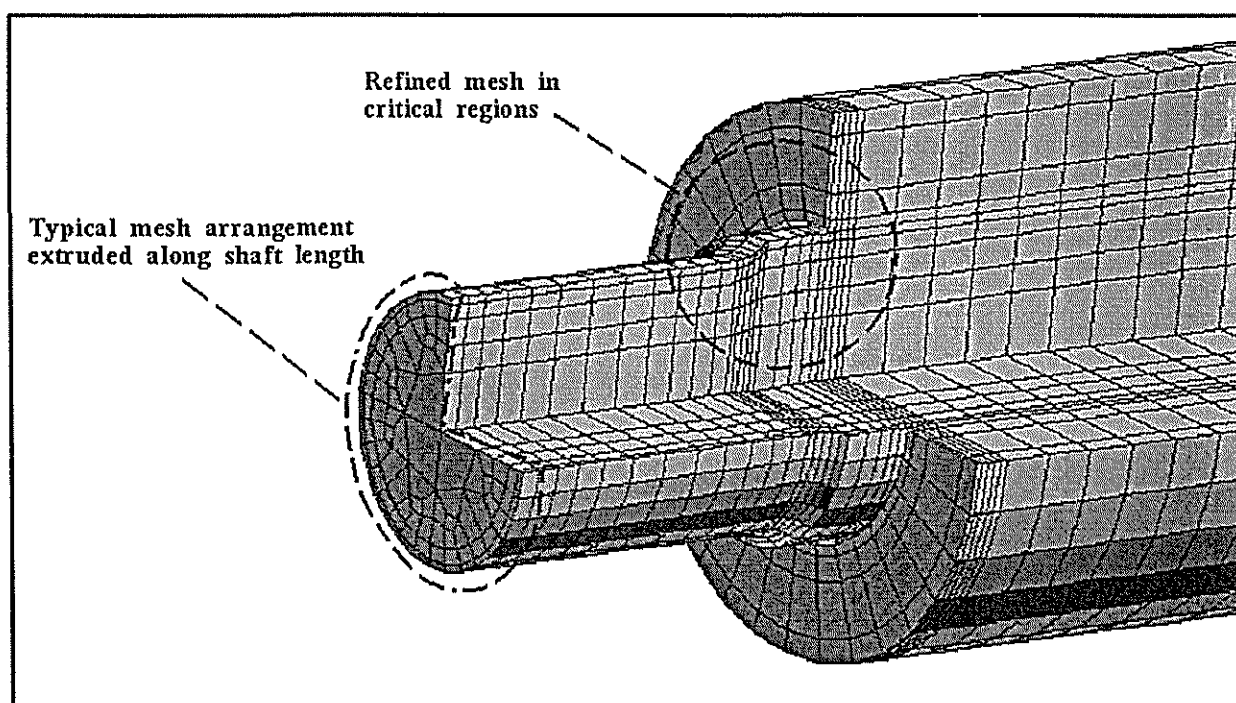


Figure 2.25 Sectioned view of 3D model highlighting element density.

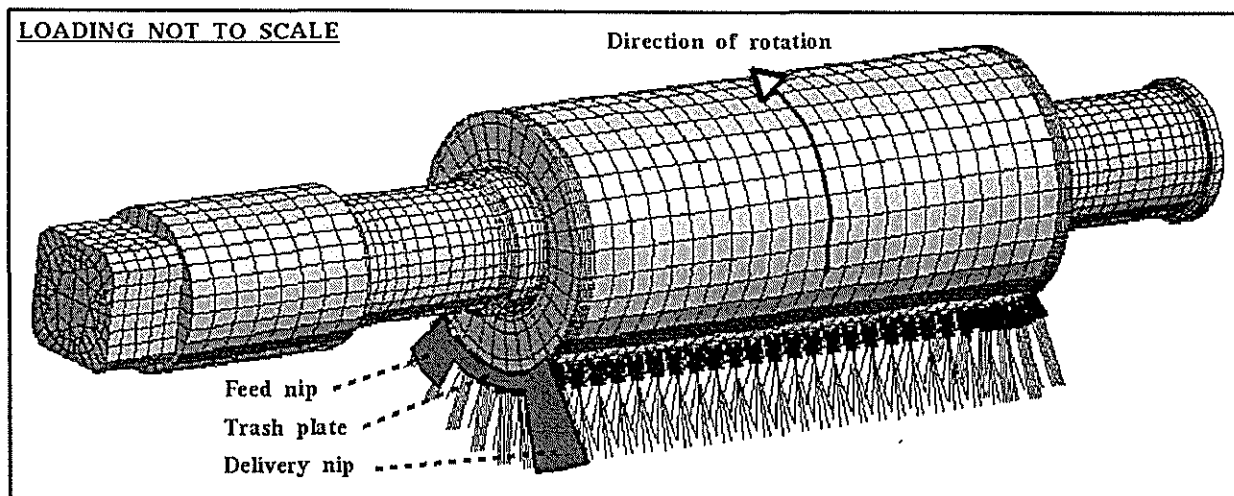


Figure 2.26 3D model with associated pressure distribution representing roll loads.

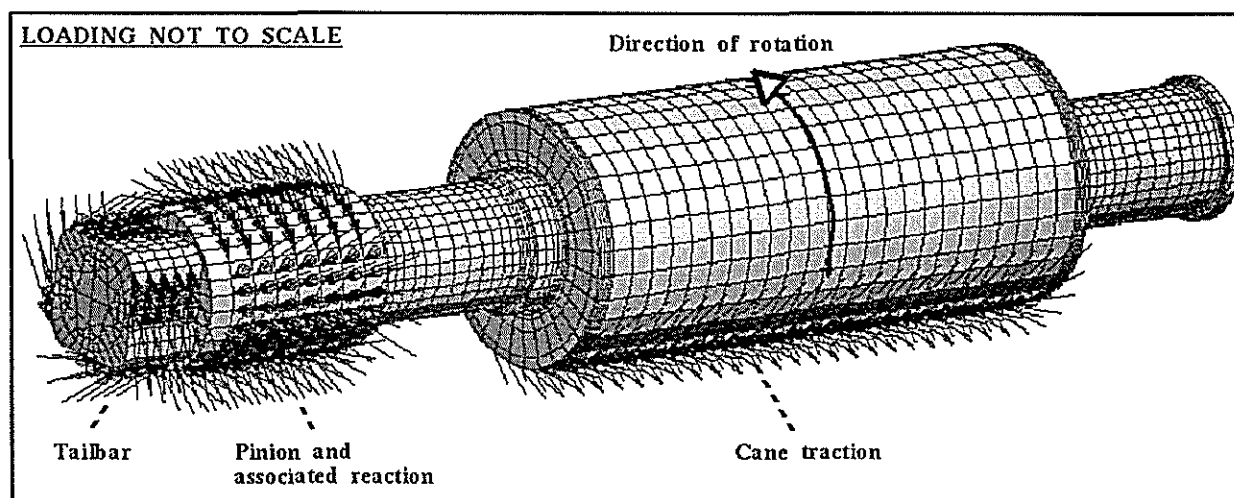


Figure 2.27 3D model with associated force distribution representing torsional loads.

The multi-point constraint (MPC) type 'BEAM' option was used to control the movement of the brasses, stop the roller turning due to any torque loading imbalance and to apply misalignment induced forces through the tailbar square. MPCs are a useful modelling option which allow constraints to be imposed between different degrees of freedom of a model. The MPC type 'BEAM' provides a rigid link between two nodes to constrain the displacement and rotation at a 'dependent' node to the displacement and rotation at a predefined 'independent' node.

Hydraulic rams usually contact a spherical seat on top of the mill brasses. The purpose of this seat is to allow the brass to rotate and align with the roller shaft during operation. To replicate this aspect of the brass constraint, 'BEAM' MPCs were used as seen in Figure 2.28. A selection of dependent nodes located on top of each brass in the confines of the spherical seat location were connected to an independent node created in the centre of the internal brass surface. This central node (pivot point) was used to control the movement of the respective brass. For this analysis, restraint of this pivot node was such that the brass could rotate and align with any vertical

deflection of the shaft. To model the effect of the mill cheek brass guides, the brass was restricted from rotating about the shaft's axis and the vertical axis through the pivot point. The position of the brasses could also be controlled by moving the independent pivot nodes to specified positions. This option was used for modelling roll lifts. The reaction forces at the independent nodes were monitored to give some indication of loads transferring through each brass.

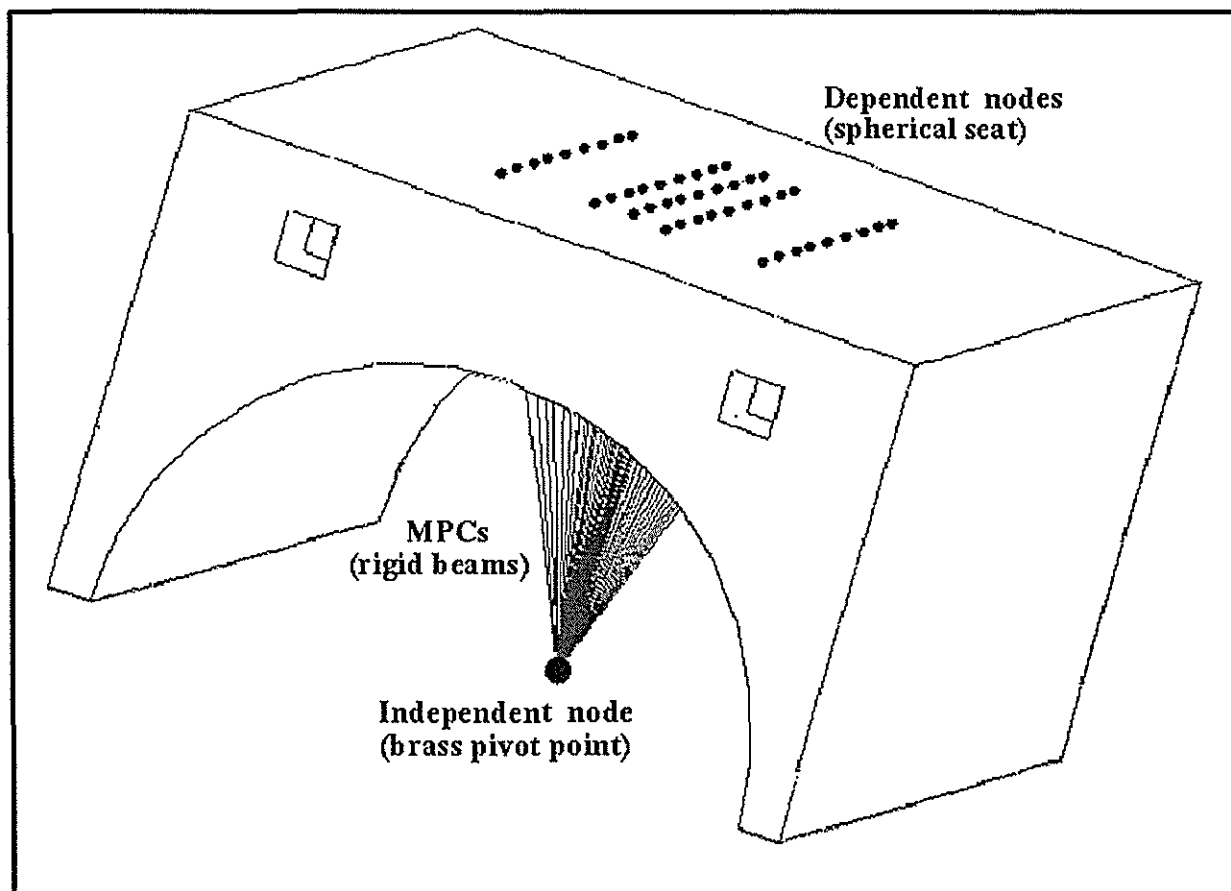


Figure 2.28 Brass outline showing application of multi-point constraints.

The effect of brass movement on shaft bending stress ( $\approx$  moment arm) is illustrated in Figure 2.29. Roller A (deflected roller) and B (uneven roll lift) show two exaggerated conditions of roller movement where the brasses were allowed to rotate and align themselves with the shaft. In these cases the effective centre of pressure (used for moment arm calculations) remains central on the journal. Roller C shows the effect of rotationally rigid brasses on the repositioning of the effective centre of pressure. Cullen (1968) found the pintle-end moment arm to increase with increasing pintle-end lift with respect to the drive-end, suggesting the brasses on the experimental mill had some restraint in aligning with the roller shaft.

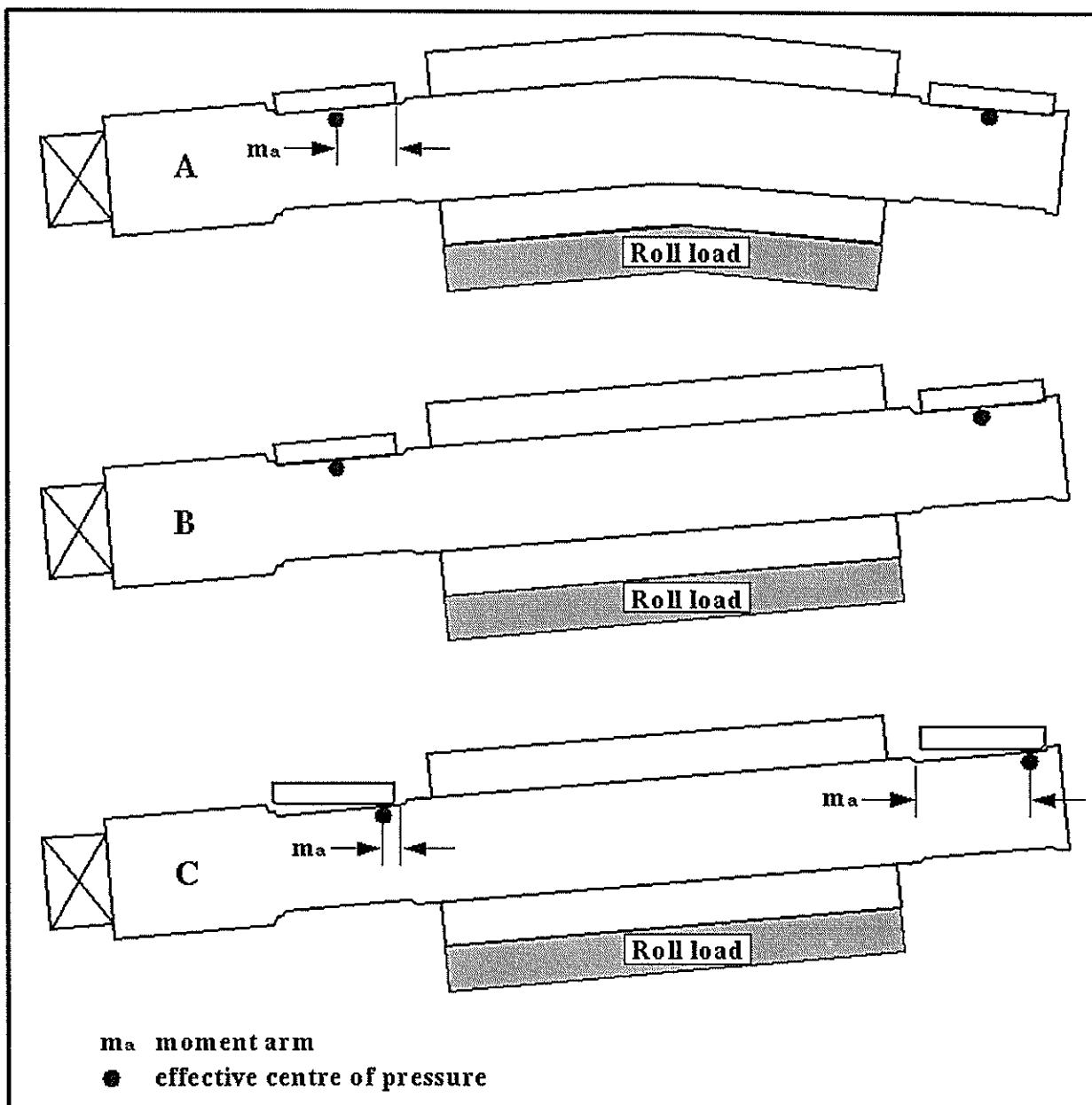


Figure 2.29 Effect of brass movement on pressure centre A) deflected roller with aligning brasses, B) misaligned roller with aligning brasses, C) misaligned roller with non-aligning brasses.

Finite element techniques do produce some force imbalances during the solution. In the case of the roller model, estimates of the bearing friction were required in order to apply feasible tailbar loads to limit force imbalances which would effectively rotate the roller during the quasi-static analysis. To avoid this, an independent node was created out from the pintle-end on the roller's axis and connected via BEAMS to nodes on the shaft's end. The independent node was only restrained from rotating around the roller's axis to prevent model rotation. The level of torque imbalance was monitored through reactions developed at this node. A similar MPC arrangement was created at the tailbar square to apply misalignment loads (Chapter 2.2.3).

The brass / journal interaction was modelled using 'softened' contact algorithms. In this situation, the pressure transmitted between two mating surfaces increases exponentially as the surfaces come into contact. This option is used when there is some soft, thin coating such as a lubrication film between two contacting bodies. Figure 2.30 illustrates the pressure versus clearance relationships for both 'softened' and 'hard' contact situations. Hard contact is basically a direct form of pressure transmission between contacting bodies and was used to model the shaft / shell interaction. In this analysis,  $C$  and  $P^0$  were set at 0.1 mm and 500 MPa respectively.

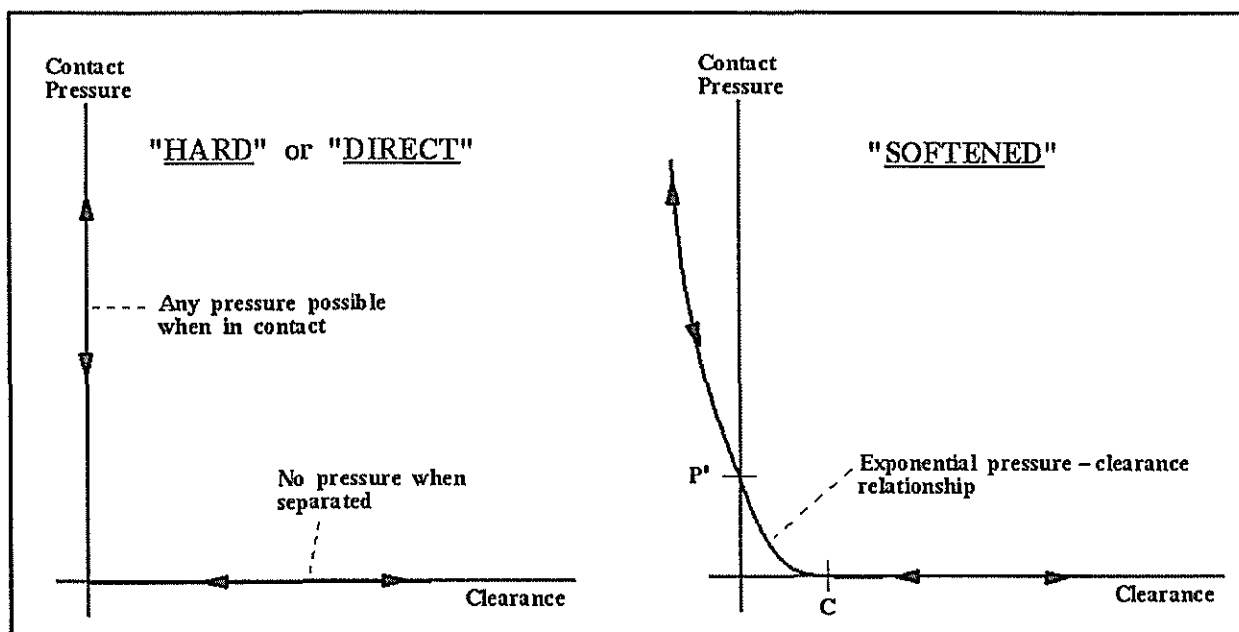


Figure 2.30 Contact pressure versus clearance relationships utilised during modelling.

### 2.2.2 Roll load, torque transmission and interference fit results

The procedure used to analyse each 3D model comprised of several solution steps to aid with post processing. This procedure allowed investigation into the effects of individual loads on the resulting stress distributions.

- Step 1: Heating of the shell until contact with the shaft was lost
- Step 2: Cooling of the shell back to its original temperature to achieve a realistic interference fit with the shaft (interference fit)
- Step 3: Application of the roll loads (interference fit + roll loads)
- Step 4: Application of the torsional loads (interference fit + roll loads + torsional loads)
- Step 5: Application of additional loads such as tailbar misalignment forces or roll lift (interference fit + roll loads + torsional loads + additional loads)

The following reported results pertain to the 'Stage 1' analysis. This analysis assumed no additional tailbar misalignment forces and no uneven roll lift. Hence a uniform pressure distribution was applied along the shell length and the brasses were permitted to align with any vertical shaft deflections. PATRAN's post processing ability allowed investigation into the contribution of individual loads on the roller's total stress distribution. For example, step 3 results were subtracted from step 4 results to create stress results pertaining to the effect of torsional loads only, utilising the interaction of the shell / shaft interface (interference fit) and brass / journal interface (roll loads). This method was used to determine what load source or operational decision were major contributors to stress levels in a mill roller's critical regions.

Some indication of the stress flow in a mill roller is shown on sectioned rollers in the following plots. Figures 2.31 through 2.37 show stress and displacement results for the interference fit only. Figures 2.38 through 2.41 show stress results for the interference fit, roll and torsional loads combined. Figures 2.42 and 2.43 highlight the stress pattern associated with the torsional loads only, a consequence of post processing manipulation. Figures 2.44 and 2.45 show the shaft / shell interface pressure (Steps 1 and 4 respectively) and Figures 2.46 and 2.47 shows the interface shear stress and the bearing contact pressures (Step 4). Figure 2.48 shows the vertical deflection due to roll load only. Reid (1988) noted the critical regions on a mill roller and suggested axial stresses were dominant in their failure mechanism (Chapter 1.3.1). Axial stress results from the 'Stage 1' analysis are listed in Table 2.3.

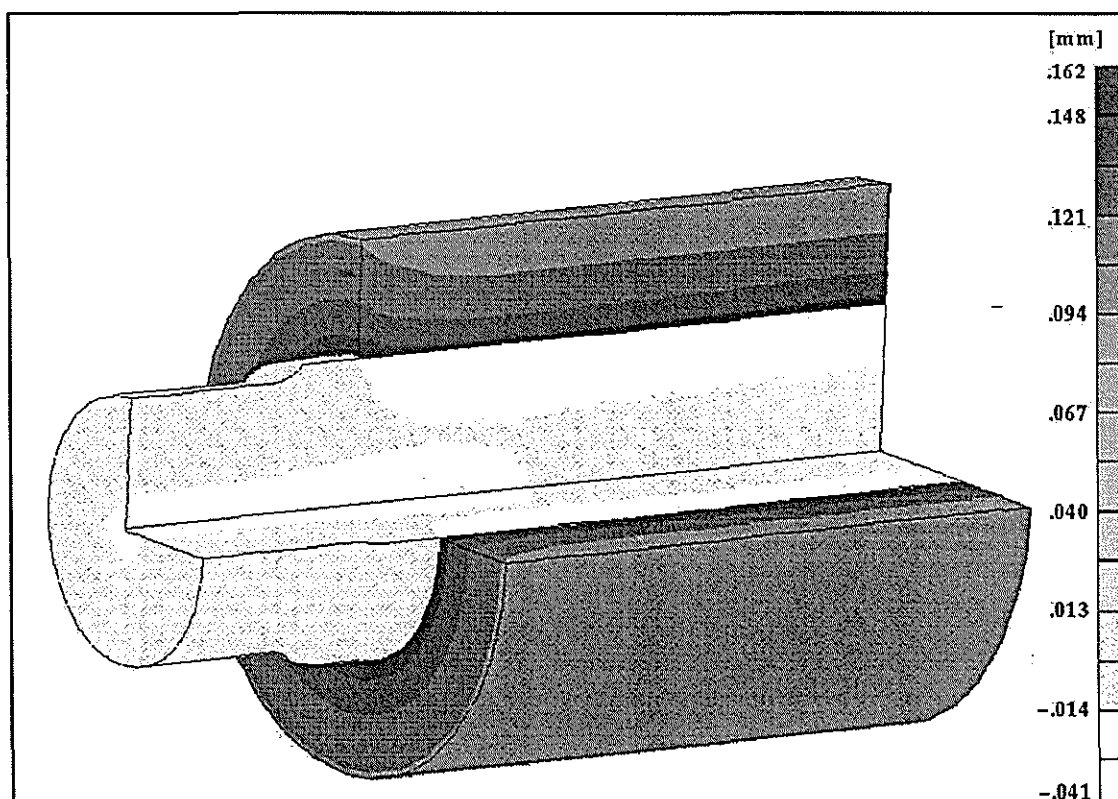


Figure 2.31 Radial displacement plot (Stage 1: interference fit only).

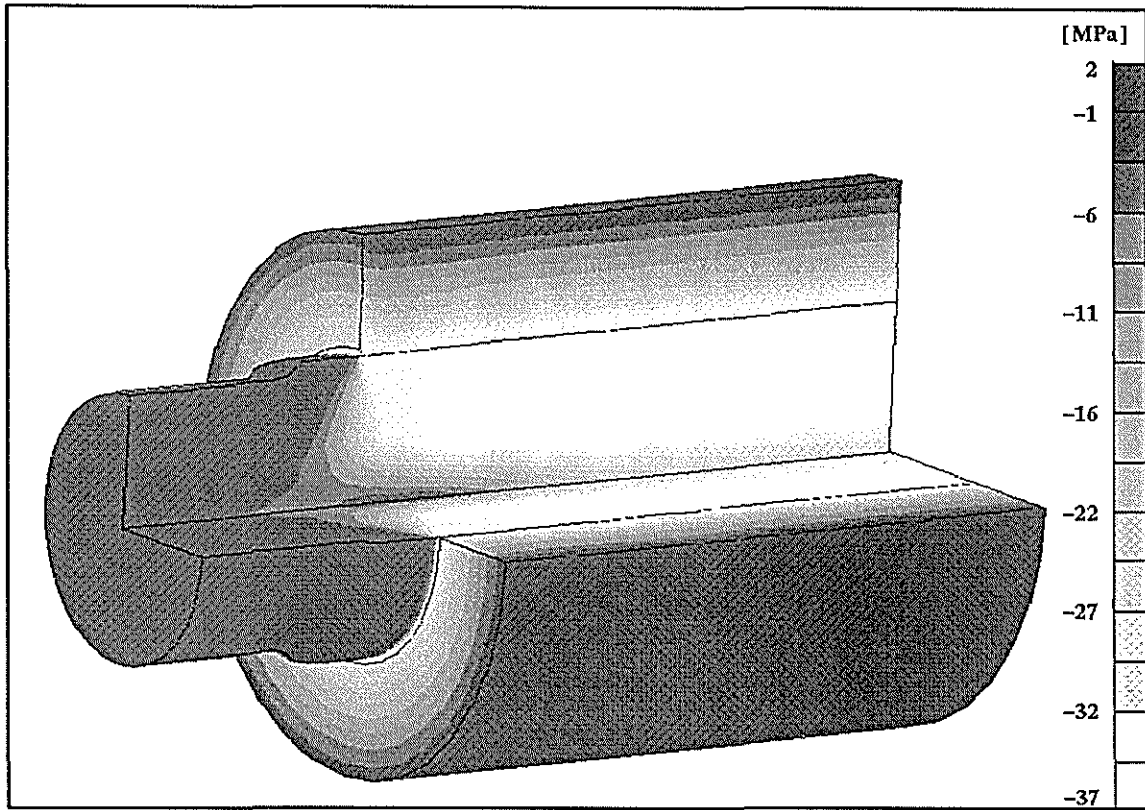


Figure 2.32 Radial stress plot (Stage 1: interference fit only).

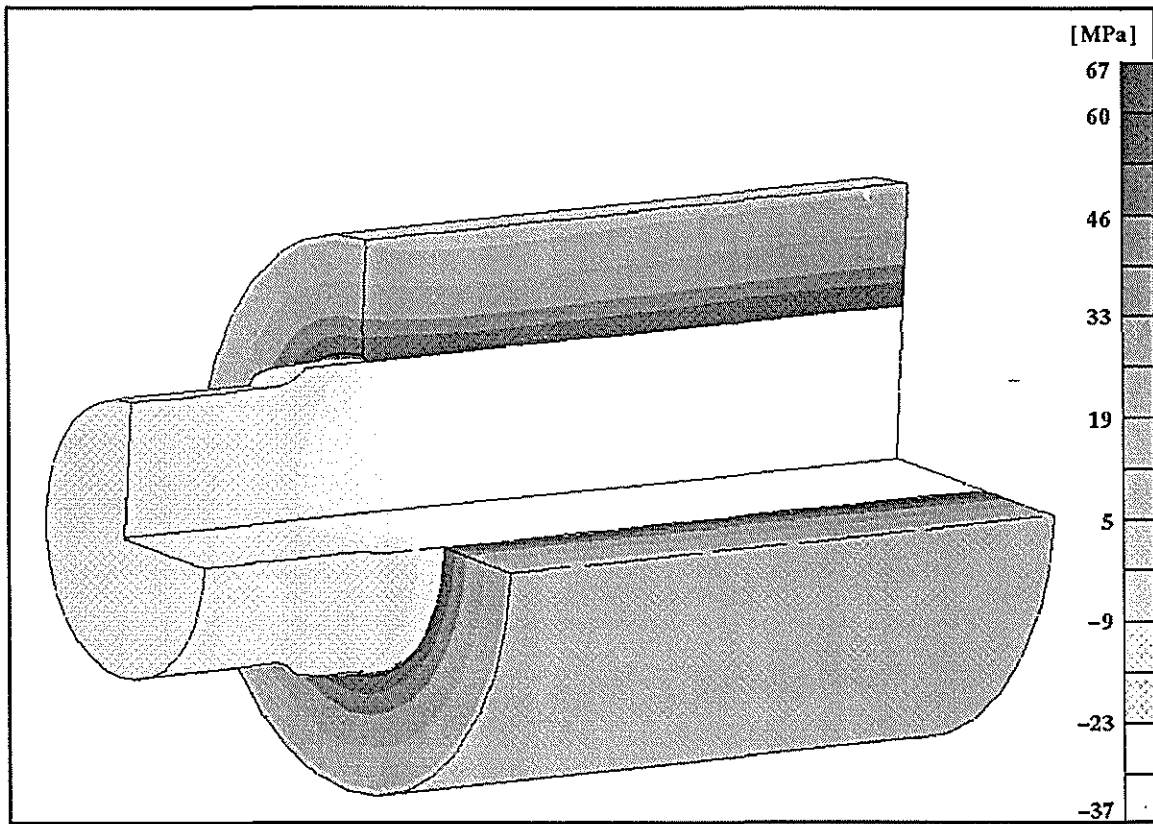


Figure 2.33 Hoop stress plot (Stage 1: interference fit only).

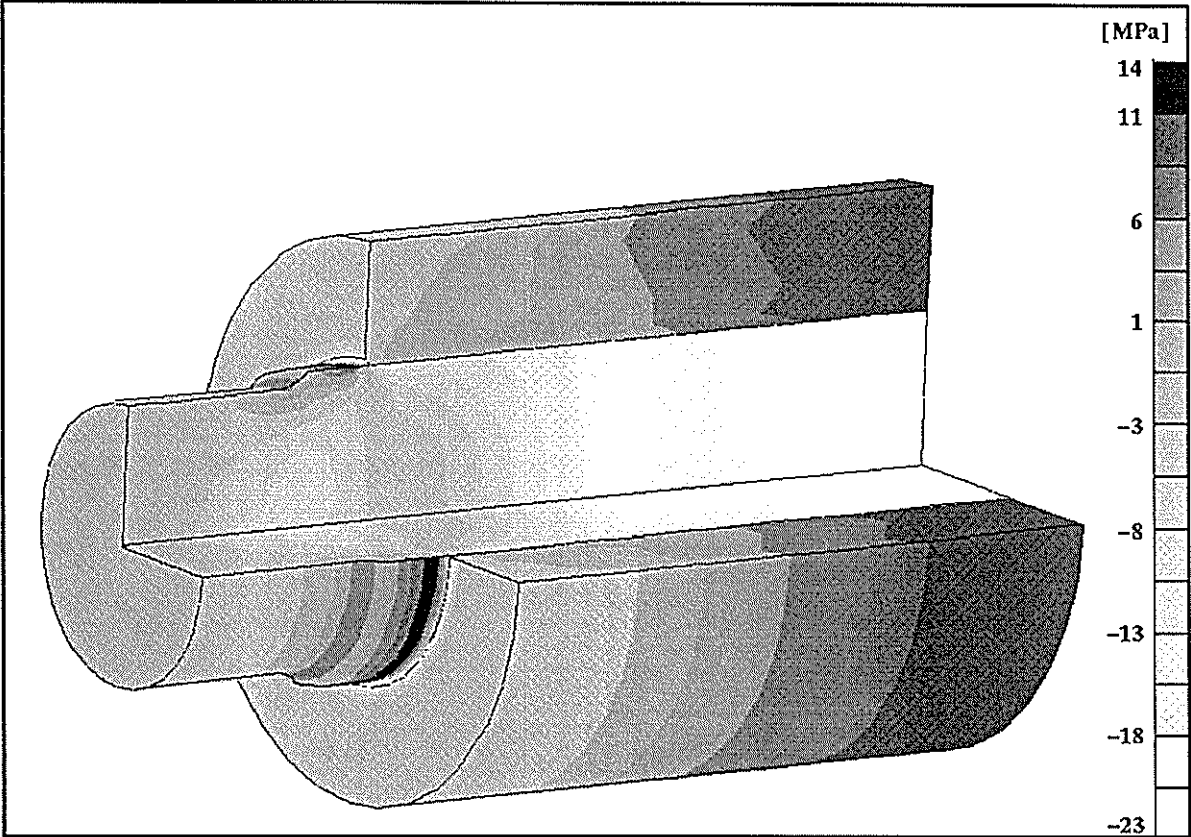


Figure 2.34 Axial stress plot (Stage 1: interference fit only).

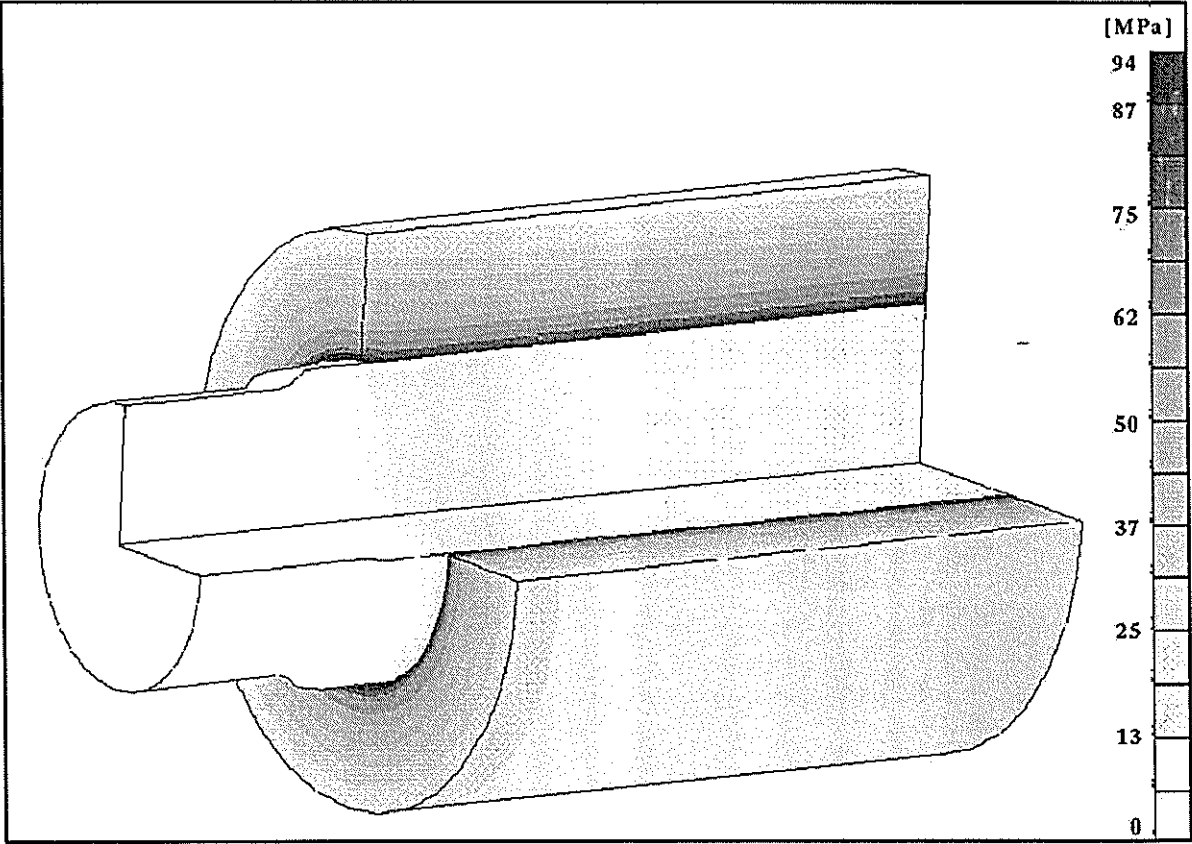


Figure 2.35 Von Mises stress plot (Stage 1: interference fit only).

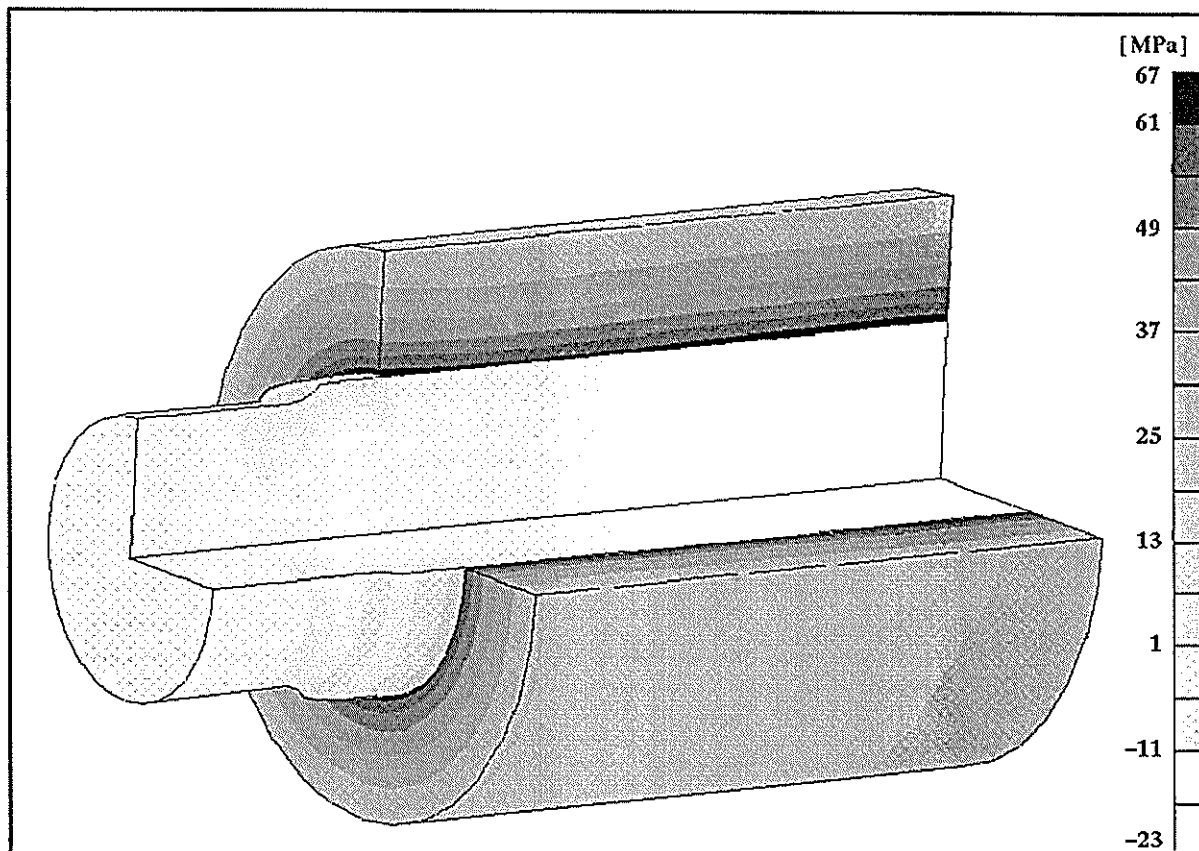


Figure 2.36 Major principal stress plot (Stage 1: interference fit only).

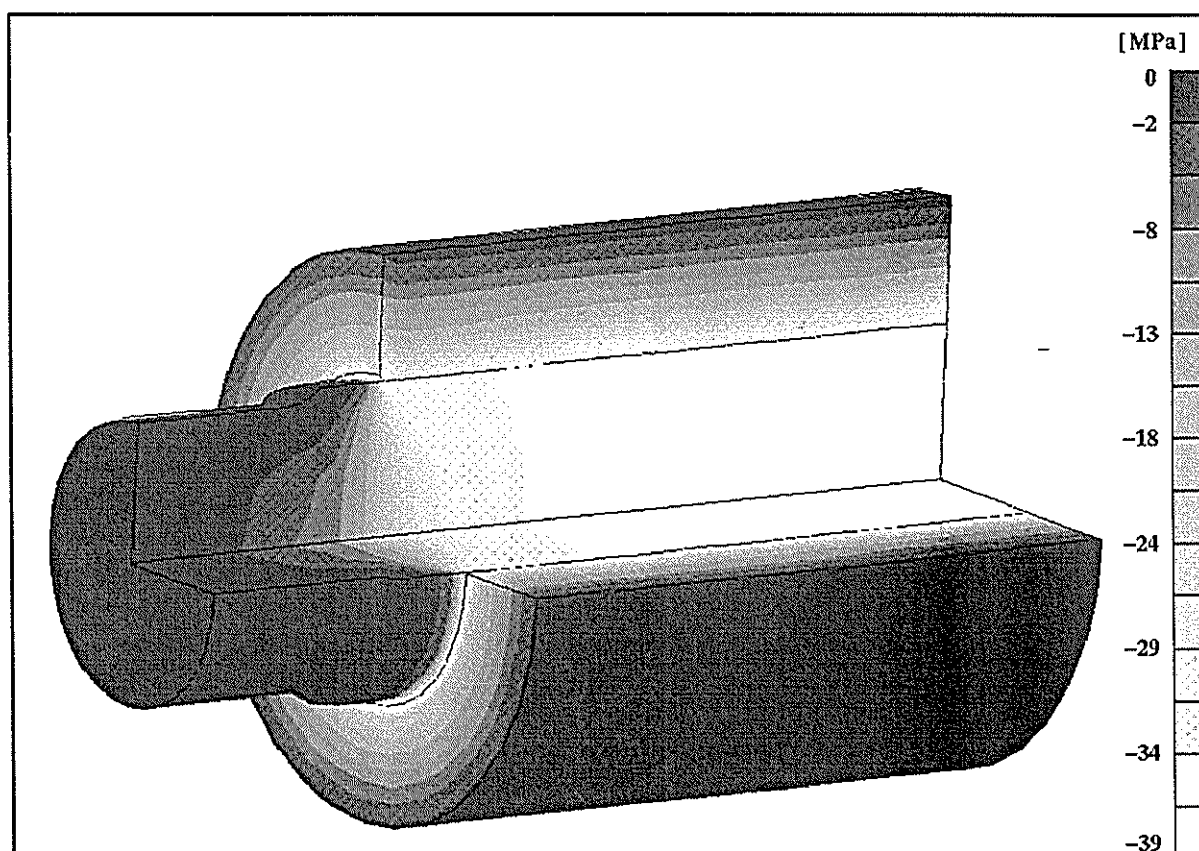


Figure 2.37 Minor principal stress plot (Stage 1: interference fit only).

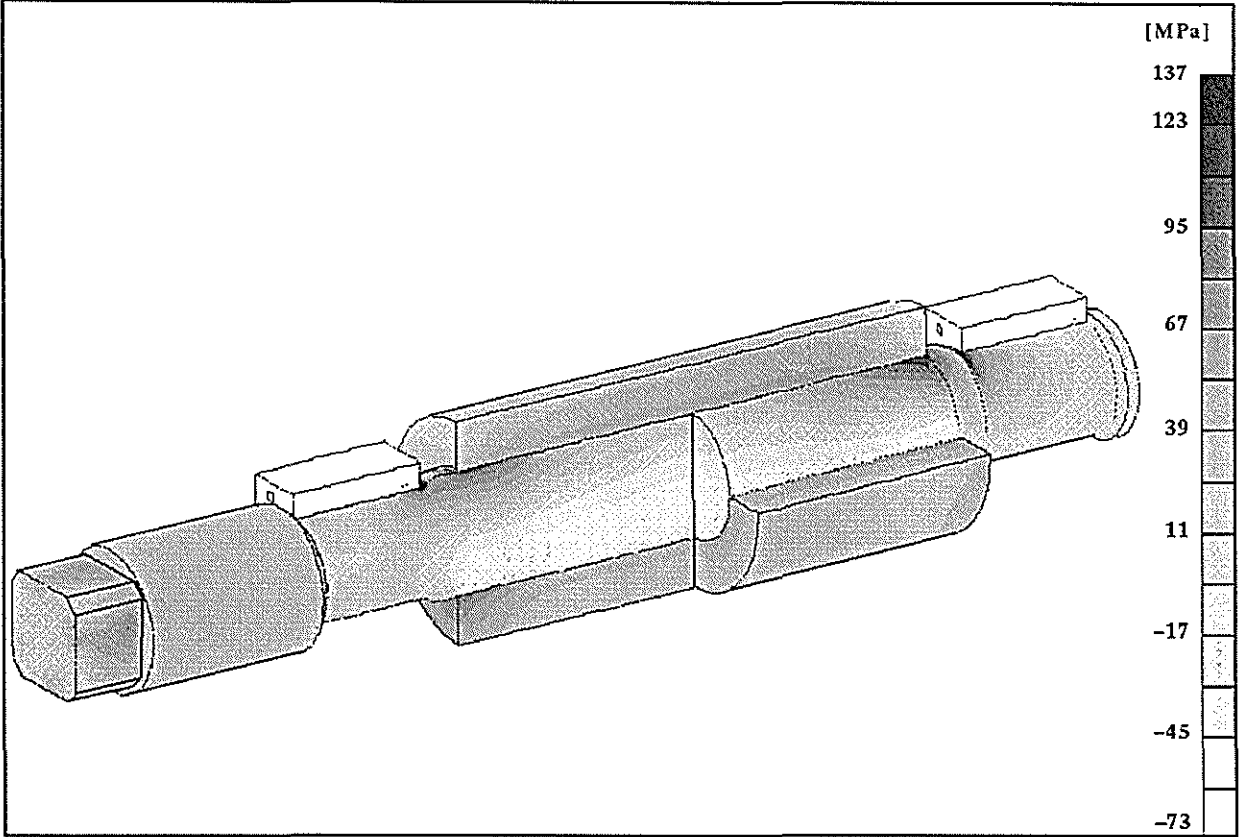


Figure 2.38 Major principal stress plot (Stage 1: combined loads).

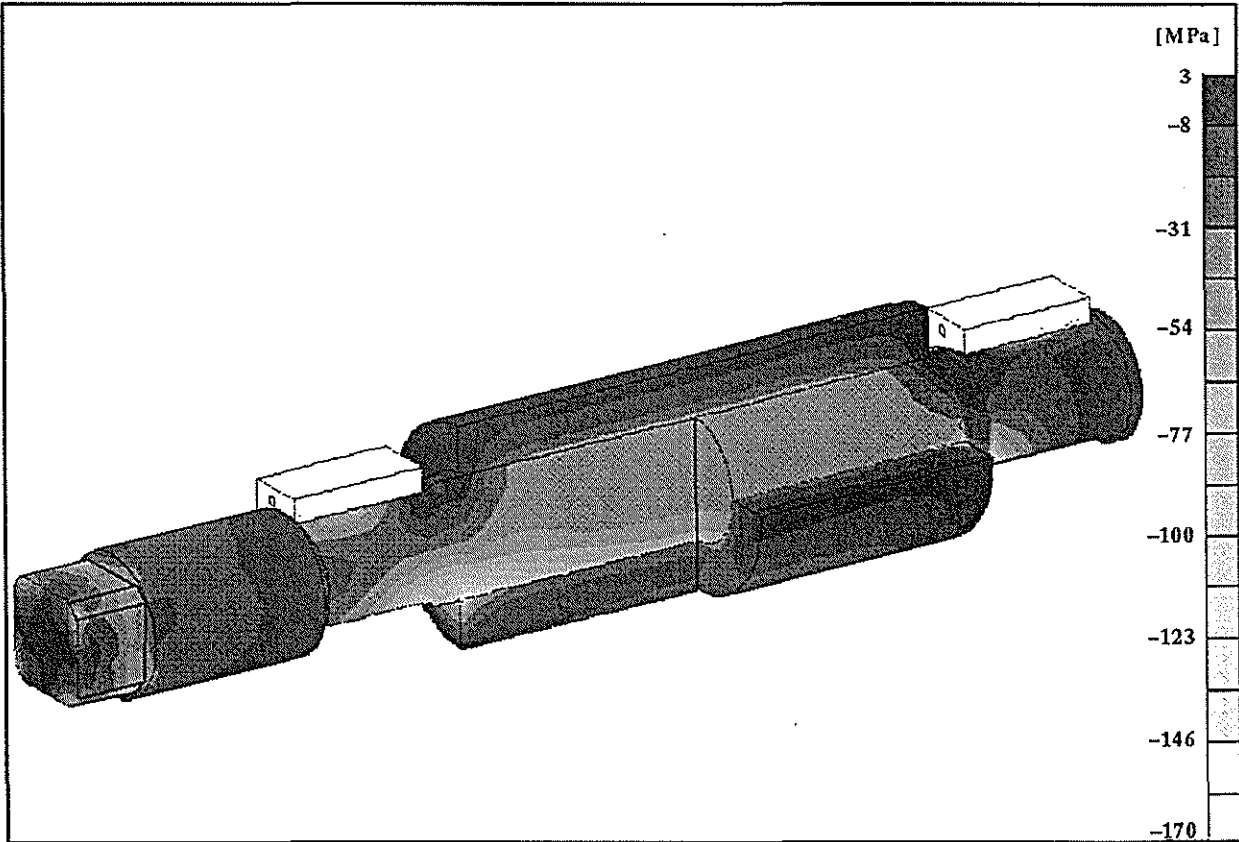


Figure 2.39 Minor principal stress plot (Stage 1: combined loads).

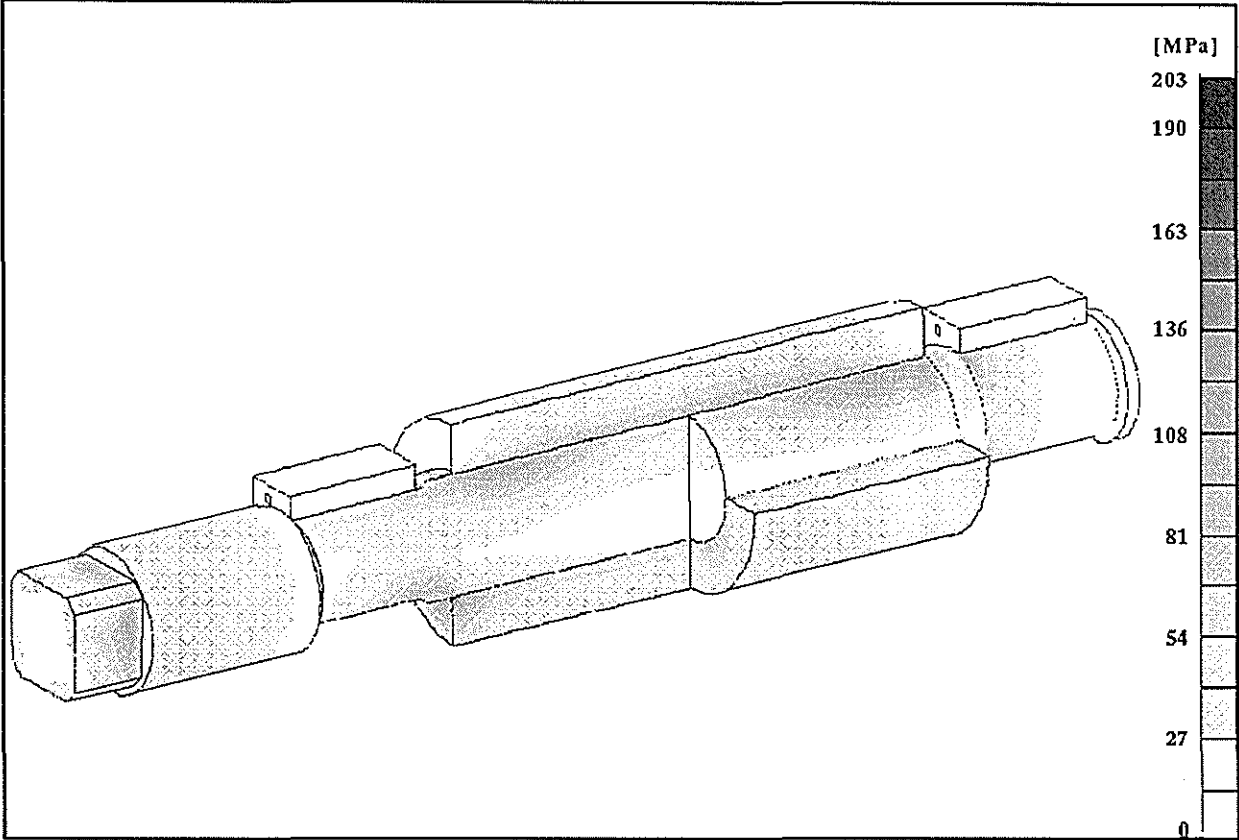


Figure 2.40 Von Mises stress plot (Stage 1: combined loads).

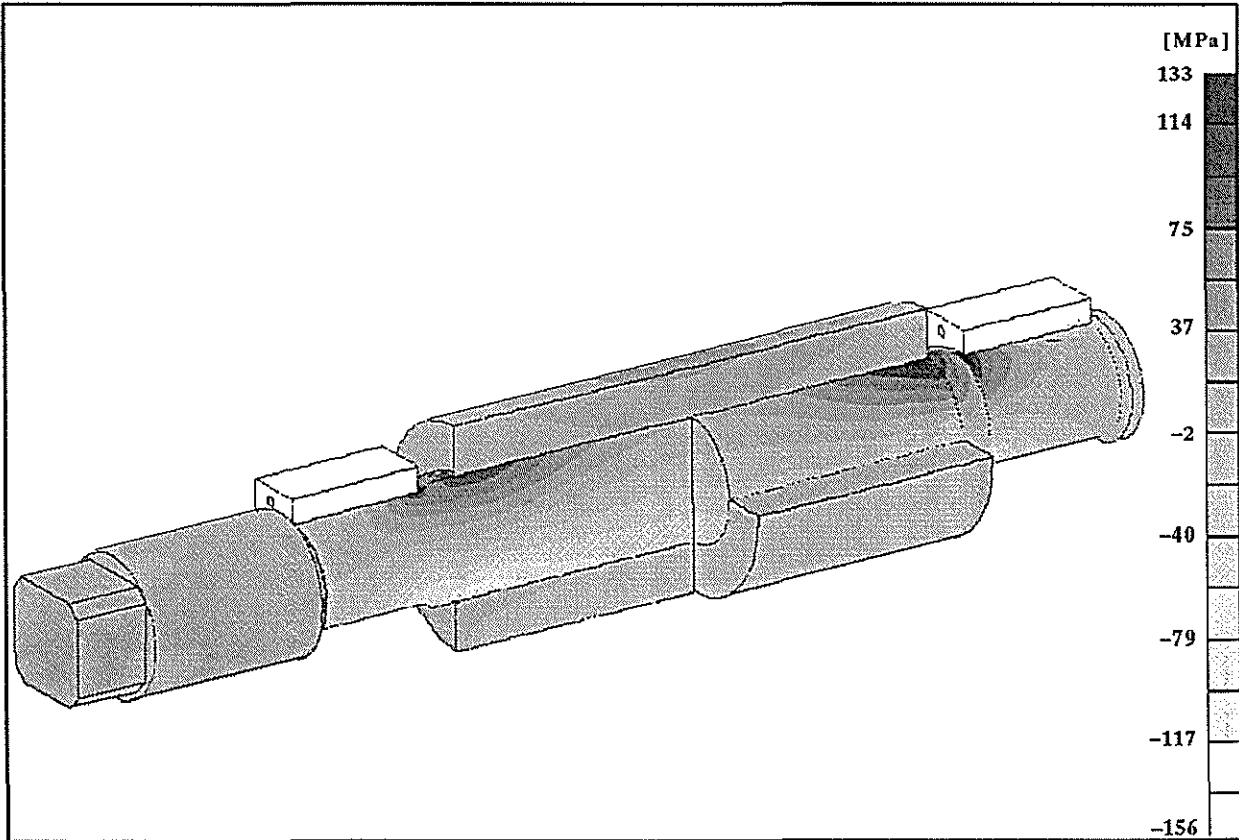


Figure 2.41 Axial stress plot (Stage 1: combined loads).

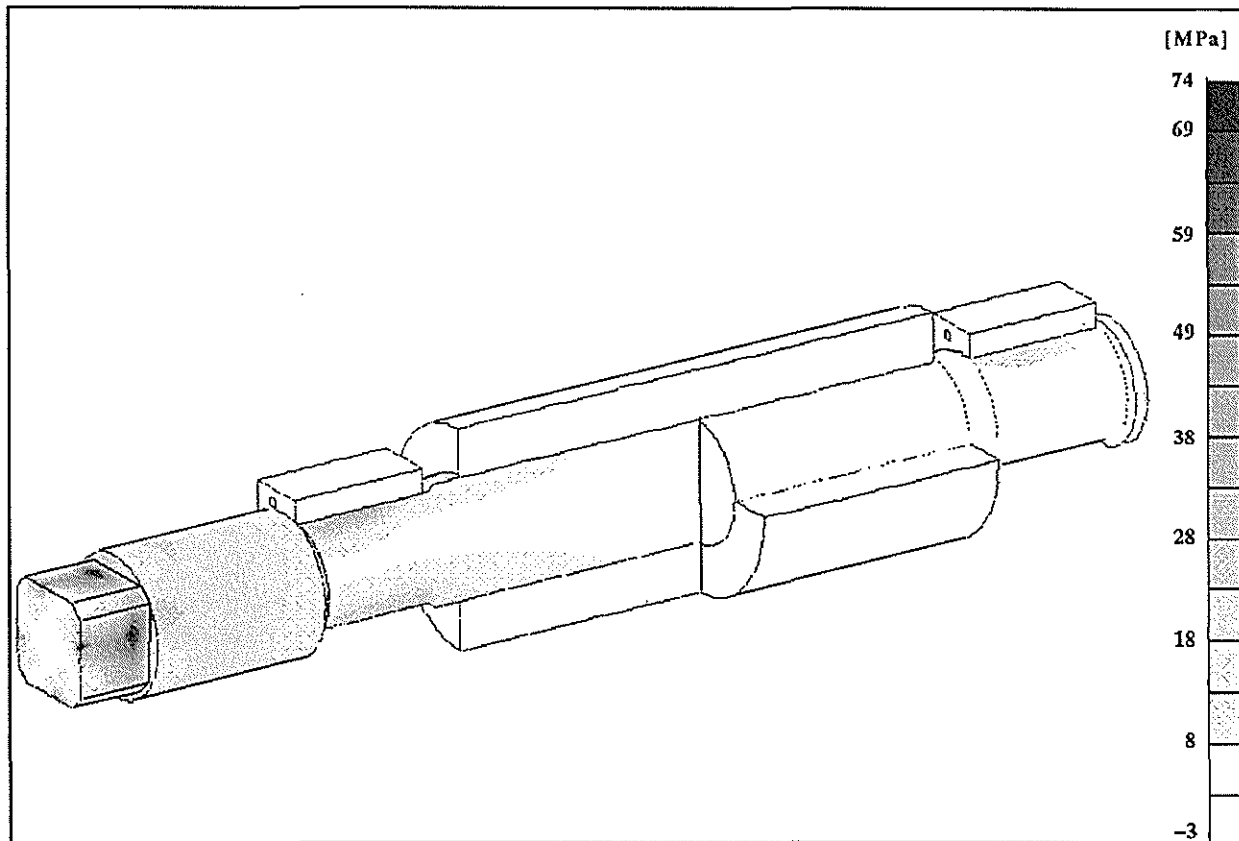


Figure 2.42 Major principal stress plot (Stage 1: torsional loads only).

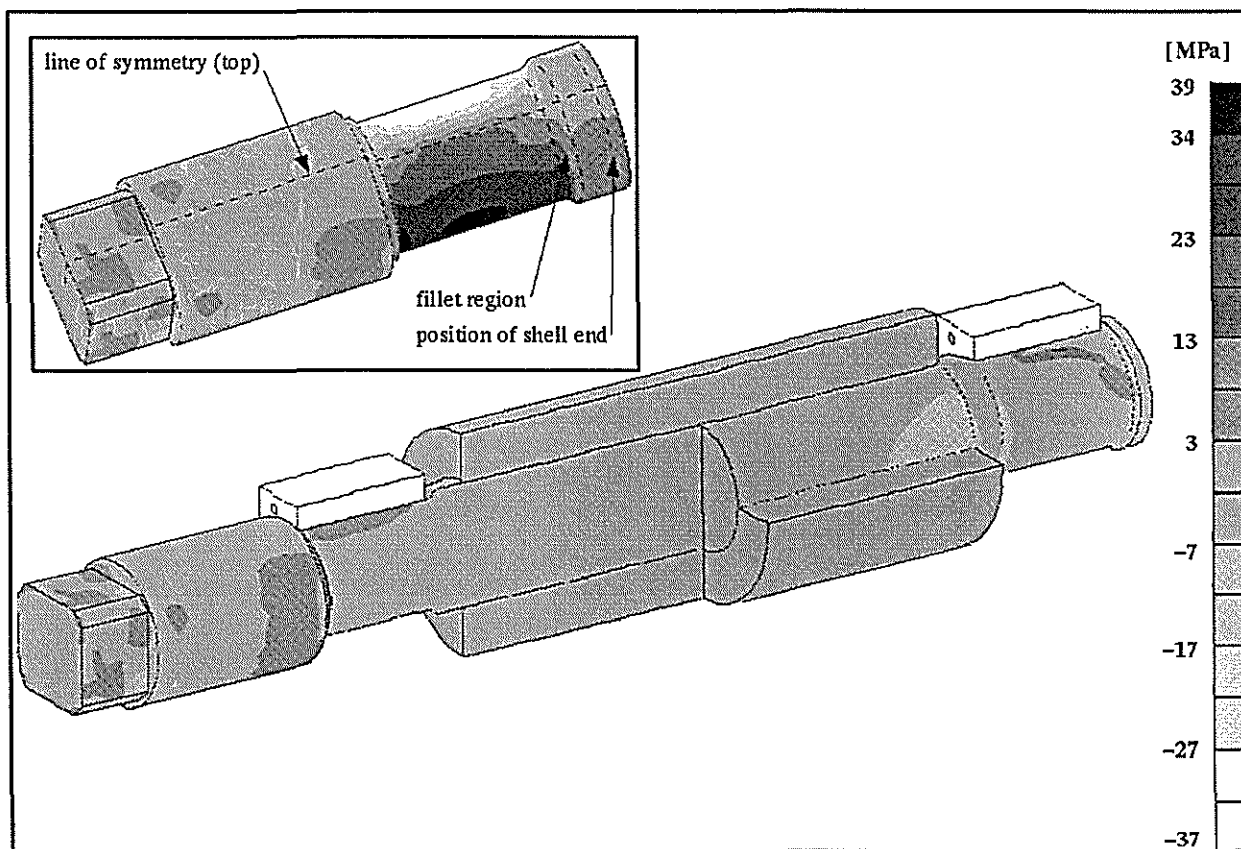


Figure 2.43 Axial stress plot (Stage 1: torsional loads only). INSET: drive-end close-up.



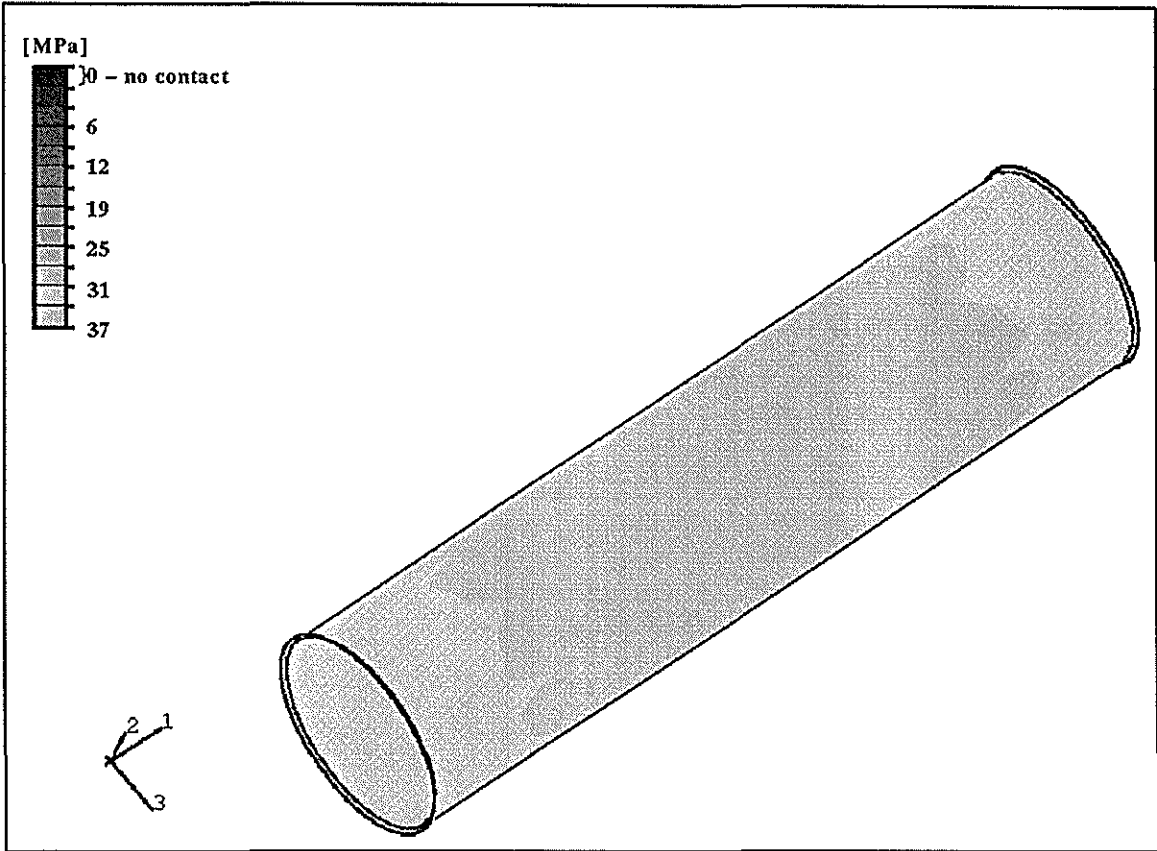


Figure 2.44 Contact pressure on inner shell surface (Stage 1: interference fit only).

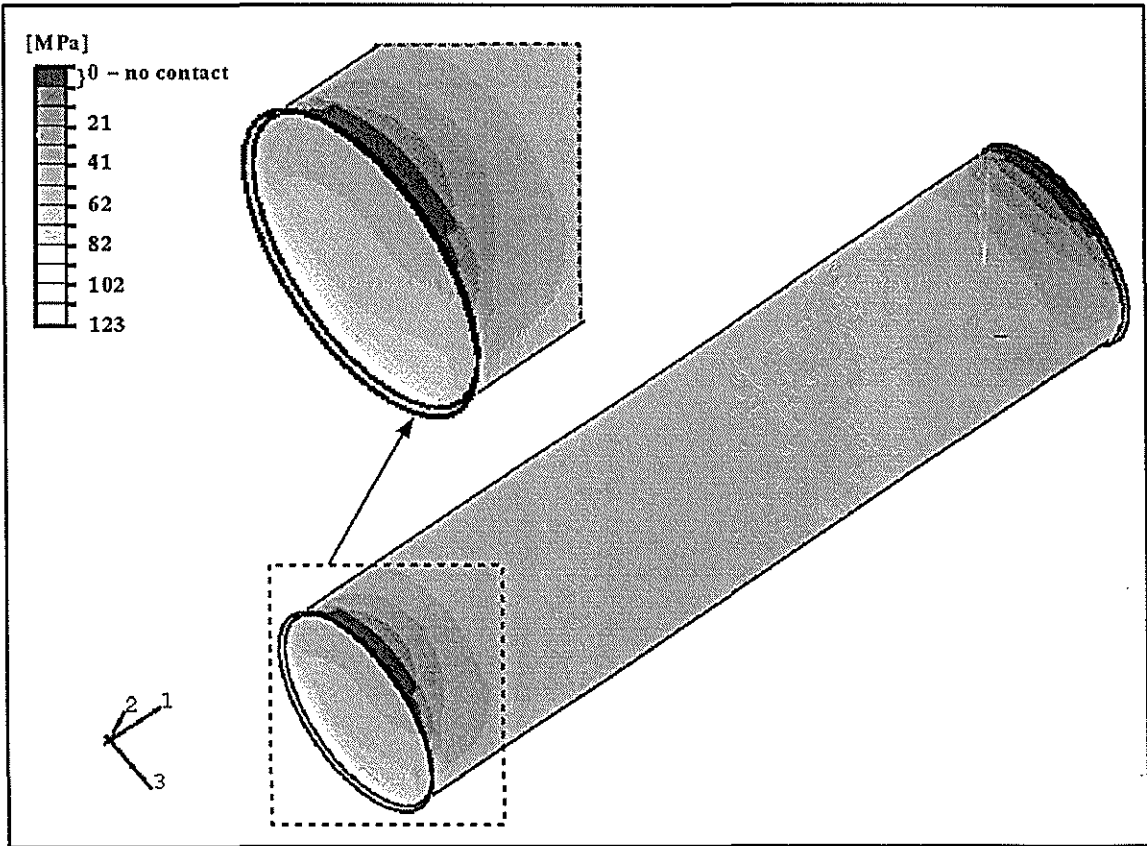


Figure 2.45 Contact pressure on inner shell surface (Stage 1: combined loads).

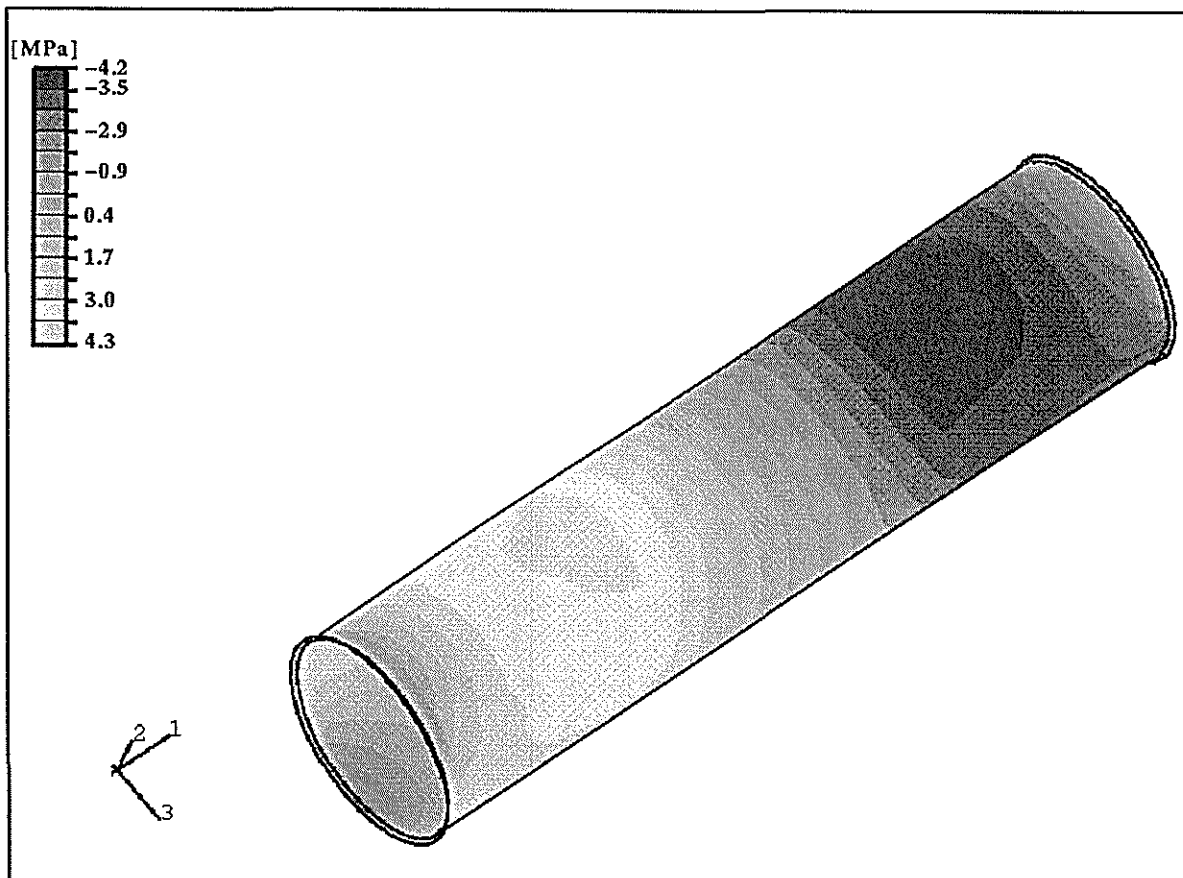


Figure 2.46 Contact shear stress on inner shell surface in direction 1 (Stage 1: combined loads).

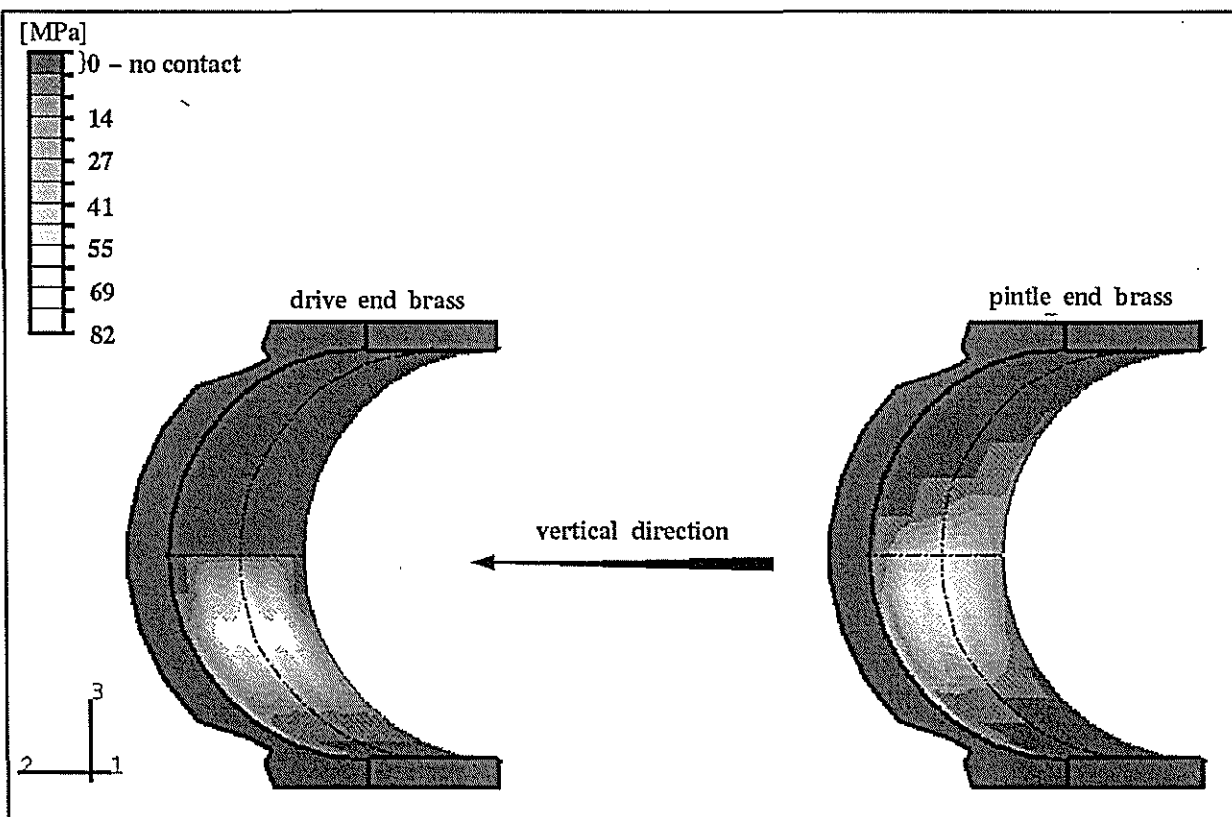


Figure 2.47 Contact pressure on inner brass surfaces (Stage 1: combined loads).

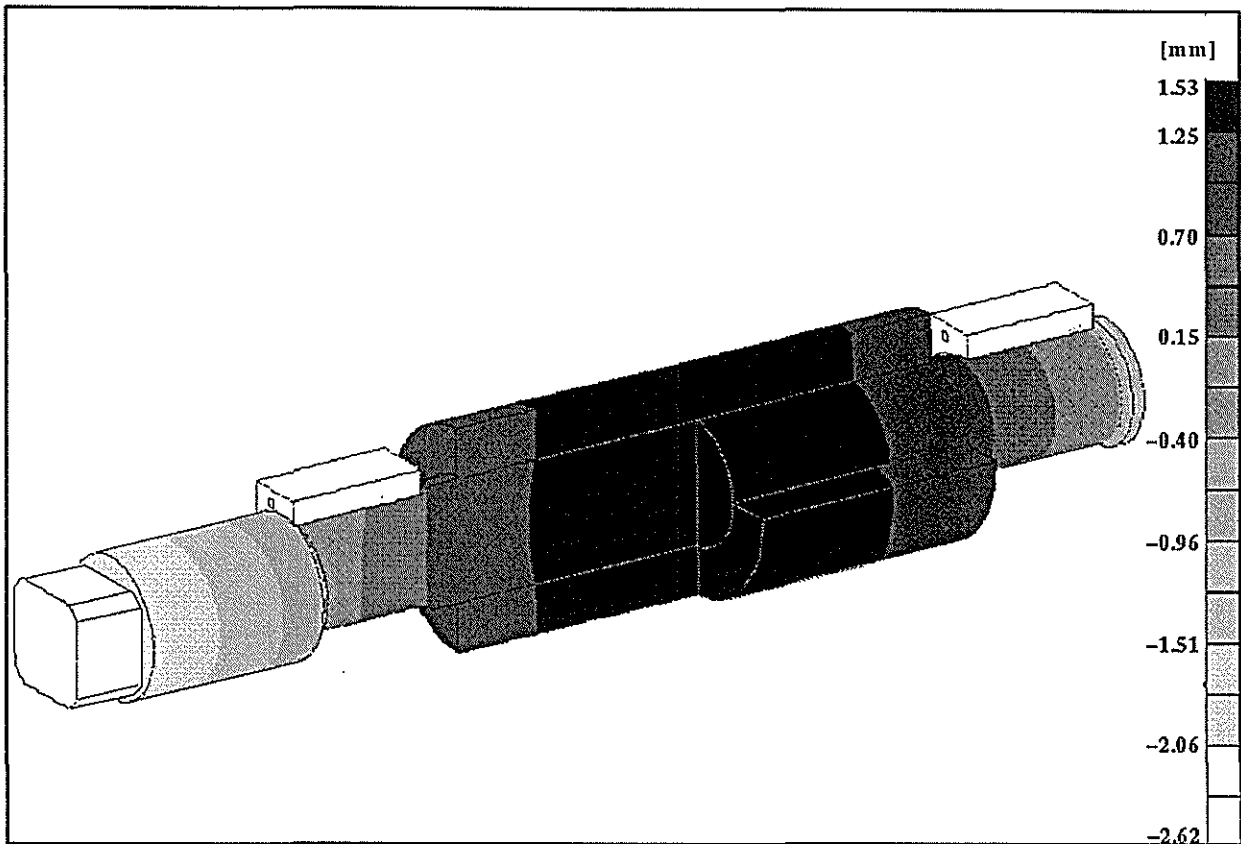


Figure 2.48 Vertical deflection plot (Stage 1: roll loads only).

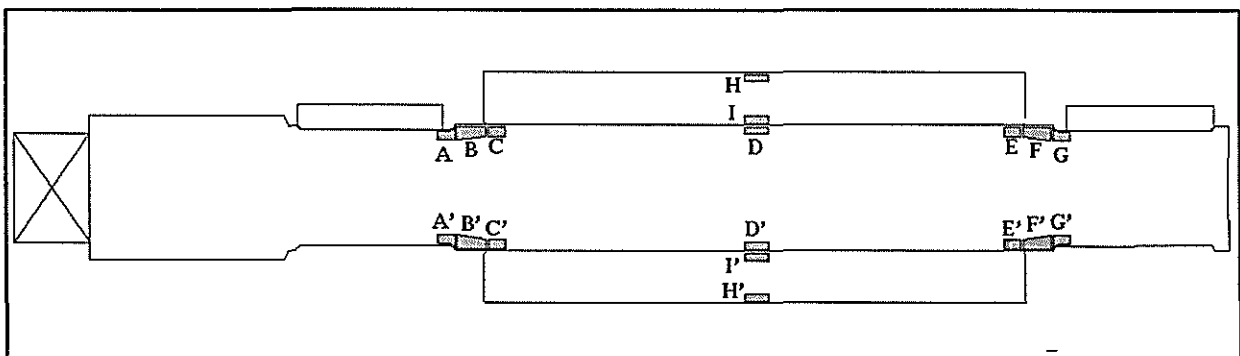


Figure 2.49 Critical locations where axial stress was examined.

In Figure 2.49, the corresponding areas A and A' represent the operational tensile and compressive regions respectively of the drive-end fillet. B and B' cover the region from the fillet transition to the first point of shell contact on the drive side, and so on.

Table 2.3 lists the maximum and minimum axial stress developed in various locations on the roller for the loading case 'Stage 1'. In addition, the axial stress developed by the interference fit only, and also by the roll loads only, are included for comparison.

Table 2.3 Axial stress results for the seven foot roller (Stage 1 analysis).

Position on roller (Figure 2.49)	Axial stress for critical locations on mill roller for specific load types. [MPa]		
	Interference fit only	Roll loads only	Combined loads
A	8	124	125
A'	8	-115	-105
B	14	103	100
B'	14	-128	-126
C	-10	127	115
C'	-10	-140	-150
D	-22	44	22
D'	-22	-38	-62
E	-10	127	119
E'	-10	-140	-156
F	14	103	104
F'	14	-128	-132
G	8	124	133
G'	8	-115	-109
H **	10	31	41
H' **	10	-35	-26
I	10	15	25
I'	10	-18	-9

\*\* results do not include the effect of the groove root stress concentration.

### 2.2.3 Tailbar misalignment / roll lift and bearing restraint effects

Operational mill loading and consequently model boundary restraint and load application become increasingly more difficult to calculate when roll lift and associated misalignment effects are considered. The most common scenario for mill roller operation and control is as follows. Work openings between the top roller and both the feed and delivery rollers are set according to compaction values required to achieve a certain juice extraction level for a predetermined cane fibre rate. The mill hydraulics are such that the resultant roll load required for the chosen compaction values can be accounted for. Usually the drive-end ram is more highly loaded than the pintle-end ram to account for the pinion reaction. Ideally, the top roller will operate horizontally aligned with the final motion gear axis. Modelling of this ideal case ('Stage 1') was reported in Chapter 2.2.2. Realistically, the height and angle of the roller varies continually with variations in cane fibre rates. Such roll lift fluctuations result in additional tailbar forces which were discussed in Chapter 1.8.3 and illustrated in Figure 2.50. During Cullen's experimental investigation into roller stress (Chapter 1.7), the centres of both drive and pintle-end journals were above the gears' axis for all drive and pintle load combinations tested. Due to the increased loading and stiffening effect of the tailbar and mill coupling arrangement on the drive-end of the mill roller, the pintle-end generally lifts higher compared to the drive-end. As a result of roll lift, uneven cane blanket loading and misalignment induced forces are expected. Unfortunately little has been published on prediction of such loads for sloping roller shafts. A further complication is the degree of brass bearing alignment with the deflected shaft (Figure 2.29).

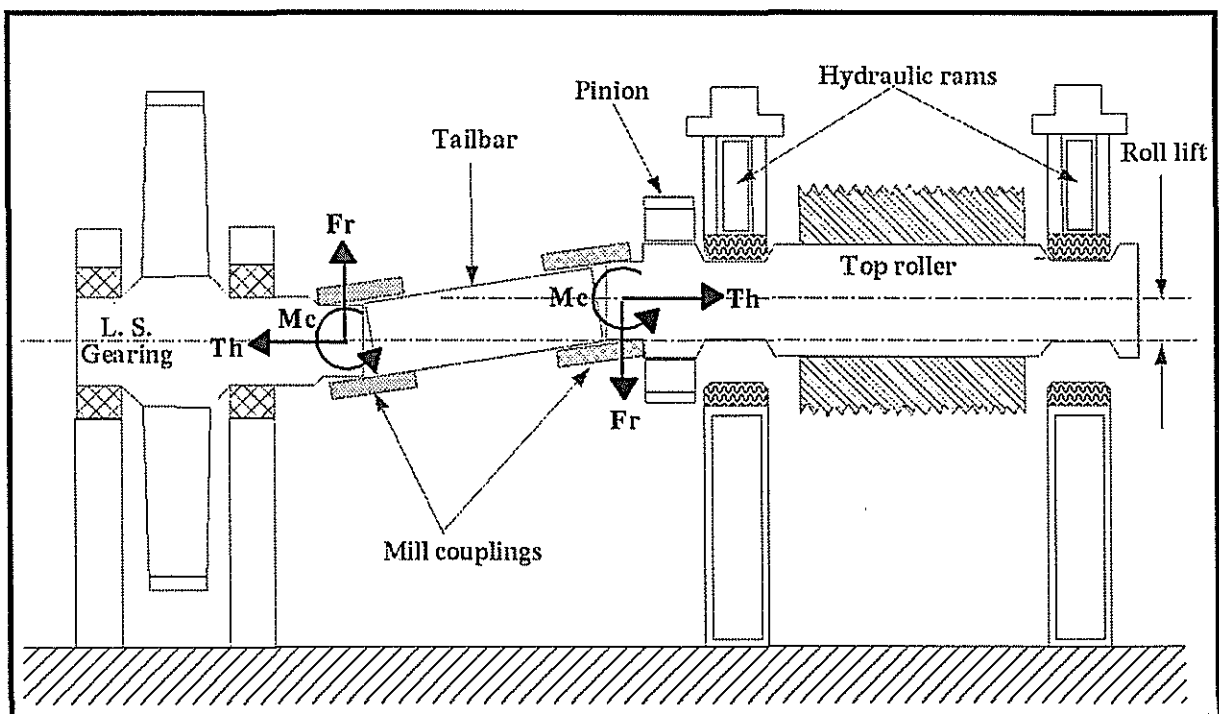


Figure 2.50 Additional tailbar forces resulting from horizontal roll lift.

The following results pertain to the 'Stage 2' analyses. Three cases were analysed to investigate the effect of misalignment loads, roll lifts and non-aligning bearings on roller stress. For all the analyses, the roll and torsional loads were applied as in the 'Stage 1' analysis (see Figures 2.26 and 2.27). Note that roll loads were applied through uniform pressure distributions along the roller's length while the bearings acted as reaction points. In factories, the loads are transmitted through the bearings and the cane blanket supplies the reaction force to the shell. Appendix A4 contains the calculations for the misalignment loads induced by a 10 mm parallel roll lift .

Case 1 considered misalignment loads induced by a 10 mm parallel roll lift, assuming a tailbar length of 2.0 m (see Figure 2.50). The brass bearings were allowed to align with shaft deflection. The additional misalignment loads (324 kN downward radial force and 425 kNm counter-clockwise moment) were applied to a single node located 118 mm in from the square-end on the shaft's axis. Figures 2.51 through 2.55 show the stress and bearing pressure results for Case 1.

Case 2 was identical to the 'Stage 1' analysis (no roll lift) except that the bearings were held rigid. Figures 2.56 through 2.60 show the stress and bearing pressure results for Case 2.

Case 3 was identical to the Case 2 analysis (rigid bearings) except that the pintle-end brass bearing was allowed to rise 10 mm above the gear axis (see Figure 2.29, roll C). In practice, the pressure distribution between the top and other rollers increases towards the drive-end of the shell. However, in the FEA, roll loads were applied uniformly along the length of the shell as in 'Stage 1' analysis. No misalignment loads were applied as their value in the case of a sloping roller is not known with any certainty. Figures 2.61 through 2.65 show the stress and bearing pressure results for Case 3.

Chapter 2.2.4 discusses the results from both 'Stage 1' and 'Stage 2' analyses and the consequence of assumptions made regarding the load application for Case 3.

Table 2.4 lists the maximum and minimum axial stress developed in various locations on the roller for all 'Stage 2' cases.

Table 2.5 lists the maximum and minimum axial stress developed in various locations on the roller for both 'Stage 1' and 'Stage 2' (Case 1) analyses. Theoretical values (Appendix A5) employing simple beam theory for compound cylinders (used to derive equation 1.29) are also included. This theoretical approach is frequently adopted in current mill roller design.

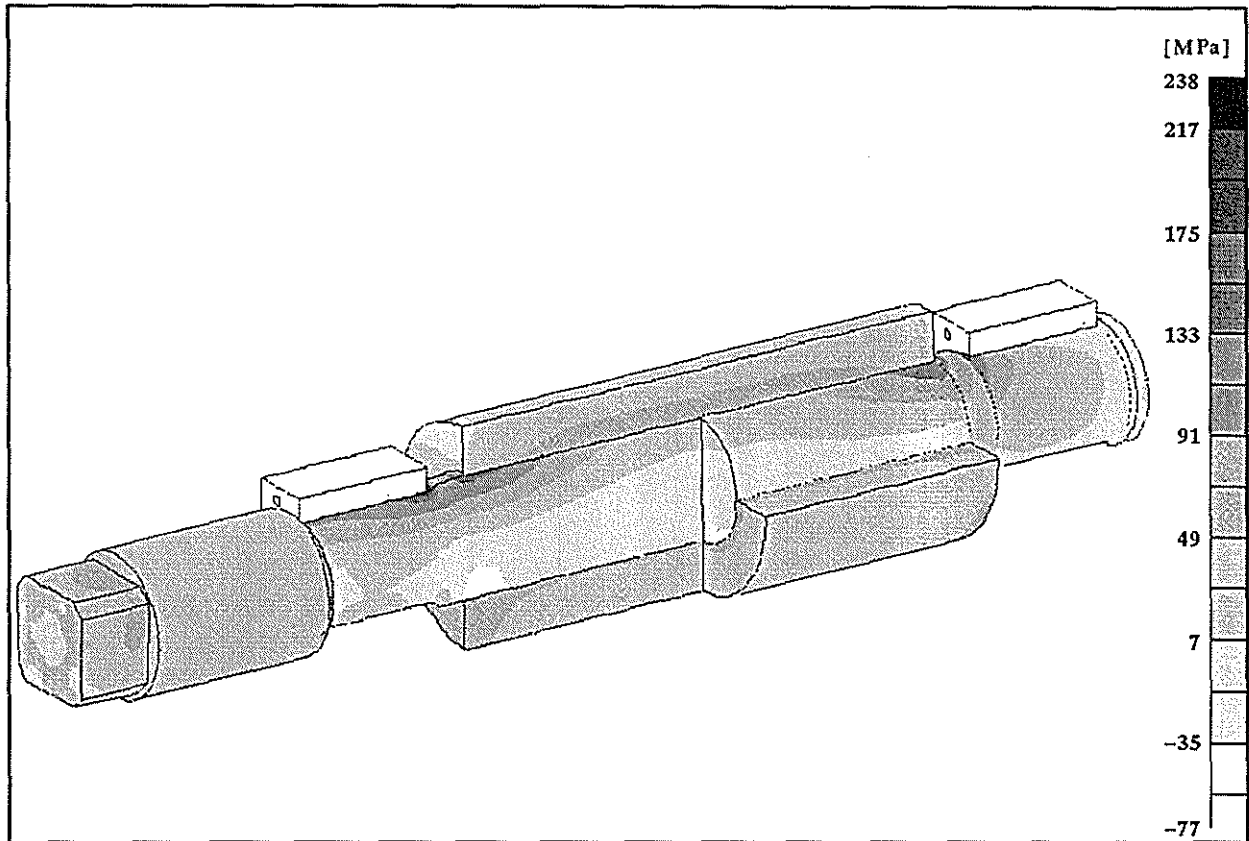


Figure 2.51 Major principal stress plot (Stage 2: Case1 - misalignment loads).

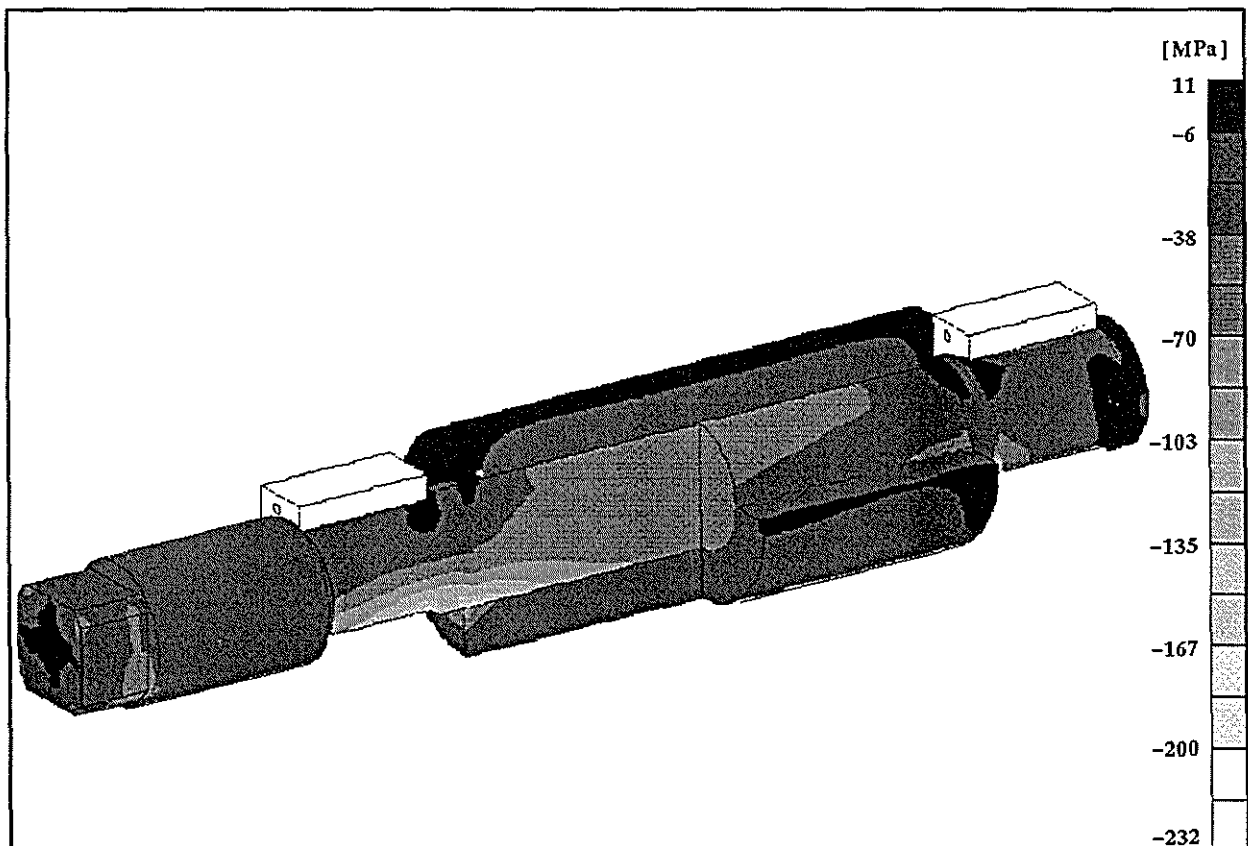


Figure 2.52 Minor principal stress plot (Stage 2: Case1 - misalignment loads).

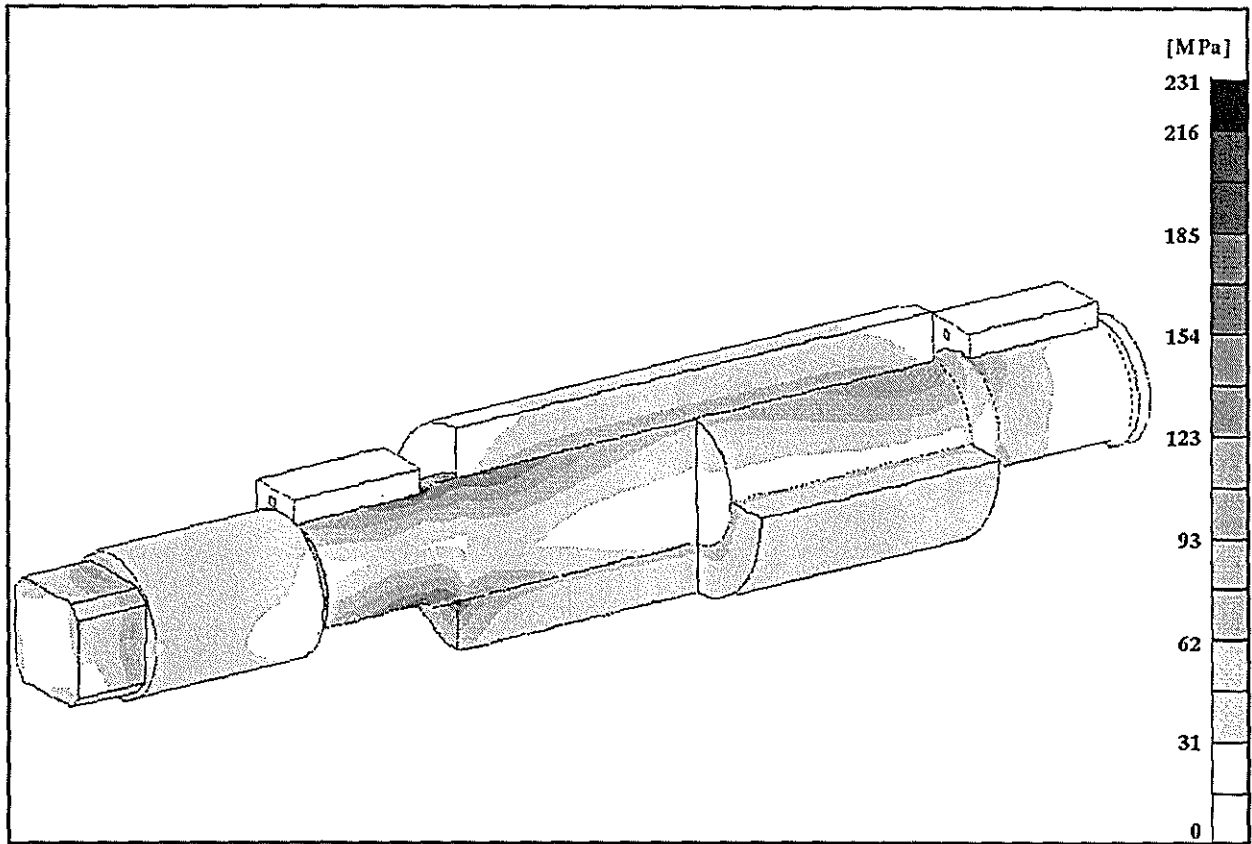


Figure 2.53 Von Mises stress plot (Stage 2: Case1 - misalignment loads).

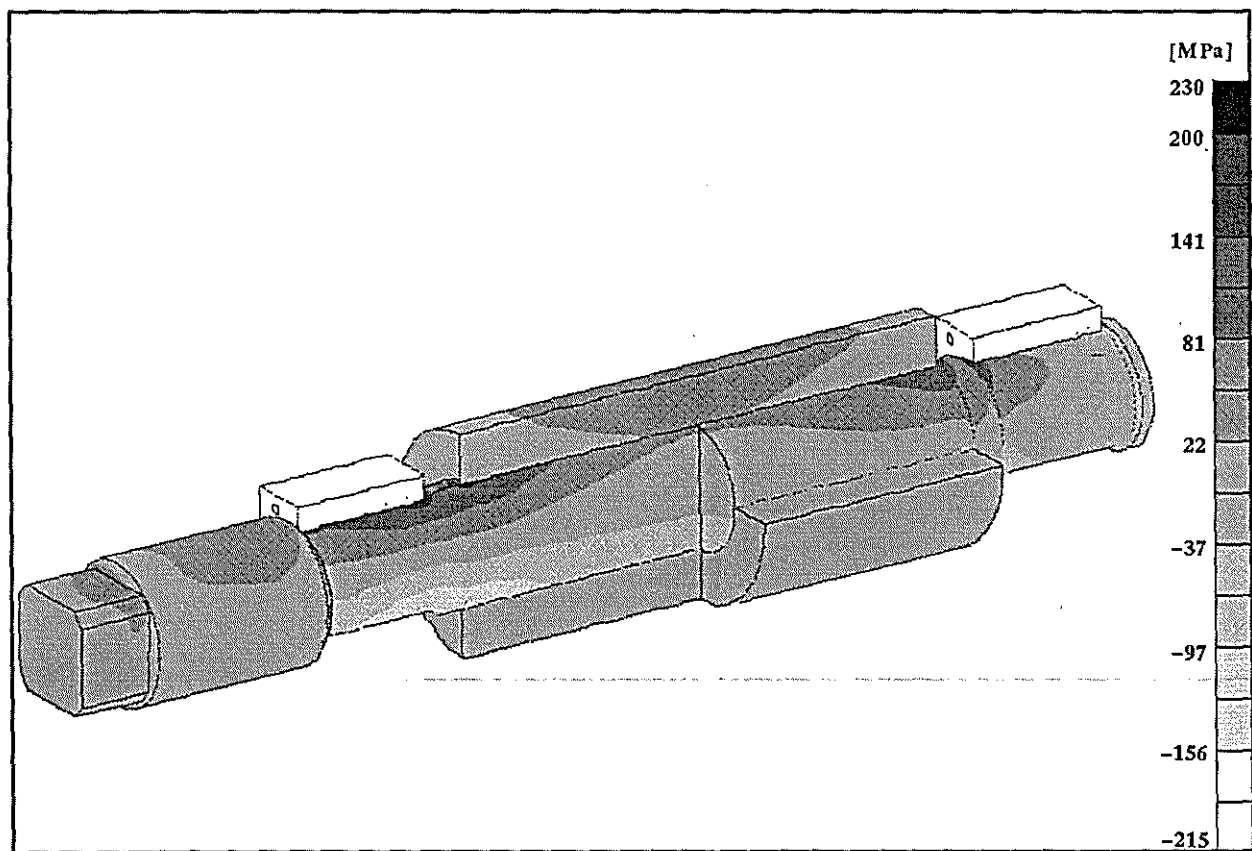


Figure 2.54 Axial stress plot (Stage 2: Case1 - misalignment loads).

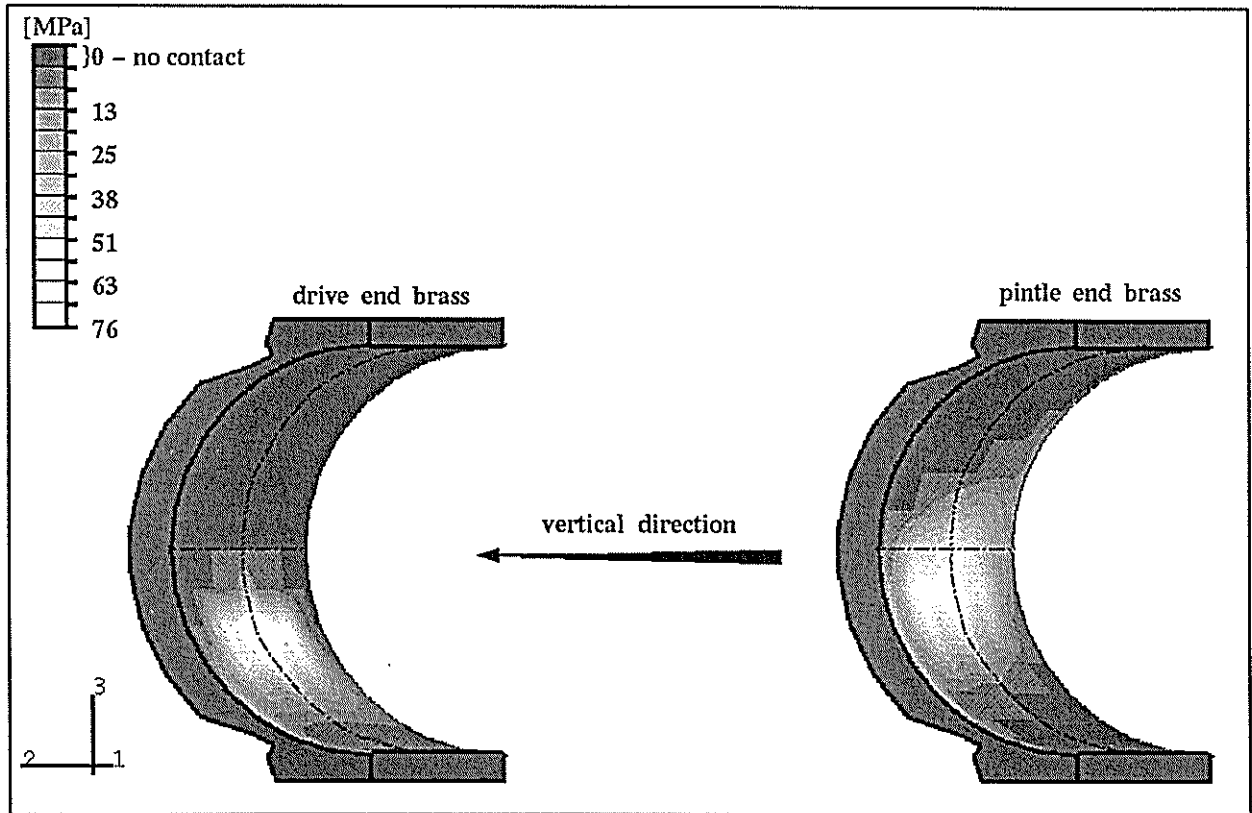


Figure 2.55 Contact pressure on inner brass surfaces (Stage 2: Case1 - misalignment loads).

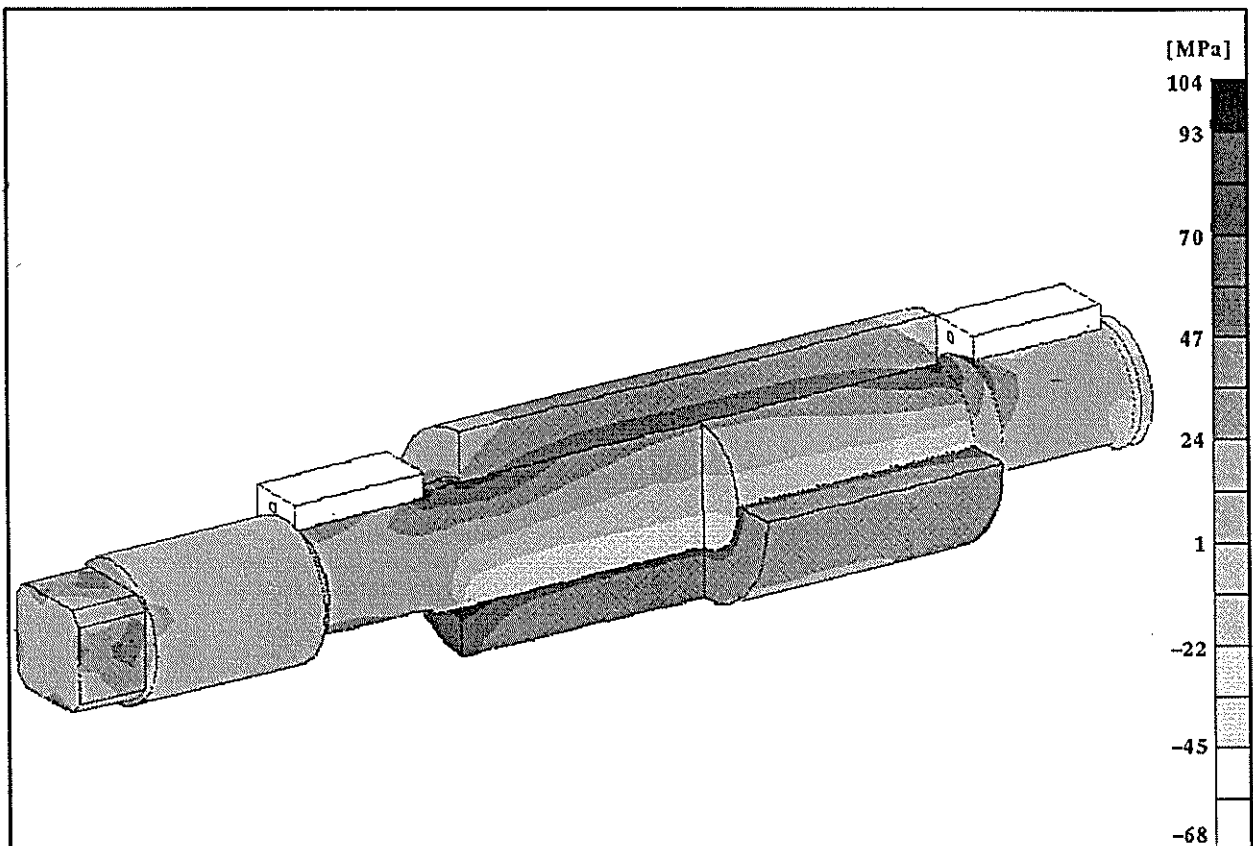


Figure 2.56 Major principal stress plot (Stage 2: Case2 - rigid bearings / no roll lift).

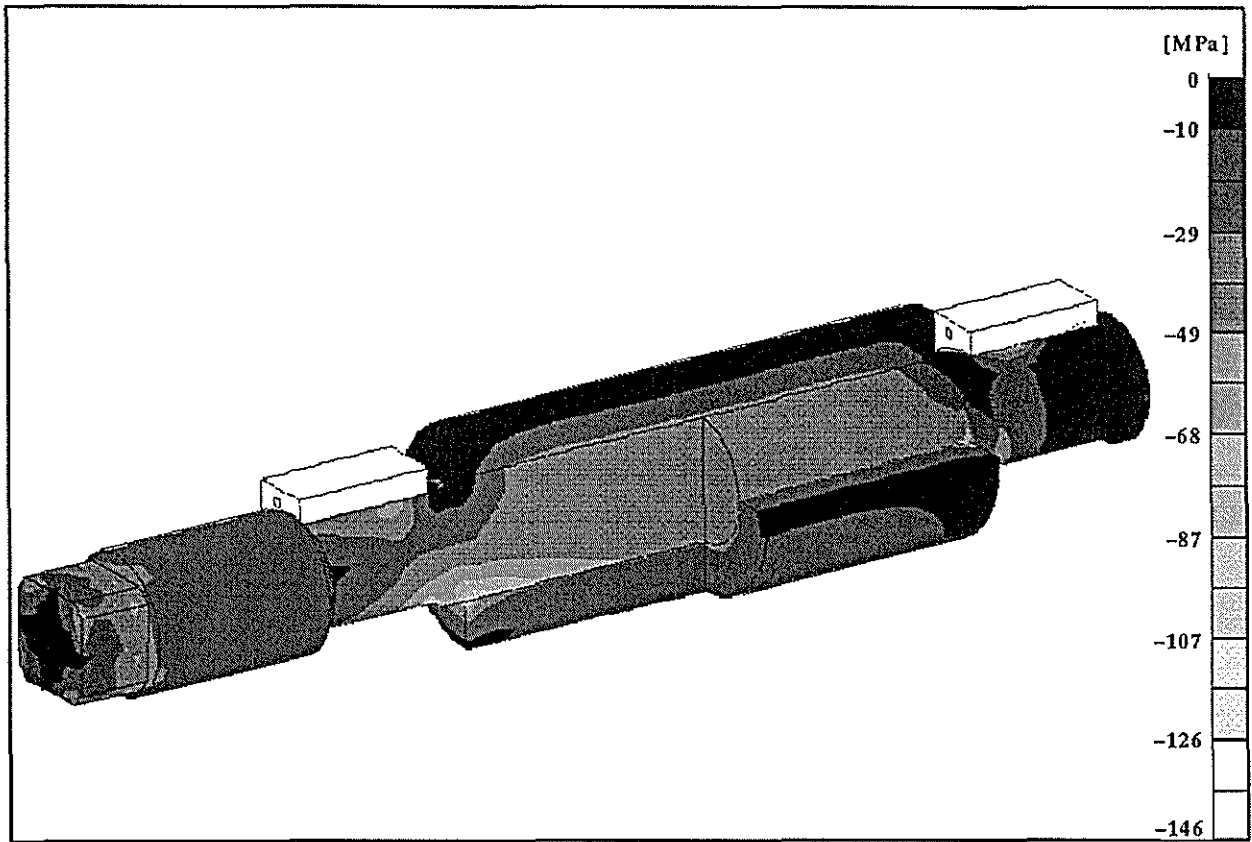


Figure 2.57 Minor principal stress plot (Stage 2: Case2 - rigid bearings / no roll lift).

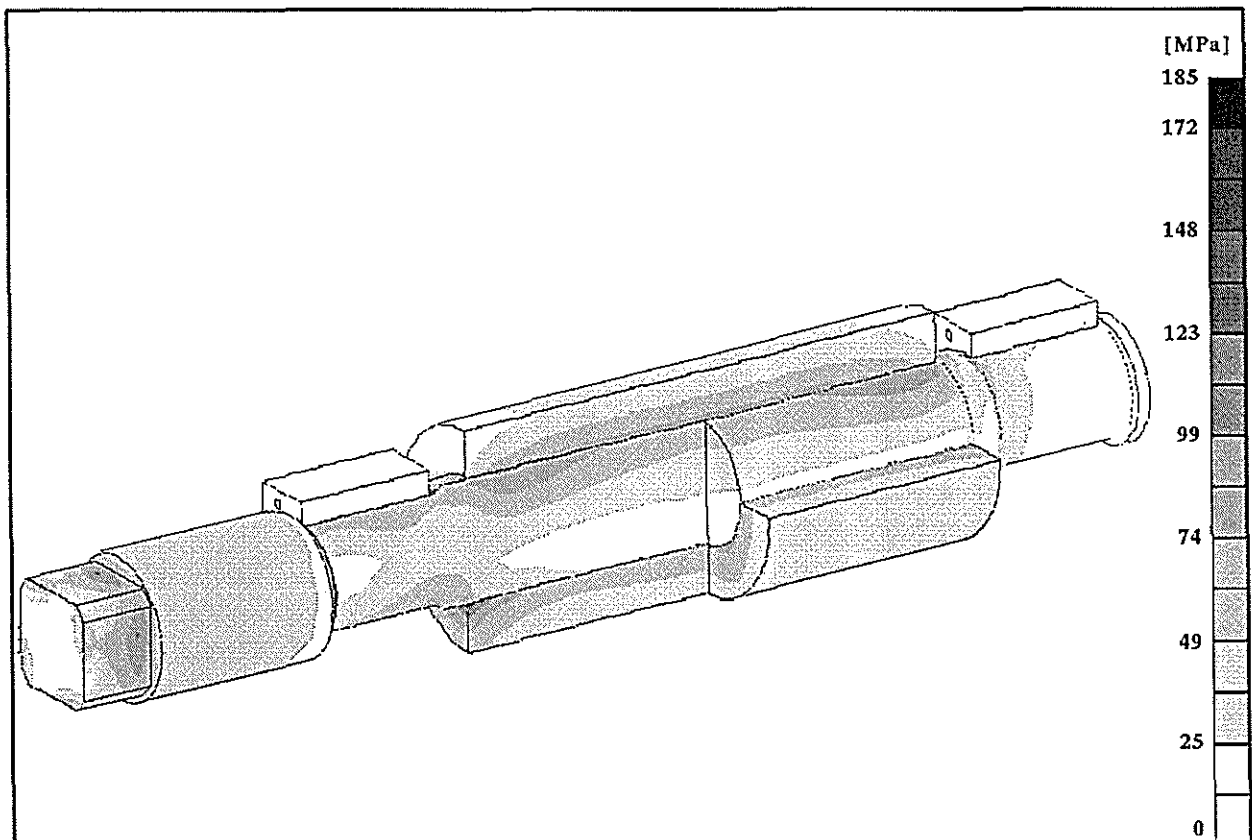


Figure 2.58 Von Mises stress plot (Stage 2: Case2 - rigid bearings / no roll lift).

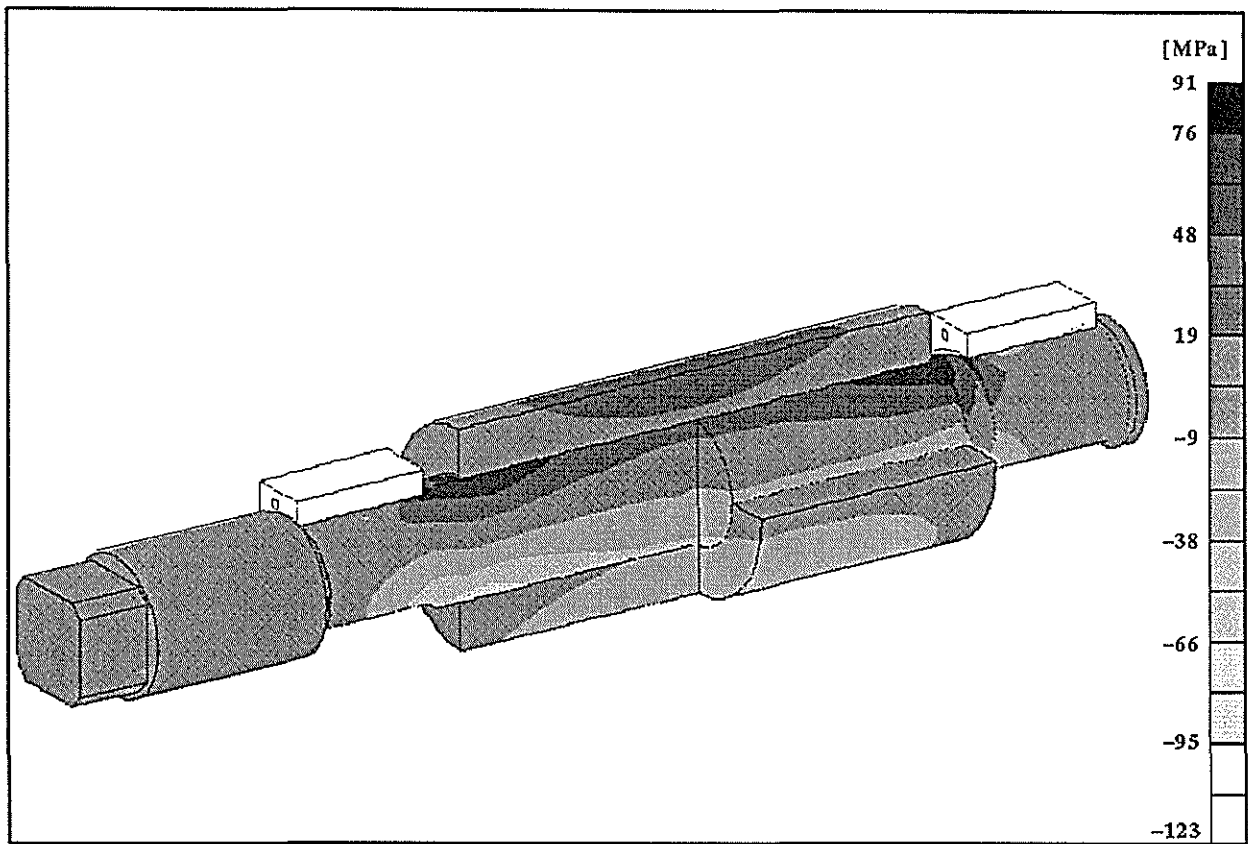


Figure 2.59 Axial stress plot (Stage 2: Case2 - rigid bearings / no roll lift).

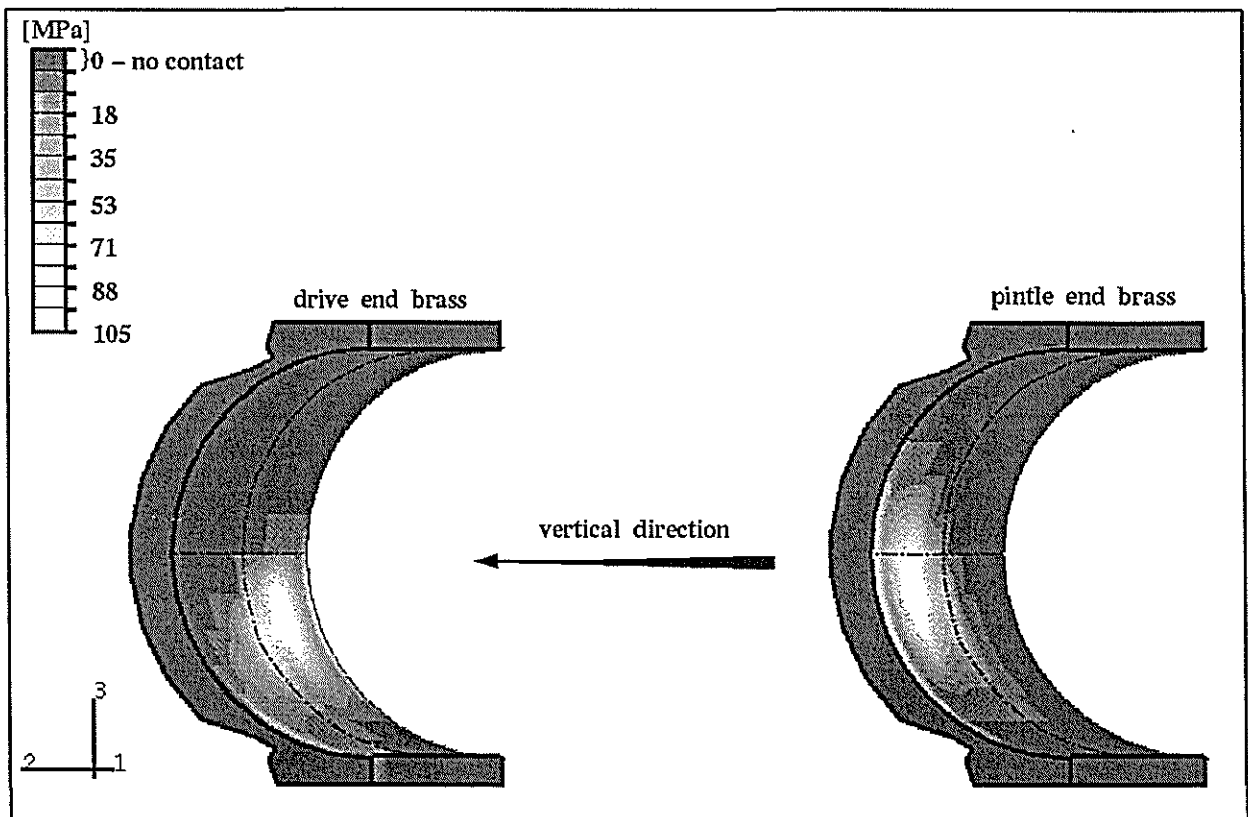


Figure 2.60 Contact pressure on inner brass surfaces (Stage 2: Case2 - rigid bearings / no roll lift).

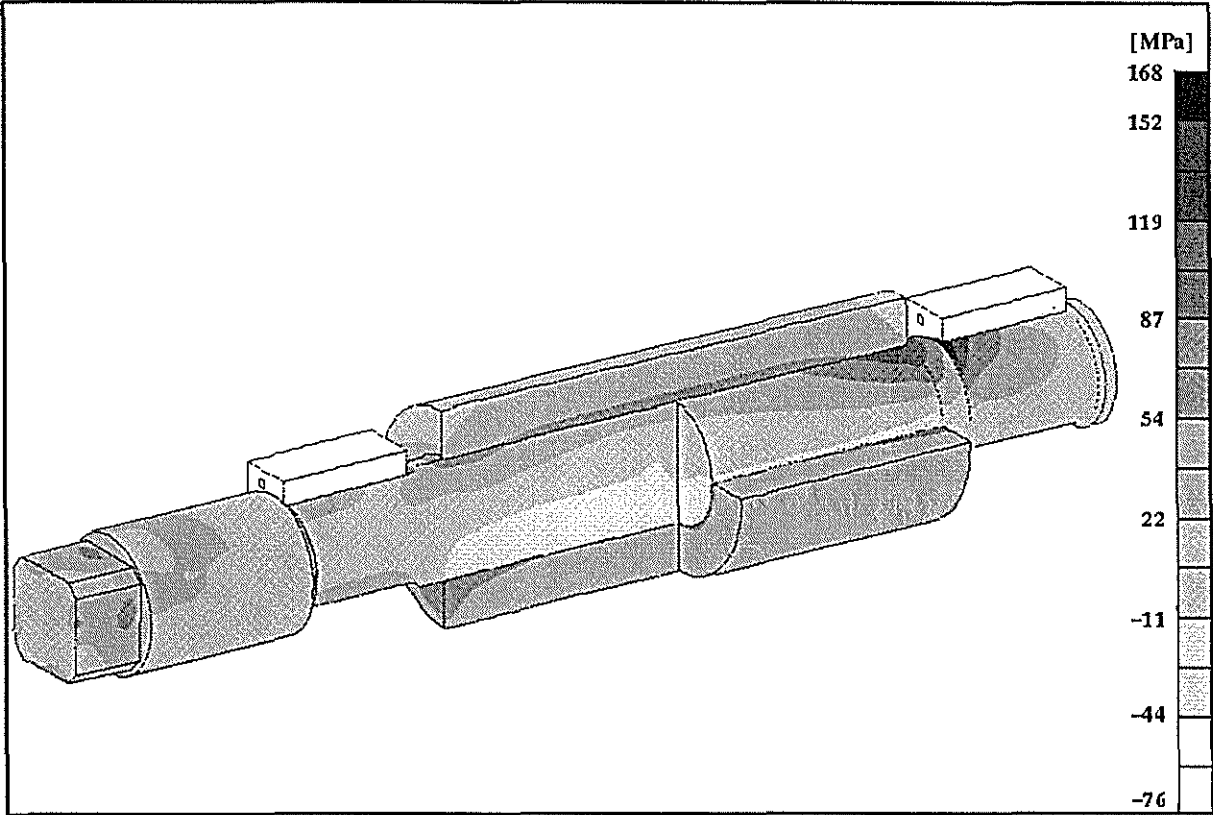


Figure 2.61 Major principal stress plot (Stage 2: Case3 - rigid bearings / 10 mm pintle-end lift).

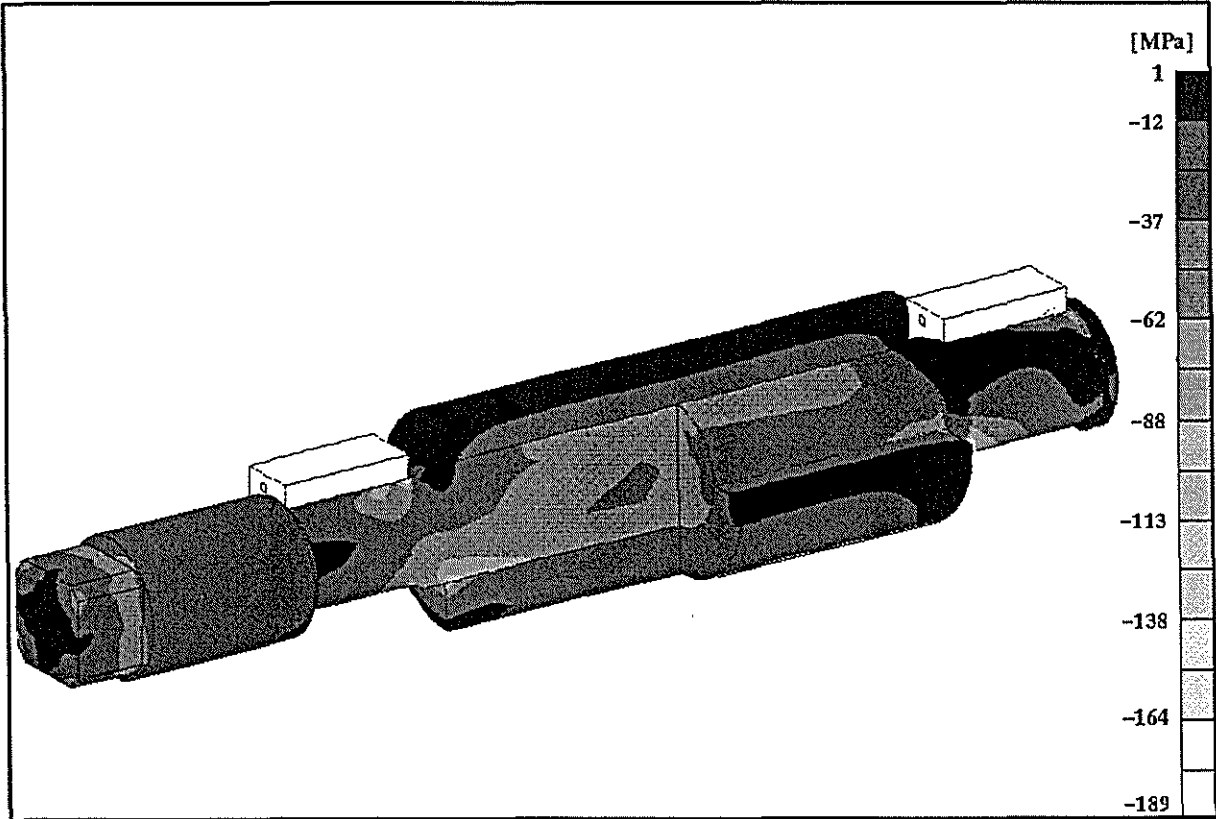


Figure 2.62 Minor principal stress plot (Stage 2: Case3 - rigid bearings / 10 mm pintle-end lift).

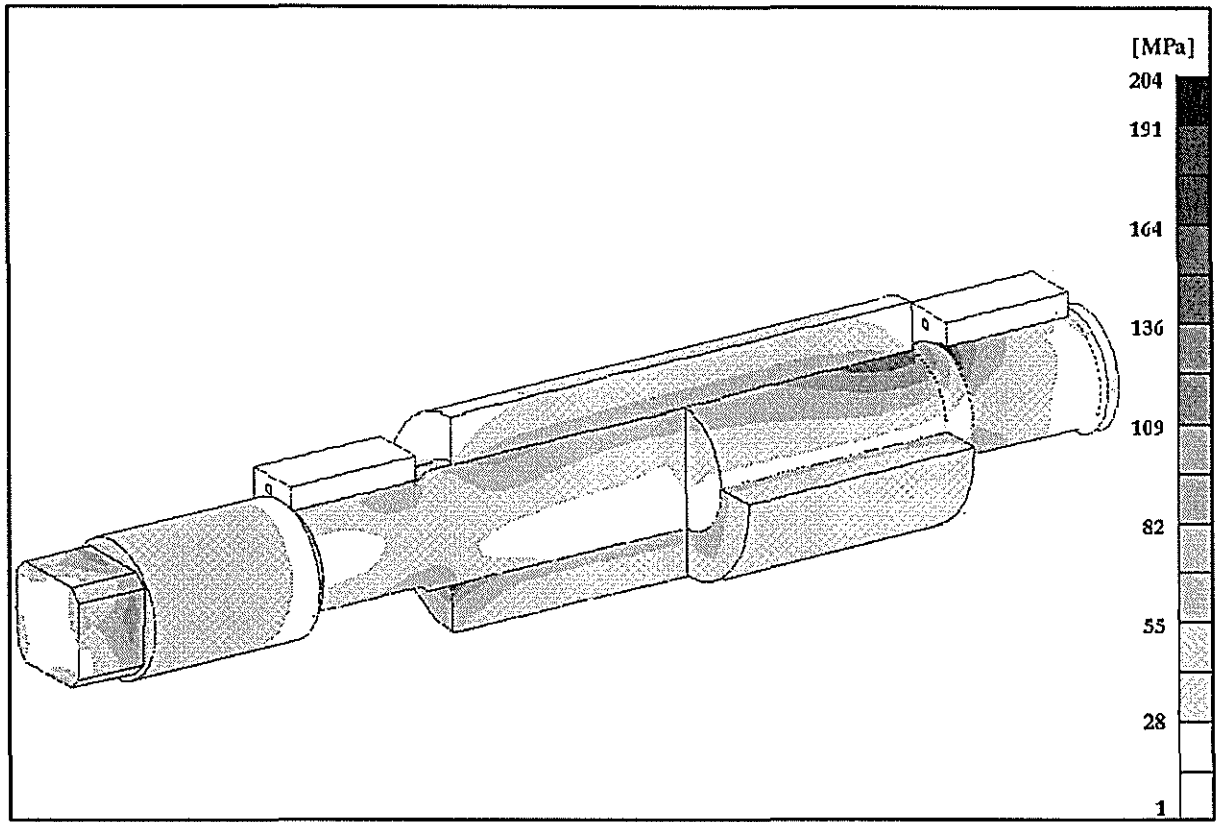


Figure 2.63 Von Mises stress plot (Stage 2: Case3 - rigid bearings / 10 mm pintle-end lift).

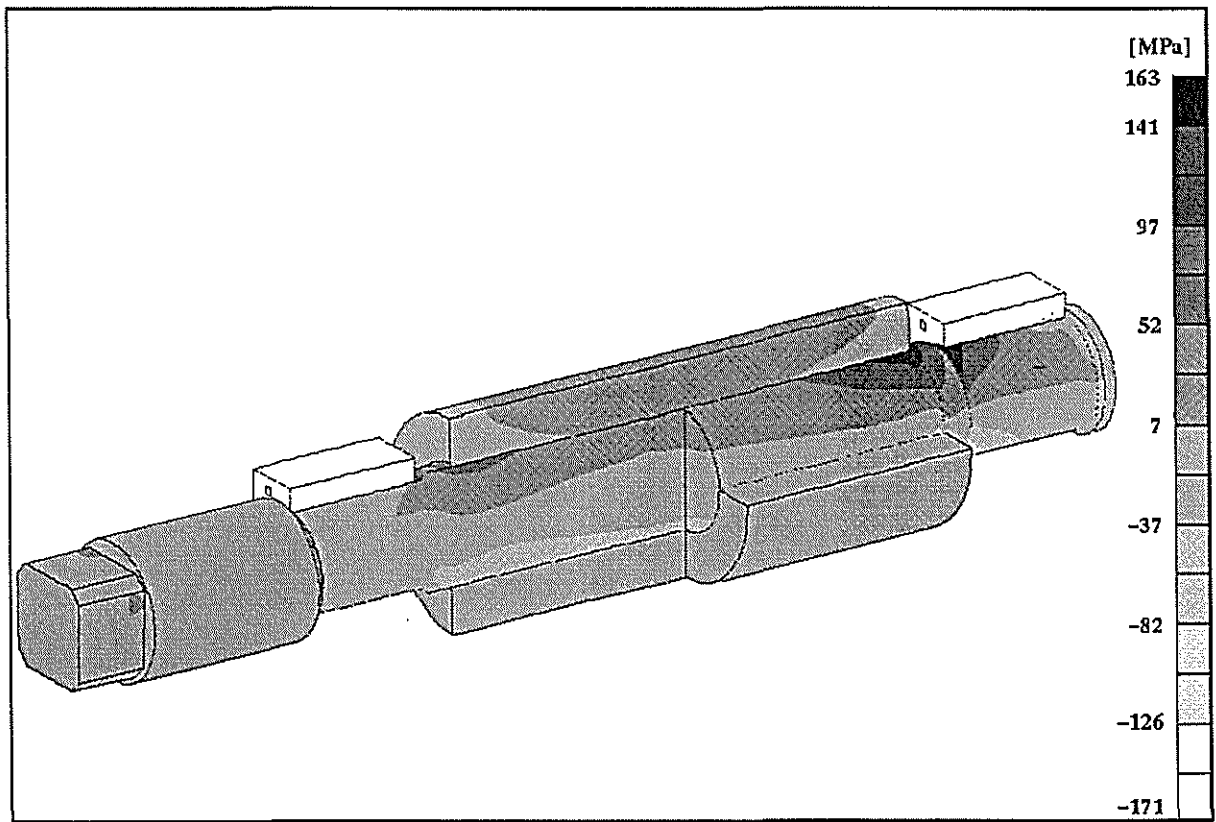


Figure 2.64 Axial stress plot (Stage 2: Case3 - rigid bearings / 10 mm pintle-end lift).

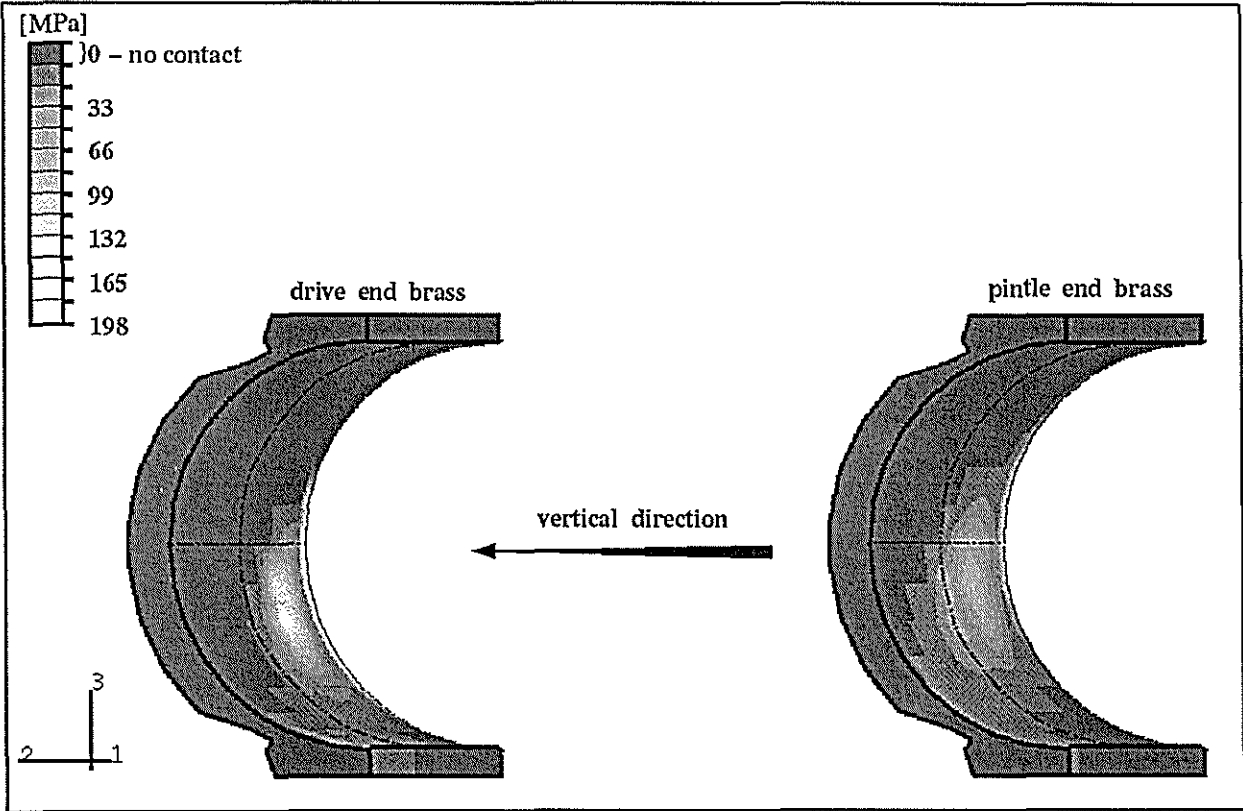


Figure 2.65 Contact pressure on inner brass surfaces (Stage 2: Case3 - rigid bearings / 10 mm pintle-end lift).

Table 2.4 Axial stress results for the seven foot roller (Stage 2 analyses).

Position on roller (Figure 2.49)	Axial stress for critical locations on mill roller for specific operating conditions. [MPa]		
	Case 1 10 mm roll lift, aligning bearings, misalignment loads.	Case 2 no roll lift, rigid bearings, no misalignment loads.	Case 3 10 mm pintle end lift, rigid bearings, no misalignment loads.
A	230	92	70
A'	-213	-75	-53
B	152	83	70
B'	-194	-105	-90
C	168	89	75
C'	-216	-124	-109
D	29	30	33
D'	-67	-45	-47
E	130	85	131
E'	-123	-123	-171
F	113	79	118
F'	-145	-103	-152
G	146	82	163
G'	-121	-60	-141
H **	45	32	34
H' **	-32	-27	-29
I	27	17	18
I'	-12	-13	-14

\*\* results do not include the effect of the groove root stress concentration.

Table 2.5 Axial stress results for the seven foot roller (FEA versus Theoretical).

Position on roller	Axial stress for critical locations on mill roller for specific operating conditions. [MPa]			
	Stage 1 (normal loads)		Stage 2:1 (misalignment loads)	
	FEA (all loads)	Theoretical (bending loads)	FEA (all loads)	Theoretical (bending loads)
drive-end inboard fillet	125 to -106	107 to -107	230 to -213	227 to -227
drive-end shell region	115 to -150	146 to -146	168 to -216	242 to -242
pintle-end shell region	119 to -156	146 to -146	130 to -145	163 to -163
pintle-end inboard fillet	133 to -109	107 to -107	146 to -121	120 to -120
shell outside centre **	41 to -26	28 to -28	45 to -32	34 to -34

\*\* results do not include the effect of the groove root stress concentration.

#### 2.2.4 Review of critical regions and associated stress states

The 3D modelling has focussed on the inboard journal fillets and regions under the shell-ends as history has shown these locations to be the most critical. The effect of roll loads, torque transmission, pinion reactions, bearing movement and contacts, tailbar loads and misalignment, interference fits and combinations of the above on stress states throughout the roller has been evaluated. Major findings resulted from the 3D modelling include:

1. Predictions using simple beam theory and modelling give comparable stress results;
2. Both inboard journal fillets and shell-end regions are highly stressed during crushing;
3. Misalignment (roll lift) increases the overall stress state in a mill roller;
4. Bearing restraint has an effect on the bending stress in the critical regions; and
5. A gap (50 mm deep with an opening of 0.025 mm) between the shell-ends and the top of the shaft is formed under a 70 tonne / ft roll load.

Confidence in modelling results was achieved through comparison with theoretical stress predictions using simple beam theory for compound cylinders (Table 2.5). This theoretical approach is frequently adopted in current mill roller design. The 'theoretical' results in Table 2.5 were calculated using only loads which contribute bending stress to the roller whereas the results pertaining to 'FEA' include torsional load effects. Generally, axial stress levels predicted by finite element methods were marginally greater than the stress levels determined by beam theory for the critical inboard fillet regions. However, the reverse was true for the shell-end regions. Any differences can be attributed to the torsional load and interference fit contributions to the overall stress state. This reasonable comparison of FEA and theoretical results relating to the axial stress state in mill rollers suggests that equation 1.29, derived from beam theory and the SN fatigue

approach, gives an adequate estimation of roll loads possible for a given roller design. However, as operating conditions vary, simply considering roll loads when determining safe load levels may prove insufficient in terms of shaft life.

FEA results throughout Chapter 2.2 have shown the inboard fillet and shell-end regions to be highly stressed. This finding supports the original efforts to concentrate on these critical regions with increased mesh density for greater accuracy. The maximum Von Mises stress for the roller model was 203 MPa, located at the shell-end regions on the underside of the shaft. The applied loads for this case included a uniform roll load (70 tonne / ft), tailbar torque of 930 kNm and an interference fit (0.0007 mm / mm). Axial stress in both the inboard fillet regions ranged between 130 and -110 MPa. Axial stress at the shell-end regions ranged between 120 and -150 MPa. The tailbar deflected downwards by 2.6 mm and the centre of the shell deflected upwards by 1.5 mm when only the roll loads were applied. The resulting misalignment forces caused by the deflected shaft curvature interacting with the tailbar were neglected throughout this investigation. Cullen (1968) argued that the endurance limit for steel commonly used in mill rollers would be approximately 107 MPa when journal size, surface roughness from machining and reliability are accounted for. This suggests the roll load applied to the roller geometry used in the analyses was in excess of those loads considered safe for long shaft life. Substituting a safety factor of 1.4 (Cullen, 1968) into equation 1.29, the resultant roll load limit, to keep stress values below the endurance limit, is 50 tonne / ft.

Realistically, the height and angle of the top roller changes continually with variations in cane fibre rate. Such roll movement results in additional tailbar forces. Misalignment forces corresponding to a vertical lift of 10 mm to the top roller were applied in addition to the existing roll loads so as to gauge the effect of roll movement on operational stress. The maximum Von Mises stress for the roller model was 231 MPa, located at the drive-end inboard fillet. Axial stress at the drive-end inboard fillet ranged between 230 and -210 MPa. Axial stress at the drive shell-end region ranged between 170 and -220 MPa. Axial stress at the pintle-end inboard fillet ranged between 130 and -150 MPa. Axial stress at the pintle shell-end region ranged between 150 and -120 MPa. These axial stress values far exceed the endurance limit, suggesting that the roller would not survive its expected life under such misalignment conditions. These results highlight the dangers of neglecting possible operating conditions such as roll lift when designing mill rollers. Similarly, mill engineers should limit roll lift where possible to avoid overloading the mill roller so as to ensure acceptable roller life.

During experimentation, Cullen postulated that there was some restraint for the bearings to successfully align with the floating and deflected top roller during operation. Consequently, the effective lever arm between the load centre (between bearing and shaft) and the inboard fillet would not simply be one half the journal length as theory would dictate. To check the sensitivity

of the stress developed in the mill roller to bearing movement, two separate analyses were undertaken. In the first analysis, both bearings were held rigid when loads were applied to the roller. The resulting pressure distribution on the bearing surface emphasised the movement of the pressure centre towards the inboard fillet on both ends. Axial stress levels throughout the roller shaft were approximately 20 MPa lower than the case where the bearings were allowed to adjust with the shaft. The maximum contact pressure between shaft and bearing was 105 MPa for the rigid bearing case as compared to 76 MPa for the freely moving bearing case (Stage 1). The second analysis kept the bearings rotationally rigid with the pintle-end bearing being raised 10 mm. No misalignment loads were applied to the roller even though there is a height and angle differential between the shaft and tailbar. The resulting pressure distribution on the bearing surface emphasised the movement of the pressure centre towards the inboard fillet on the drive-end bearing (198 MPa) and away from the inboard fillet on the pintle-end bearing (approximately 100 MPa). Note that all bearing / shaft interactions were modelled using the 'softened' contact algorithm (Chapter 2.2.1). Axial stress was again lower at the drive-end of the roller whereas axial stress at the pintle-end was higher when compared to the freely moving bearing case (Stage 1). These findings regarding roll lifts agree with those made by Cullen during actual factory experimentation. As Cullen found and the FEA modelling supported, the bending stress is dependent on the effective lever arm of the bearing reaction which was shown to vary with differing roll lifts. In addition, the restraining effect of the tailbar can effect the angular position of the roller developing extra bending and radial loads which raise the stress levels throughout the roller.

According to Reid's survey (1988), approximately 50 per cent of mill roller failures occur at the inboard fillet regions and a further 40 per cent of failures occur at or just under the shell ends. All analyses throughout the three dimensional modelling of mill roller confirmed these two locations to be highly stressed and most likely to fail by fatigue. Cullen's experimental work concentrated on the inboard fillet regions but neglected the stress concentration effect at the end of the shell due to the difficulties associated with monitoring stress in this region. In this situation, FEA proved invaluable as stress and deflections due to the shaft and shell interaction at the shell-end could be scrutinised. As also found in the two dimensional modelling (Chapter 2.1), tensile stress at the inboard fillet regions and the shaft region near the shell-ends is induced by the interference fit alone. Cullen suspected that a gap of unknown size develops between the top of the shaft and shell-ends under sufficient roll loading, in which corrosive juice can enter and reduce the endurance limit of the shaft material in those regions. Inspections of several broken rollers and the reshelling process indicates that corrosive juice can penetrate at least 30 to 60 mm under the shell-ends for rollers adopting the interference method of shell attachment. FEA results for shell / shaft interface pressure under loading highlighted this loss of contact. A gap approximately 50 mm deep (axial), 300 mm long (circumferential) and with an opening of 0.025 mm between the top of the shaft and shell-ends was predicted. This agrees with the previous observations on

possible gap size. The contact pressure before loading the roller model was 37 MPa at the shell-ends and 33 MPa at the shell centre. After the 70 tonne / ft roll load and 930 kNm torsional load were applied, the pressure at the top of shaft and shell-end reduced to 0 MPa (gap) and increased to 123 MPa at the bottom of shaft and shell end. Relatively small contact shear stress levels (typically 5 MPa) were induced between shaft and shell under full loading conditions. The coefficient of friction between shell / shaft was set at 0.1 for all analyses.

FEA of the standard mill roller design has allowed close inspection of the stress states and interactions between shell / shaft and bearing / shaft for a variety of typical operating conditions and loading scenarios.

Chapter 3 discusses several alternatives to the standard mill design in an attempt to reduce future whole-of-life costs associated with mill rollers. Comparisons will be made with the stress states predicted in Chapter 2 to gauge the viability of any alternative design modelled.

# *Chapter 3*

*Alternative designs*

### 3.0 Alternative designs

This chapter reviews several alternative mill roller designs. The objective was to firstly gather conceptual designs for mill rollers which have the potential to reduce associated whole-of-life costs. From these designs, several were chosen which intuitively have the greatest potential to improve on the current mill roller design. These designs were analysed using finite element techniques and the results were compared with a current roller design (Chapter 2).

Factors influencing mill roller design can be separated into three main categories, namely:

1. Geometry;
2. Materials and manufacturing techniques; and
3. Operating loads and environment.

Limits were imposed on the geometry aspect of conceptual mill roller designs as any improved roller would still need to operate in existing mill cheeks and brass bearings and be powered by steam turbines, gearbox, tailbar and coupling arrangements. This left the region between the inboard fillets including shell open for redesign. Roller designs to suit hydraulic drives and roller bearings were not considered as their application in Australian factories is still relatively uncommon.

As the majority of shaft steels have essentially the same elastic modulus (typically 207 GPa), mild steel was used in all FEA models. However, cast irons do have a range of elastic moduli and therefore it was necessary to model several types of cast iron shells (90 to 170 GPa).

Loads applied to all FEA models were similar to those used in Chapter 2 and so comparison of stress and deflection results are possible. The 3D FEA roller model (Figure 2.24) was modified to the geometry of alternative designs where possible to cancel out the effect of mesh density effects on stress results.

### **3.1 Physical and economic design considerations**

This section covers several design considerations used to improve the existing mill roller design.

#### **3.1.1 Mill roller economics**

Joyce and Garson (1996) reported on a 1994 survey into the whole-of-life costs associated with current roller shell materials. The survey involved 28 Australian raw sugar factories. The major outcome from this work was an economic basis for assessing the potential viability of any proposed alternative long-life shell material. The survey (Table 3.1) requested best estimates of the costs associated with a roller from the initial purchase, roller maintenance, re-shelling to the final scrapping of the shaft.

A net present value approach was then carried out on the data from Table 3.1. The net present value is calculated by discounting future sums of money at a given rate and summing them to get a total or whole-of-life cost. Inflation (3.5 %), taxation (33 % company rate) and the factory's required rate of return (8.0 %) were used to produce Table 3.2. Table 3.2 lists the roller purchase costs along with each of the maintenance procedures as net present values of the life of the shaft. Associated tax benefits are also shown.

Table 3.3 lists the net present values representing the maximum amount of money (including taxation considerations) that, on average, could be justified on purely financial grounds to purchase one of the following three options:

1. A shaft and shell that would require no maintenance over the the average life of current shafts (from Table 3.1);
2. A shell that would require no maintenance over the the average life of current shafts; and
3. A shell that would require no maintenance over the the average life of current shell materials.

Joyce and Garson (1996) concluded that the chance of finding a practical economic shell material requiring no maintenance for the entire shaft life is remote. However, finding a shell material that will last as long as current shell materials yet require no maintenance is more feasible. Please note all data shown in Tables 3.1 through 3.3 involve large standard deviations. This result is due to varying factory practices and other unaccounted for variables. Inflation rates and required rates of return were estimated for the economic conditions at the time of the survey.

**Table 3.1** Summary of the survey results (average and standard deviation) for a 2134 mm long roller (Joyce and Garson, 1996).

Action	Top roller				Side rollers (each)				Pressure feeder rollers (each)			
	Interval (years)		Cost (\$)		Interval (years)		Cost (\$)		Interval (years)		Cost (\$)	
	Avg	Std dev	Avg	Std dev	Avg	Std dev	Avg	Std dev	Avg	Std dev	Avg	Std dev
Initial outlay *	20	16	39351	-	30	12	41536	-	40	17	40682	-
Arcing **	1	-	5920	2356	1	-	2960	1178	1	-	1480	589
Check for cracks	1.2	0.6	253	320	1.9	1.2	253	320	3.7	3.5	253	320
Re-grooving	1.4	0.7	1020	157	2.2	1.1	1020	157	4.5	2.8	1020	157
Re-shelling	4.4	1.1	19215	3440	6.3	1.3	19215	3440	9.3	4.3	19215	3440
Re-installation at re-grooving interval ***	1.4	0.7	3251	1157	2.2	1.1	5446	2020	4.5	2.8	4582	1428
Re-installation at re-shelling interval ***	4.4	1.1	3251	1157	6.3	1.3	5446	2020	9.3	4.3	4582	1428

\* The initial outlay is a combination of the initial purchase cost of a completely new shaft and shell, the cost of additional fittings, cutting chevrons, applying the initial arcing, removing the old roller and installing the new one.

\*\* The tabulated arcing costs are the annual costs incurred for a roller in each milling unit.

\*\*\* The re-installation cost is incurred whenever the roller is removed from the milling unit for maintenance. Re-installation includes the cost of removing the worn roller, returning the maintained roller into service, additional fittings, chevrons and applying the initial arcing to the newly installed roller.

Table 3.2 Net present values of the survey maintenance costs for a 2134 mm long roller (Joyce and Garson, 1996).

Action	Top rollers (20 year life)			Side rollers (each) (30 year life)			Pressure feeder rollers (each) (40 year life)		
	Cost \$		Tax benefit	Cost \$		Tax benefit	Cost \$		Tax benefit
	Avg	Std dev		Avg	Std dev		Avg	Std dev	
Initial outlay	39351	1157	13283	41546	2020	14007	40682	1428	13722
Arcing	78018	31050	25746	49078	19530	16196	27828	11075	9183
Check for cracks	2767	3500	913	1721	2177	568	850	1075	280
Re-grooving	9520	1465	3142	7491	1153	2472	3950	608	1304
Re-shelling	53460	9570	17642	45042	8064	14864	32346	5790	10674
Re-installation	39386	14017	12997	52763	19570	17412	25457	7934	8400
Totals	222502	35608	73723	197641	28976	65519	131113	14973	43563

Table 3.3 Net present values (including taxation advantages) of 2134 mm rollers (Joyce and Garson, 1996).

	Top roller	Side roller (each)	Pressure feeder roller (each)
Net present value (shaft and shells for life of shaft)	\$148780 (20 year shaft life)	\$132120 (30 year shaft life)	\$87550 (40 year shaft life)
Net present value (shells for life of shaft)	\$135910 (20 year shaft life)	\$119950 (30 year shaft life)	\$75960 (40 year shaft life)
Net present value (single shell)	\$38590 (4.4 year shell life)	\$37630 (6.3 year shell life)	\$29210 (9.3 year shell life)

Due to widely varying factory practices with regards to roller use and maintenance, no attempt was made in this investigation to produce an economic model to evaluate the viability of mill roller alternatives analysed in Chapter 3.3.

### 3.1.2 Geometry restraints

Retro-fitting rollers with major geometrical design changes to existing mill sets would intuitively be too costly to be considered by the industry. This effectively places a limit on the geometry of feasible roller design alternatives. For this investigation, all conceptual roller designs were such that they could still be used in existing mill sets, supported by brass bearings and be powered by steam turbines, gearbox, tailbar and coupling arrangements. Nevertheless, the roller designs presented in Chapter 3.3 could still be modified to suit hydraulic drives and roller bearings.

All roller design changes analysed in Chapter 3.3 were restricted to the region between the inboard fillets. Inboard fillets, shell materials, roller geometries near the landing region and shell attachment methods were open to redesign. Dimensions including effective shell diameter (920 mm), shell length (2138 mm), journal diameter (457.2 mm) and bearing centre distance (3048 mm) were unchanged from Chapter 2 analyses.

### 3.1.3 Materials and manufacturing procedure

From a modelling perspective, low alloy steels currently used in mill roller shafts have virtually the same elastic modulus (typically 207 GPa) as the more expensive alloy steels. Therefore, the deflections and stress states predicted from the FE analyses for the roller shaft will intuitively be the same for any steel chosen assuming stress levels remain below the yield limit (eg. 250 MPa for K1035). The end result from the roller modelling will be known operating stress levels for the shaft corresponding to a certain loading condition. Therefore, the design engineer can select a steel type with suitable strength and fatigue properties to best cope with the predicted operating stress states. Selection of a shaft steel can then be an educated compromise between initial cost and expected service life and associated costs.

Manufacturing considerations for alternate roller designs is beyond the scope of this investigation and best left to foundry design staff who produce mill rollers. Machinability of the shaft and shell materials, heat treatment, tolerancing, surface finish and treatments, assembly procedures and associated costs are factors which complicate the final choice of roller materials and manufacturing methods. However, it is believed that all roller designs analysed in Chapter 3.3 would not increase manufacturing time to any great extent as compared to current roller designs. The benefits of a refined surface finish and surface treatments will be discussed in Chapter 4.

## 3.2 Conceptual designs

Conceptual roller designs were accrued from several sources, namely:

1. Mechanical and machine design texts covering shaft design and stress concentrations;
2. Fastening and joining handbooks covering assembly techniques including adhesives; and
3. Personal communications with researchers and mill staff involved with the sugar industry.

The current roller design consists of a simple shaft design supported by two journal bearings with a shell shrunk onto a raised landing between the two journal landings. The top roller shaft is driven via a box coupling attached to the shaft square. Some of this supplied torque is diverted to the feed and delivery rollers via a pinion keyed onto the shaft between the square section and the drive-end journal landing. As mentioned in Chapter 3.1.2, only the region between the inboard fillets including the fillets themselves, shell materials, roller geometries near the landing region and shell attachment methods were open to redesign.

A range of feasible roller design alternatives will be discussed in the following sections. From this range, several designs were selected for further consideration using FE analysis for comparison against the current roller design.

### 3.2.1 Shell design and attachment alternatives

At present, roller shells require replacement every 4.4 years on average. Replacement involves transporting the entire roller to the manufacturer, where upon the shell is removed, necessary repairs are made to the shaft and a new shell is manufactured and assembled back onto the shaft before returning it to the factory.

Current roller designs incorporate a cast iron shell which is shrunk onto the shaft. The intricacies of shrink fits were discussed in Chapter 1.6 and analysed in Chapter 2.1. Several conclusions can be made regarding shrink fits, namely:

1. The shrink fit design is relatively inexpensive and simple in terms of assembly method, however, the process can only be carried out at foundries;
2. Assuming concentric machining of the shaft landing and shell bore to suitable tolerances, the current interference factors used are conservative, producing higher stress levels in the shell and shaft than necessary;
3. On average, 40 percent of roller failures occur at the shell-end region (Reid, 1988) where a stress concentration develops due to the shell-end pinching the shaft landing;
4. Above a certain roll load a gap is developed between the shell-ends and shaft which aids juice ingress and the onset of stress corrosion, lowering the structural integrity of the roller; and
5. The current tapered shaft design used to reduce the shell-end effect is inadequate.

Keys which basically provide a lock between the shaft and shell for the purpose of transmitting torque were superseded by the shrink fit design some forty years ago in the Australian raw sugar industry. The keyways machined in the shaft acted as stress concentrations and allowed corrosive sugar juice to enter between the shaft and shell. Key usage is best suited when the torsional stiffness of the shaft and shell are similar so as the transmitted torque can be distributed evenly along the key and also where the environment is non-corrosive.

Connecting the shell onto the shaft via adhesive has yet to be proven as a viable alternative to the current shrink fit technique. Parmley (1989) describes the background to adhesive joints and bonding. Adhesive types, advantages and disadvantages, selection, joint design, surface preparation, application and testing of adhesives are discussed. Following, is a brief discussion of these topics.

Some of the possible advantages of using adhesives to connect a shell onto a shaft are:

1. Stress concentrations are minimised;
2. Most adhesives excel at joining dissimilar materials;
3. Ease of assembly; and
4. Cost reductions during roller manufacture.

Some of the possible disadvantages of using adhesives to connect a shell onto a shaft are:

1. Selecting an adhesive capable of surviving all operational conditions (environment and loads);
2. Surface preparation of surfaces to be bonded is often critical to adhesive's performance; and
3. Disassembly of roller at end of shell's useful life.

Choosing an adhesive suitable for attaching a shell onto a roller shaft is not a simple matter. Parmley suggests ways to avoid problems and minimise costs.

1. Adhesive manufacturers require an accurate description of the two materials to be joined and the conditions under which the component will operate;
2. Bond-strength values for adhesives are highly dependent on surface preparation, cure conditions and materials involved;
3. Strength retention of adhesives is affected by cyclic loads and operational conditions;
4. Thermal expansion of the adherends can produce severe stresses at the bond line;
5. Adhesive bonds can have either high tensile strength or high peel strength, but generally not both; and
6. Time spent properly preparing, assembling and curing bonds is worth the cost and effort.

Adhesive bonds undergo a variety of stresses, usually a combination of shear, tension, compression, cleavage or peel. Of these, cleavage and peel forces are much less desirable as the

load is concentrated at the end of bond and the adhesive fails gradually from that point. Peel forces may be substantial when considering the shell-end region of a roller as indicated during analysis of the existing roller design. Parmley (1989) also described the benefits of using an adhesive joint in conjunction with interference fits to improve the strength and fatigue characteristics of the joint. However, all testing in this field has been restricted to small scale shafts and fitted hubs. Extrapolating this theory to shafts of mill roller scale would not be advised at this stage.

Choosing a method to apply an adhesive is almost as critical as selection of the adhesive itself. Such methods include manual application and machine applications including roll coaters, curtain coaters and extrusion devices. Correct application can avoid breakdown, waste and worker dissatisfaction.

The objective of the modelling in Chapter 3.3, regarding the use of adhesives, is to provide an insight in the stress states experienced in the bonded joint between shaft and shell. This leads to a strength specification for a suitable adhesive. However, specifying environmental conditions to which the adhesive must handle is beyond the scope of this investigation.

Alternatives to the shrink fit method for attaching the shell to the roller shaft have been directed at reducing the stress levels at the shell-end region. This stress concentration at the shell-end can be attributed to the shell stiffness in this region. Therefore, reducing the shell stiffness in this region may indeed reduce the undesirable stress. This can be achieved by removing (recessing) material from the end faces of the shell or using a shell material with a lower elastic modulus. Chapter 3.3 analyses the effect of two different shell geometries involving recessed ends.

Shell connections such as oil-injection fits, taper fits and spline shafts are not considered in this investigation but should not be ruled out in future roller designs.

### **3.2.2 Shaft design alternatives**

Current roller shaft designs incorporate transitional fillets between the journal landings and the shell landing. Redesign of the region between the inboard fillets can be achieved without affecting the operation of tailbar connection and pinion. The general aim for the shaft redesign was to reduce the operating stress levels caused by inherent stress concentrations reported in Chapter 2 for the current roller design, specifically the inboard fillets and the shell-end region. Note that the inboard fillets on current roller shafts are not considered as locating devices.

A fundamental design technique such as maximising fillet size is definitely one method of reducing the stress levels in a roller shaft. Peterson (1974) lists theoretical stress concentration factors for

stepped shafts and numerous other geometries for a range of loading conditions including bending moments, axial and torsional forces.

Peterson (1974) suggests alternatives to certain design geometries. He discusses the option of using streamlined (compound) or relief-groove fillets in place of the standard constant radius fillets. With respect to the shell-end stress concentration due to shrink fit, Petersen suggests two alternate designs. The first being the recessed shell-ends as discussed in Chapter 3.2.1 and the second being an additional fillet shoulder at each end of the shell landing zone. This second option will be referred to as a raised landing design throughout this report.

Apart from geometric changes to the shaft design, manufacturing techniques can be used successfully to improve the structural integrity of existing roller designs. Correct heat treatment procedures can avoid detrimental residual stresses and poor grain structure as discussed in Chapter 1.2.2. Maintaining a good surface finish on the roller shaft by correct machining processes during manufacture or protection from wear and corrosion during use will improve shaft life. The benefits of introducing compressive residual stresses in the shaft's surface, in particular the fillet regions was briefly mentioned in Chapter 1.3.2. These compressive stresses can be achieved through shot peening, cold rolling or nitriding the critical areas. Residual stresses will not be included in the analysis of alternate roller designs.

To gauge the effect of shell attachment options, an analysis of a one piece roller comprising of shaft steel was undertaken for comparison.

### 3.3 FEA of alternative roller designs

This section reviews the analysis of several roller designs (mentioned in Chapter 3.2) and compares results against the current roller design.

#### 3.3.1 Alternative designs and associated results

In total, ten alternate roller designs were analysed. To avoid element mesh density effects during comparison, each model was a modified version of the model used in Chapter 2.2. Similar modelling techniques were applied to all alternate roller designs. Applied loads to all models were: roll load = 70 tonne/ft; tailbar torque = 931 kNm; pinion torque = 363 kNm; and shell traction = 448 kNm. Note that misalignment loads were not included. A brief explanation of design is given along with reference to pertinent figures which are contained at the end of this section. Tables 3.4 through 3.7 list the axial stress levels at various roller locations (Figure 2.49). Discussion of the results follow in Chapter 3.3.2. Figure 3.1 shows the element density for the current mill roller model as analysed in Chapter 2.2.

##### Stiff Shell

This design involved the use of a spheroidal graphite iron ( $E = 170$  GPa,  $\nu = 0.275$ ) in place of the current shell material (cast iron,  $E = 120$  GPa,  $\nu = 0.26$ ). The radial interference between the shell and shaft was set at 0.1352 mm to retain the same maximum torque capacity (2874 kNm from equation 1.6) as that of the current roller design. Figure 3.2 shows the element density for the 'stiff shell' model. Figures 3.3 through 3.8 show stress and interface pressure results. Table 3.4 reports axial stress levels.

##### Flexible Shell

This design involved the use of a lower grade iron ( $E = 90$  GPa,  $\nu = 0.24$ ) in place of the current shell material. The radial interference between the shell and shaft was set at 0.2270 mm to retain the same maximum torque capacity. Figure 3.9 shows the element density for the 'flexible shell' model. Figures 3.10 through 3.15 show stress and interface pressure results. Table 3.4 reports axial stress levels.

##### Large Fillet

This design involved the use of 150 mm inboard fillets in place of the 75 mm fillets currently used. According to Peterson (1974), the stress concentration factor at the fillets should reduce from 1.47 to 1.28 for bending moments due to roll loading. Figure 3.16 shows the element density for the 'large fillet' model. Figures 3.17 through 3.20 show stress results. Table 3.4 reports axial stress levels.

### Small Recess

This design involved the introduction of a small recess in the end face of the current shell design to a maximum depth of 35 mm. Figure 3.21 shows the element density for the 'small recess' model. Figures 3.22 through 3.27 show stress and interface pressure results. Table 3.5 reports axial stress levels.

### Large Recess

This design involved the introduction of a large recess in the end face of the current shell design to a maximum depth of 60 mm. Figure 3.28 shows the element density for the 'large recess' model. Figures 3.29 through 3.34 show stress and interface pressure results. Table 3.5 reports axial stress levels.

### Adhesive (0 mm thickness)

This design involved the removal of the radial interference between the shell and shaft. The shaft landing surface and the inner shell bore surface were then effectively 'tied' together for analysis, ie the two interacting surfaces could not separate during loading. This analysis allows the specification of the strength for a very thin adhesive line capable of surviving the static stress state in an operational roller. Figure 3.35 shows the element density for the 'adhesive' model. Figures 3.36 through 3.41 show stress and interface stress results. Table 3.6 reports axial stress levels.

### Epoxy (1.0 mm thickness)

This design involved an initial radial clearance of 1.0 mm between the shell and shaft. This 1.0 mm gap was then modelled as an epoxy ( $E = 2.8$  GPa,  $\nu = 0.4$ , Adams et al, 1984) glue-line. Figure 3.42 shows the element density for the 'epoxy' model. Figures 3.43 through 3.48 show stress and interface stress results. Table 3.6 reports axial stress levels.

### Double Shell

This design involved two separate concentric shells. The inner shell, made of spheroidal graphite iron ( $E = 170$  GPa,  $\nu = 0.275$ ) had an outer diameter of 800 mm. The radial interference between this inner shell and shaft was set at 0.1589 mm to retain the same maximum torque capacity. The outer shell (ie consumable component) had an outer diameter of 920 mm and was specified as the current shell material. A 1.0 mm gap between the outer and inner shells was modelled as an epoxy ( $E = 2.8$  GPa,  $\nu = 0.4$ , Adams et al, 1984) glue-line. Figure 3.49 shows the element density for the 'double shell' model. Figures 3.50 through 3.55 show stress and interface stress results. Table 3.6 reports axial stress levels.

### Raised Landing

This design involved the use of an increased shaft landing diameter of 580 mm underneath the shell. The original shaft landing diameter of 510 mm blended into the raised landing via compound fillets at either end. The radial interference between the shell and shaft was set at 0.1835 mm to retain the same maximum capacity. Figure 3.56 shows the element density for the 'raised landing' model. Figures 3.57 through 3.62 show stress and interface pressure results. Table 3.7 reports axial stress levels.

### Solid

This design involved the use of a one piece shaft / shell composite. The shaft was similar to the 'raised landing' design, however, the shell geometry was now incorporated into the shaft. Figure 3.63 shows the element density for the 'solid' model. Figures 3.64 through 3.67 show stress results. Table 3.7 reports axial stress levels.

Table 3.4 Axial stress results for the alternate roller designs (shell material and journal fillet).

Position on roller (Figure 2.49)	Axial stress for critical locations on mill roller for specific design alternatives. [MPa]			
	Original	Stiff Shell	Flexible Shell	Large Fillet
A	125	125	125	119
A'	-105	-105	-106	-100
B	100	99	101	99
B'	-126	-136	-127	-126
C	115	115	109	114
C'	-150	-157	-145	-150
D	22	24	45	22
D'	-62	-37	-59	-62
E	119	119	113	118
E'	-156	-163	-151	-155
F	104	103	105	103
F'	-132	-142	-132	-131
G	133	133	133	125
G'	-109	-109	-110	-104
H **	41	38	34	41
H' **	-26	-34	-29	-26
I	25	20	18	25
I'	-9	-16	-14	-9

\*\* results do not include the effect of the groove root stress concentration.

Table 3.5 Axial stress results for the alternate roller designs (shell-end recess).

Position on roller (Figure 2.49)	Axial stress for critical locations on mill roller for specific design alternatives. [MPa]		
	Original	Small Recess	Large Recess
A	125	125	124
A'	-105	-107	-108
B	100	101	101
B'	-126	-106	-94
C	115	115	117
C'	-150	-149	-143
D	22	35	36
D'	-62	-48	-49
E	119	119	121
E'	-156	-155	-149
F	104	104	104
F'	-132	-110	-98
G	133	133	132
G'	-109	-111	-112
H **	41	36	36
H' **	-26	-31	-31
I	25	19	19
I'	-9	-15	-15

\*\* results do not include the effect of the groove root stress concentration.

Table 3.6 Axial stress results for the alternate roller designs (adhesive based).

Position on roller (Figure 2.49)	Axial stress for critical locations on mill roller for specific design alternatives. [MPa]			
	Original	Adhesive	Epoxy (1 mm)	Double Shell
A	125	119	119	125
A'	-105	-114	-114	-105
B	100	155	124	102
B'	-126	-154	-122	-134
C	115	140	110	114
C'	-150	-141	-112	-154
D	22	32	30	27
D'	-62	-32	-31	-42
E	119	146	114	118
E'	-156	-147	-117	-161
F	104	161	129	106
F'	-132	-161	-127	-140
G	133	128	128	133
G'	-109	-117	-117	-109
H **	41	33	33	28
H' **	-26	-34	-34	-30
I	25	19	19	25
I'	-9	-21	-21	-17

\*\* results do not include the effect of the groove root stress concentration.

Table 3.7 Axial stress results for the alternate roller designs (geometry based).

Position on roller (Figure 2.49)	Axial stress for critical locations on mill roller for specific design alternatives. [MPa]		
	Original	Raised Landing	Solid (One-piece)
A	125	126	122
A'	-105	-110	-116
B	100	112	117
B'	-126	-107	-116
C	115	63	
C'	-150	-72	
D	22	43	
D'	-62	-52	
E	119	66	
E'	-156	-75	
F	104	117	122
F'	-132	-111	-121
G	133	134	131
G'	-109	-114	-120
H **	41	32	35
H' **	-26	-28	-37
I	25	19	
I'	-9	-15	

\*\* results do not include the effect of the groove root stress concentration.

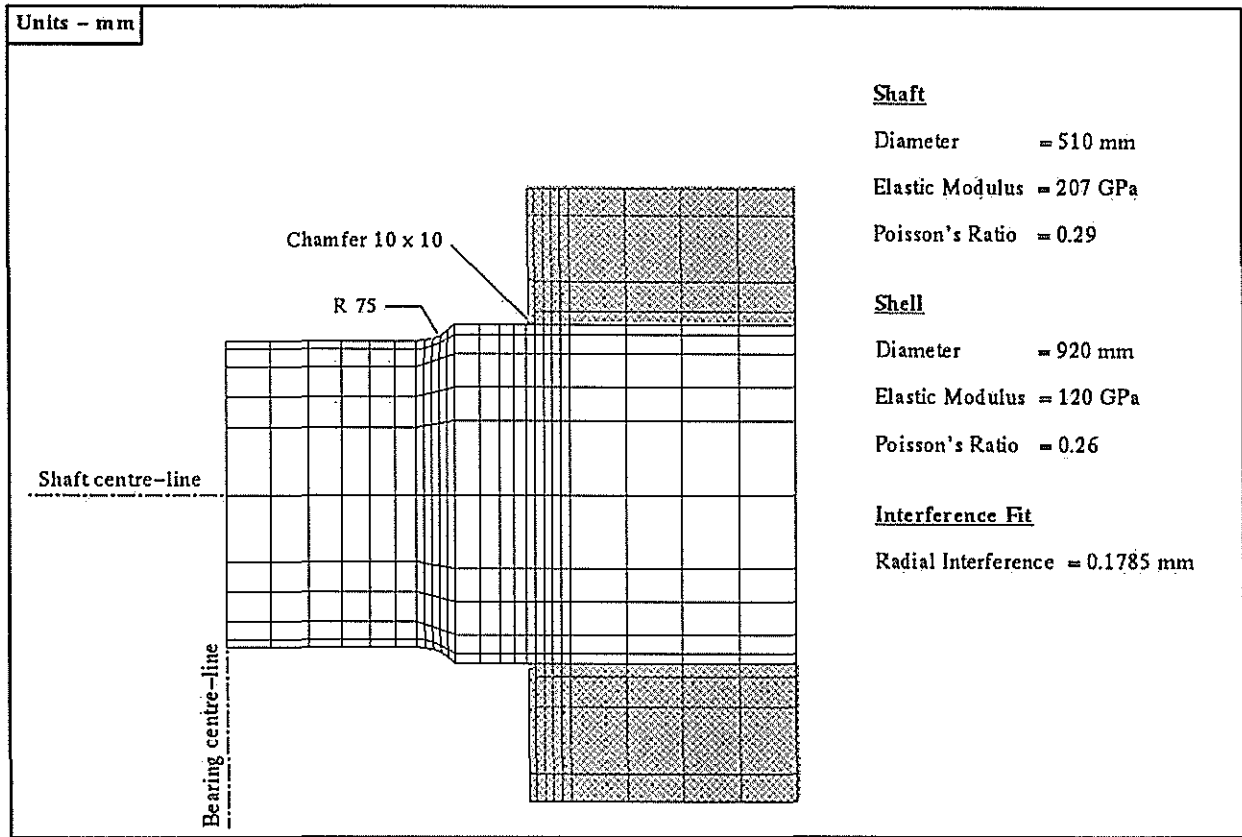


Figure 3.1 Sectioned view of shell-end region for current roller design model.

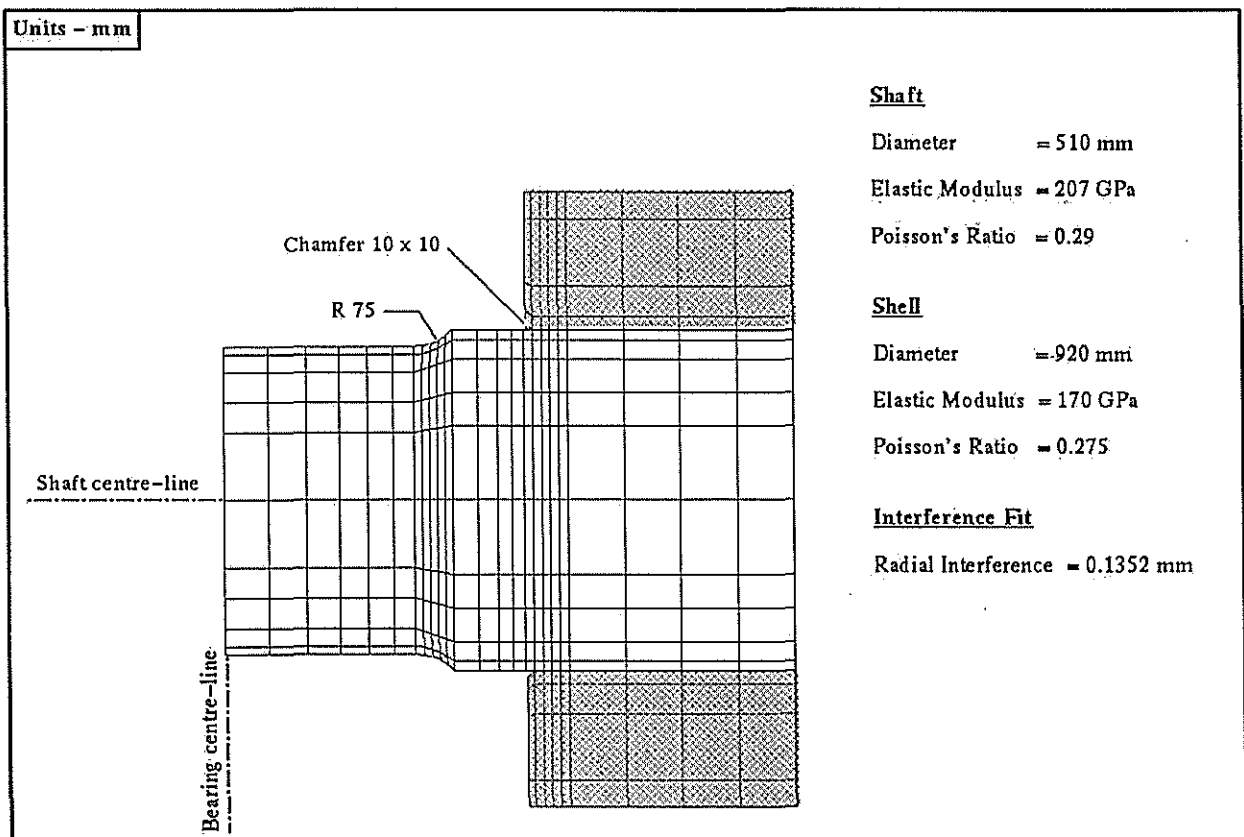


Figure 3.2 Sectioned view of shell-end region for stiff shell model.

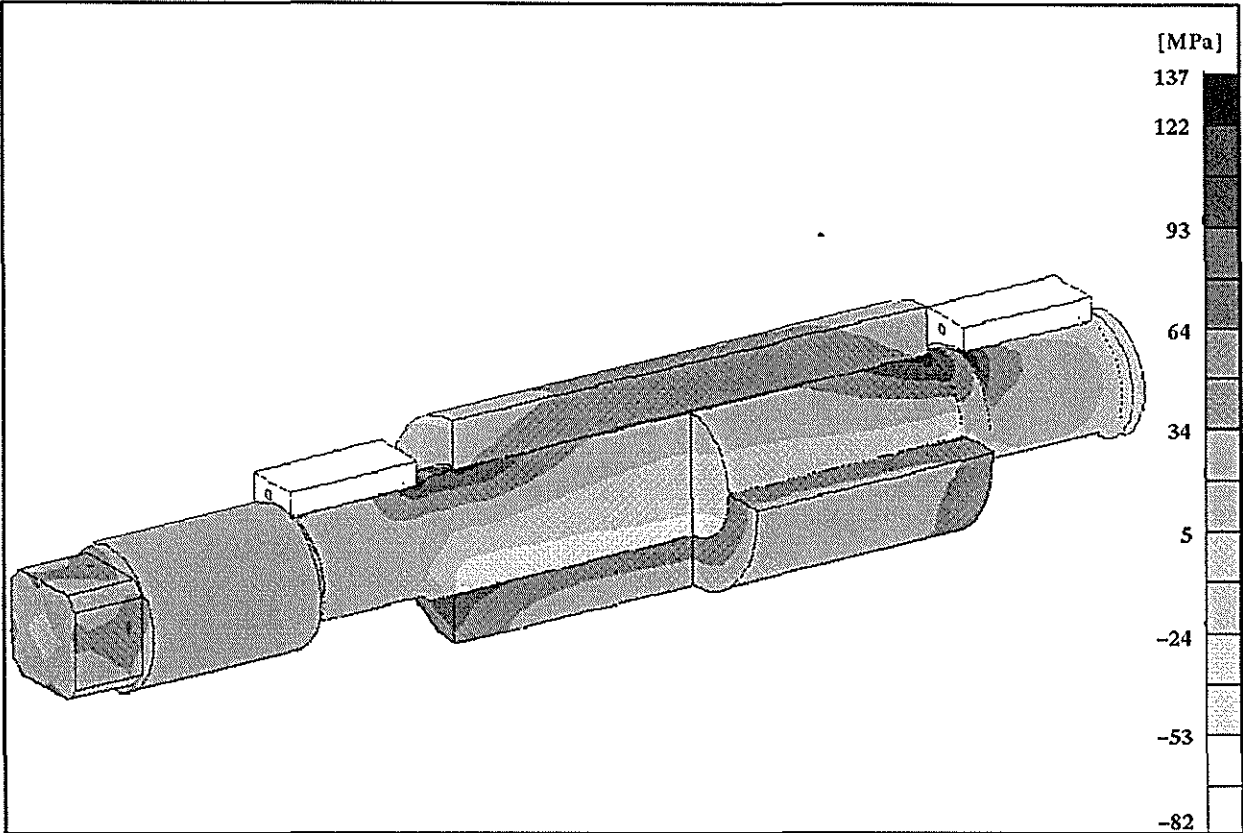


Figure 3.3 Major principal stress plot (Stiff shell : combined loads).

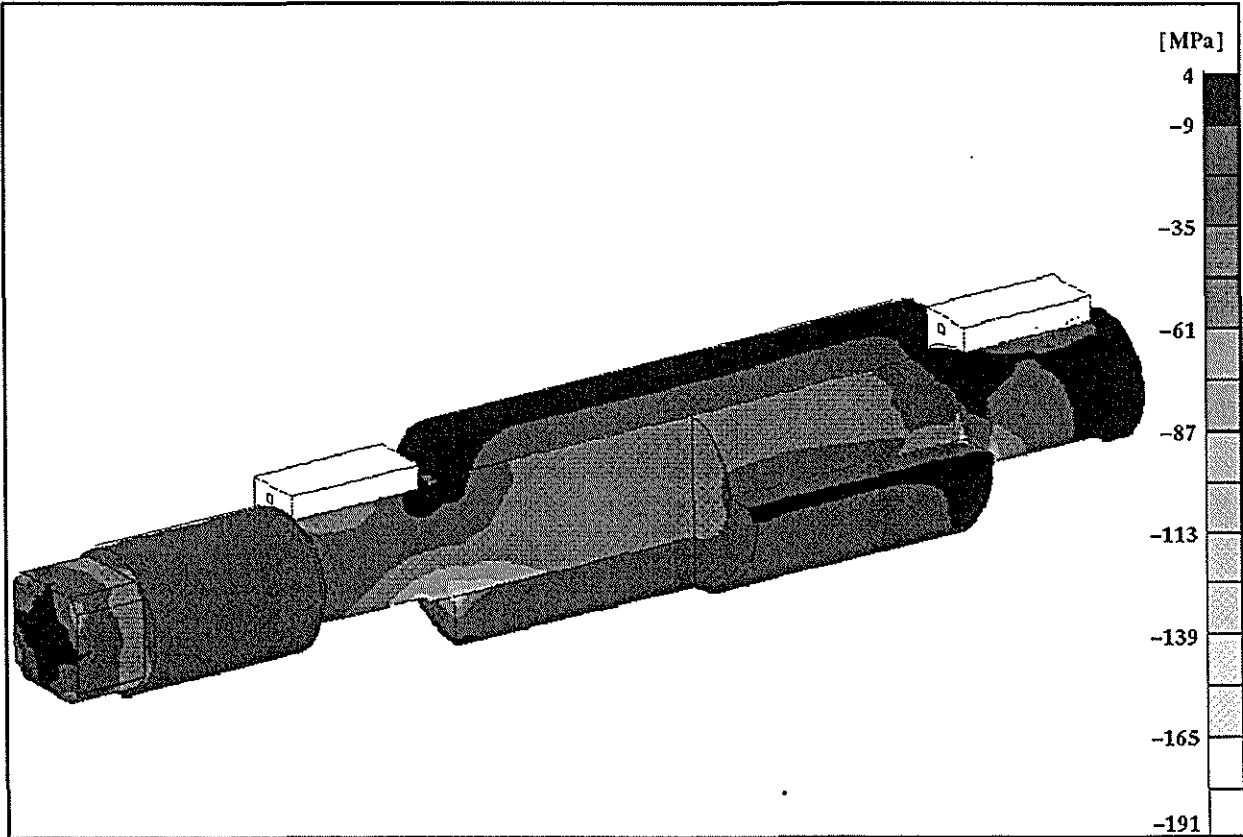


Figure 3.4 Minor principal stress plot (Stiff shell : combined loads).

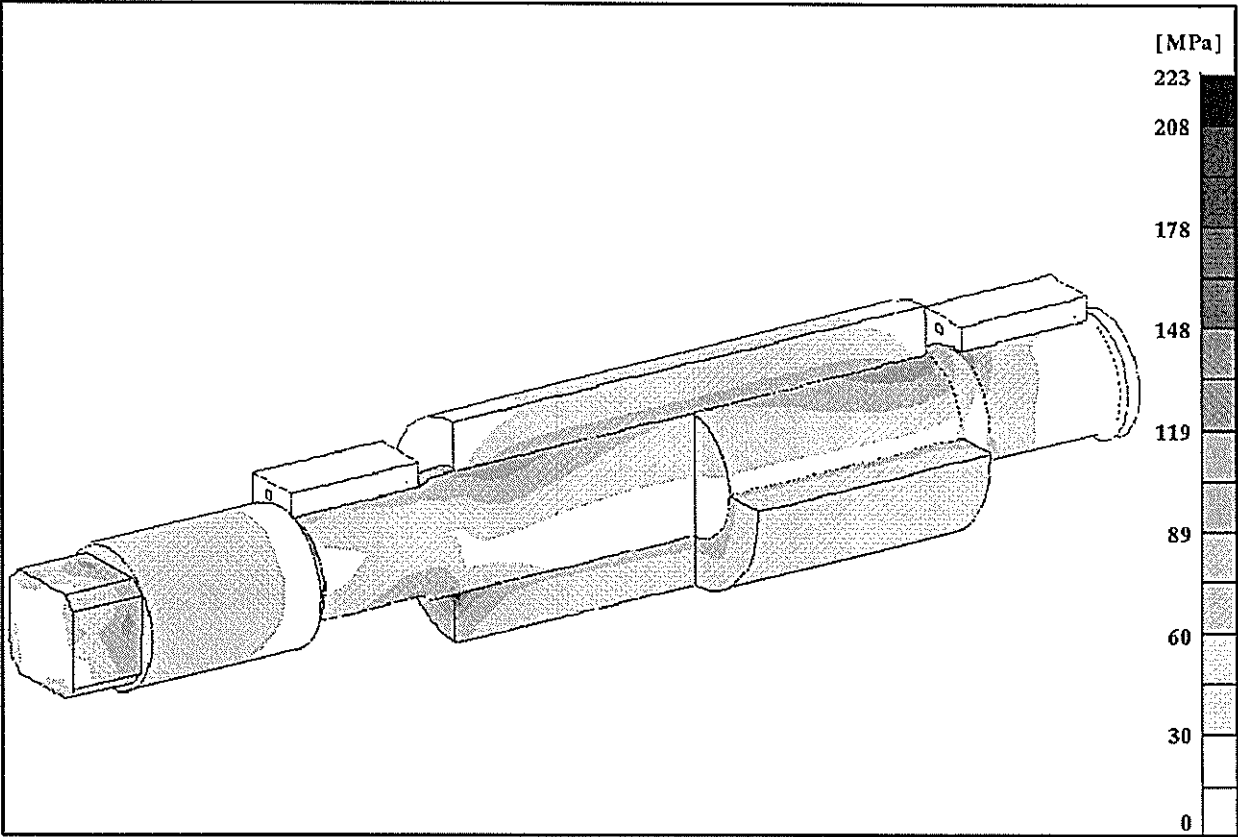


Figure 3.5 Von Mises stress plot (Stiff shell : combined loads).

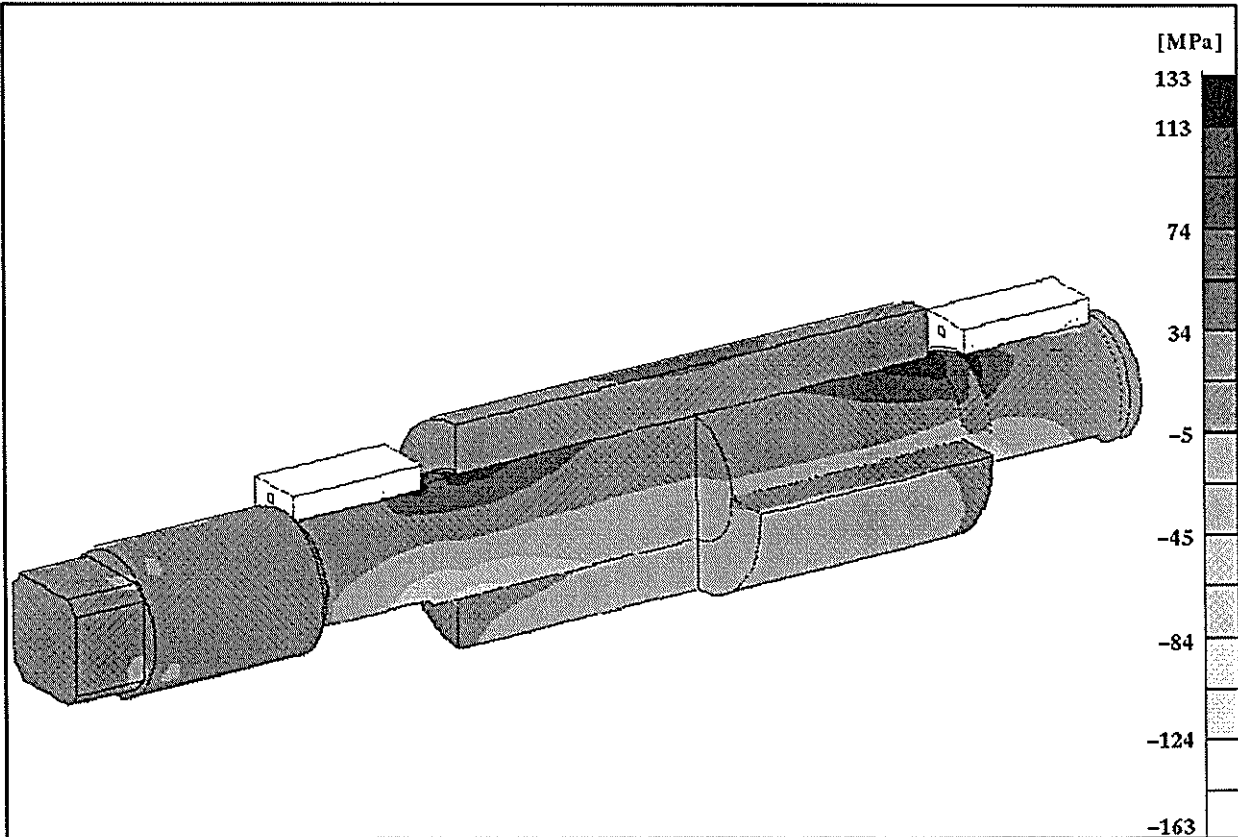


Figure 3.6 Axial stress plot (Stiff shell : combined loads).

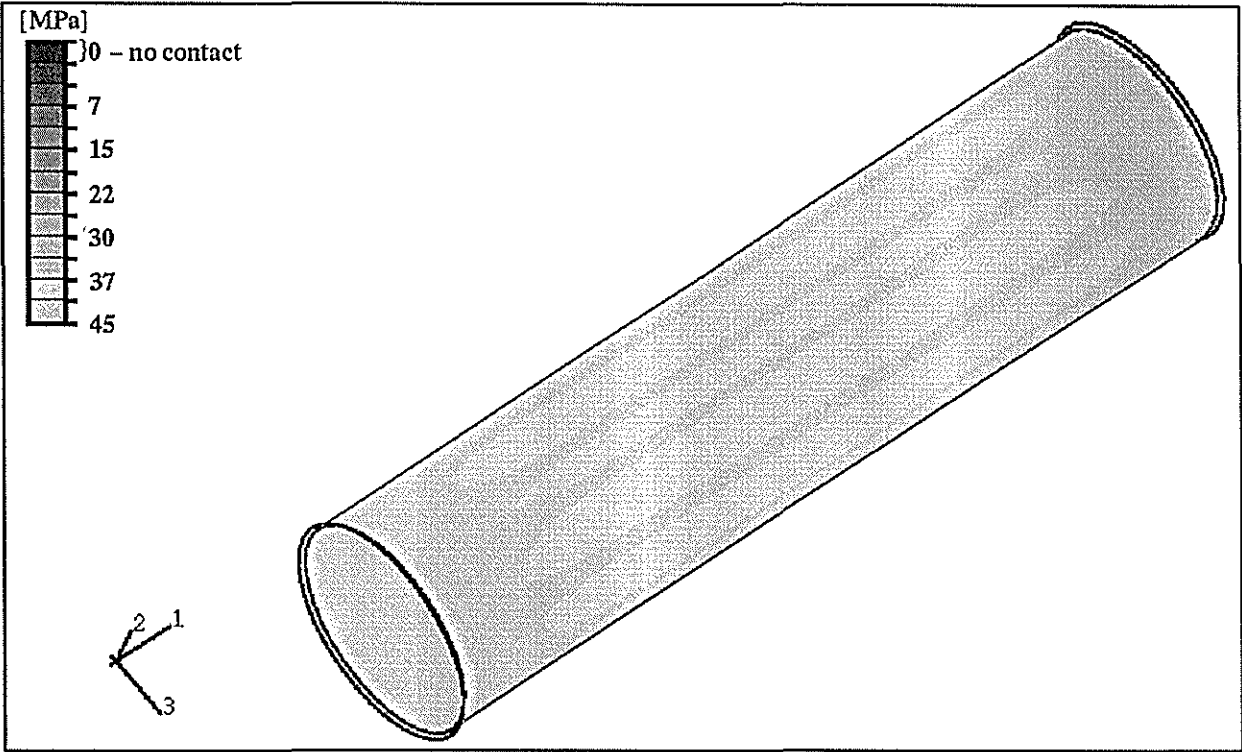


Figure 3.7 Contact pressure on inner shell surface (Stiff shell : interference load only).

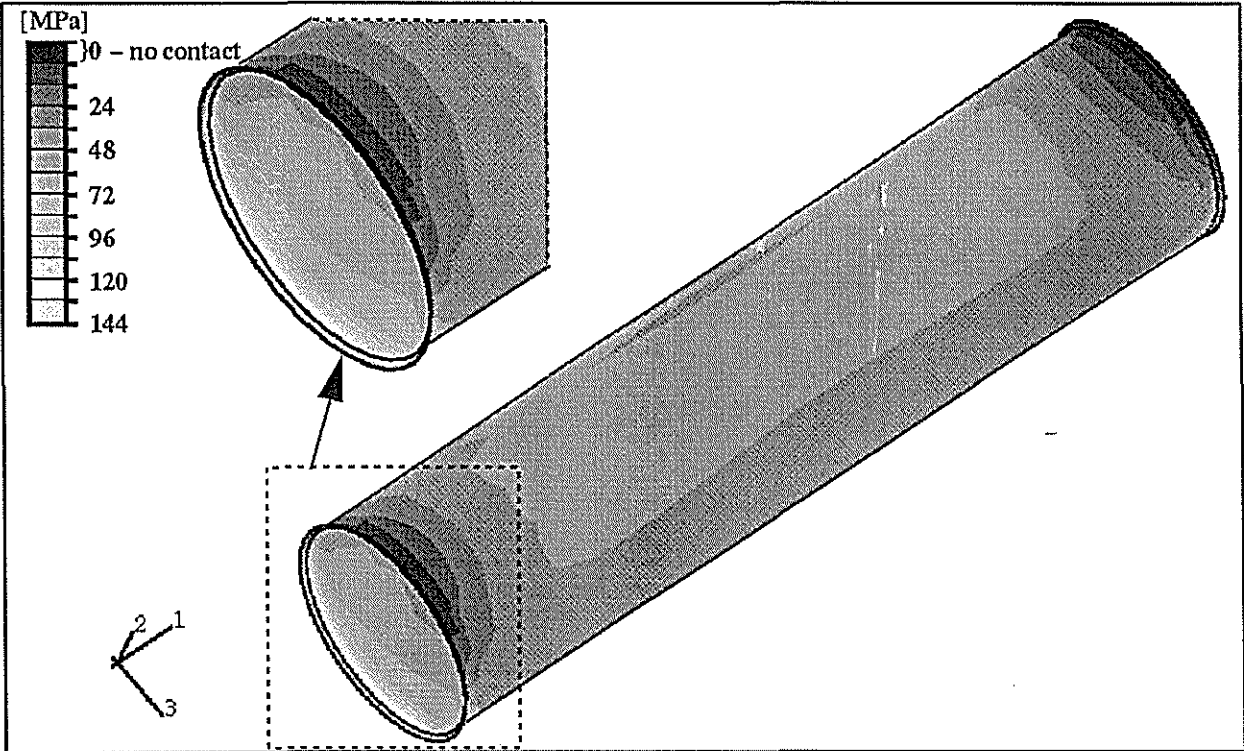


Figure 3.8 Contact pressure on inner shell surface (Stiff shell : combined loads).

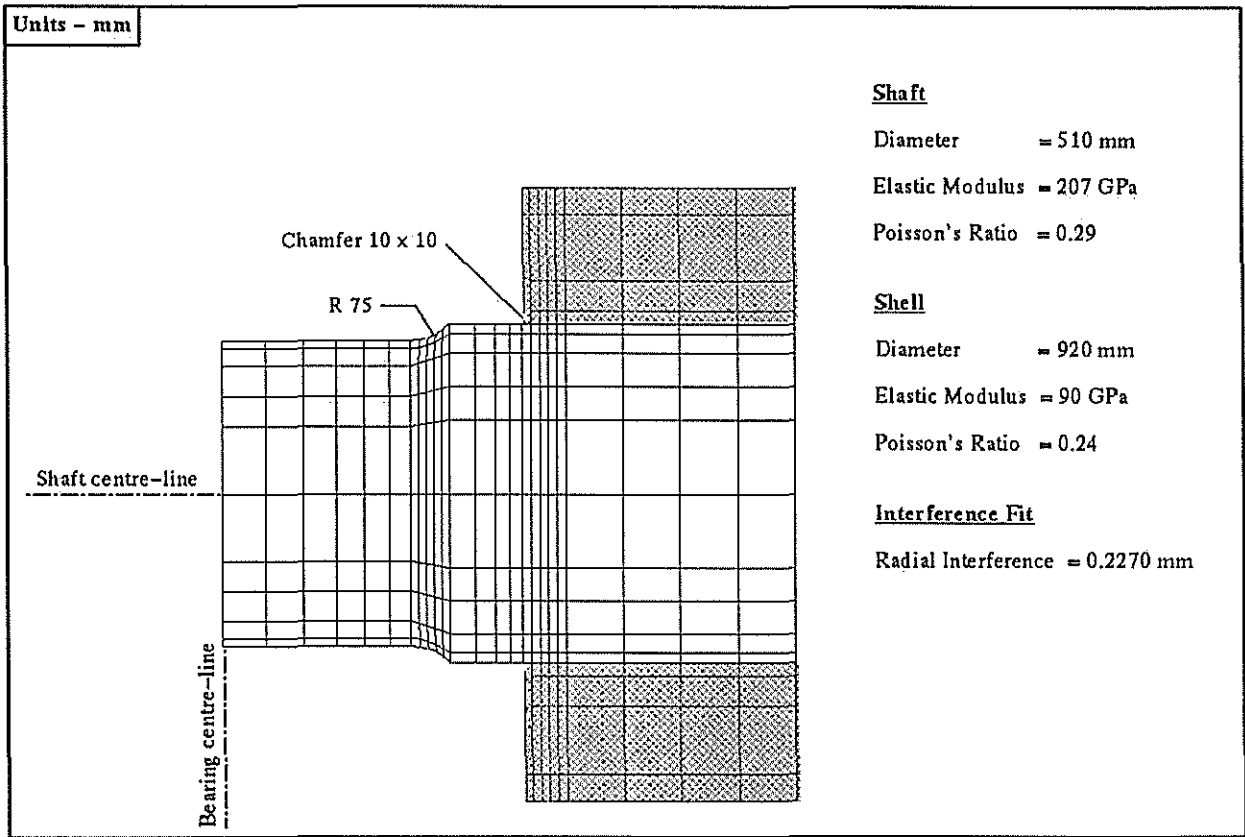


Figure 3.9 Sectioned view of shell-end region for flexible shell model.

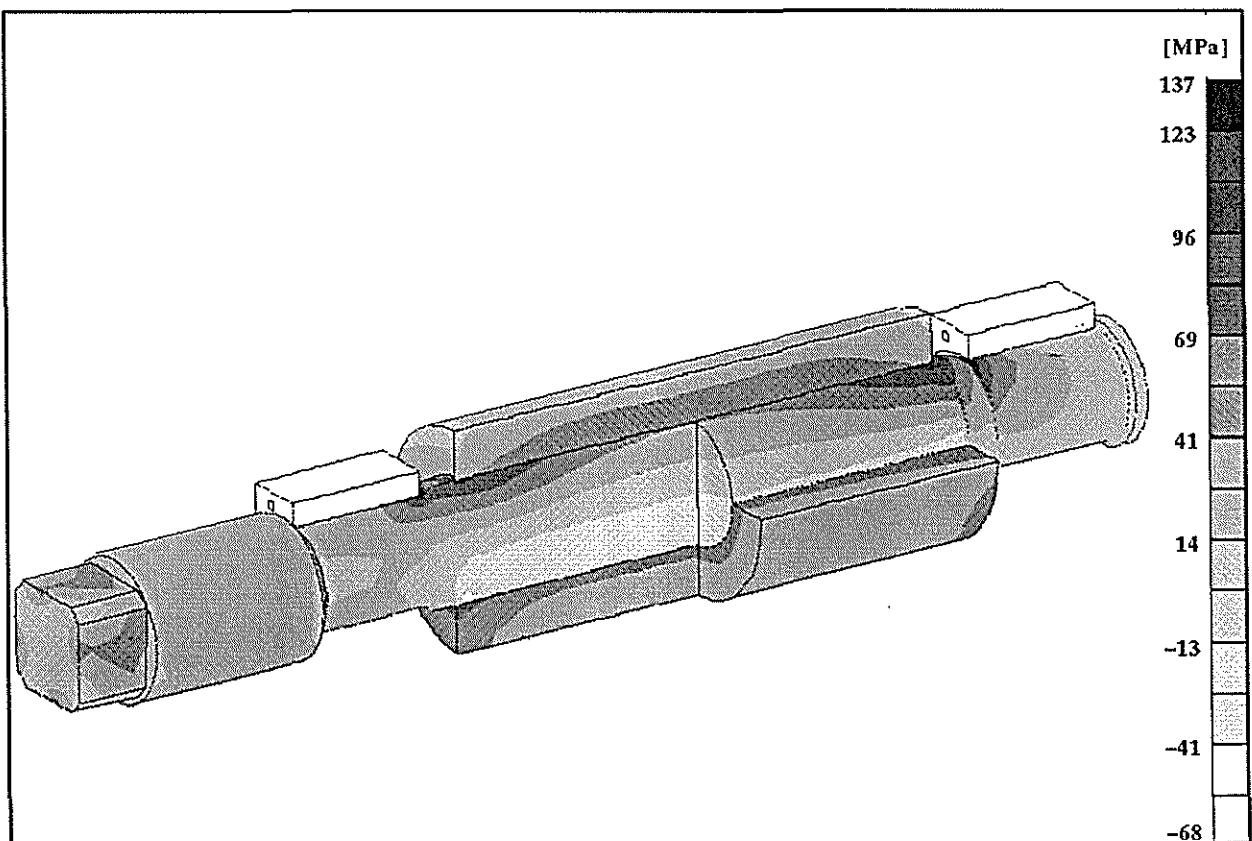


Figure 3.10 Major principal stress plot (Flexible shell : combined loads).

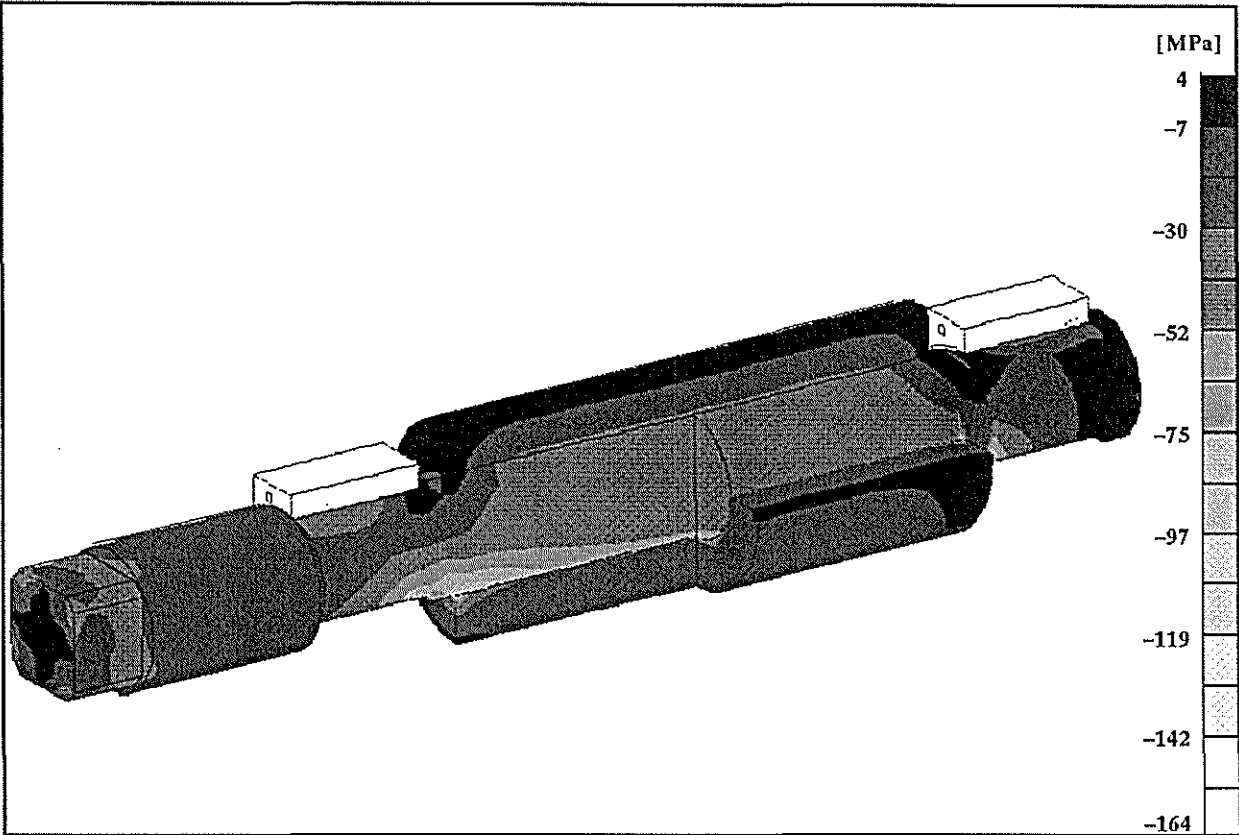


Figure 3.11 Minor principal stress plot (Flexible shell : combined loads).

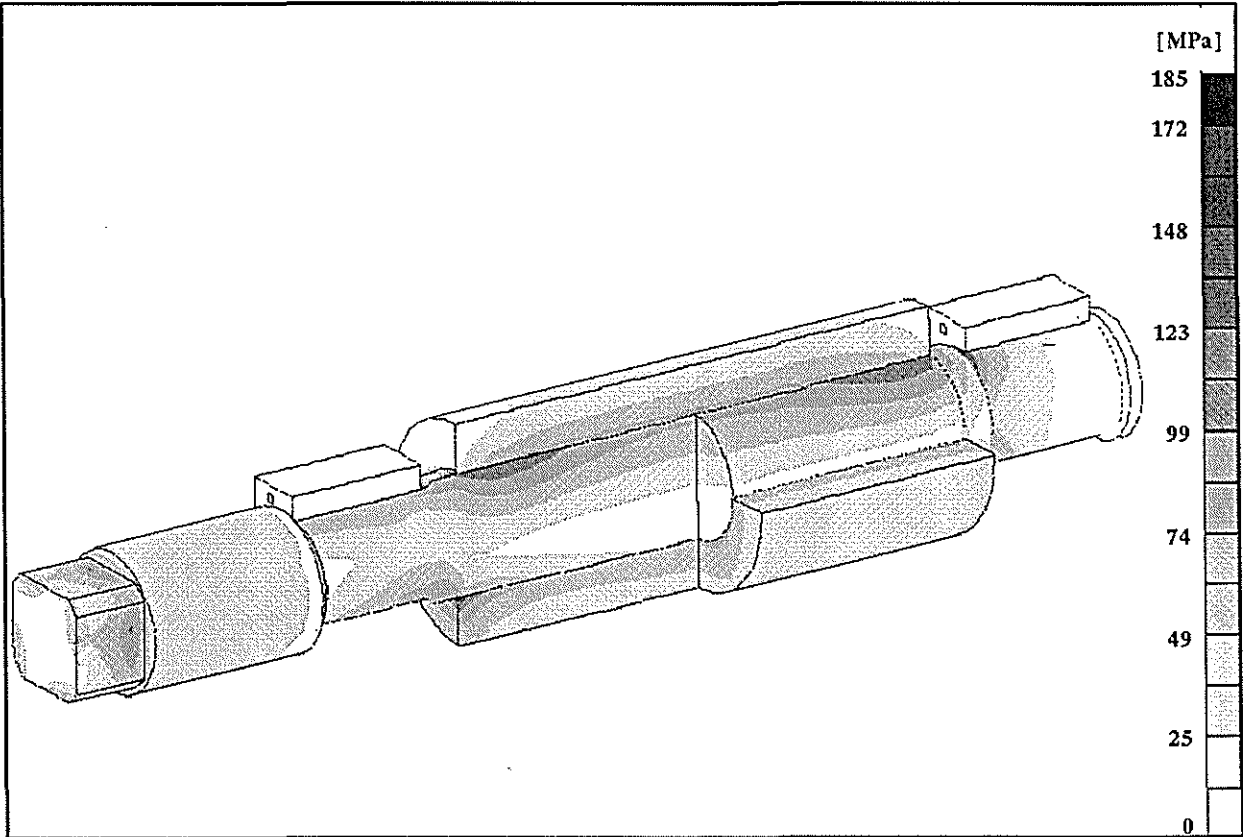


Figure 3.12 Von Mises stress plot (Flexible shell : combined loads).

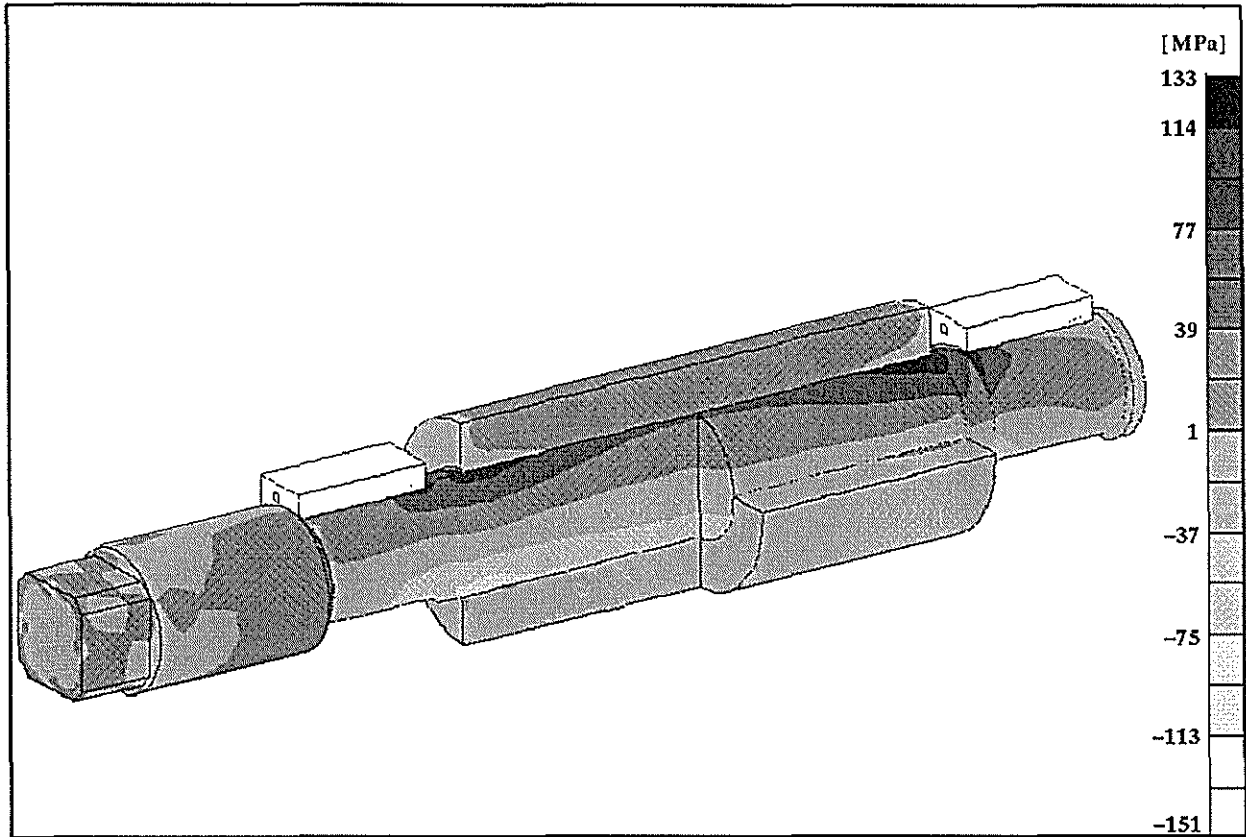


Figure 3.13 Axial stress plot (Flexible shell : combined loads).

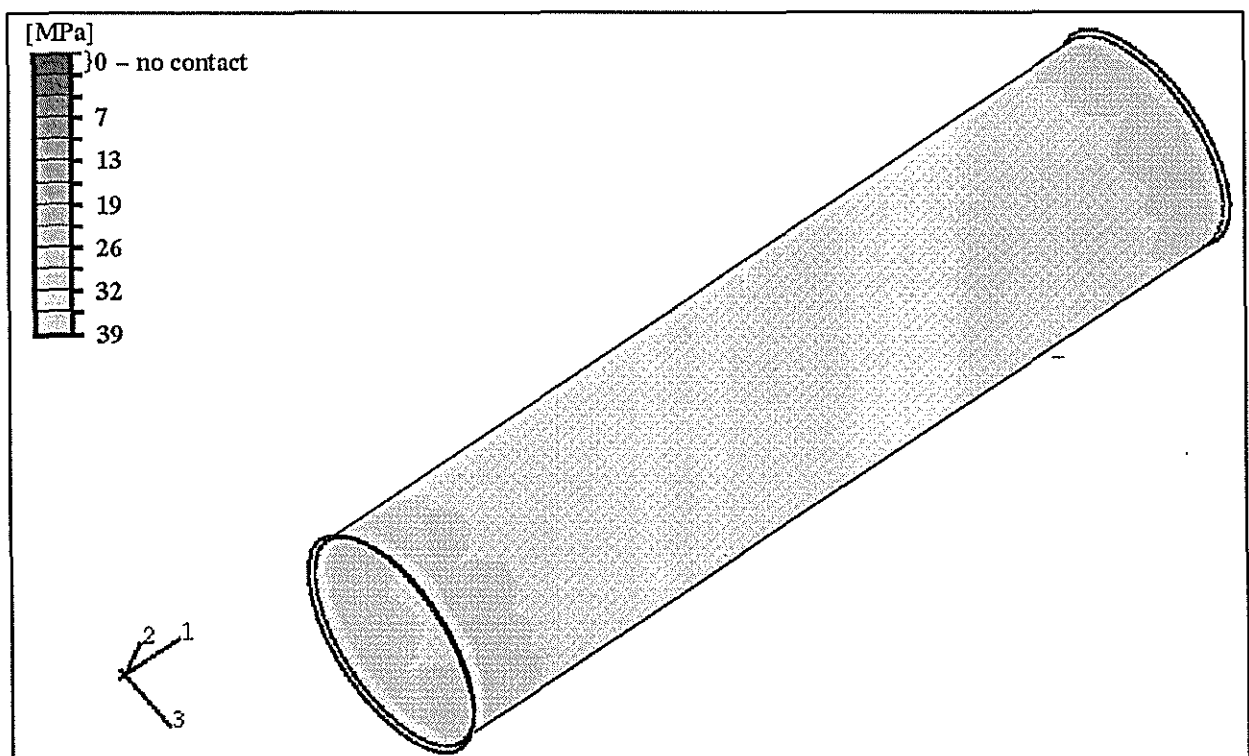


Figure 3.14 Contact pressure on inner shell surface (Flexible shell : interference load only).

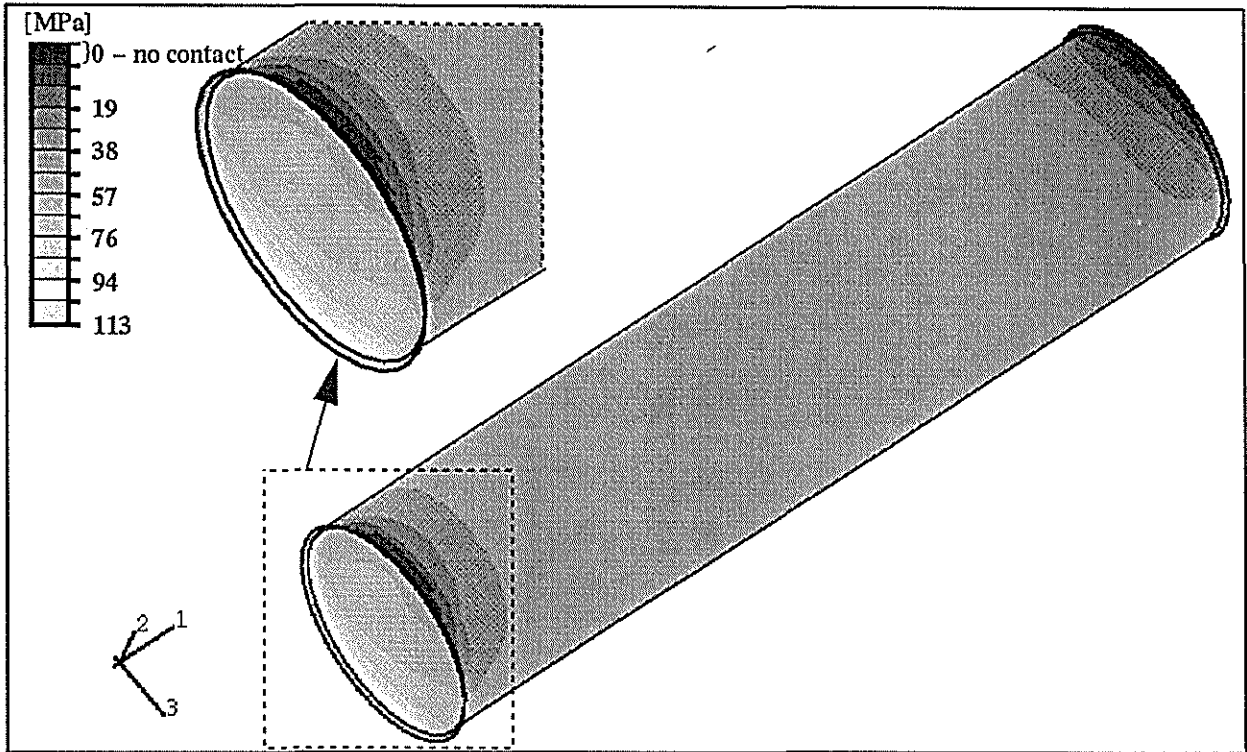


Figure 3.15 Contact pressure on inner shell surface (Flexible shell : combined loads).

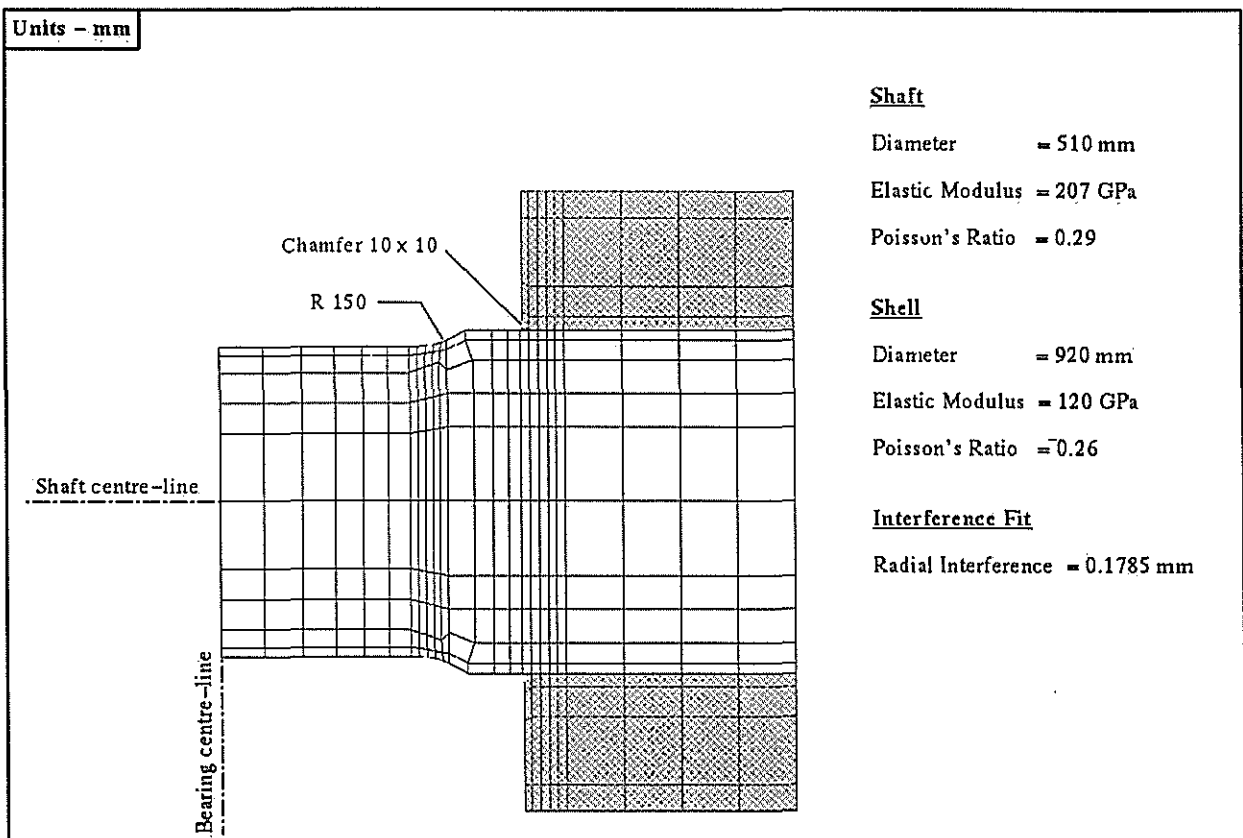


Figure 3.16 Sectioned view of shell-end region for large fillet model.

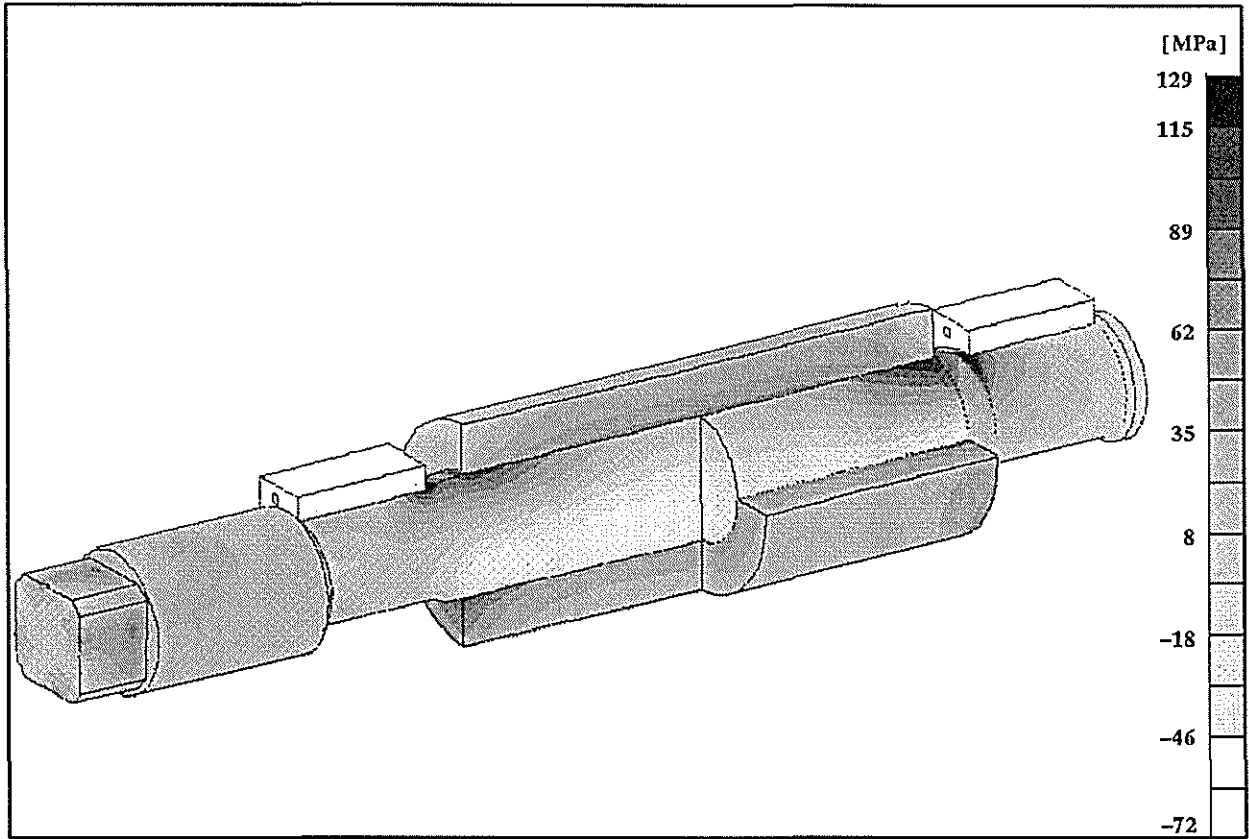


Figure 3.17 Major principal stress plot (Large fillet : combined loads).

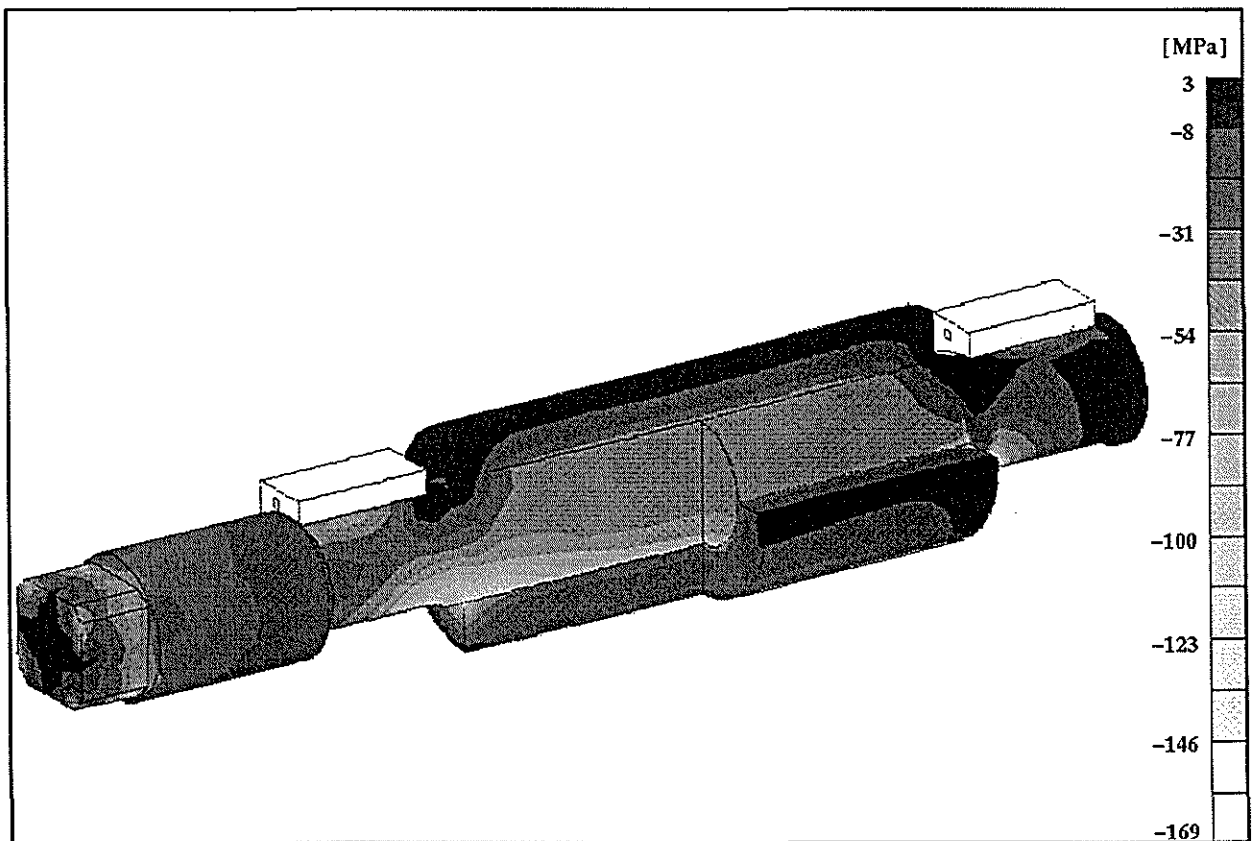


Figure 3.18 Minor principal stress plot (Large fillet : combined loads).

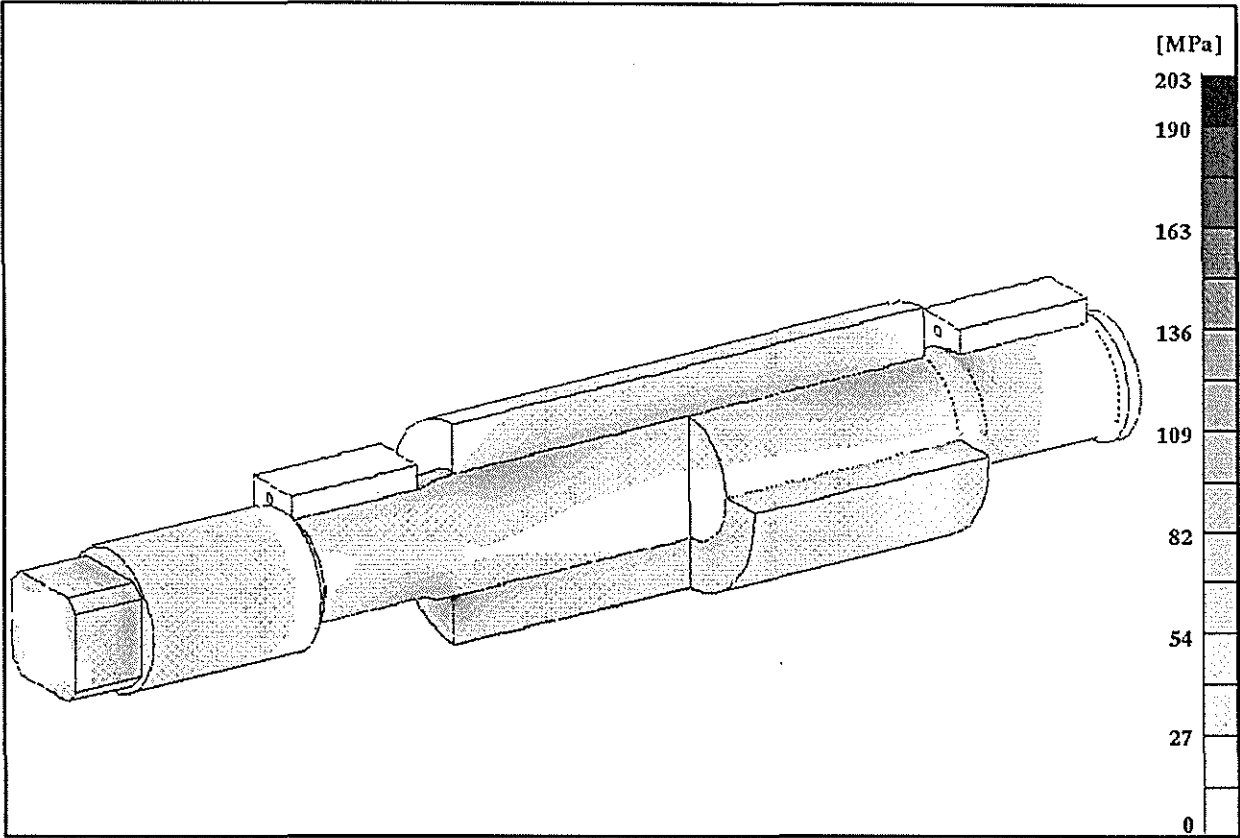


Figure 3.19 Von Mises stress plot (Large fillet : combined loads).

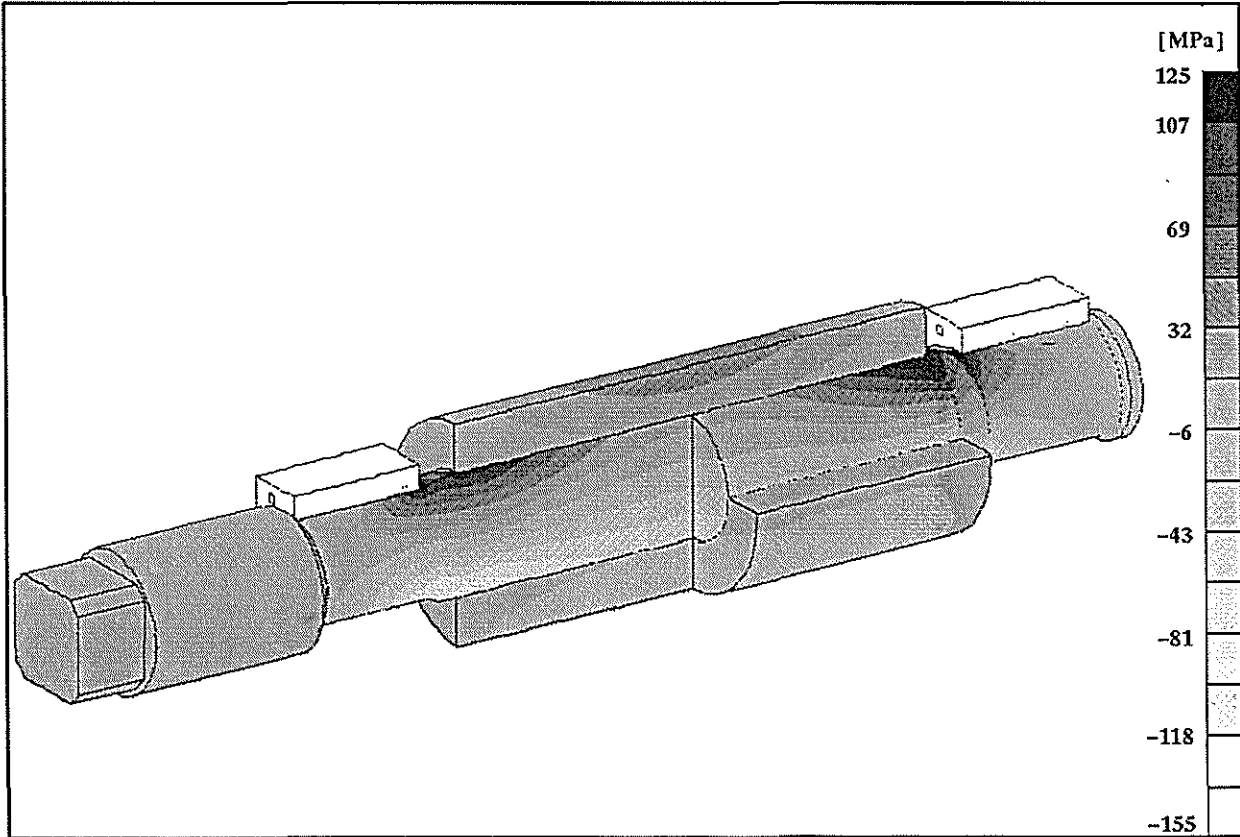


Figure 3.20 Axial stress plot (Large fillet : combined loads).

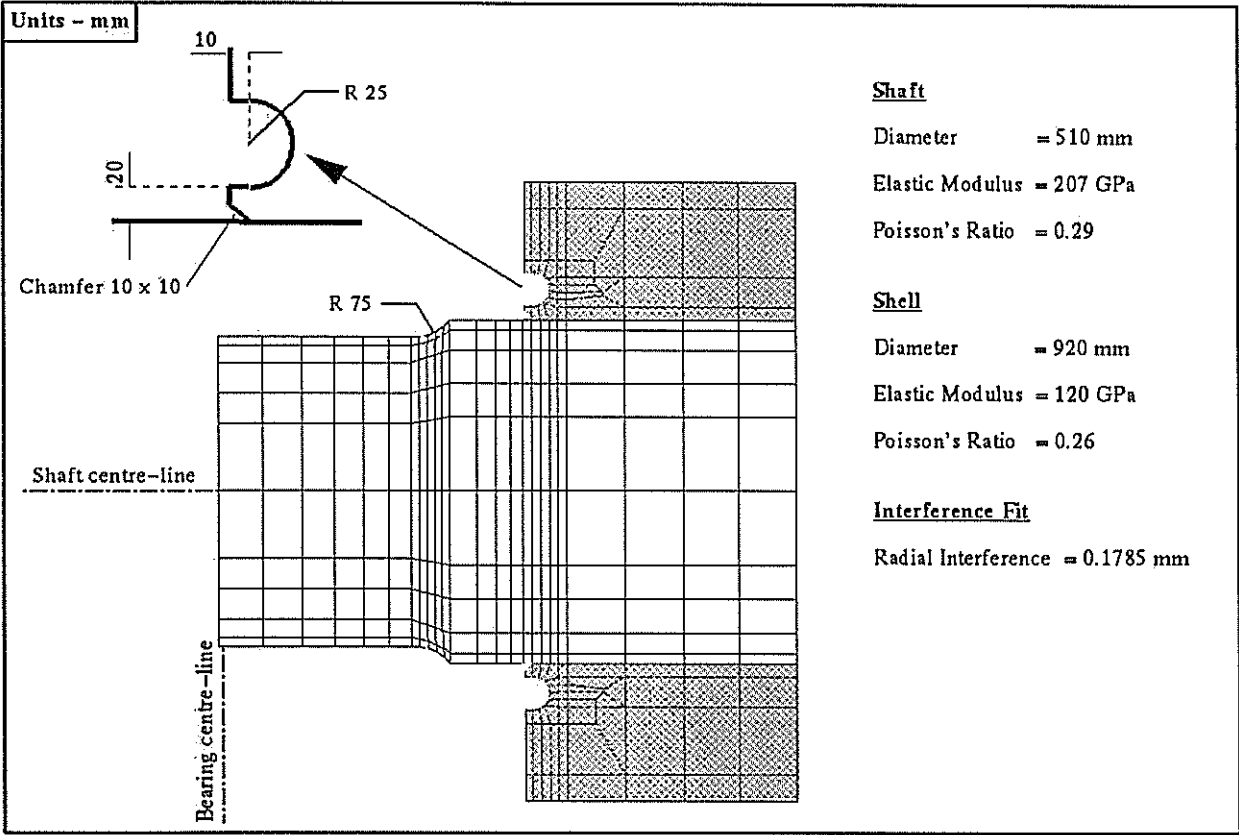


Figure 3.21 Sectioned view of shell-end region for small recess model.

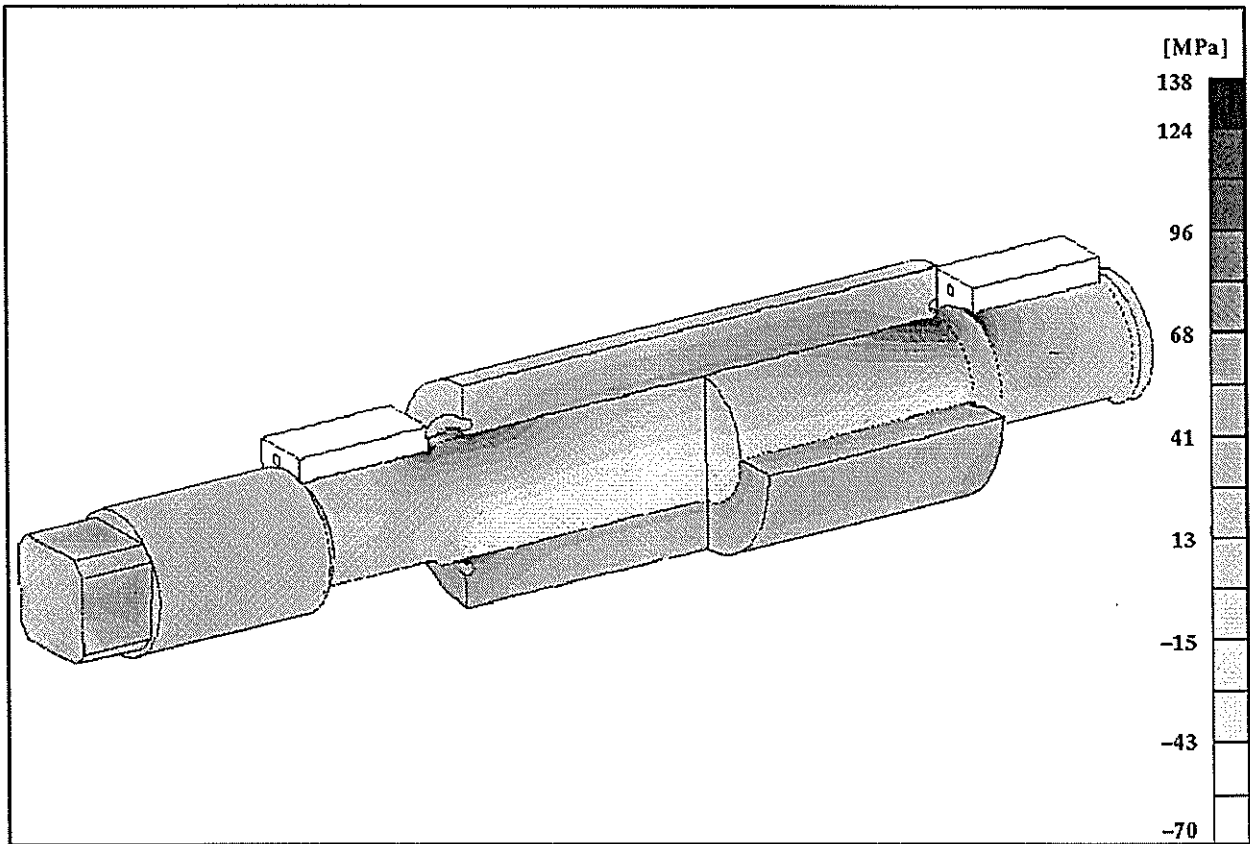


Figure 3.22 Major principal stress plot (Small recess : combined loads).

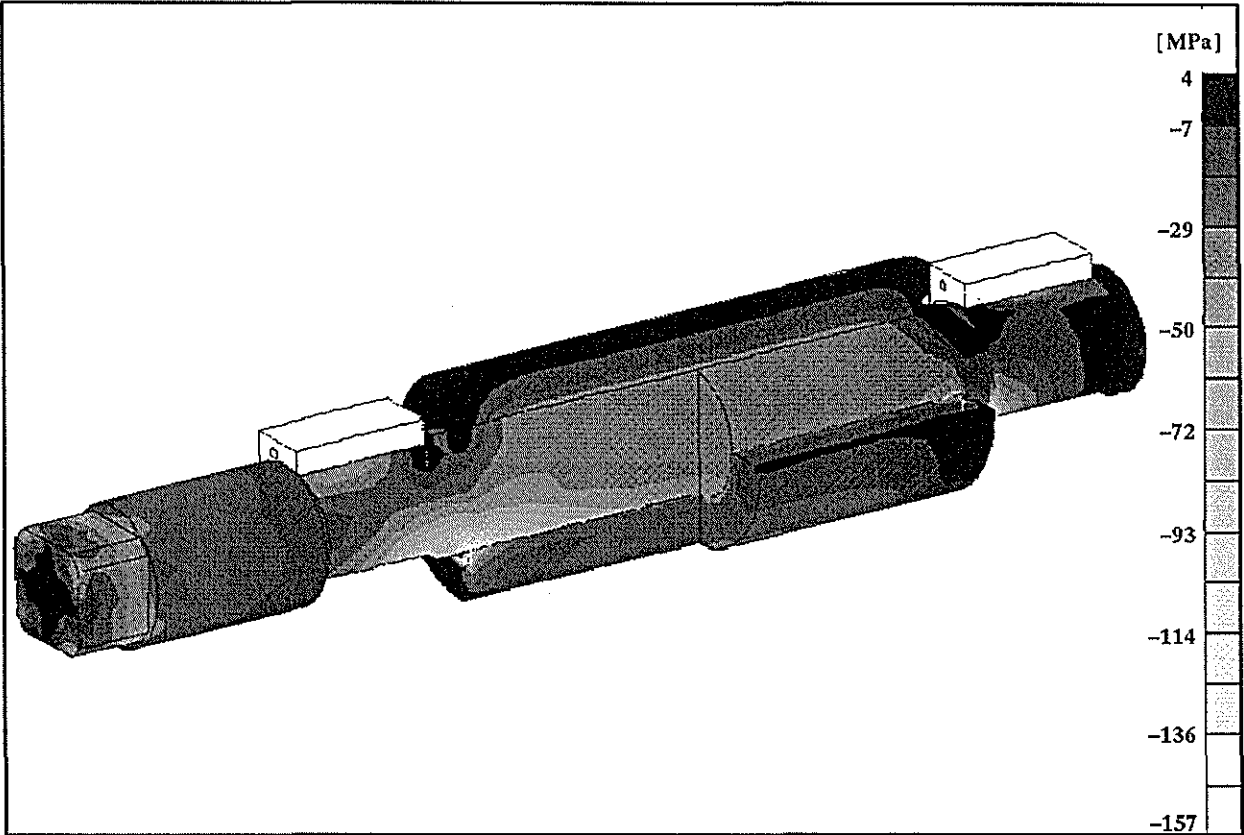


Figure 3.23 Minor principal stress plot (Small recess : combined loads).

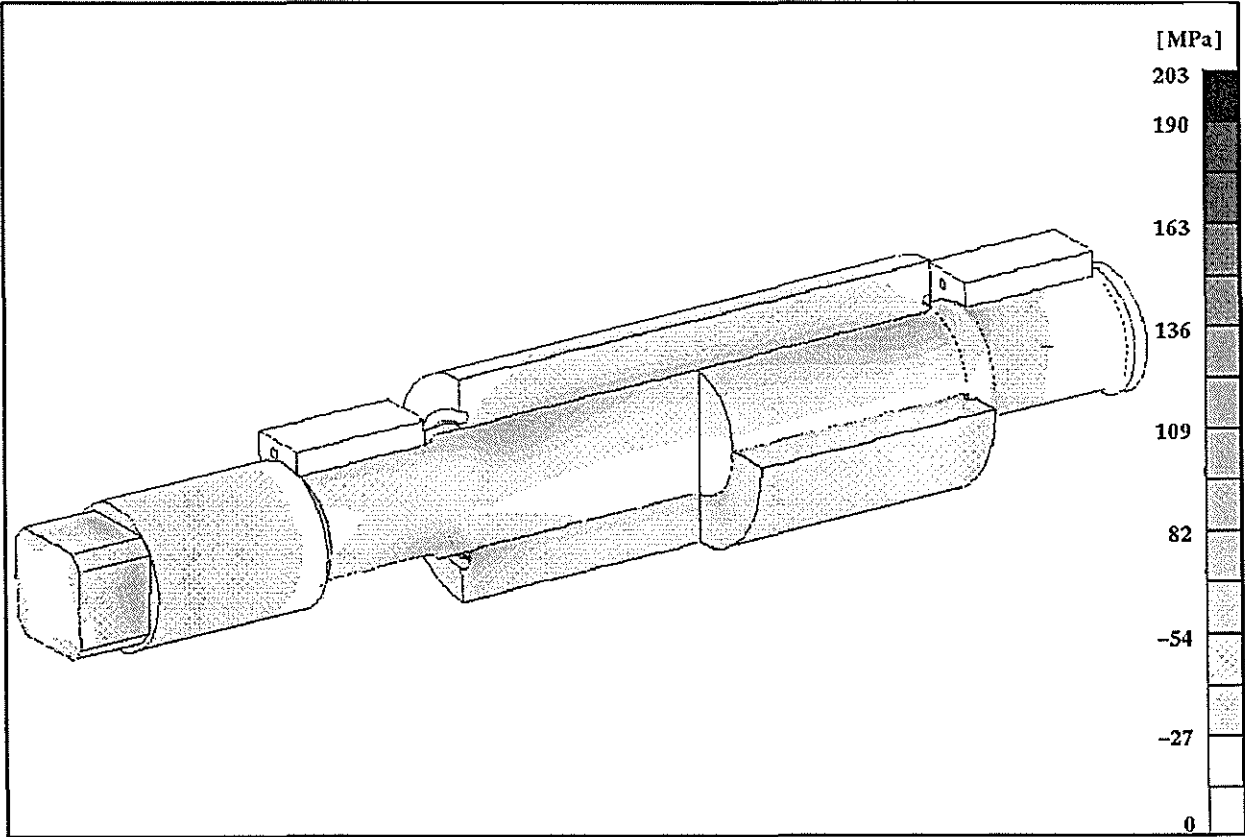


Figure 3.24 Von Mises stress plot (Small recess : combined loads).

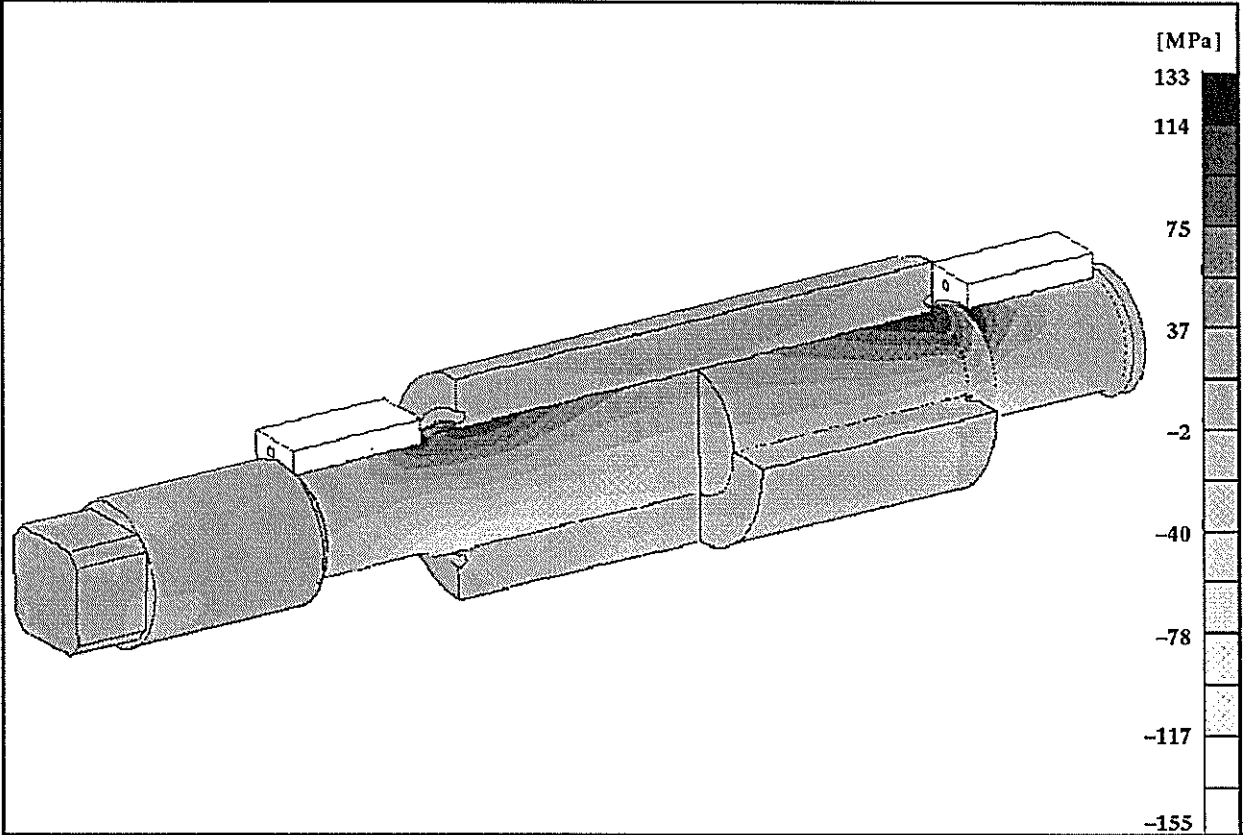


Figure 3.25 Axial stress plot (Small recess : combined loads).

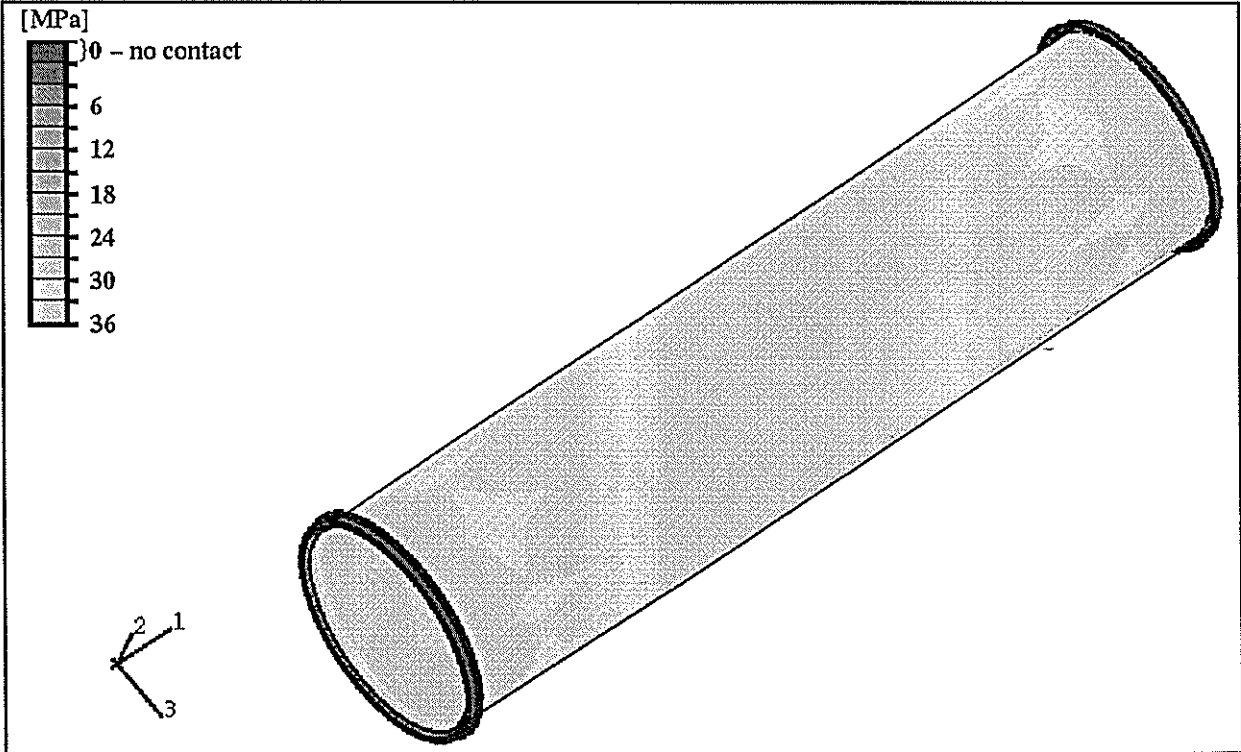


Figure 3.26 Contact pressure on inner shell surface (Small recess : interference load only).

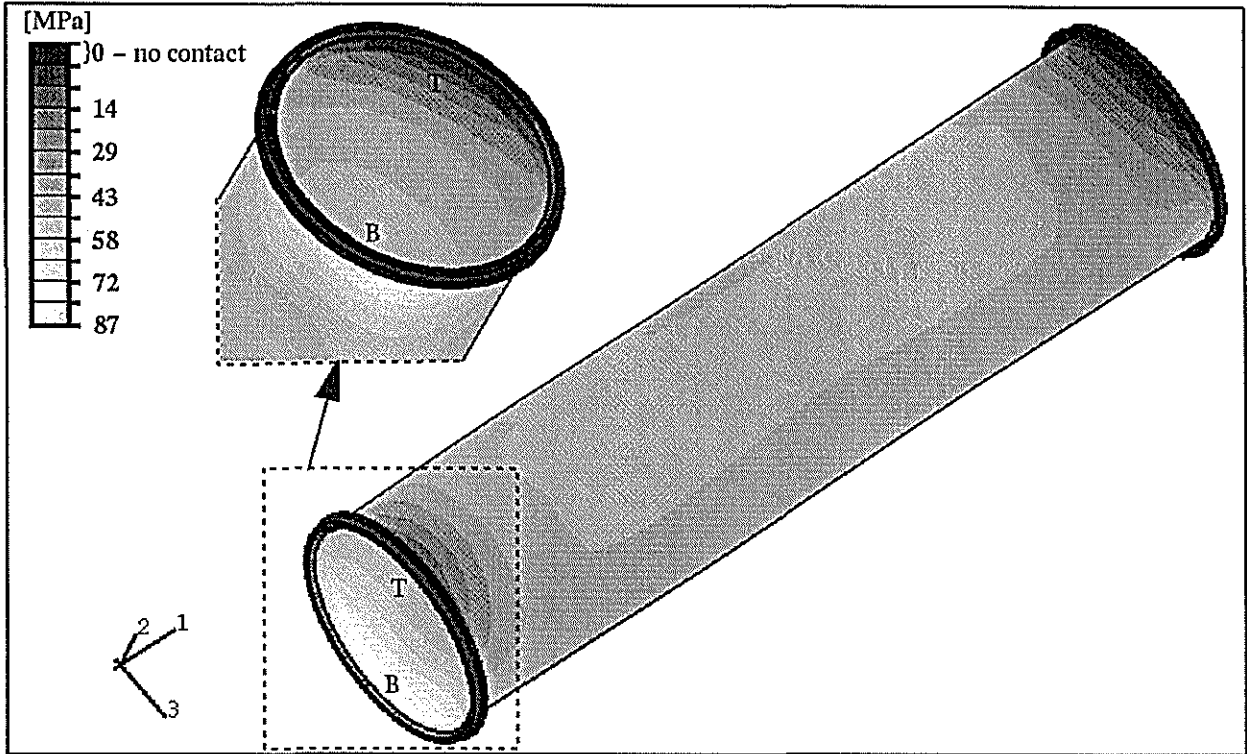


Figure 3.27 Contact pressure on inner shell surface (Small recess : combined loads).

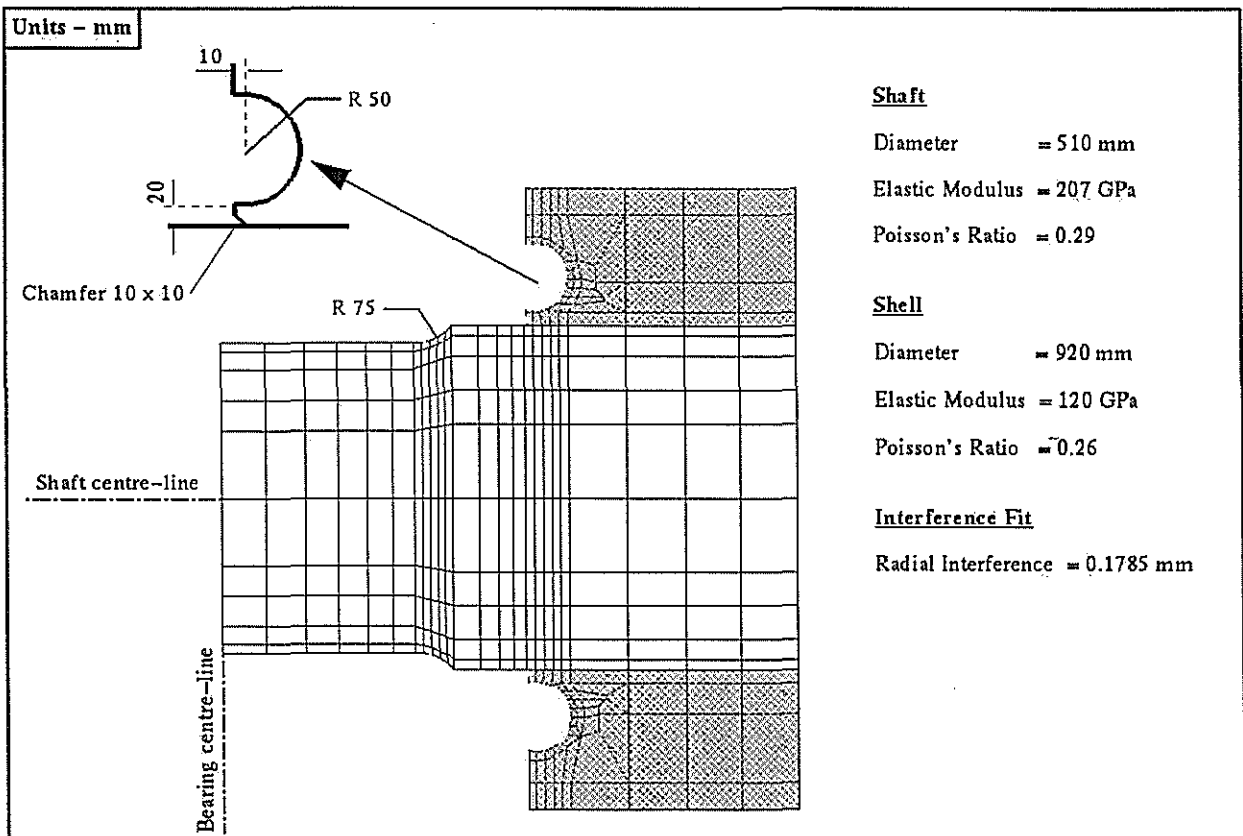


Figure 3.28 Sectioned view of shell-end region for large recess model.

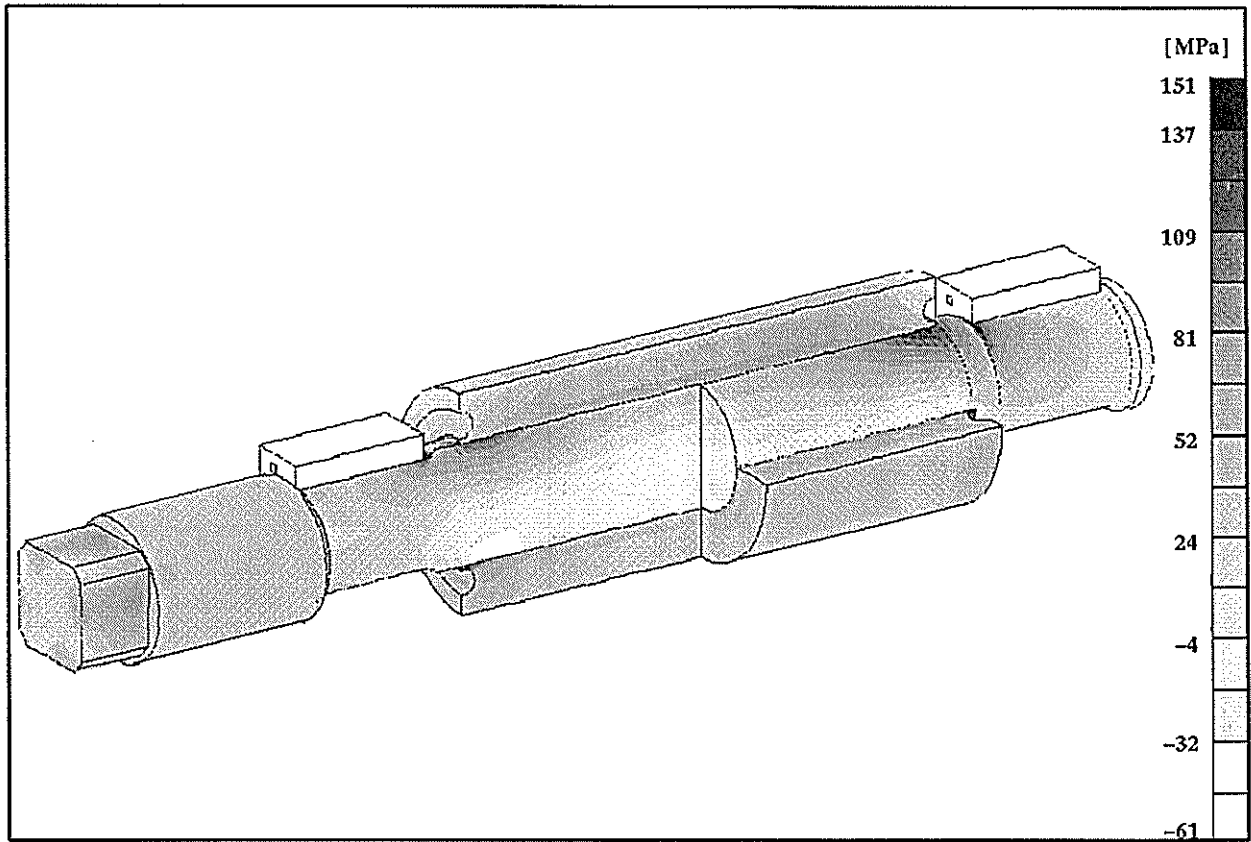


Figure 3.29 Major principal stress plot (Large recess : combined loads).

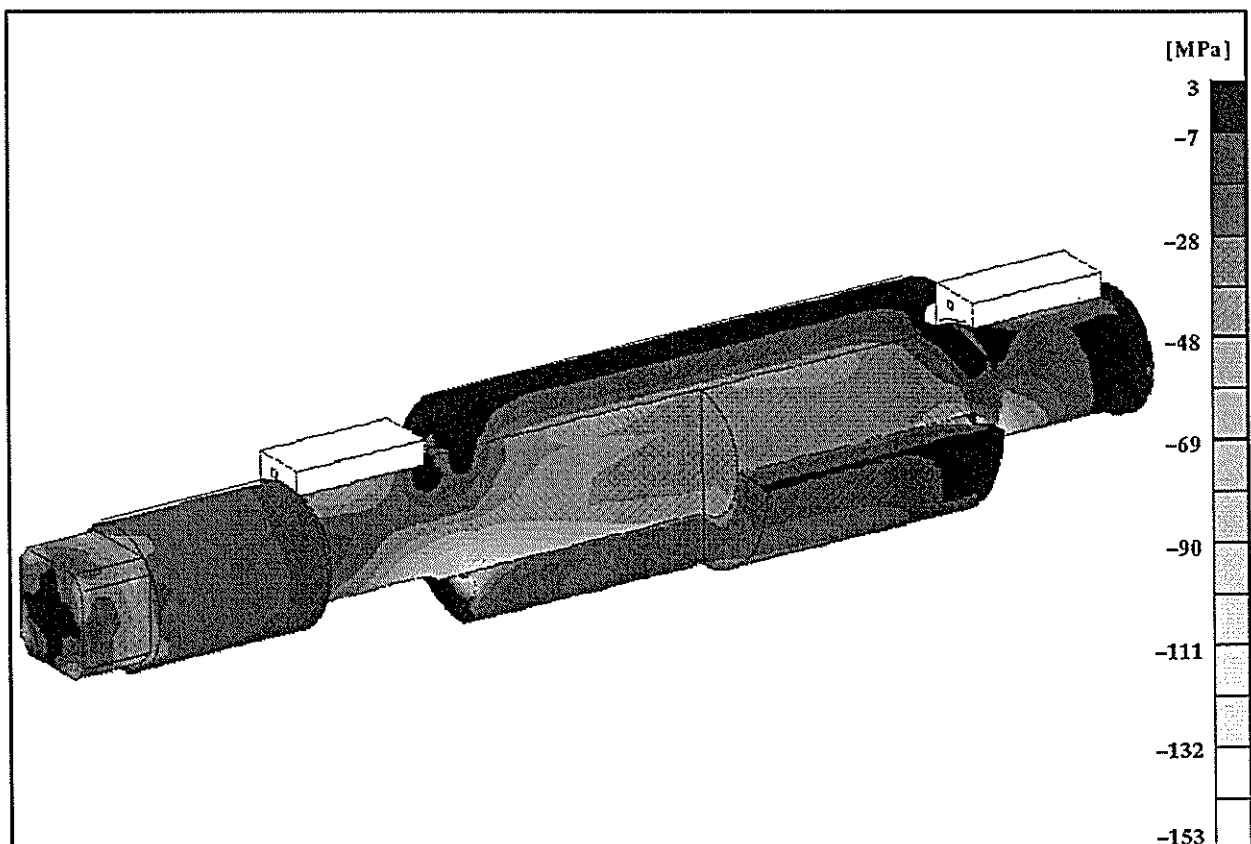


Figure 3.30 Minor principal stress plot (Large recess : combined loads).

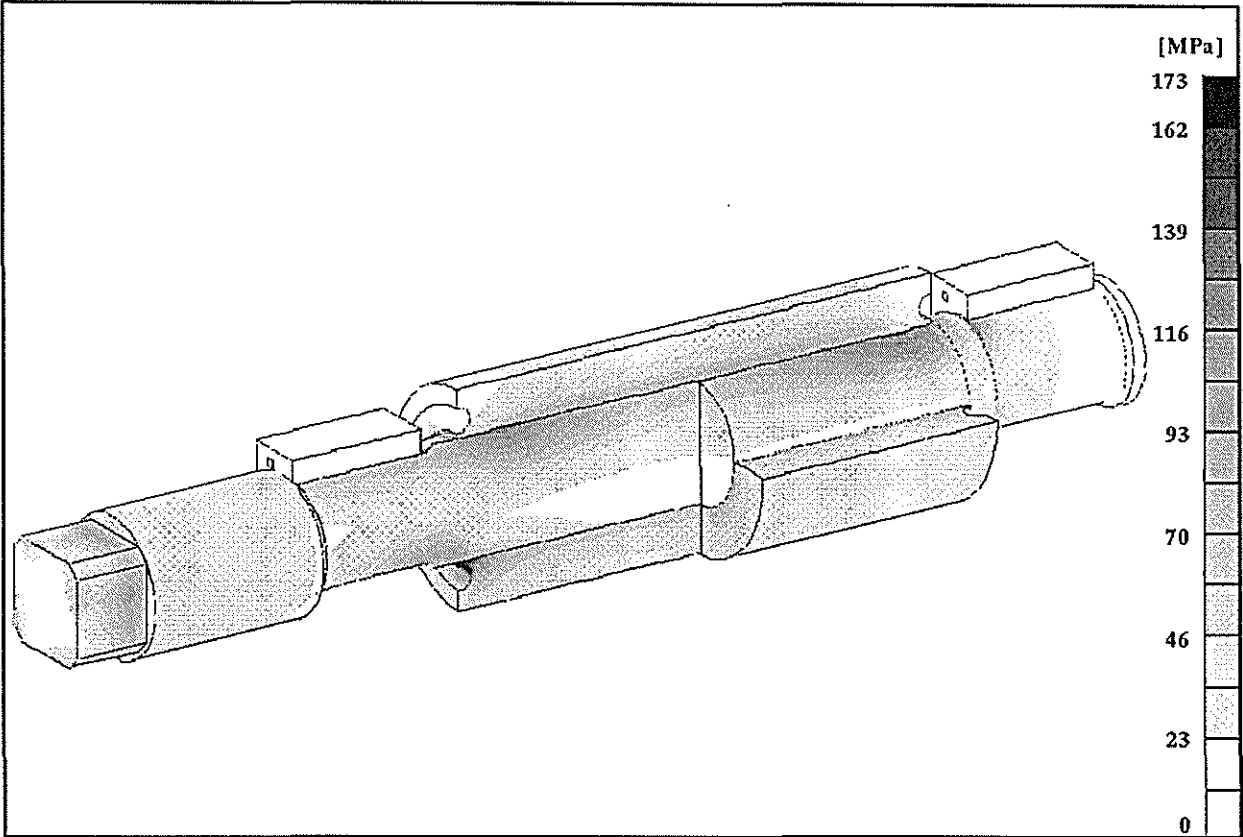


Figure 3.31 Von Mises stress plot (Large recess : combined loads).

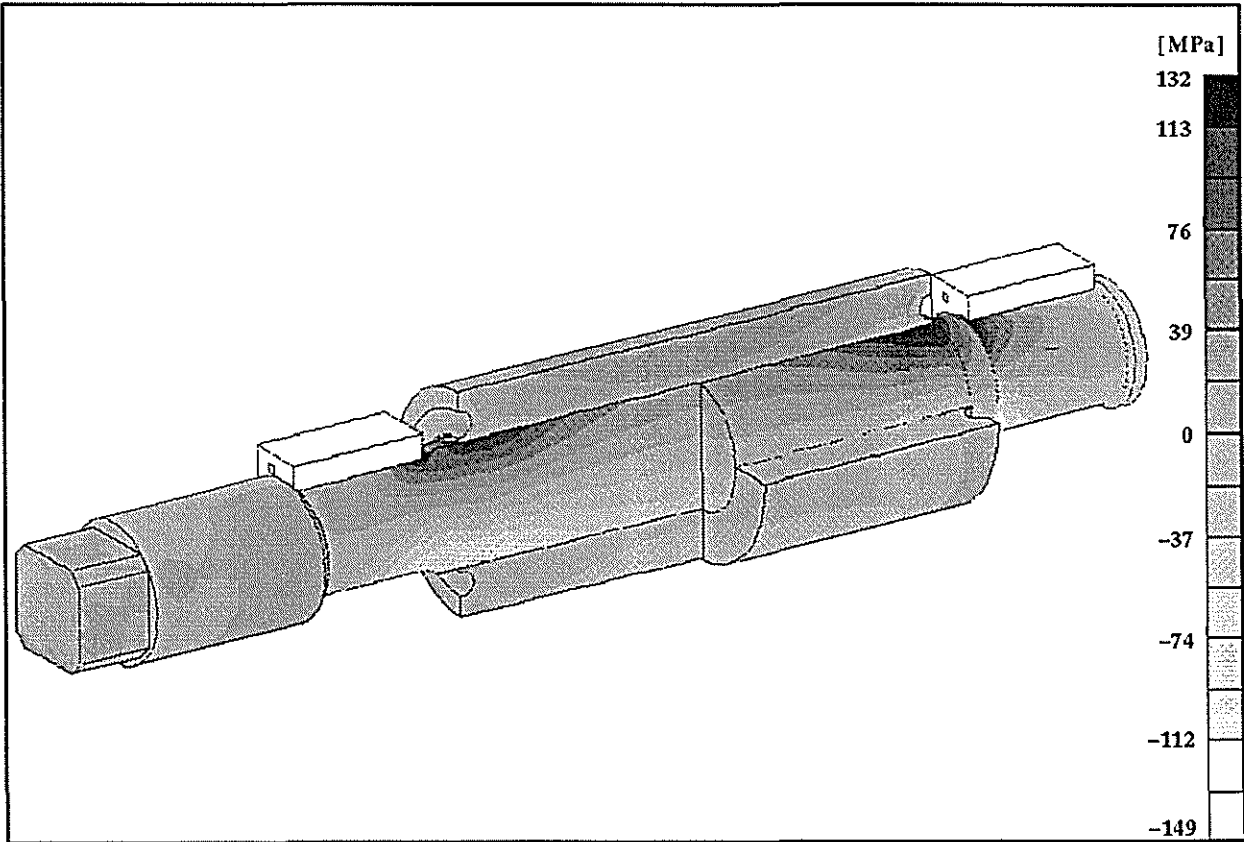


Figure 3.32 Axial stress plot (Large recess : combined loads).

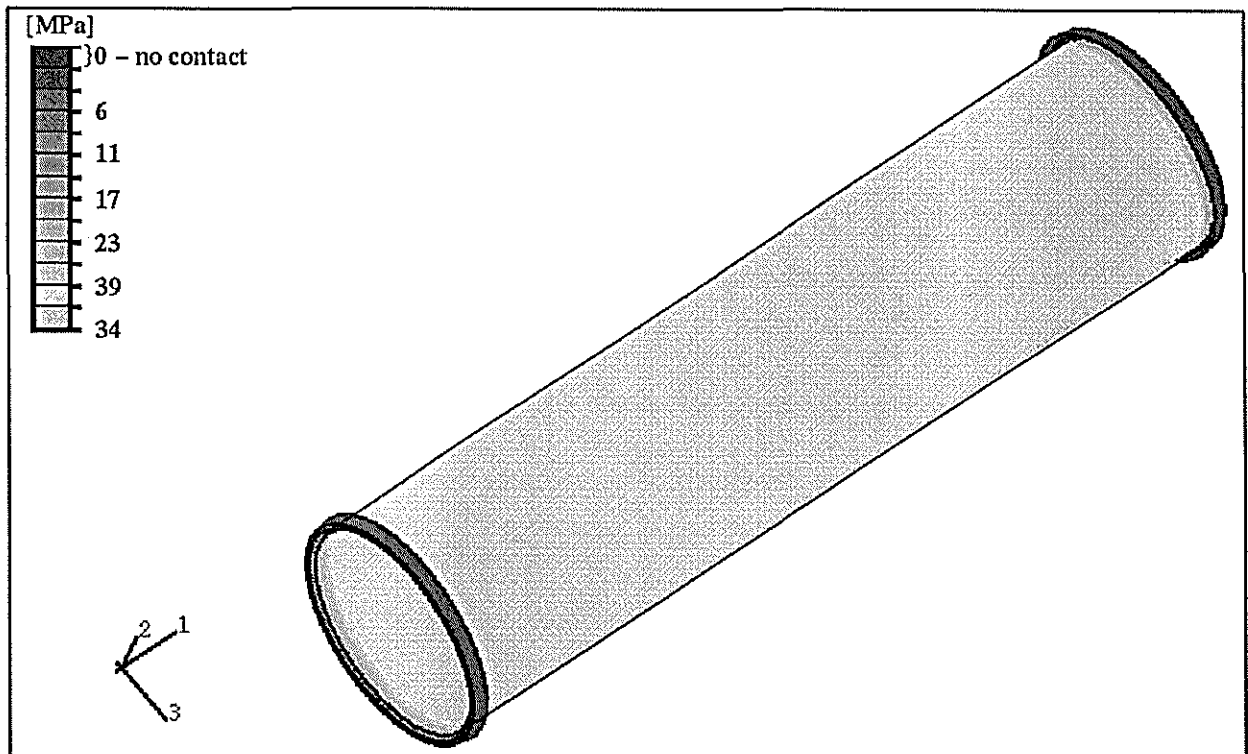


Figure 3.33 Contact pressure on inner shell surface (Large recess : interference load only).

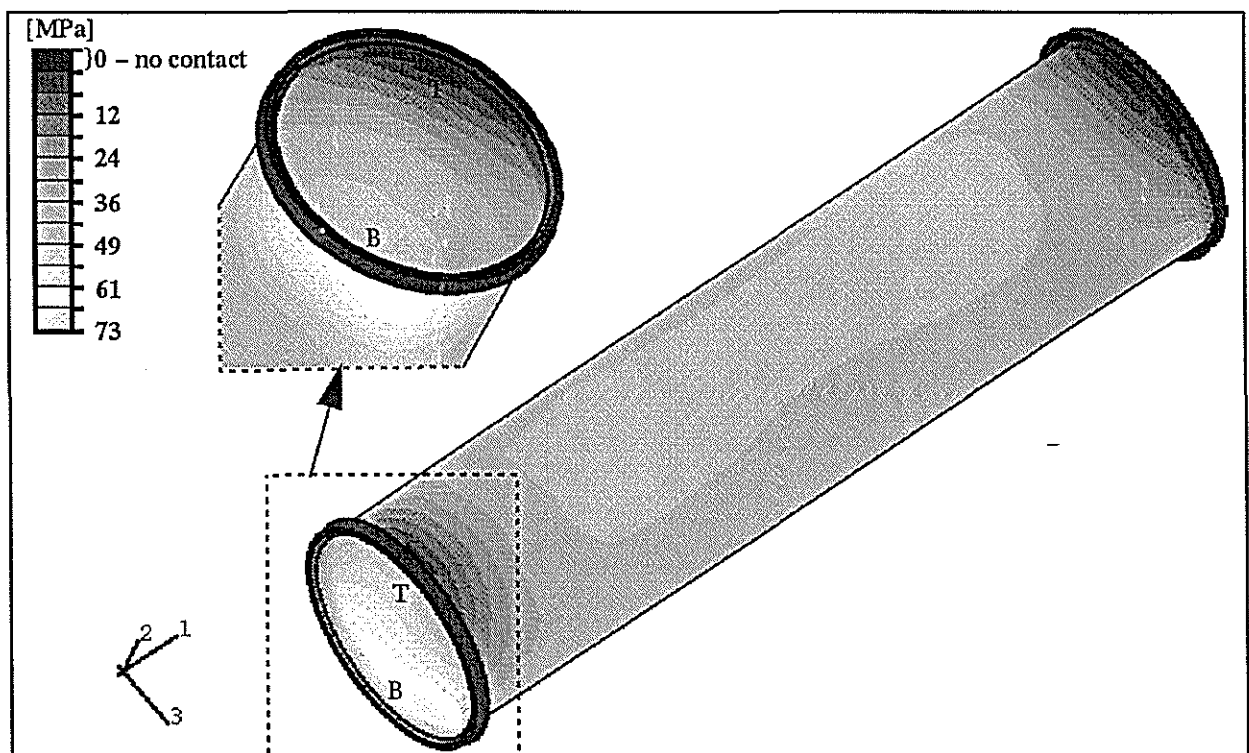


Figure 3.34 Contact pressure on inner shell surface (Large recess : combined loads).

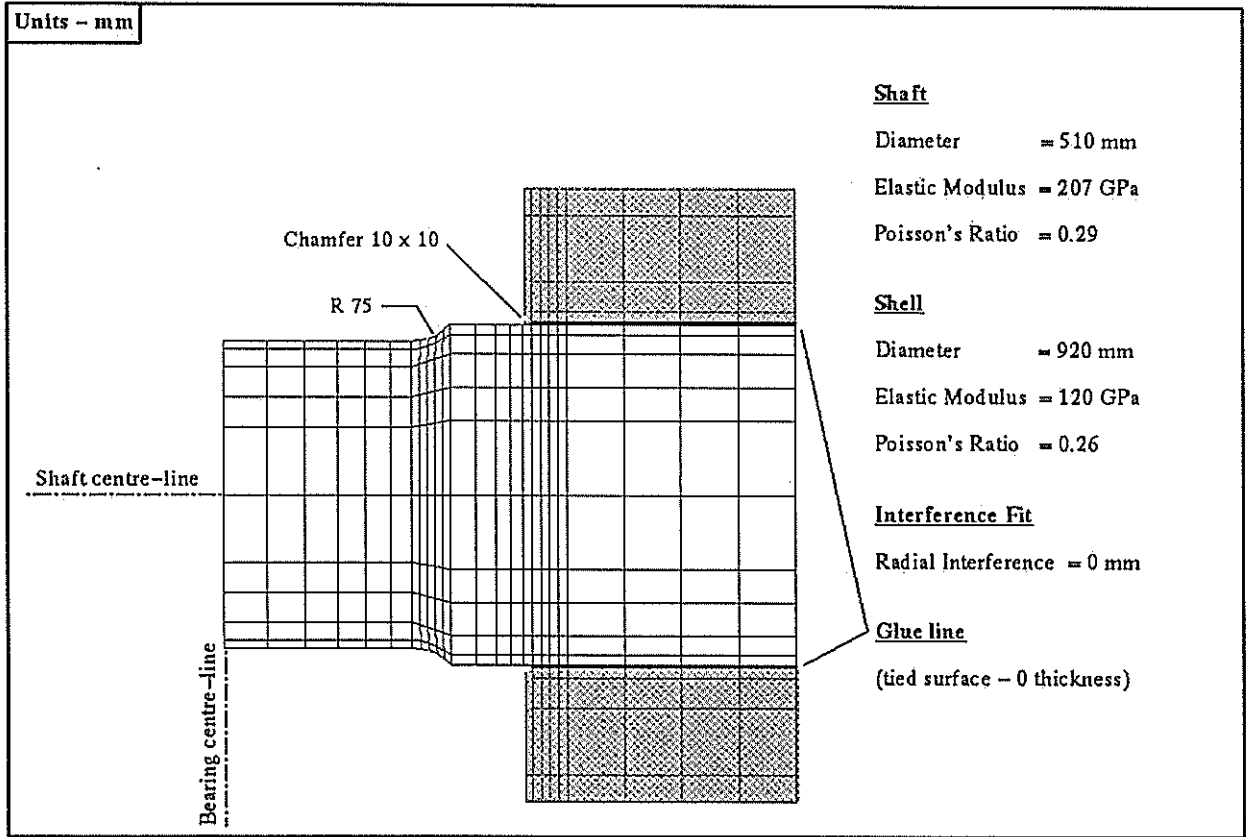


Figure 3.35 Sectioned view of shell-end region for adhesive model.

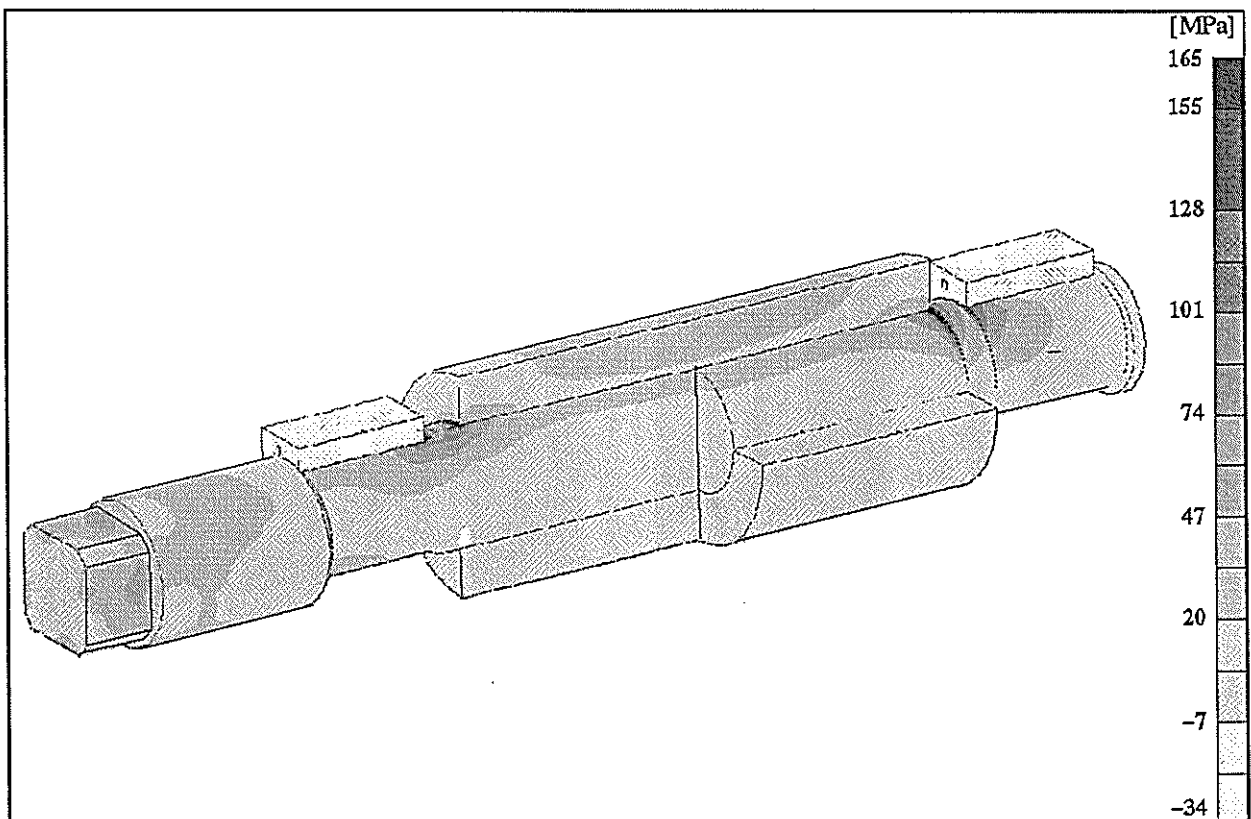


Figure 3.36 Major principal stress plot (Adhesive : combined loads).

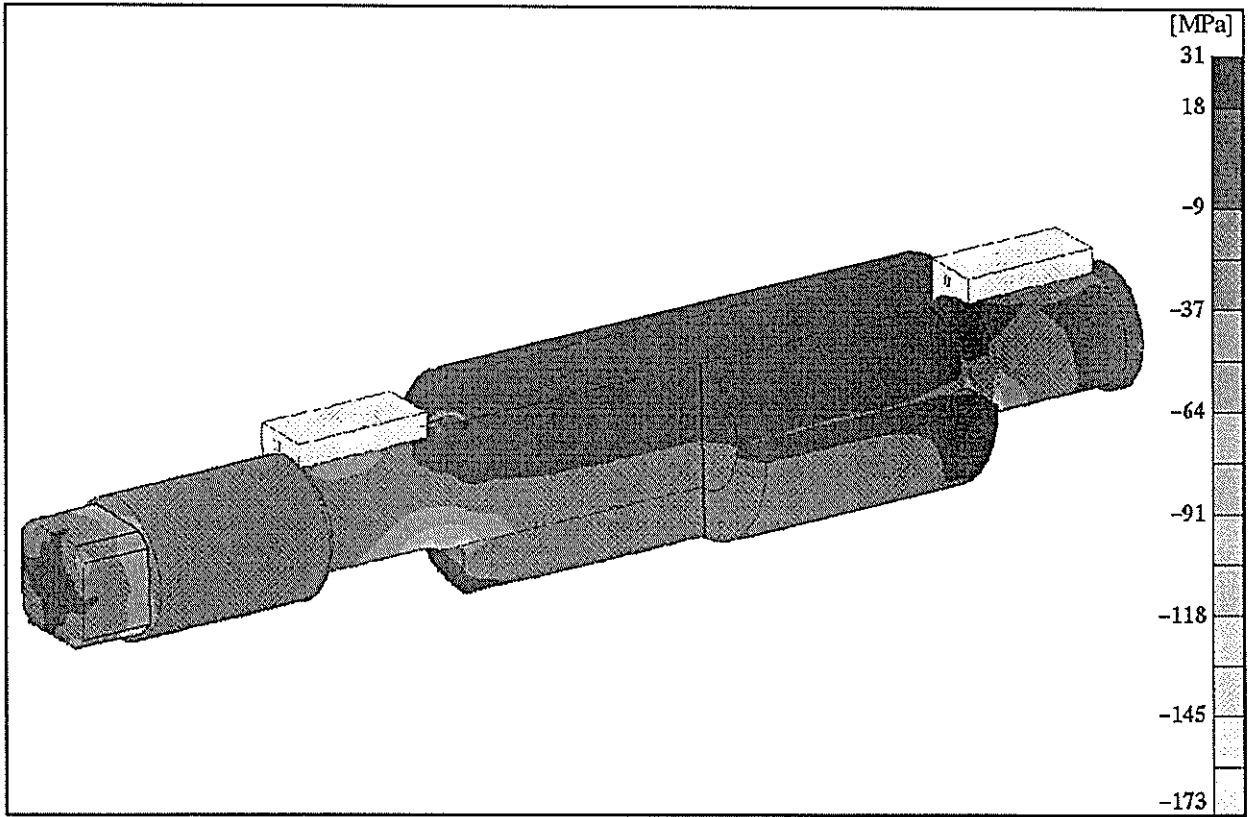


Figure 3.37 Minor principal stress plot (Adhesive : combined loads).

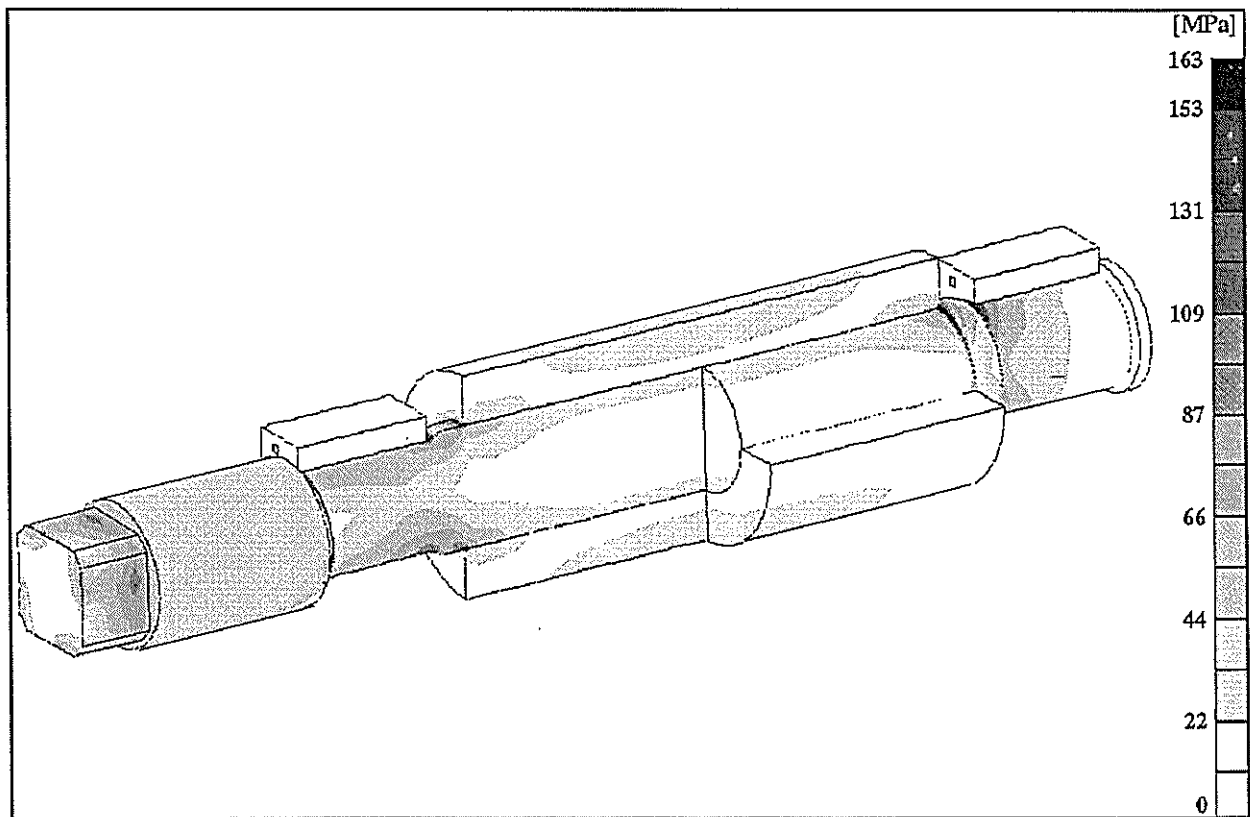


Figure 3.38 Von Mises stress plot (Adhesive : combined loads).

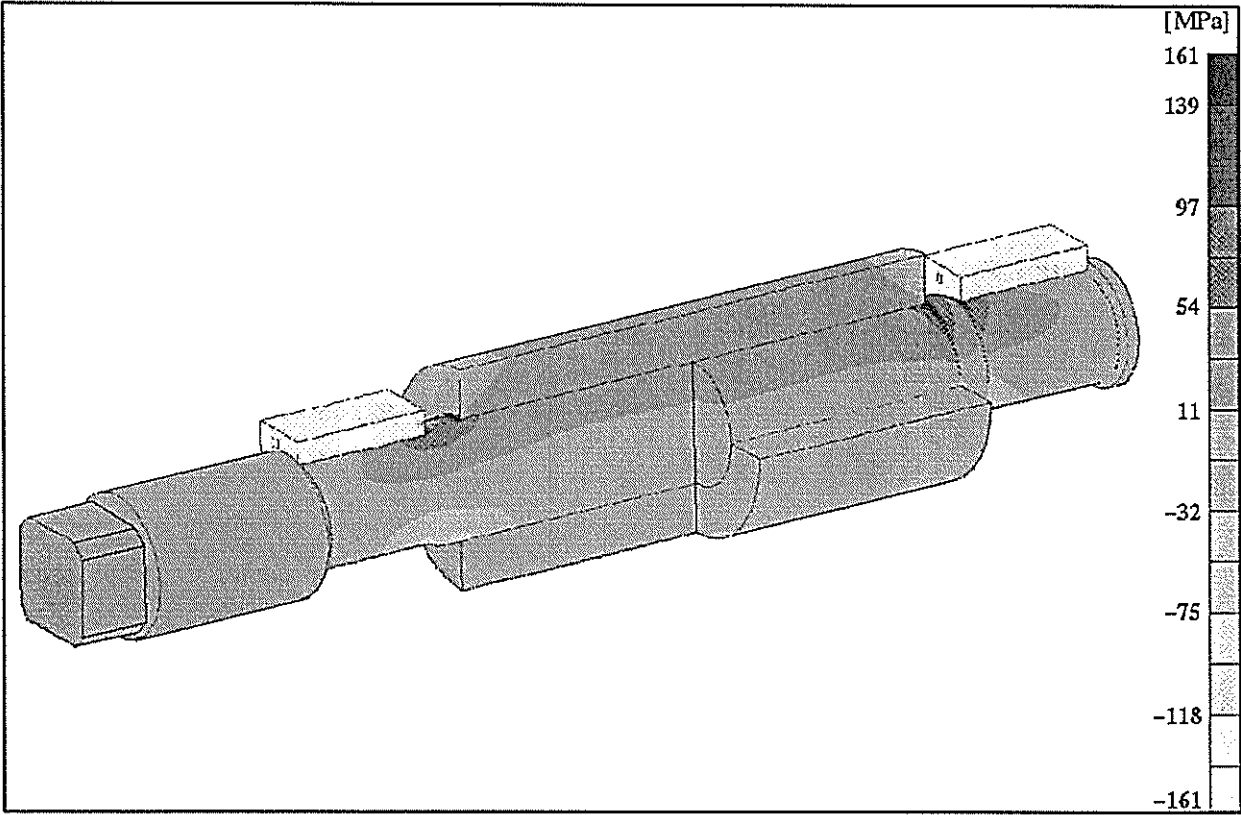


Figure 3.39 Axial stress plot (Adhesive : combined loads).

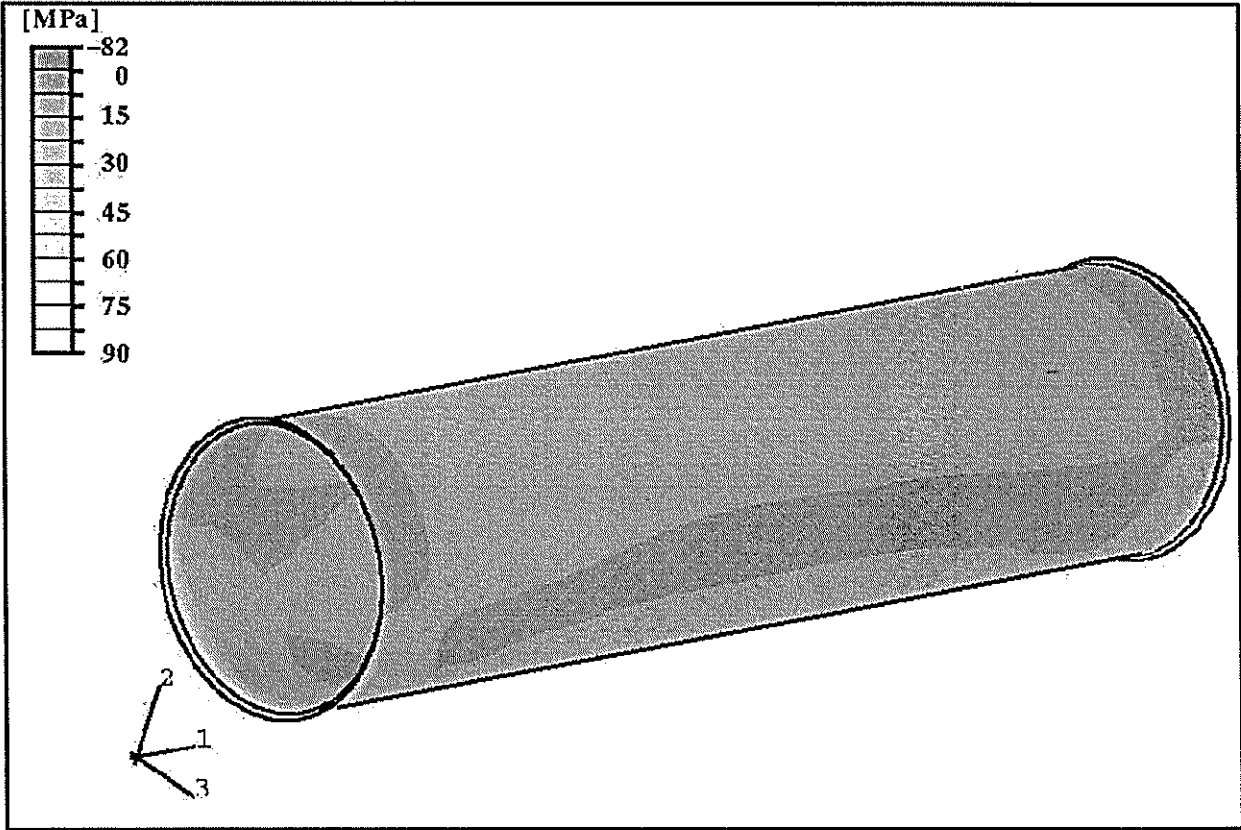


Figure 3.40 Radial stress on inner shell surface (Adhesive : combined loads).

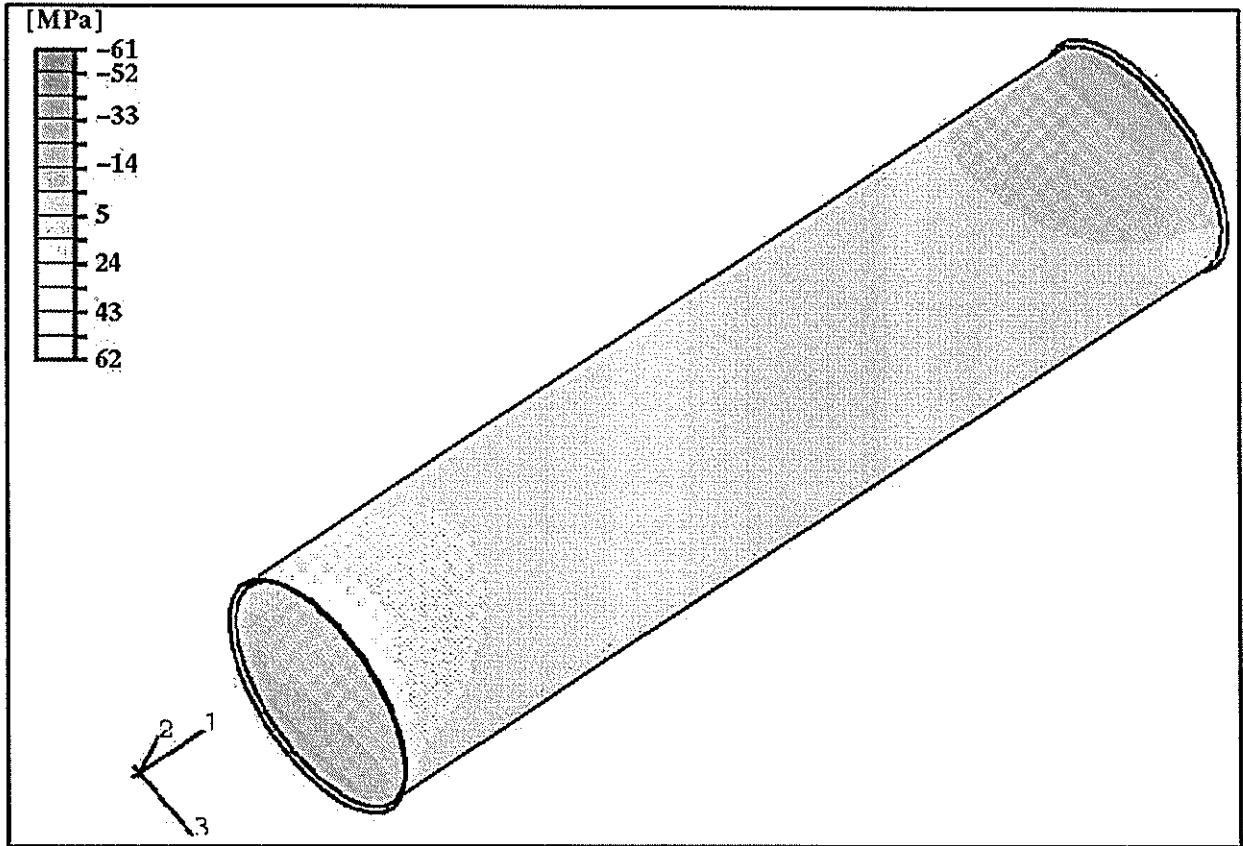


Figure 3.41 Shear stress in direction 1 on inner shell surface (Adhesive : combined loads).

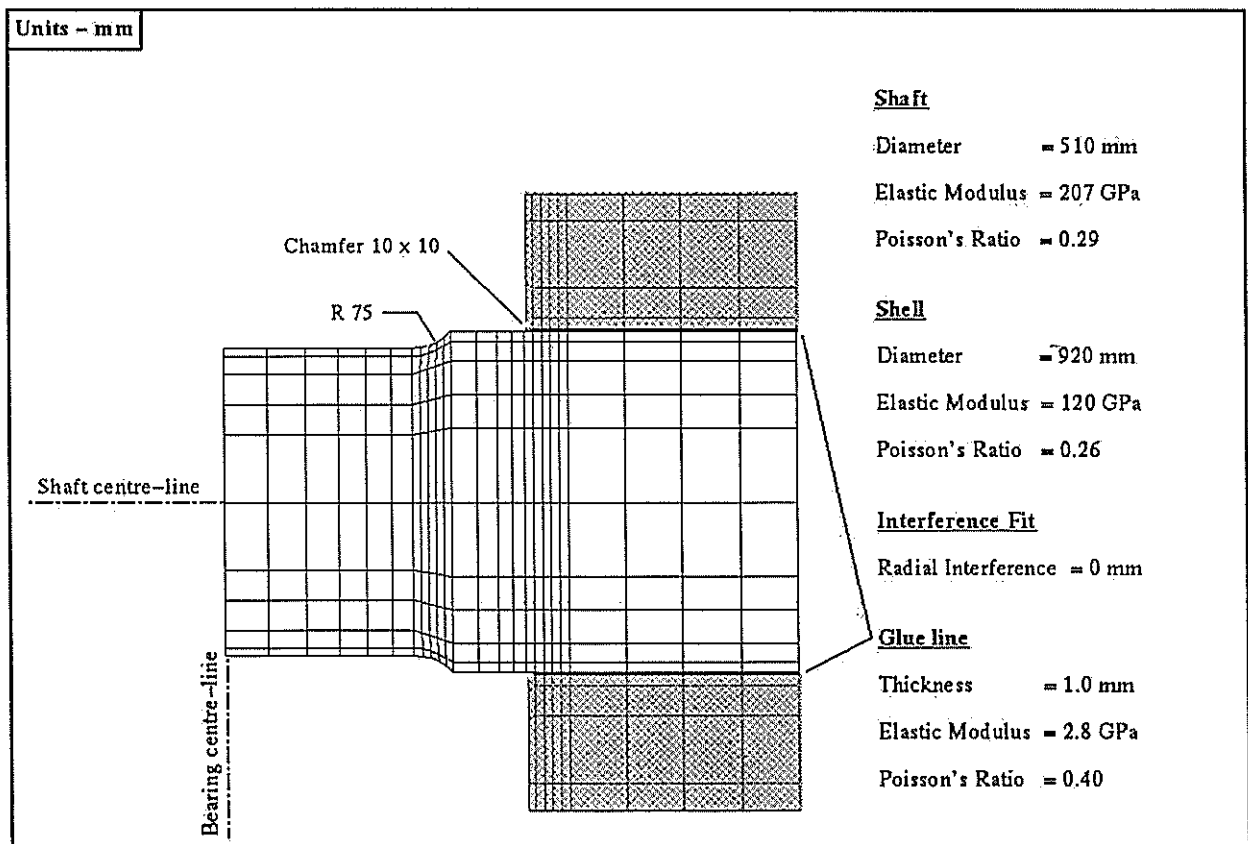


Figure 3.42 Sectioned view of shell-end region for epoxy model.

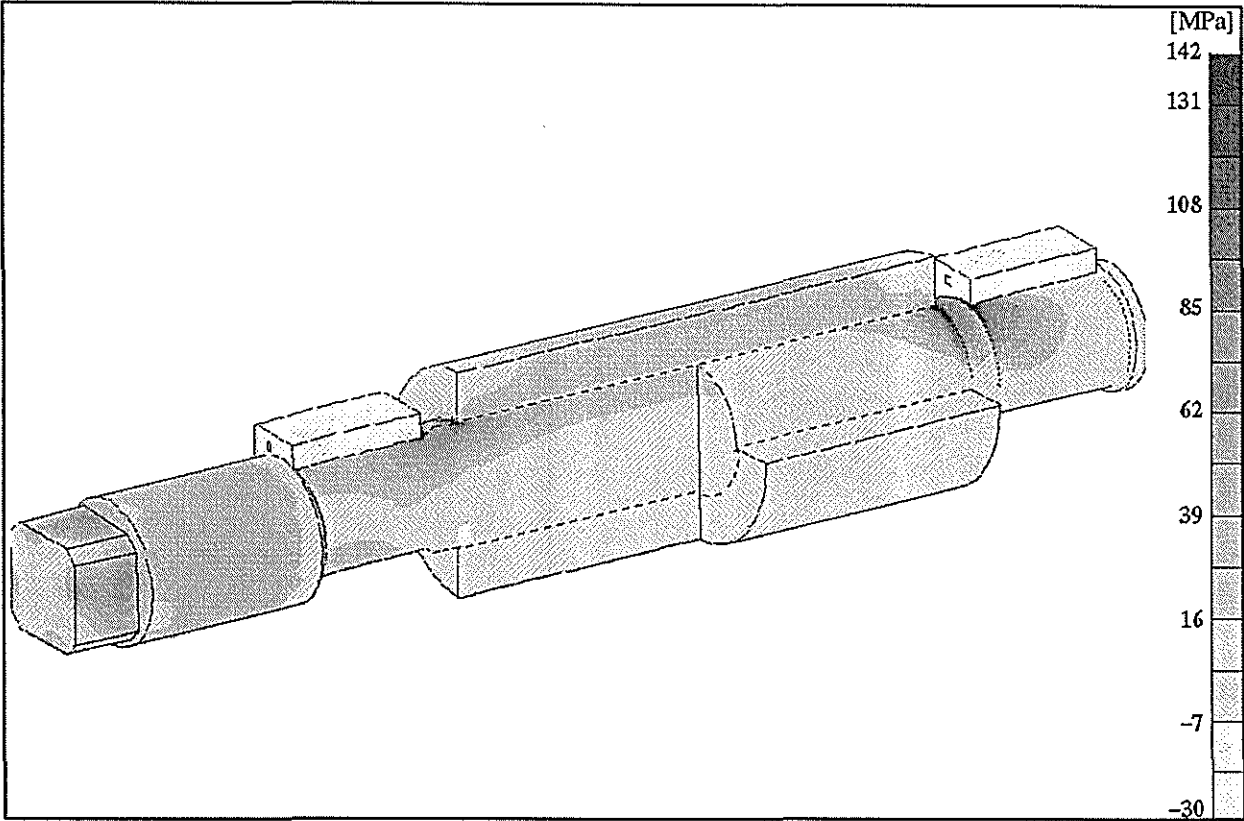


Figure 3.43 Major principal stress plot (Epoxy : combined loads).

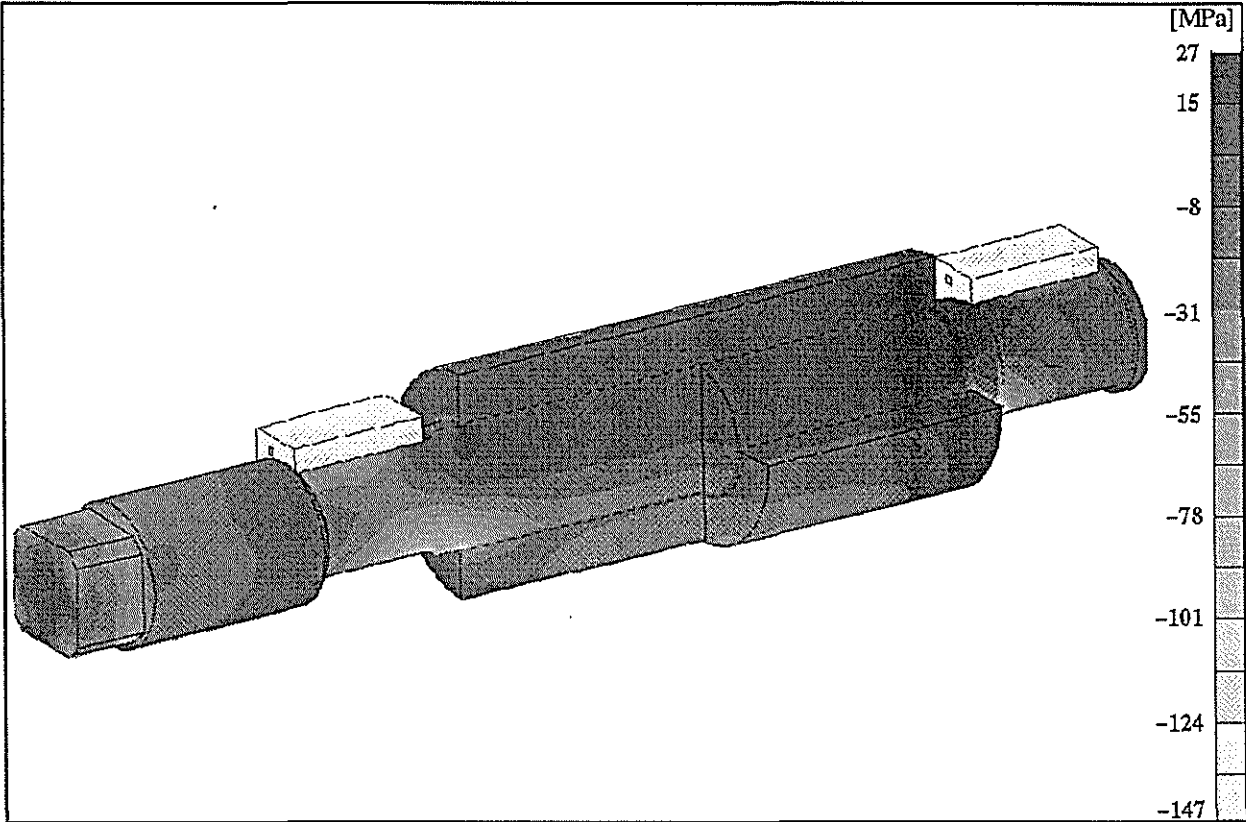


Figure 3.44 Minor principal stress plot (Epoxy : combined loads).

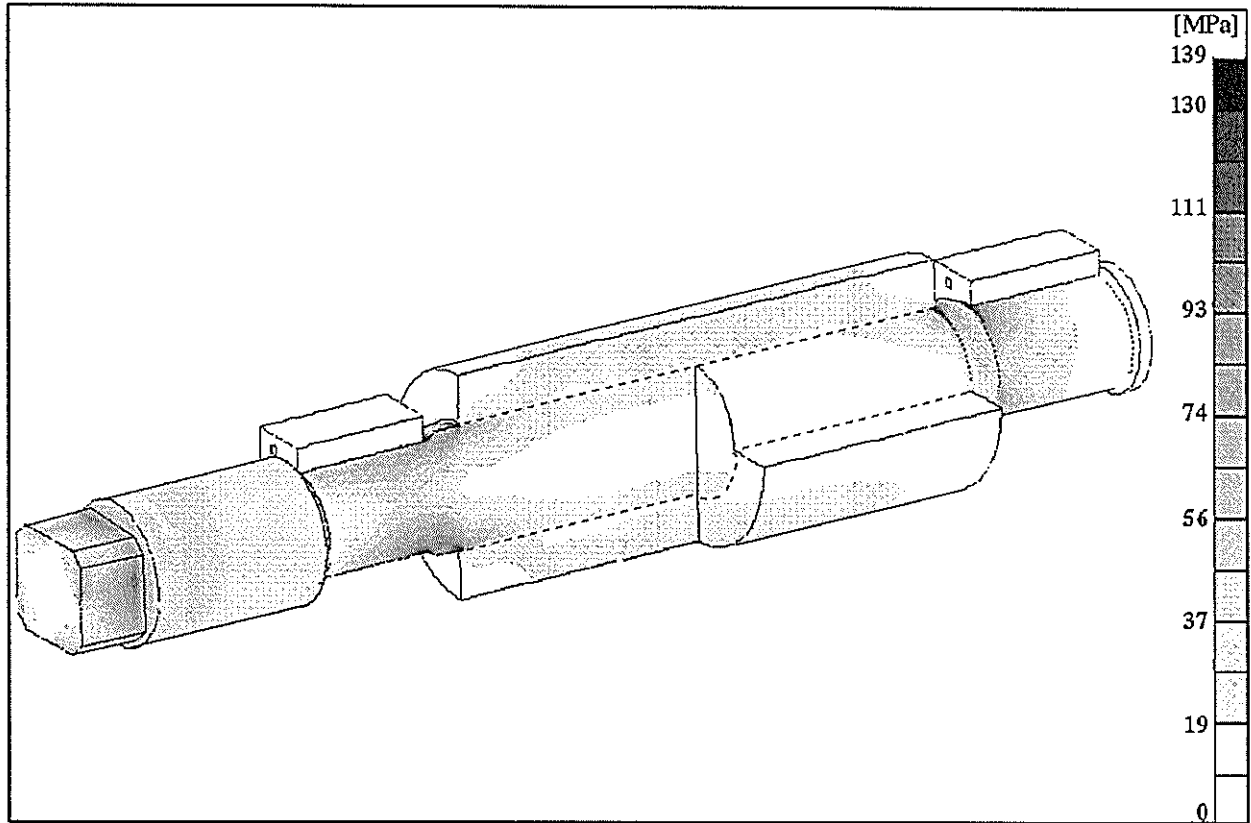


Figure 3.45 Von Mises stress plot (Epoxy : combined loads).

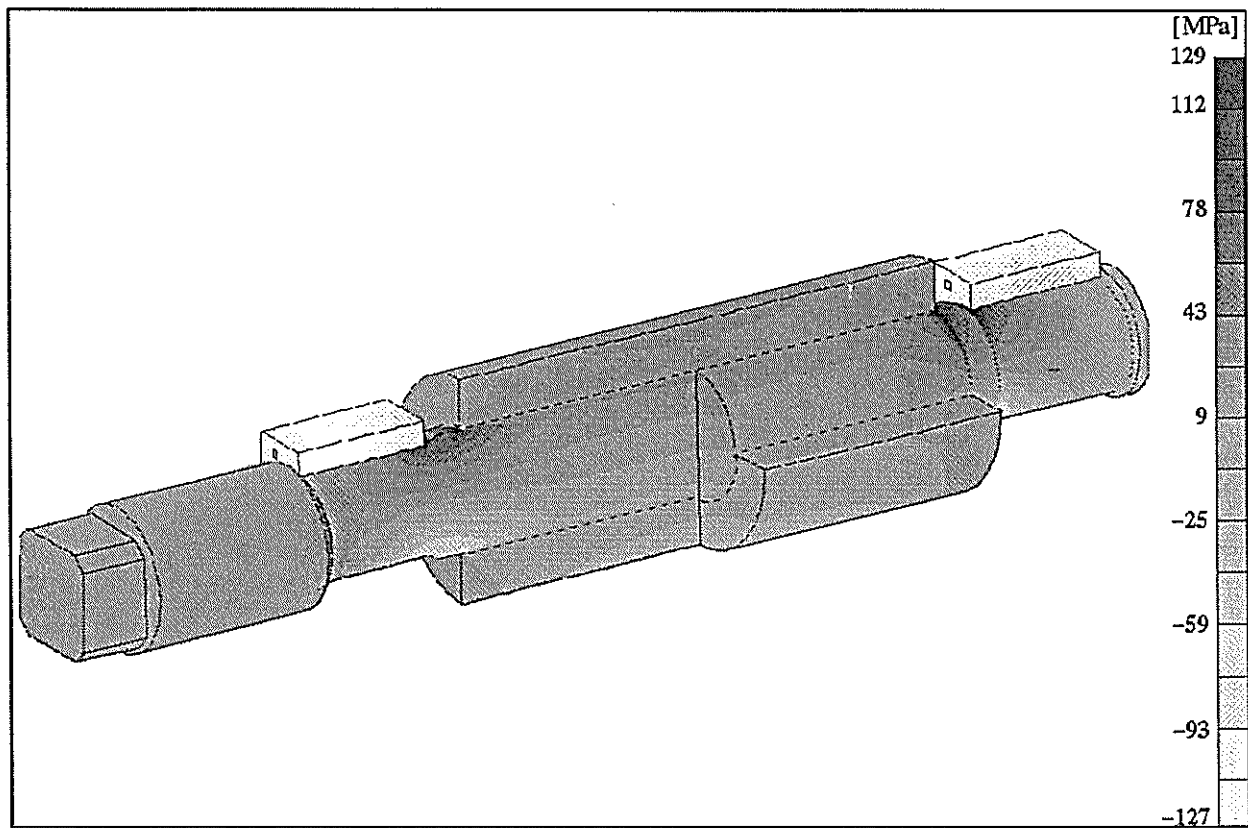


Figure 3.46 Axial stress plot (Epoxy : combined loads).

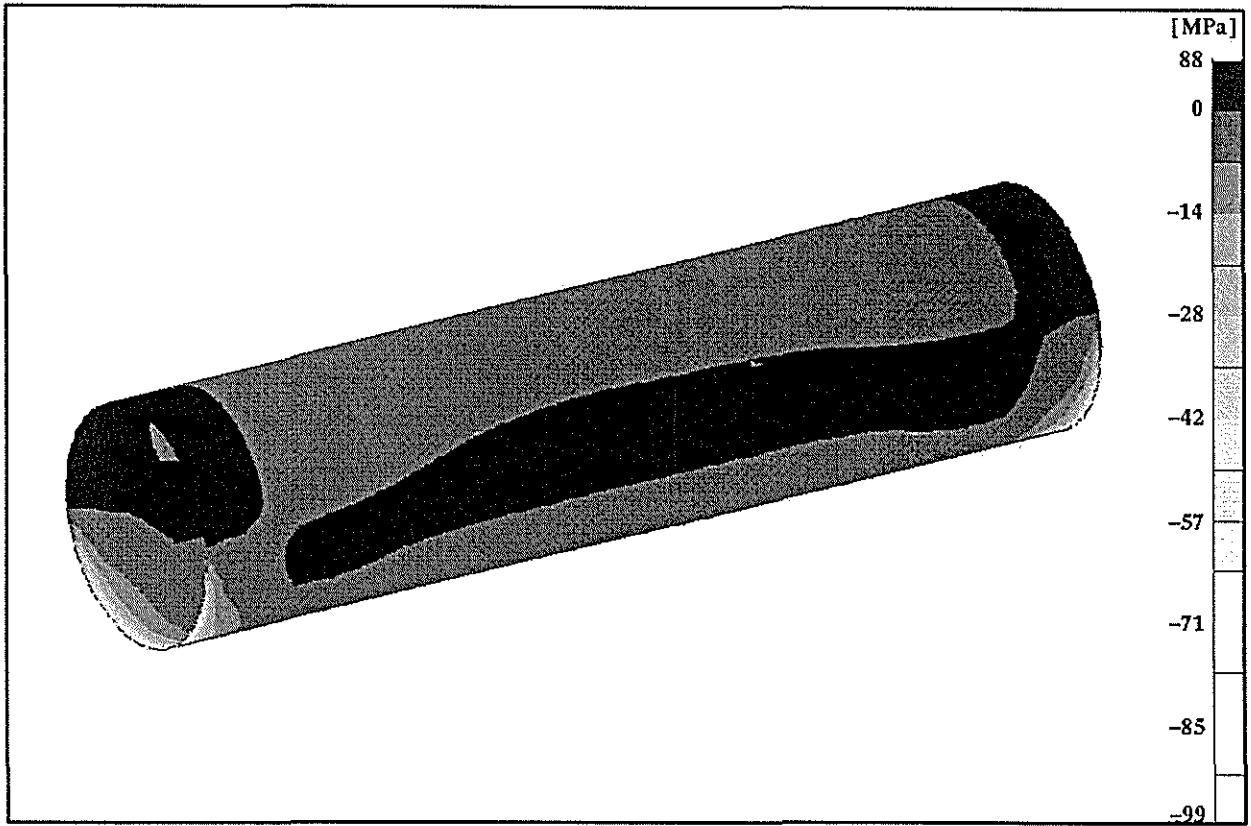


Figure 3.47 Radial stress in epoxy layer (Epoxy : combined loads).

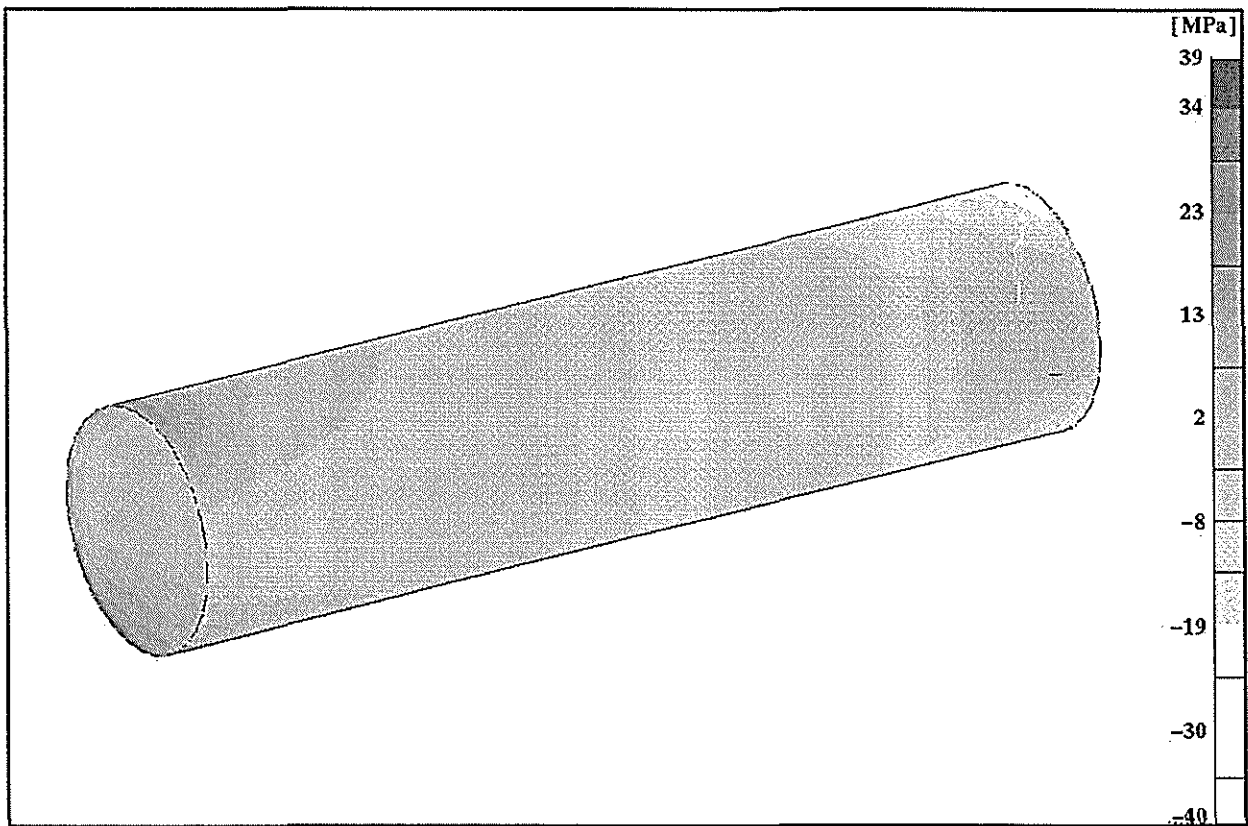


Figure 3.48 Shear stress (axial direction) in epoxy layer (Epoxy : combined loads).

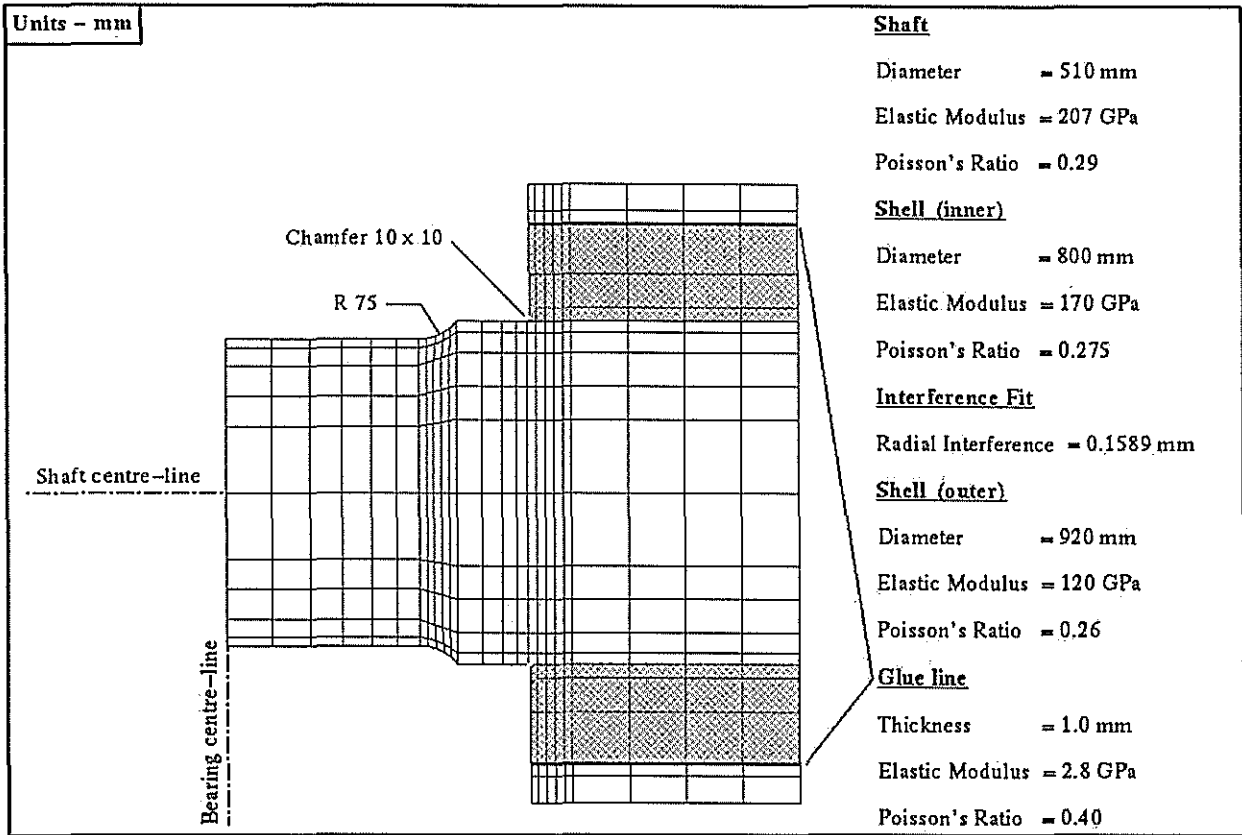


Figure 3.49 Sectioned view of shell-end region for double shell model.

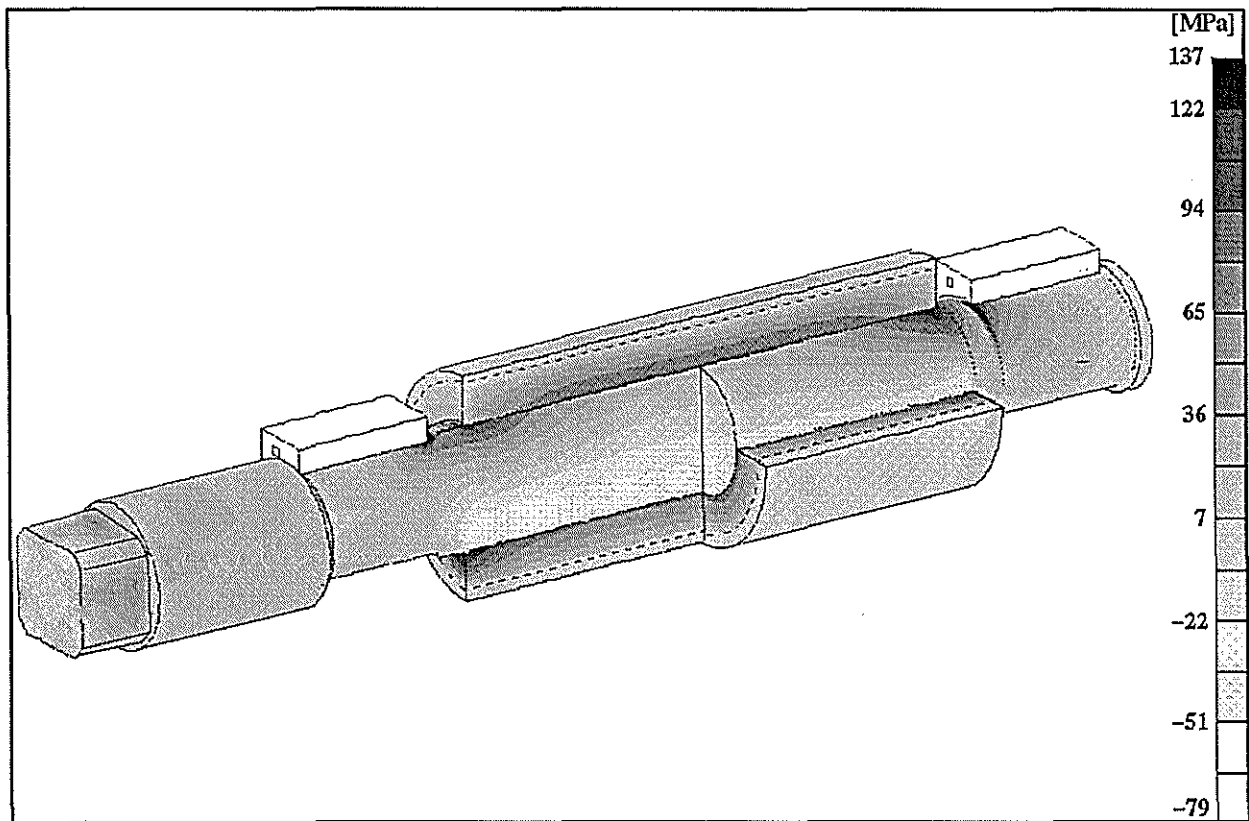


Figure 3.50 Major principal stress plot (Double shell : combined loads).

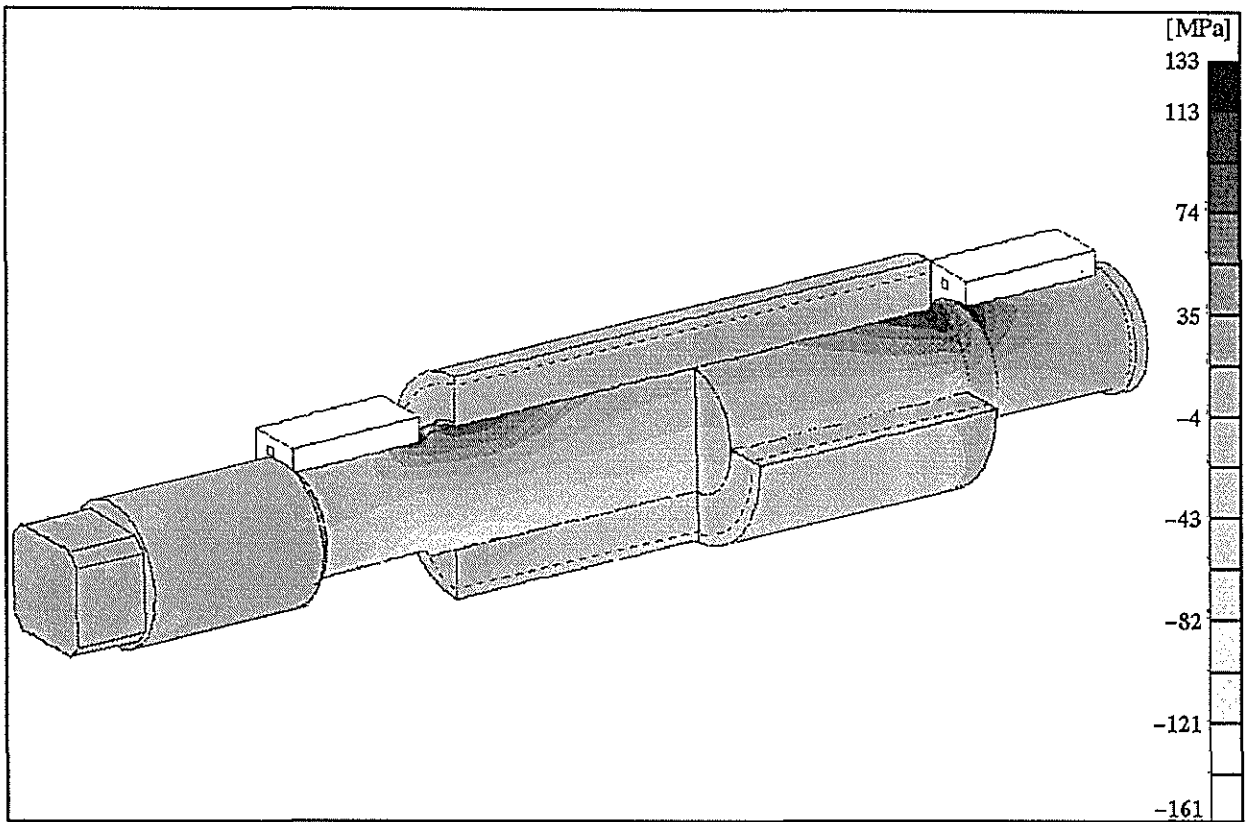


Figure 3.53 Axial stress plot (Double shell : combined loads).

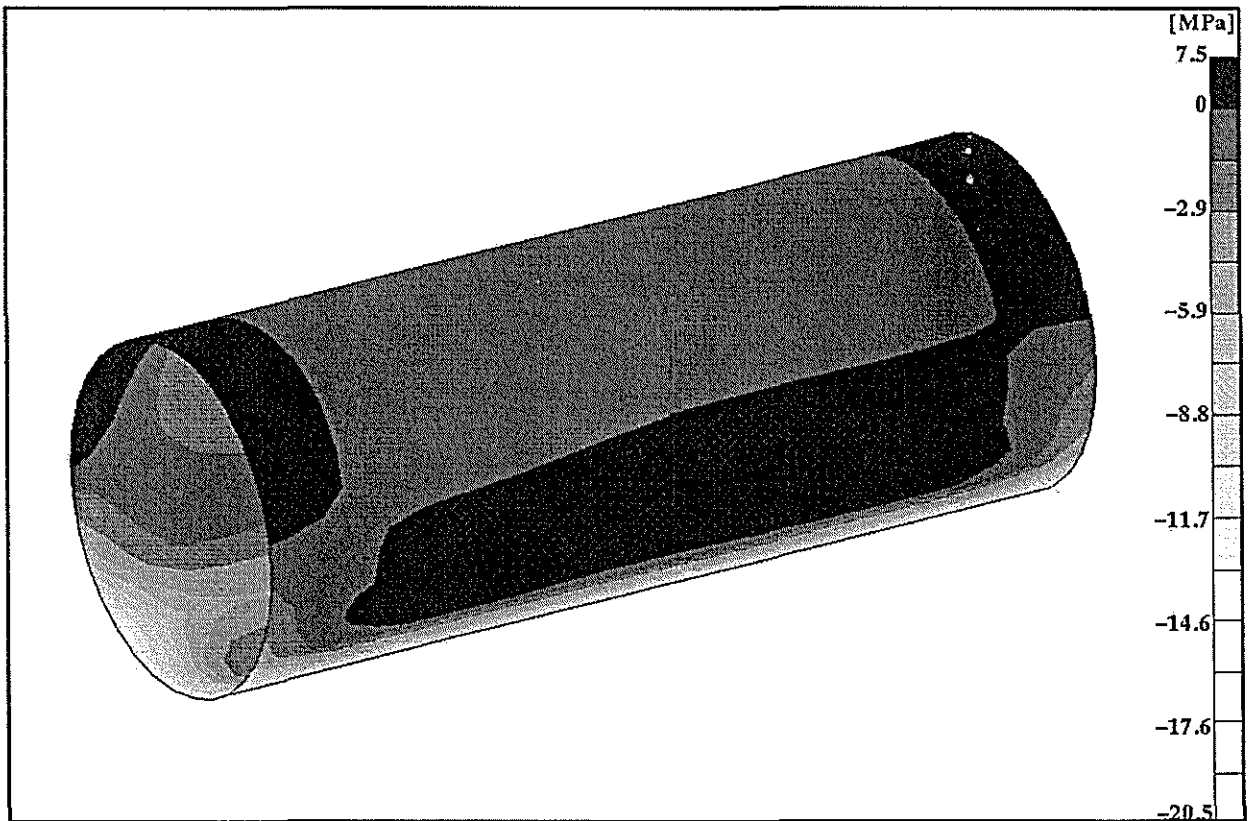


Figure 3.54 Radial stress in epoxy layer (Double shell : combined loads).

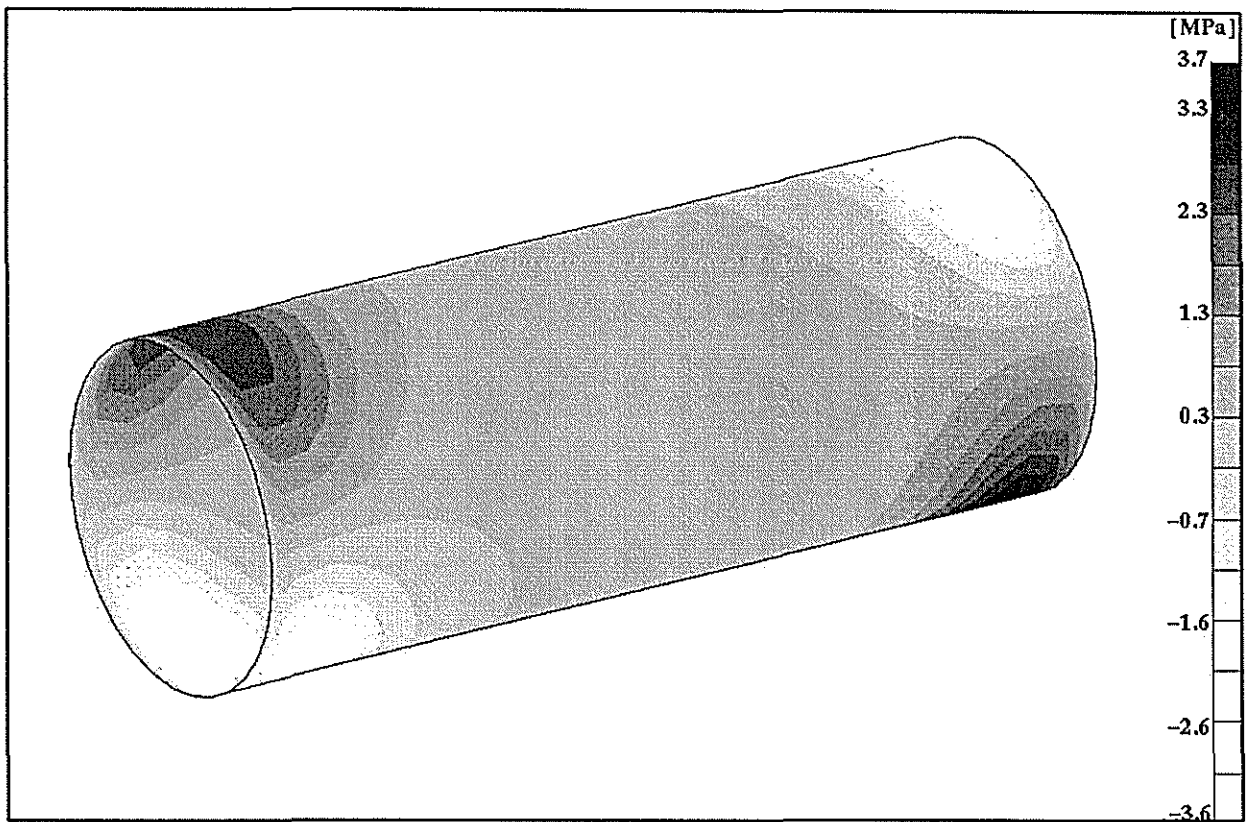


Figure 3.55 Shear stress (axial direction) in epoxy layer (Double shell : combined loads).

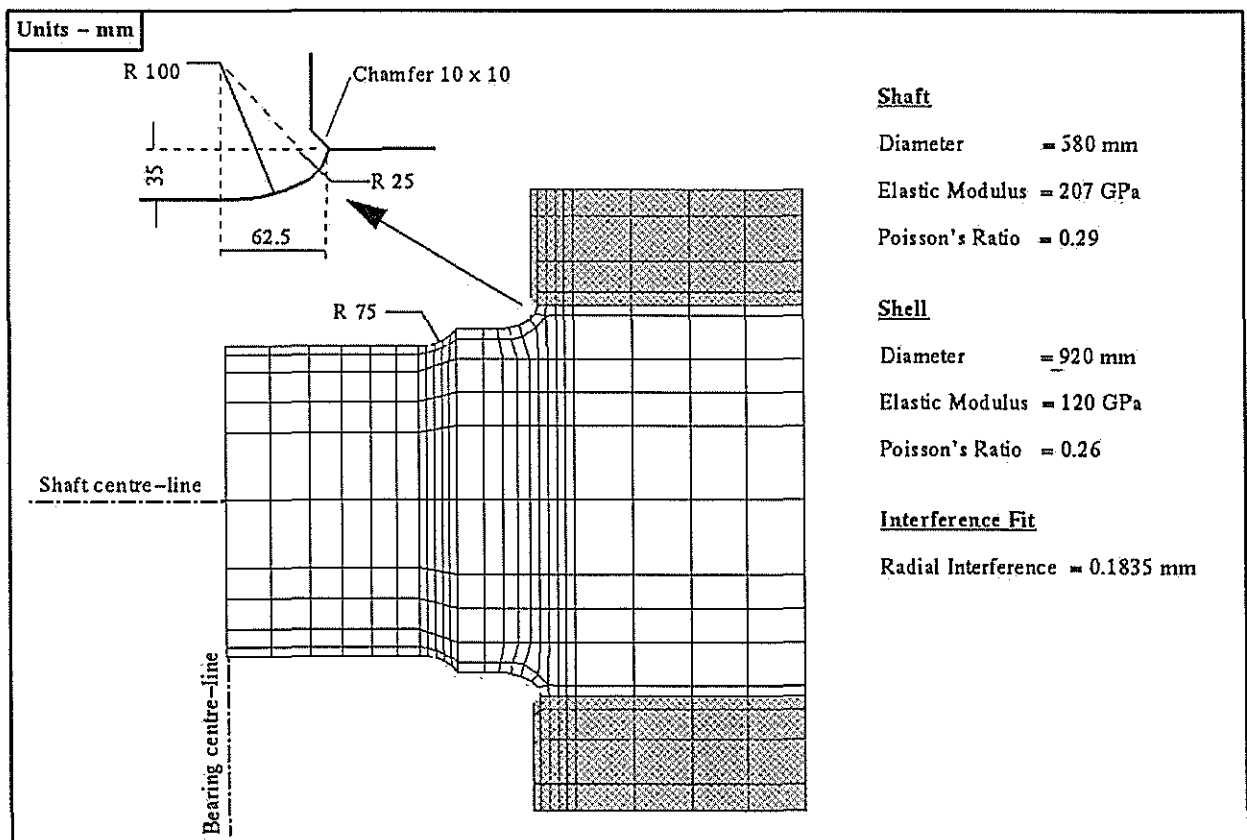


Figure 3.56 Sectioned view of shell-end region for raised landing model.

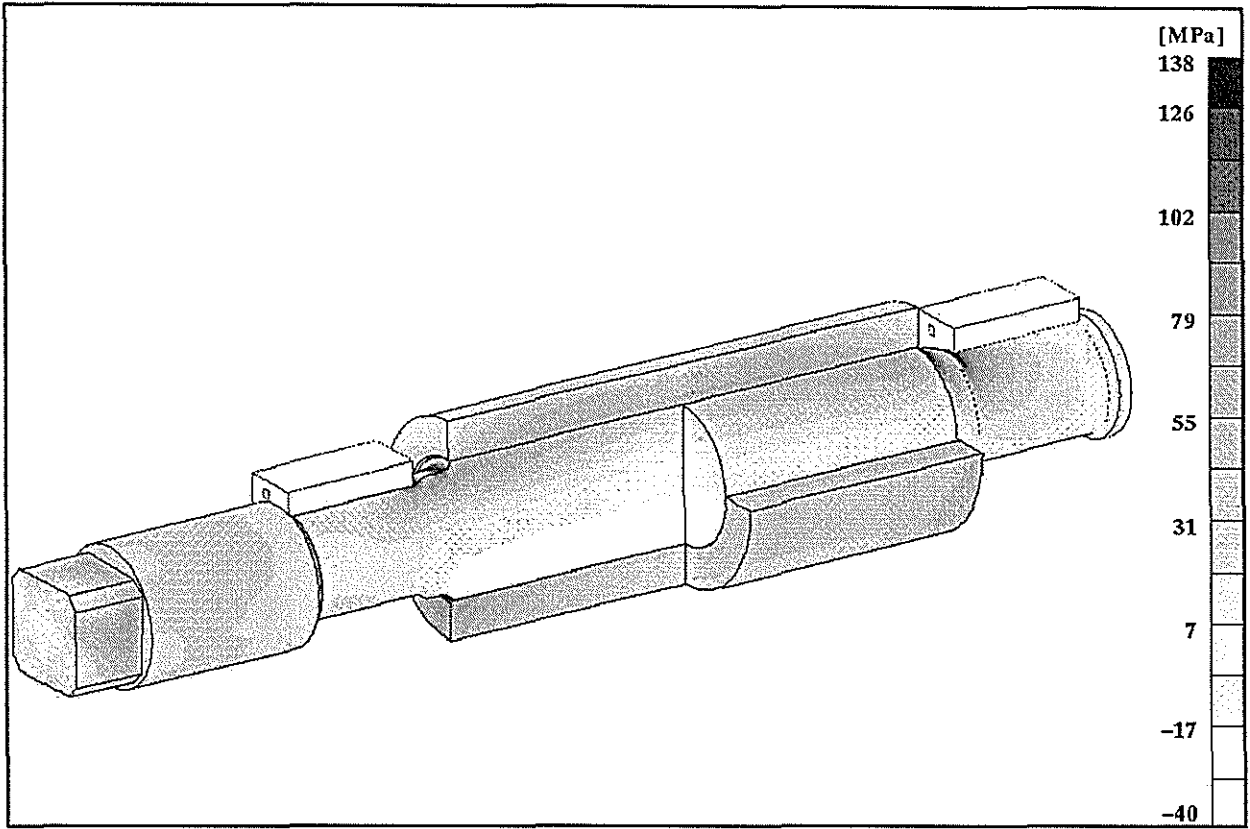


Figure 3.57 Major principal stress plot (Raised landing : combined loads).

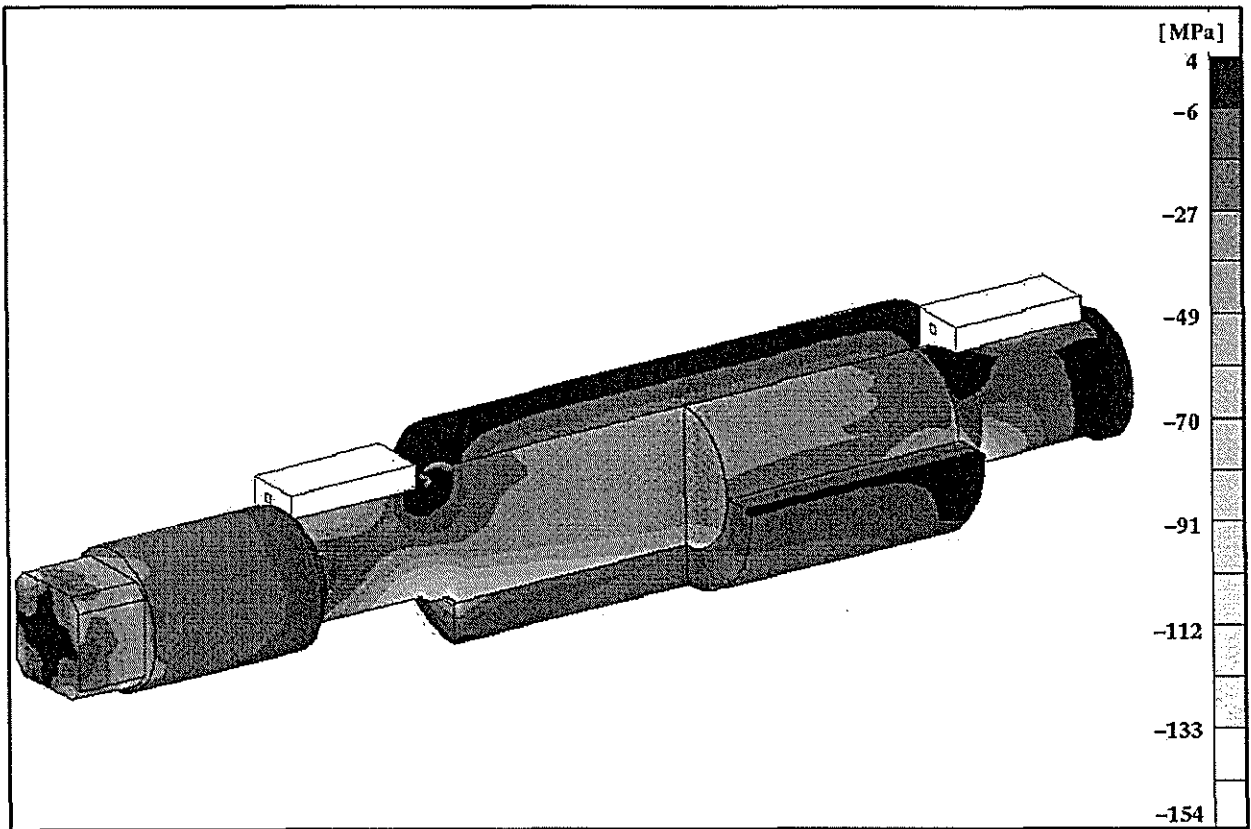


Figure 3.58 Minor principal stress plot (Raised landing : combined loads).

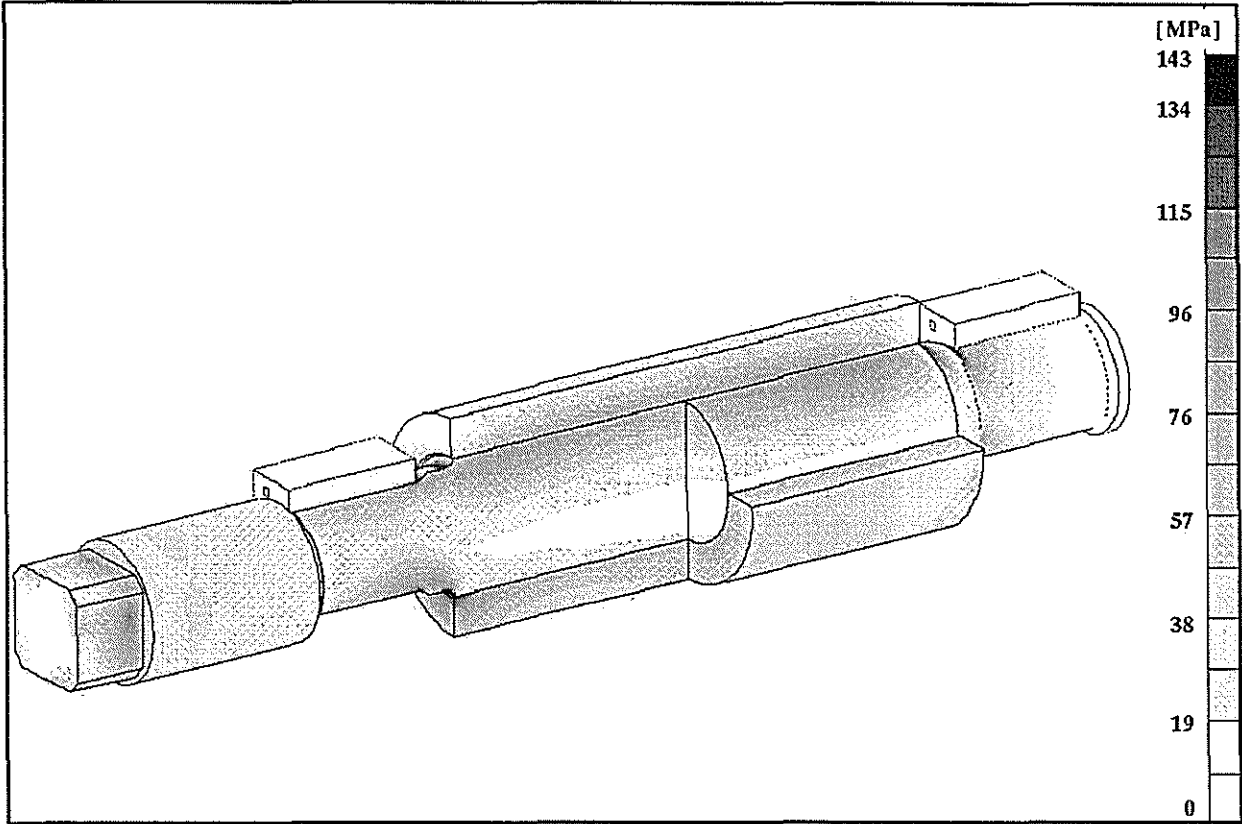


Figure 3.59 Von Mises stress plot (Raised landing : combined loads).

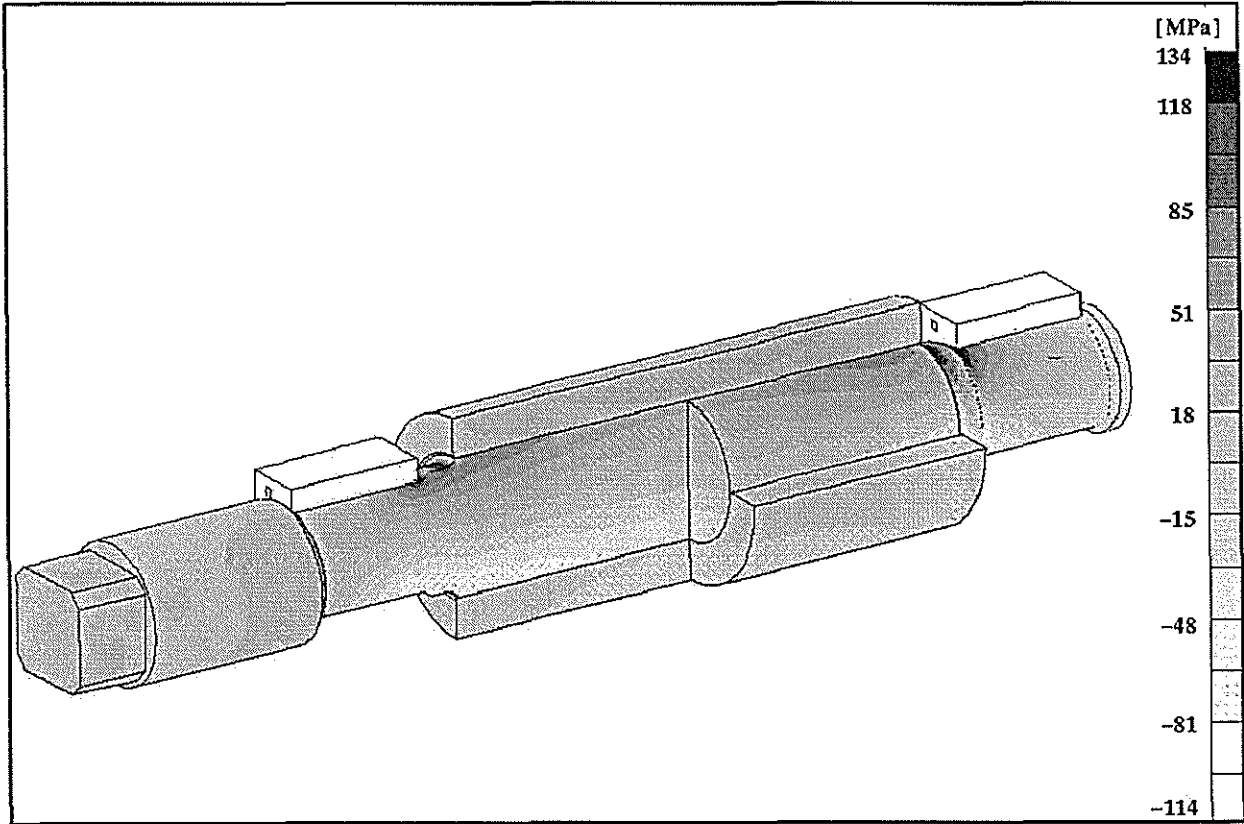


Figure 3.60 Axial stress plot (Raised landing : combined loads).

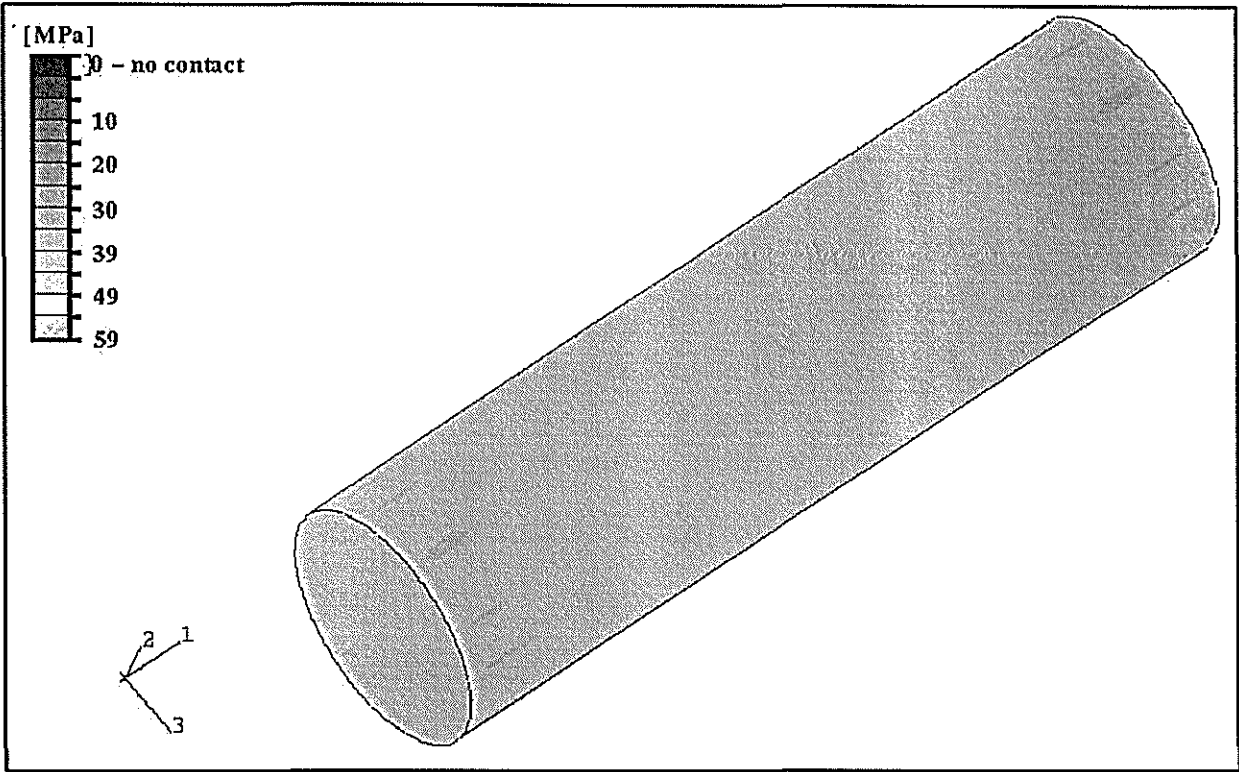


Figure 3.61 Contact pressure on inner shell surface (Raised landing : interference load only).

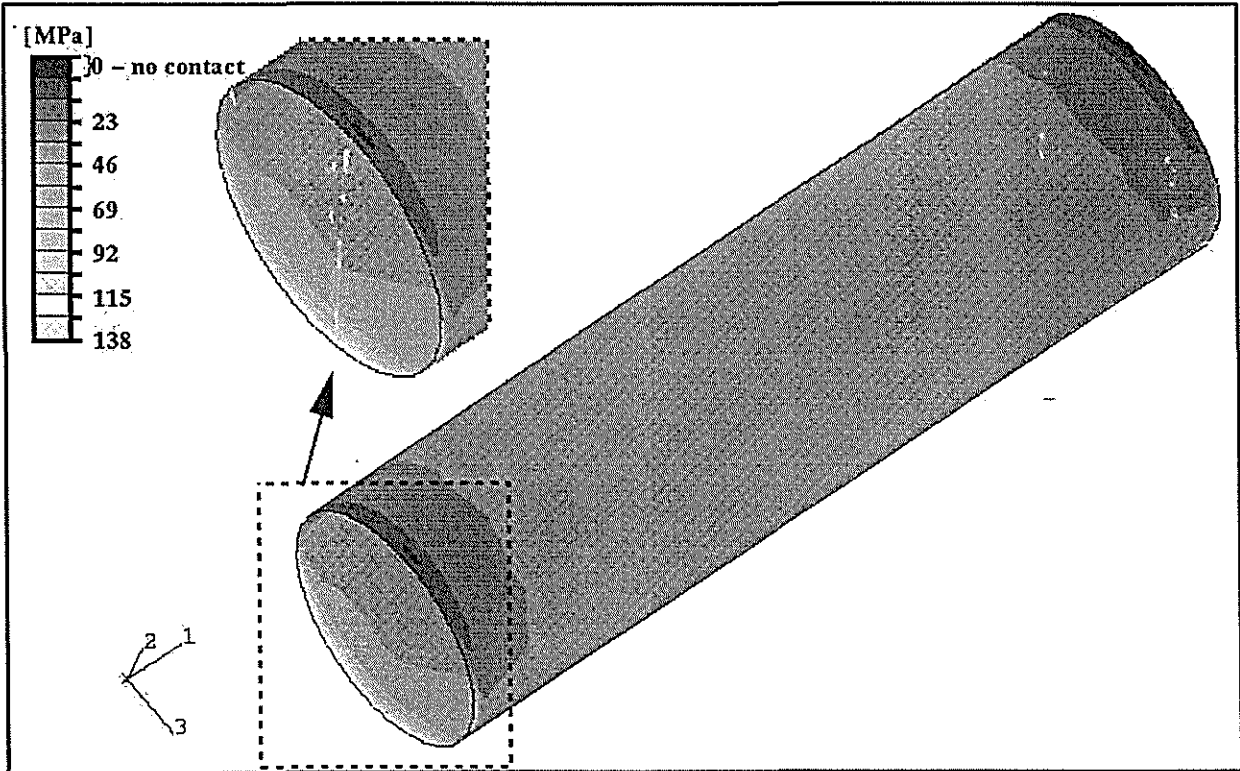


Figure 3.62 Contact pressure on inner shell surface (Raised landing : combined loads).

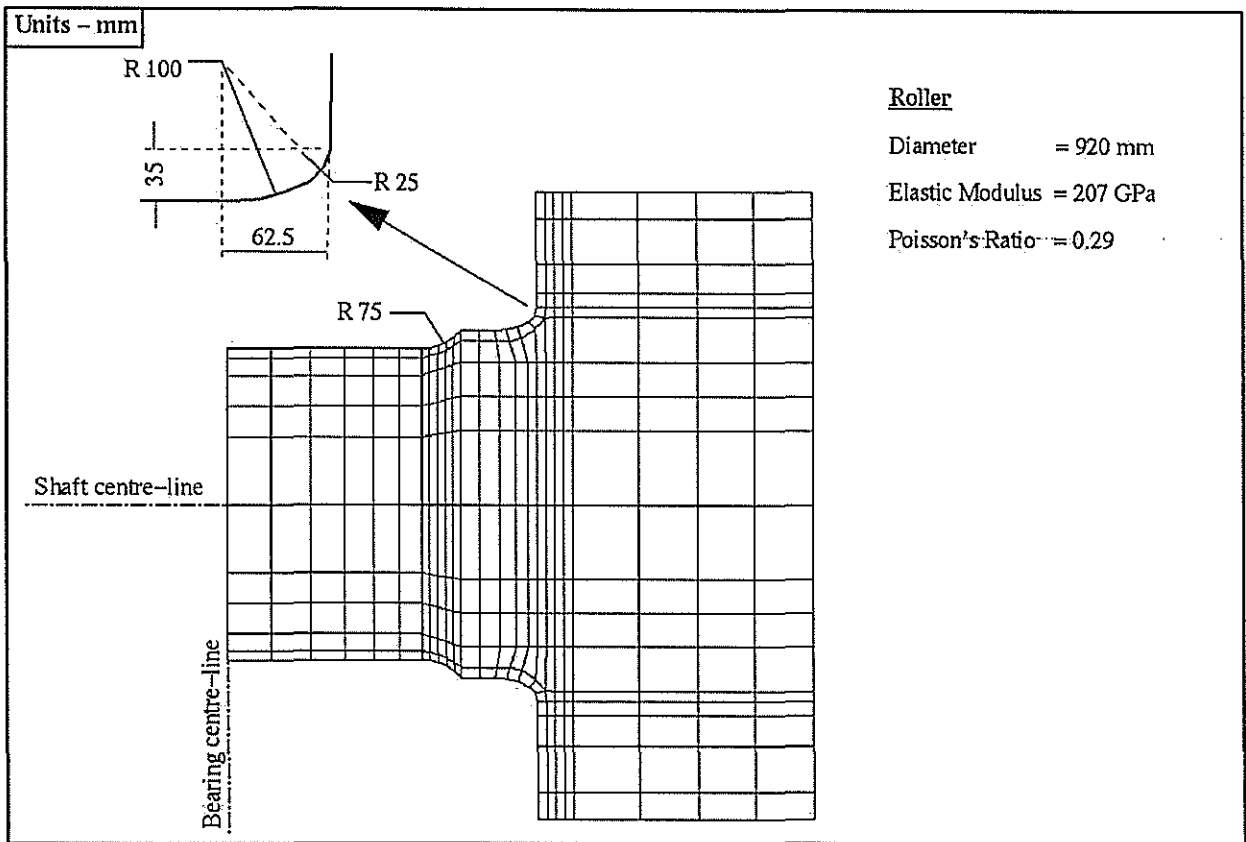


Figure 3.63 Sectioned view of shell-end region for solid roller model.

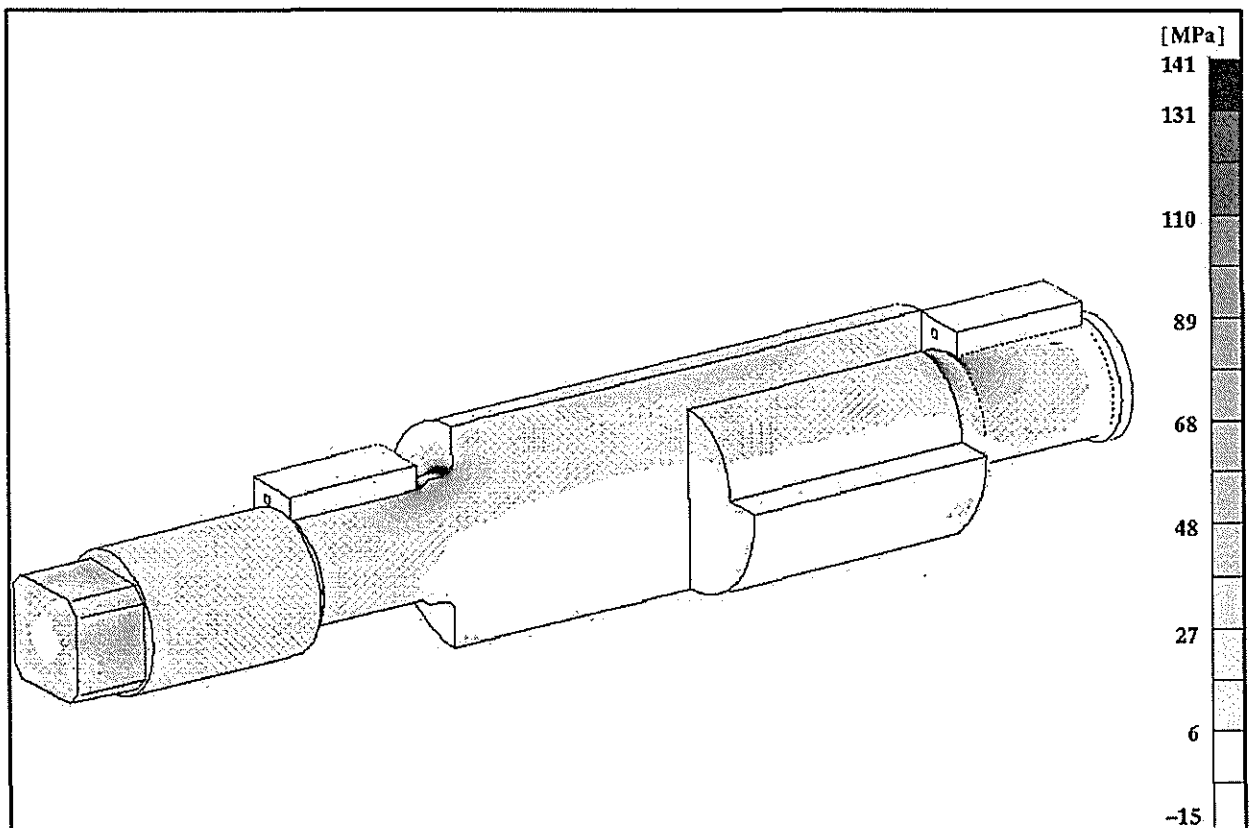


Figure 3.64 Major principal stress plot (Solid roller : combined loads).

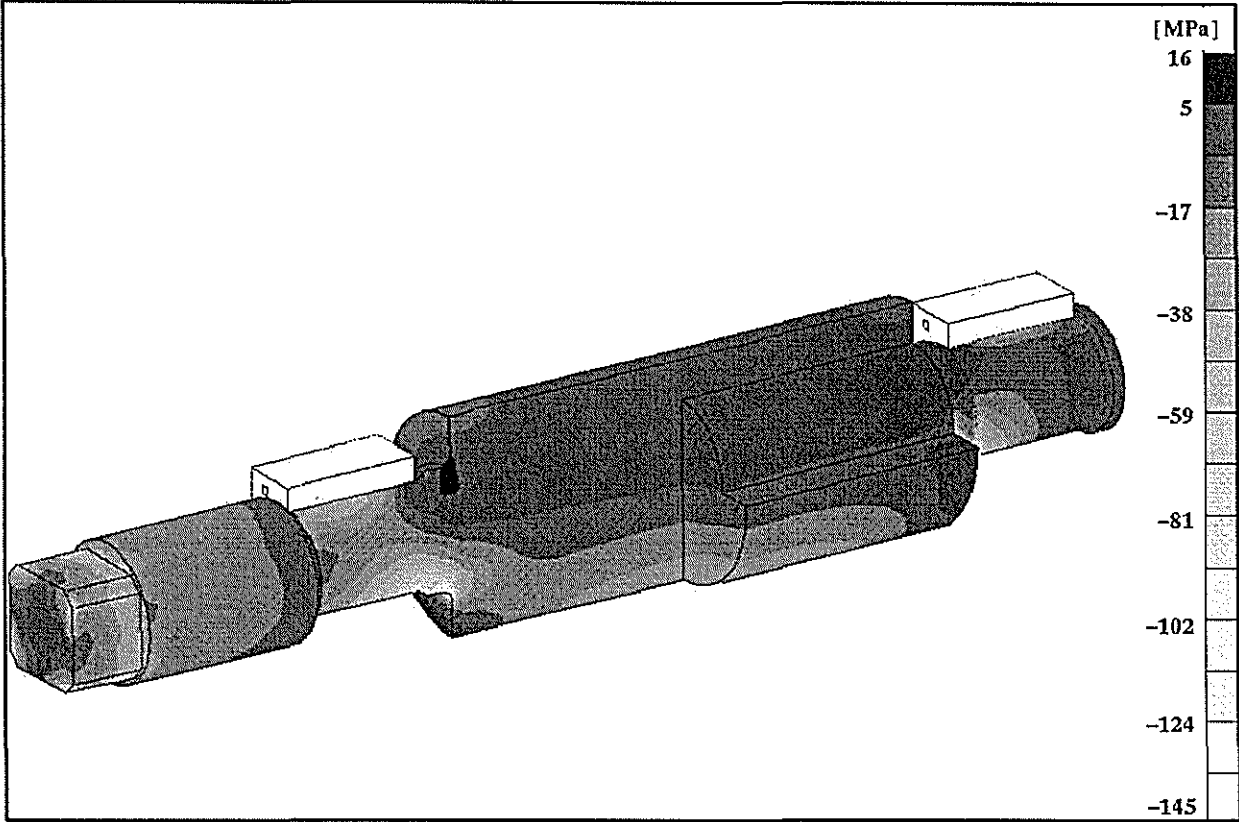


Figure 3.65 Minor principal stress plot (Solid roller : combined loads).

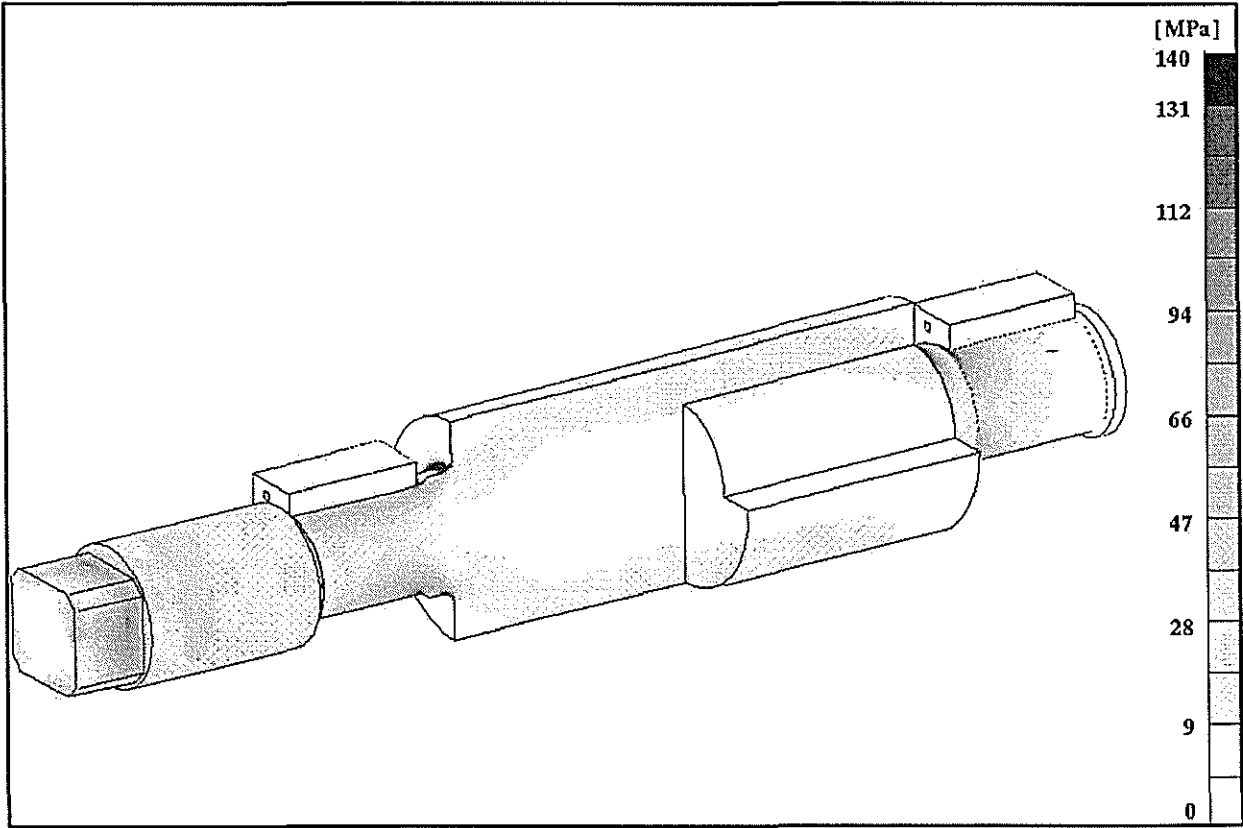


Figure 3.66 Von Mises stress plot (Solid roller : combined loads).

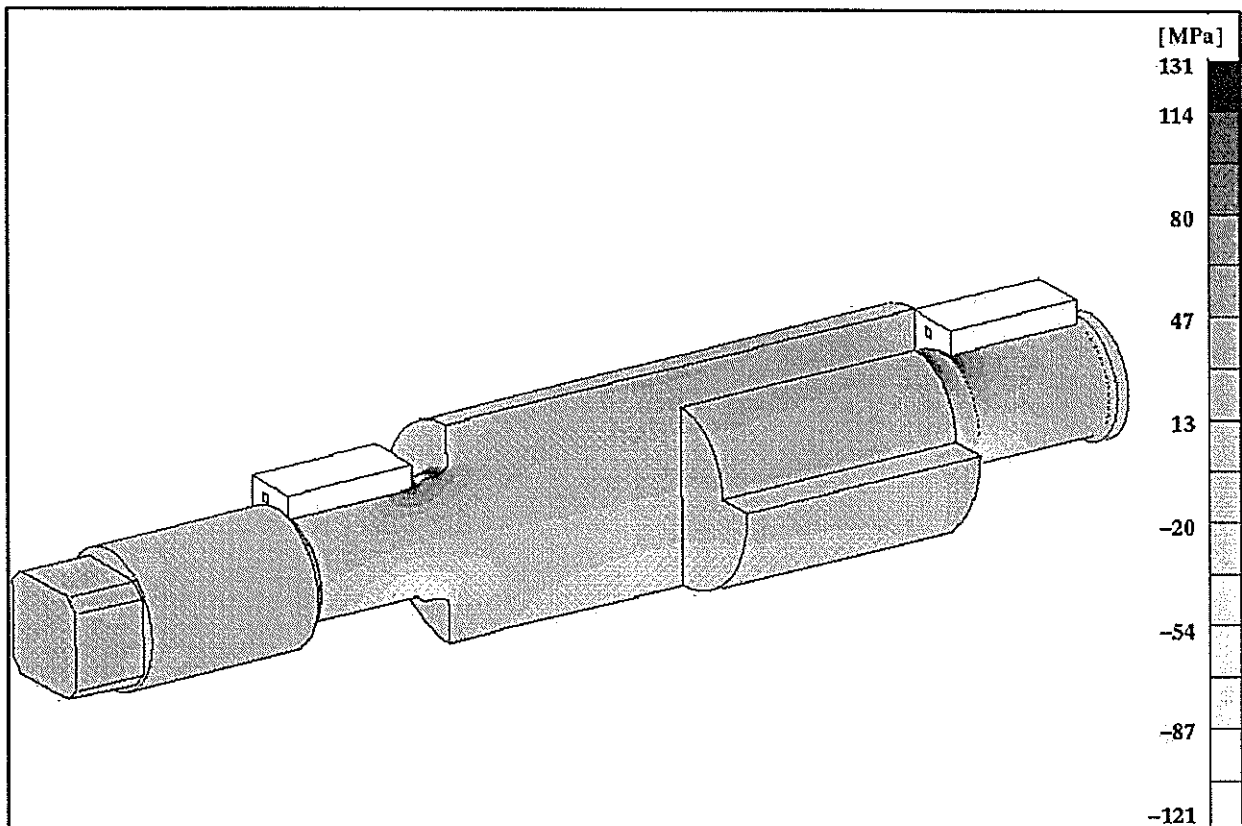


Figure 3.67 Axial stress plot (Solid roller : combined loads).

### 3.3.2 Discussion

The analyses of the ten roller design alternatives were aimed at reducing the overall stress levels, particularly at the inboard fillets and shell-end regions. Results shown pertain to the applied loads: roll load = 70 tonne/ft; tailbar torque = 931 kNm; pinion torque = 363 kNm; and shell traction = 448 kNm. The effect of misalignment loads was not included in the analyses. General discussions of results relating to each alternate design follow. Chapter 3.4 summarises the most plausible of the roller alternatives.

#### Shell materials - 'Stiff Shell' and 'Flexible Shell'

The choice of shell material seems to have little effect on the stress state throughout the roller when compared to the current roller design. The maximum Von Mises stress for the 'stiff shell' and 'flexible shell' analyses were 223 MPa and 185 MPa respectively compared to 203 MPa for the current roller design. The maximum interface pressures between the shell and shaft under full roll loading for the 'stiff shell' and 'flexible shell' analyses were 144 MPa and 113 MPa respectively compared to 123 MPa for the current roller design. Comparison of axial stress levels are listed in Table 3.4. All shell materials trialled showed evidence of shell-end separation from the shaft. On average, the shell material with the lowest elastic modulus resulted in the most acceptable stress levels.

### Inboard fillet - 'Large Fillet'

Replacing the inboard fillets (originally 75 mm) with 150 mm fillets did not significantly reduce stresses in this region when compared to the current roller design. The interface pressures between the shell and shaft under full roll loading were unchanged. Comparison of axial stress levels are listed in Table 3.4. Only the stress state in close proximity to the inboard fillets was affected (reduced) by the introduction of a larger fillet radius.

### Shell-end geometry - 'Small Recess' and 'Large Recess'

Modifying the shell-end geometry in an attempt to reduce the shell-end stress concentration due to the shrink fit also had little effect on the stress state throughout the roller when compared to the current roller design. However, interface pressures did show significant reduction. The maximum interface pressures between the shell and shaft under full roll loading for the 'small recess' and 'large recess' analyses were 87 MPa and 73 MPa respectively compared to 123 MPa for the current roller design. The maximum Von Mises stress for the 'small recess' and 'large recess' analyses were 203 MPa and 173 MPa respectively compared to 203 MPa for the current roller design. Comparison of axial stress levels are listed in Table 3.5. All shell-end geometries trialed showed evidence of shell-end separation from the shaft. On average, the larger shell-end recess resulted in the most acceptable stress levels.

### Adhesives - 'Adhesive (0 mm thickness)' and 'Epoxy (1.0 mm thickness)'

Modelling the replacement of the shrink fit with an adhesive provided an insight to the strength specifications for a candidate adhesive for the application. The maximum Von Mises stress for the 'adhesive' and 'epoxy' analyses were 163 MPa and 139 MPa respectively compared to 203 MPa for the current roller design. The normal interface stress between the shell and shaft under full roll loading for the 'adhesive' and 'epoxy' analyses ranged from 90 to -82 MPa and 88 to -99 MPa respectively compared to 123 and 0 MPa (loss of contact) for the current roller design. The maximum shear stress in the glue-line for the 'adhesive' and 'epoxy' analyses were 87 MPa and 65 MPa respectively. This result indicates that the thickness of the glue-line has an effect on the stress state where an adhesive is used. Comparison of axial stress levels are listed in Table 3.6. Given environmental, creep and fatigue considerations, the stress levels quoted for the glue-line are unacceptably high for adhesives currently on the market.

### Multiple shells - 'Double Shell'

The general theory behind the double shell design is that the permanent inner shell, possibly made of spheroidal graphite iron, can absorb the roll loading whilst the consumable outer shell simply resists wear and provides enough friction to aid effective mill feeding. Using adhesive to attach the outer shell is seen as an opportunity for sugar mills to replace worn shells on site. Modelling this adhesive layer provided an insight to the strength specifications for a candidate adhesive for the application. The maximum Von Mises stress for the 'double shell' analysis was 233 MPa

compared to 203 MPa for the current roller design. The normal interface stress between the shell and shaft under full roll loading for the 'double shell' analysis ranged from 8 to -21 MPa. The maximum shear stress in the glue-line for the 'double shell' analysis was 29 MPa. The stress levels quoted for the glue-line between the outer and inner shells are markedly lower than those for the glue-line in the 'epoxy' analysis. This suggests that use of an adhesive to attach a replaceable outer shell may be an acceptable option. However, environmental, creep and fatigue effects must first be considered. Comparison of axial stress levels are listed in Table 3.6.

#### Modified shell landing - 'Raised Landing'

Increasing the shell landing diameter on the shaft plus the shell's inner diameter did result in reduced stresses in the shell-end region when compared to the current roller design. The maximum Von Mises stress for the 'raised landing' analysis was 143 MPa compared to 203 MPa for the current roller design. The maximum interface pressure between the shell and shaft under full roll loading for the 'raised landing' analysis was 138 MPa compared to 123 MPa for the current roller design. Comparison of axial stress levels are listed in Table 3.7. Note that the axial stress levels are markedly lower under the shell-ends compared to the current roller design. In addition, the separation gap between the shaft and shell-ends has also reduced.

#### One-piece roller - 'Solid'

Combining the shell and shaft geometries together was seen as a future possibility when a suitable wear resistant coating is developed, capable of surviving the current life of mill roller shafts (20 years). This design would intuitively eliminate shell-end failures and shrink fit stresses. The maximum Von Mises stress for the 'solid' analysis was 140 MPa compared to 203 MPa for the current roller design. Comparison of axial stress levels are listed in Table 3.7.

### 3.4 Alternative design summary

Summarising the results pertaining to all alternate roller designs analysed, it can be seen that the current roller design has the potential to be optimised in terms of stress level reduction and hopefully whole-of-life costs. Some general observations are:

1. The choice of cast iron used for the shell manufacture is not critical to the stress state in the roller shaft;
2. Increasing the inboard fillet radius will reduce the stress levels in this region;
3. The addition of shell-end recesses does marginally reduce the shell-end stress concentration;
4. Joining the shell and shaft via adhesive joints appears impractical at this stage;
5. The thickness of the glue-line does affect the strength specification for any adhesive used;
6. Adhesives for use in the double shell design would be worth considering;
7. Introducing a raised landing on the shaft does effectively reduce the shell-end stress concentration effects; and
8. A one-piece roller does appear to be a feasible option from a stress level viewpoint.

Considering separately, the alternative designs analysed show some potential for future mill roller manufacture. However, if combinations of these design techniques were trialled, further benefits to roller life may evolve. Unfortunately, time has not allowed analysis of such combinations. Listed below are some suggested roller designs and the intuitive benefits:

- Shell-end recess and adhesives in place of the shrink fit. Expected benefits include reduced stress in glue-line near shell-end and the elimination of shrink fit induced stresses;
- Large inboard fillets and any other design alternative. Expected benefits include reduced stress levels in both shell-end and fillet regions; and
- Introduced compressive residual stresses during manufacture and any other design alternative. Expected benefits include reduced tensile stress levels in critical regions.

Concluding this chapter, the authors suggests that a roller design which includes large inboard fillets, the raised landing geometry, shell-end recesses and possibly shot peening of the critical regions is the most practical and effective roller design option from a whole-of-life perspective.

# *Chapter 4*

*Durability modelling*

## 4.0 Durability modelling

This chapter reviews durability modelling of the existing roller design. The objective was to provide mill engineers with a simple method to evaluate the structural integrity of a cracked mill roller. A suitable method was chosen and then verified using finite element methods. Comparisons between FEA outcomes and the corresponding results from fracture mechanics theory were made.

The fatigue failure of a component can be classified into two distinct stages, namely; crack initiation and crack propagation to failure. Generally, small cracks are initiated at the surface of a roller shaft from a combination of cyclic bending stresses and surface conditions such as machining defects, corrosion and wear. Ritchie (1994) provided life estimates based on crack initiation times for roller shafts for varying surface conditions (Table 1.1). These small cracks then propagate under repeated loads in a process which can be described using fracture mechanics theory.

Mill rollers are currently designed to survive anticipated maximum roll loads (equation 1.29) based on the S-N approach for determining component life. The S-N approach predicts the entire life of a component, from new to failed, neglecting crack initiation and crack propagation times. Both the S-N approach and crack initiation method are not well suited to life predictions of large diameter shafts (> 150 mm). Size effects and environmental conditions are the major contributors to prediction errors. In addition, both methods cannot predict the remaining life of a cracked component. Therefore, fracture mechanics theory must be used to evaluate the structural integrity and remaining life of a cracked roller.

Reid (1988) examined 93 failed rollers and found that the inboard fillets accounted for approximately 50 per cent of failures and the shell-end region accounted for approximately 40 per cent of failures. From the analyses of the current roller design (Chapter 2), these two regions, both susceptible to the corrosive environment, were found to endure the greatest stress levels. A decision was therefore made to analyse two rollers, the first with an introduced crack in the drive-end inboard fillet and the second with an introduced crack in the shaft under the shell on the drive side (approximately 50 mm from the shell-end face). The purpose of this analysis was to provide an insight into critical crack sizes relating to applied loading conditions for the current mill roller design.

This chapter contains:

1. A brief discussion of fracture mechanics theory applicable to mill roller design;
2. Modelling and results of two cracked rollers (inboard fillet and shell-end cracks); and
3. Discussion of results and method for determining the structural integrity and the estimated remaining life of a cracked mill roller.

## 4.1 Fracture mechanics theory

This section covers basic fracture mechanics theory which can be used for assessing the stability of cracks in mill rollers. The following is an abstract from Anderson and Loughran (1995).

### 4.1.1 Stress intensity theory

Under repeated loads above a certain level, a crack in a structure will grow in time (Broek, 1974). The larger the crack, the higher the stress concentration at the crack tip. Hence, the crack propagation rate should increase with time (Figure 4.1). The presence of a crack reduces the strength of the structure. The residual (remaining) strength decreases progressively as the crack size increases (Figure 4.2) and may decrease to a level where the structure would fail from an unexpected high service load. If such a load was not experienced, the crack would continue to grow whilst reducing the residual strength until it became so low that failure (fracture) would occur under normal service loading. In general, design engineers should account for the possibility of fatigue in structures. To ensure safety, a prediction of how fast cracks propagate (ie. how fast the residual strength decreases) needs to be made. Such predictions can be made by applying the theory of fracture mechanics.

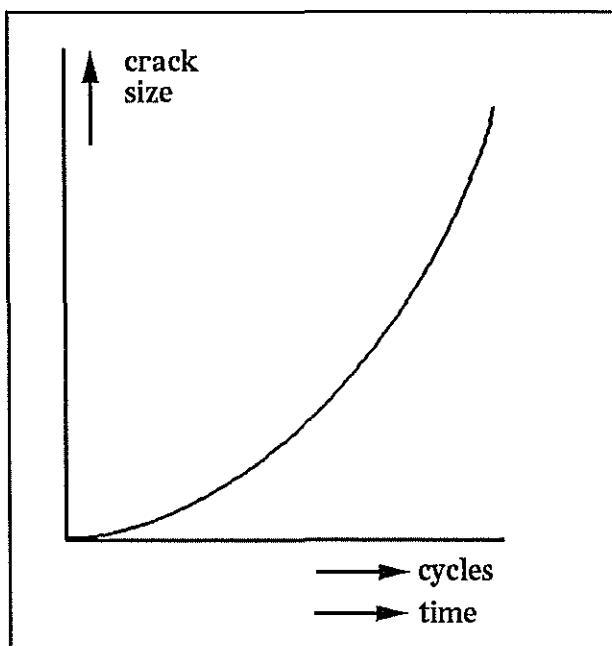


Figure 4.1 Crack growth curve, (after Broek, 1974).

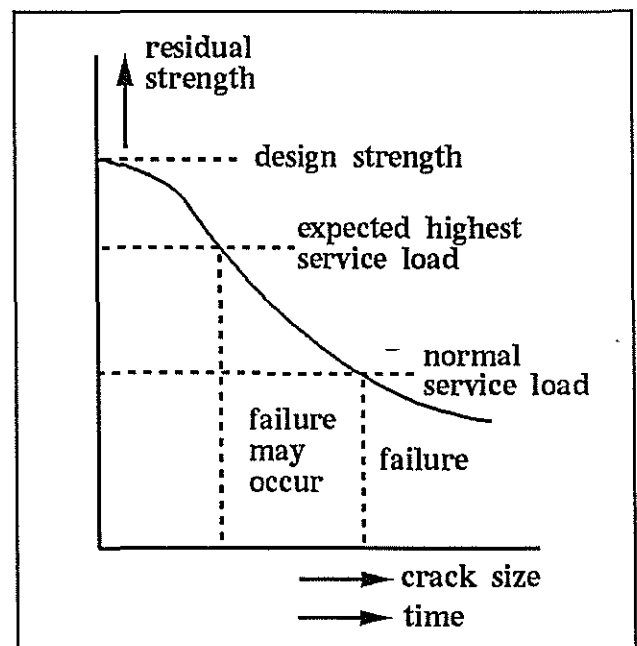


Figure 4.2 Residual strength curve, (after Broek, 1974).

A crack in a solid can be stressed in one or a combination of three different modes (Figure 4.3). From a practical viewpoint, the most common of these modes is the opening mode 'Mode I' (Broek, 1974).

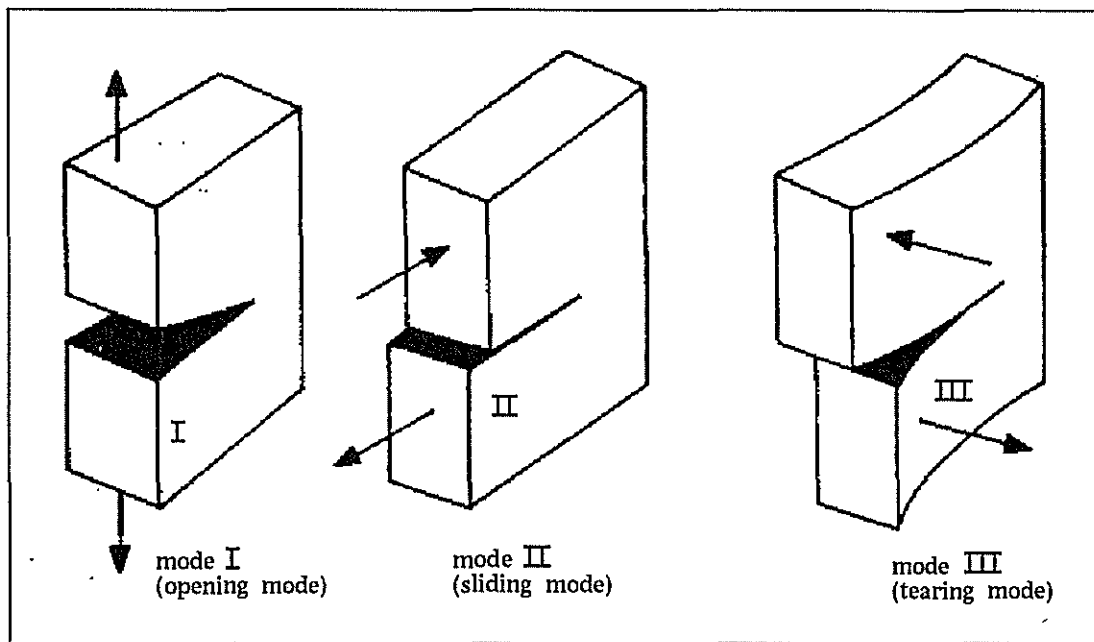


Figure 4.3 The three modes of loading (after Broek, 1974).

The elastic stress field ( $\sigma_{ij}$ , remote from the crack tip (position  $r$ ,  $\theta$ )) of a 'through the thickness' crack in an arbitrary body experiencing a mode I loading (Figure 4.4) can be expressed as:

$$\sigma_{ij} = \frac{K_I}{\sqrt{2\pi r}} f_{ij}(\theta) \quad (4.1)$$

where  $f_{ij}(\theta)$  are known functions of  $\theta$ , and  $K_I$  is the stress intensity factor for mode I loading. Similar solutions are obtained for the other modes but with differing  $\theta$  functions.

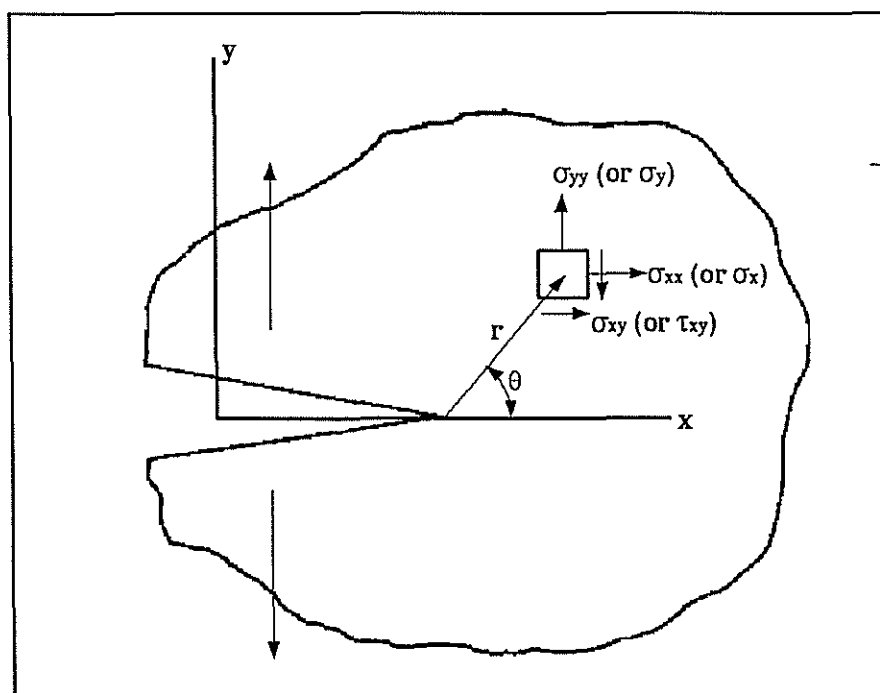


Figure 4.4 Crack in arbitrary body. (after Broek, 1974)

Combining the situation of an infinite plate under constant load or stress  $\sigma$  (Figure 4.5) with a central crack of length  $2a$  and applying equation 2.1 gives:

$$K_I = \beta \sigma \sqrt{a} \quad (4.2)$$

If, however, the width of the plate (Figure 4.5) is finite (of width  $W$ ), the crack tip stresses would increase from the case of the infinite plate. This suggests that  $K_I$  must increase with a decrease in  $W$ . Therefore equation 4.2 should be modified to include a function of crack length divided by the width  $W$  for the case of the finite plate. Usually the stress intensity factors are expressed in relation to the stress intensity of the infinite plate mentioned previously, and therefore equation 4.2 becomes:

$$K_I = \beta \left( \frac{a}{L} \right) \sigma \sqrt{\pi a} \quad (4.3)$$

where  $L$  is a generalised size parameter and  $\beta \left( \frac{a}{L} \right)$  is a geometry function.

The entire crack tip stress field can be described once the function  $\beta \left( \frac{a}{L} \right)$  is known. The fact that the net section stress increases with decreasing  $W$  is accounted for in  $\beta$ .

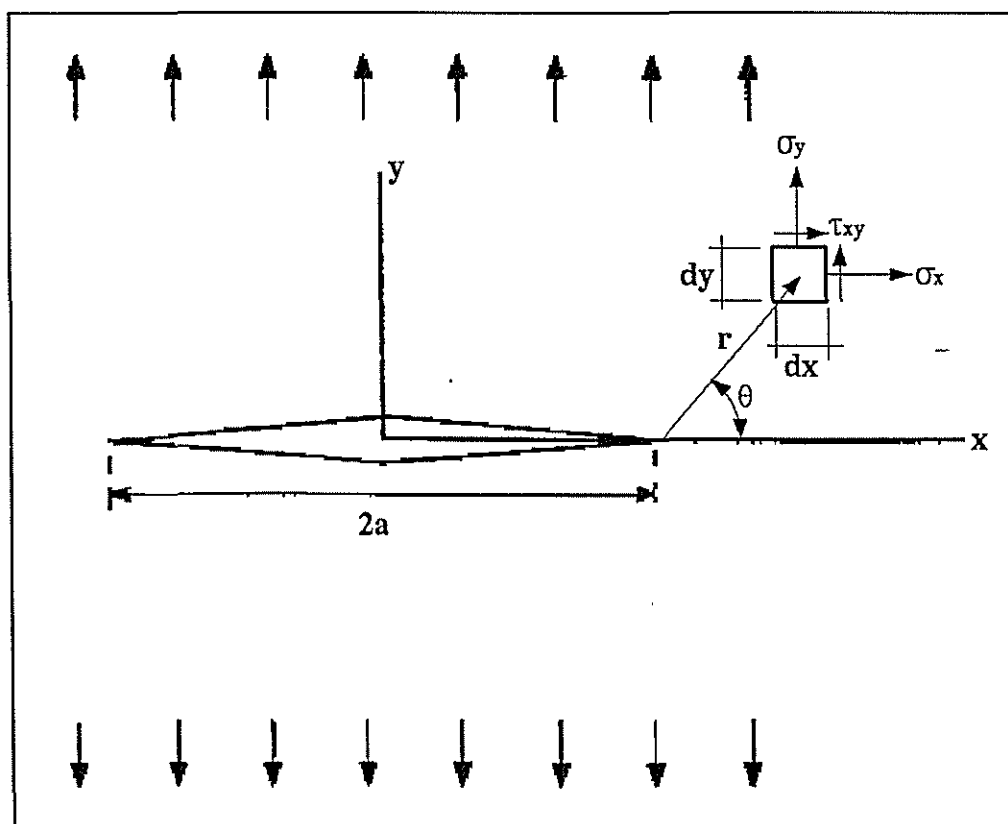


Figure 4.5 Crack in an infinite plate. (after Broek, 1974).

The function  $\beta$  has been estimated for many geometries. Geometry functions are generally written as high order polynomials such as:

$$\beta = C_1 + C_2\left(\frac{a}{L}\right) + C_3\left(\frac{a}{L}\right)^2 + C_4\left(\frac{a}{L}\right)^3 + C_5\left(\frac{a}{L}\right)^4 \dots \quad (4.4)$$

Tada et al (1985) list the theoretical geometry functions for a shaft containing a circumferential crack under various loading conditions (Figure 4.6). Important parameters required when calculating the geometrical function and then the stress intensity include:

- a - depth of the circumferential crack;
- d - diameter of the remaining shaft ligament;
- D - diameter of shaft;
- P - axial load transferred through shaft at crack location;
- M - bending moment at crack location; and
- T - torsion load at crack location.

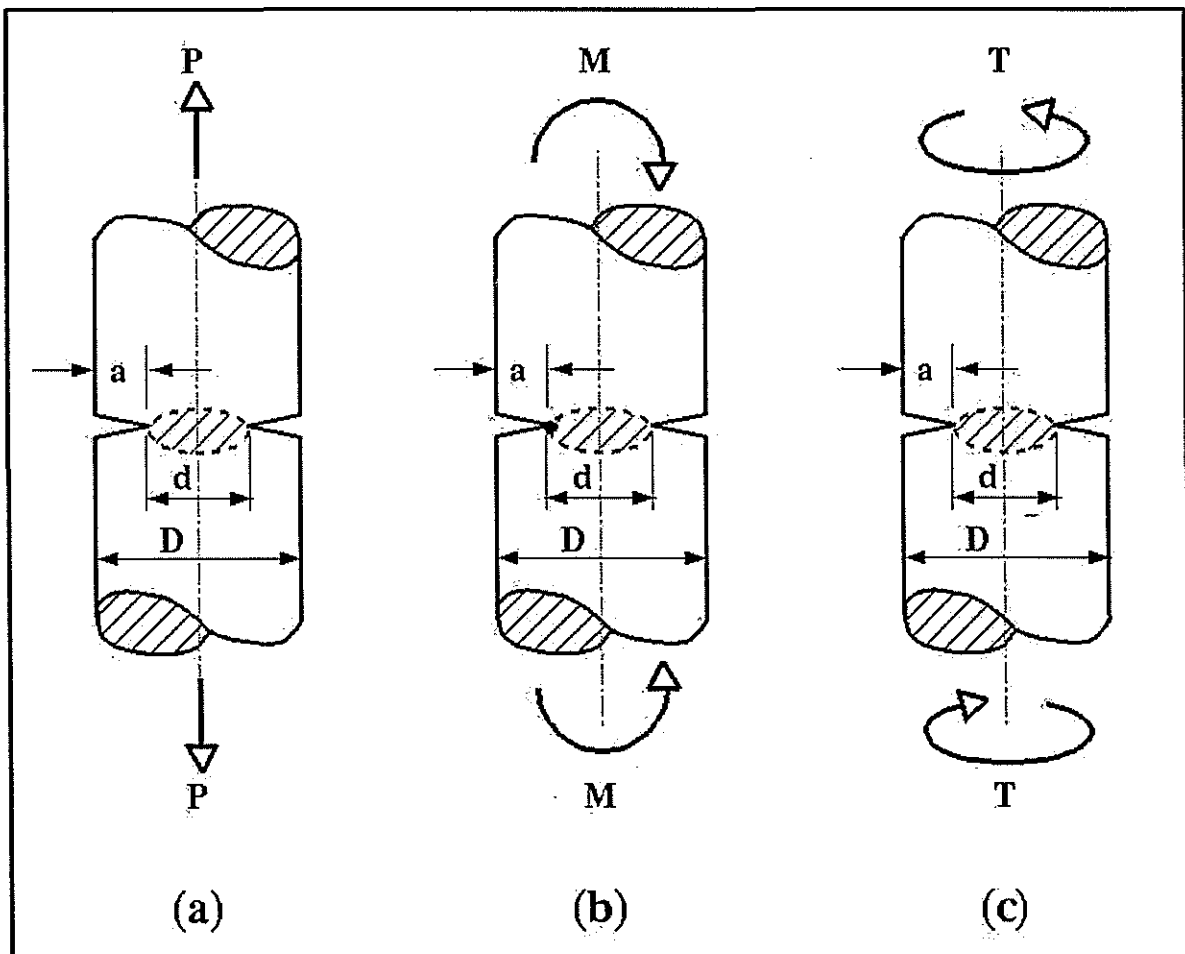


Figure 4.6 Circumferential crack in a cylinder under various loading conditions, (a) axial, (b) bending moment and (c) torsion.

Applying equation 4.3 with  $K_{II}$  and  $K_{III}$  equal zero for the 'Axial' case (Figure 4.6 (a)):

$$\sigma = \frac{4P}{\pi d^2} \quad \text{and}$$

$$\beta = 0.5 \left(\frac{d}{D}\right)^{\frac{1}{2}} + 0.25 \left(\frac{d}{D}\right)^{\frac{3}{2}} + 0.1875 \left(\frac{d}{D}\right)^{\frac{5}{2}} - 0.1815 \left(\frac{d}{D}\right)^{\frac{7}{2}} + 0.3655 \left(\frac{d}{D}\right)^{\frac{9}{2}}$$

Likewise for the 'Bending moment' case (Figure 4.6 (b)):

$$\sigma = \frac{32M}{\pi d^3} \quad \text{and}$$

$$\beta = 0.375 \left(\frac{d}{D}\right)^{\frac{1}{2}} + 0.1875 \left(\frac{d}{D}\right)^{\frac{3}{2}} + 0.1406 \left(\frac{d}{D}\right)^{\frac{5}{2}} + 0.1172 \left(\frac{d}{D}\right)^{\frac{7}{2}} \\ + 0.1025 \left(\frac{d}{D}\right)^{\frac{9}{2}} + 0.2014 \left(\frac{d}{D}\right)^{\frac{11}{2}}$$

However, for the 'Torsion' case (Figure 4.6 (c)), a modified equation 4.3 ( $K_{III} = \beta \tau \sqrt{\pi a}$ ) with  $K_I$  and  $K_{II}$  equal zero can be applied:

$$\tau = \frac{16T}{\pi d^3} \quad \text{and}$$

$$\beta = 0.375 \left(\frac{d}{D}\right)^{\frac{1}{2}} + 0.1875 \left(\frac{d}{D}\right)^{\frac{3}{2}} + 0.1406 \left(\frac{d}{D}\right)^{\frac{5}{2}} + 0.1172 \left(\frac{d}{D}\right)^{\frac{7}{2}} \\ + 0.1025 \left(\frac{d}{D}\right)^{\frac{9}{2}} + 0.078 \left(\frac{d}{D}\right)^{\frac{11}{2}}$$

When the stress intensity of a crack reaches a certain value for that particular material, it will rapidly propagate causing component failure. Similarly, if the stress intensities for two cracked bodies (different physical size and crack size but of the same material) are equal then there is exact similitude. In other words, an equal stress intensity signifies similitude in stress at the crack tip.

The stress intensity at which a cracked component fails is known as the fracture toughness (or critical stress intensity) for that material. Although, the fracture toughness varies with temperature and environmental conditions, these are of second order importance compared to component thickness (Broek, 1974). The thickness of a component affects the fracture toughness value as the out-of-plane stresses (dependent on the thickness) determine the final size of the plastic zone at the crack tip.

The presence of this additional stress at the crack tip affects the size of the plastic zone and stress field in front of the crack tip. Hence, the response of the crack changes depending on the thickness of the component. For cracks in thin section components there is no restriction of the contraction of the crack tip plastic zone and this is referred to as 'plane stress'. In contrast where

there is restriction of the crack tip plastic zone (eg cracks in thick section plate), this is referred to as 'plane strain'. The plane strain plastic zone is markedly smaller than the plane stress plastic zone. The effective yield stress in plane strain can be as high as three times the uniaxial yield stress (Broek, 1974).

For plane strain to exist along the majority of a crack tip front, the component thickness must be adequately large. For example, the thickness of a cracked plate ( $B_s$ ) to ensure the condition of plane strain is :

$$B_s \geq 2.5 \left( \frac{K_I}{\sigma_{ys}} \right)^2 \quad (4.5)$$

where  $K_I$  is the applied stress intensity and  $\sigma_{ys}$  is the yield stress for the material. The fracture toughness is given the notation  $K_{IC}$  to represent mode I cracking. The dependency of  $K_{IC}$  and residual strength, upon thickness is shown in Figures 4.7 and 4.8. It can be seen that  $K_{IC}$  reaches a constant level after a certain thickness is obtained. The lower value for  $K_{IC}$  will be used in this research to ensure conservative results when predicting the behaviour of cracks in roller shafts.

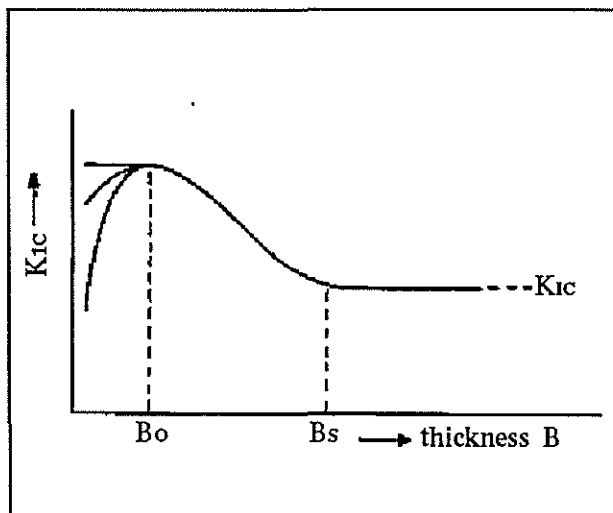


Figure 4.7  $K_{IC}$  vs. thickness.  
(after Broek, 1974).

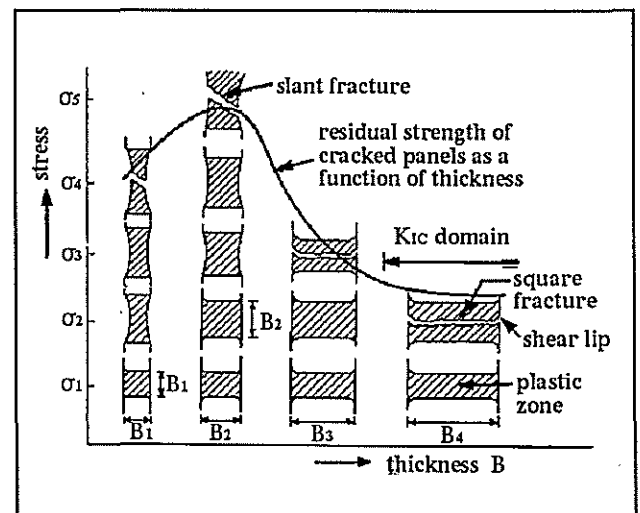


Figure 4.8 Residual strength vs. thickness.  
(after Broek, 1974).

As previously mentioned, Tada et al (1985) provided geometry functions and hence a method for approximating the stress intensity for cracked shafts under various loading conditions. Numerical methods will be applied to cracked roller models for comparison with these theoretical solutions. The non-linear analysis computer code 'ABAQUS (standard)' employs crack-tip finite elements enabling three dimensional geometries and included cracks to be analysed. ABAQUS utilises the energy release theory for propagating cracks to calculate stress intensity values. Following Broek (1974), if a crack length is increased by a small amount, the energy released per unit area of crack extension, ( $G$ ), is given by :

$$G_I = \left( \frac{\partial U}{B \partial a} \right) \quad (4.6)$$

where B is the thickness of the component and U is the potential energy. The stress intensity and the energy release rate have the following relationship (Suresh, 1991):

$$G_I = \frac{K_I^2}{E} \quad (\text{plane stress}) \quad (4.7)$$

or

$$G_I = \frac{K_I^2 (1 - \nu^2)}{E} \quad (\text{plane strain}) \quad (4.8)$$

or

$$G = G_I + G_{II} + G_{III} = \frac{(1 - \nu^2) (K_I^2 + K_{II}^2)}{E} + \frac{(1 + \nu) (K_{III}^2)}{E} \quad (\text{combined case}) \quad (4.9)$$

ABAQUS calculates a J-Integral value (contour integral surrounding the crack tip) to determine the energy release rate  $G_I$  (J-Integral value =  $G_I$ ). This J-Integral calculation is a useful method for evaluating stress intensities. The plane strain equation will be used in this research to ensure conservative results when predicting the behaviour of cracks in roller shafts.

#### 4.1.2 Crack propagation theory

From equation 4.3, it is possible to predict the crack length for which a certain load would cause component failure if the fracture toughness was known and vice versa. The time it takes for a crack to reach a critical length for a known loading history is also of importance to a designer. Computer codes (eg. PFATIGUE, NSOFT) can be used to assess the propagation of a crack in a structure. These codes utilise the relationship between the increase in crack length per loading cycle and the change in the stress intensity per loading cycle. The basic form of this relationship as proposed by Paris in 1966 is based on experimental work carried out on pre-cracked samples of material. The Paris Law (equation 4.10) in simplistic form, is obtained from the straight line section shown in Figure 4.9 which is representative of a steady state crack growth region.

$$\frac{da}{dN} = C(\Delta K)^m \quad (4.10)$$

where C and m are proposed material constants and N is the number of repeated load cycles. Equation 4.10 is based on the case where the repeated loads are tensile (positive).

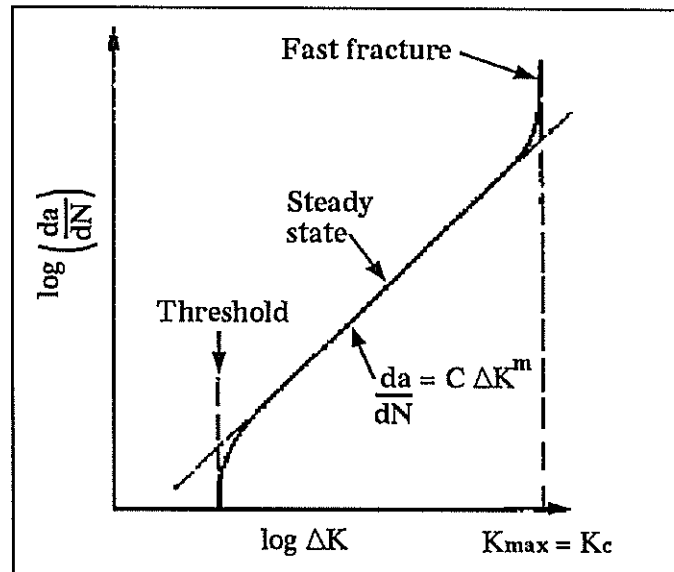


Figure 4.9 Common fatigue crack-growth rates.  
(after Ashby *et al*, 1982)

From Figure 4.9, it can be seen that the crack growth rate remains at zero (no crack growth) until the change in stress intensity for a load cycle surpasses a threshold level. This threshold stress intensity level varies for different materials. Also of interest is the rapid increase in crack growth rate when the maximum stress intensity during a load cycle approaches or equals the fracture toughness value for a given material. At this point rapid failure occurs. Figure 4.10 illustrates the steady state growth of a crack and the increase in stress intensity for a cracked component under constant positive load cycling.

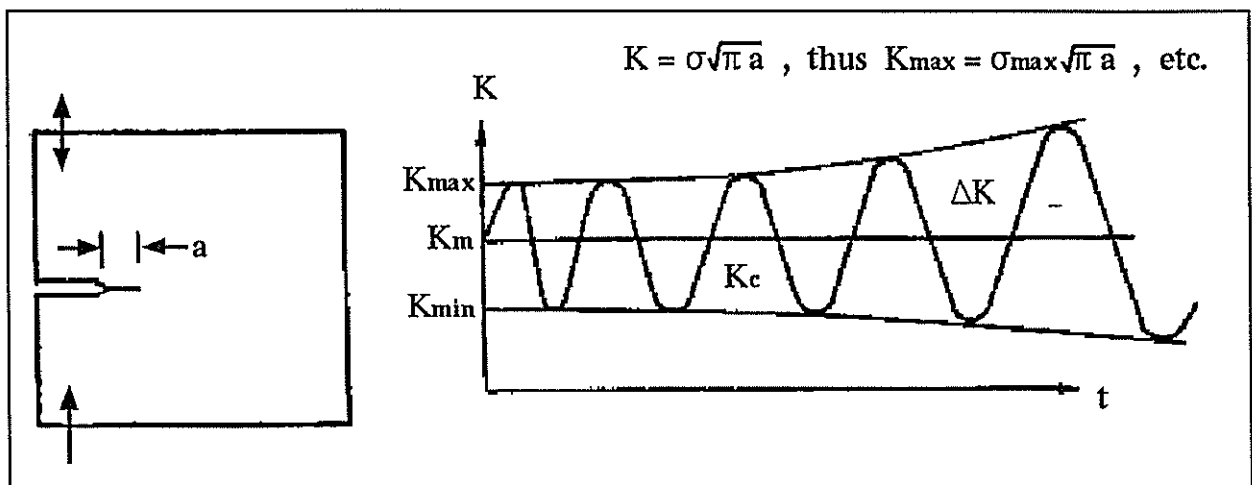


Figure 4.10 Example of fatigue crack growth.  
(after Ashby *et al*, 1982)

There often exists a minimum crack size (short crack parameter) in components of a certain material and loading condition for which fracture mechanics theory is not applicable. According to Figure 4.9, the rate of propagation reduces significantly (assumed 0) when the operating stress

intensity range ( $\Delta K$ ) falls below the material's threshold stress intensity level ( $K_{th}$ ). Figure 4.11 shows the 'Kitagawa Diagram' which relates threshold stress and threshold stress intensity to fatigue crack size. Equation 4.3 can then be altered to determine the short crack parameter ( $l_o$ ) as follows:

$$l_o = \frac{1}{\pi} \left( \frac{\Delta K_{th}}{\Delta \sigma_o} \right)^2 \quad (4.11)$$

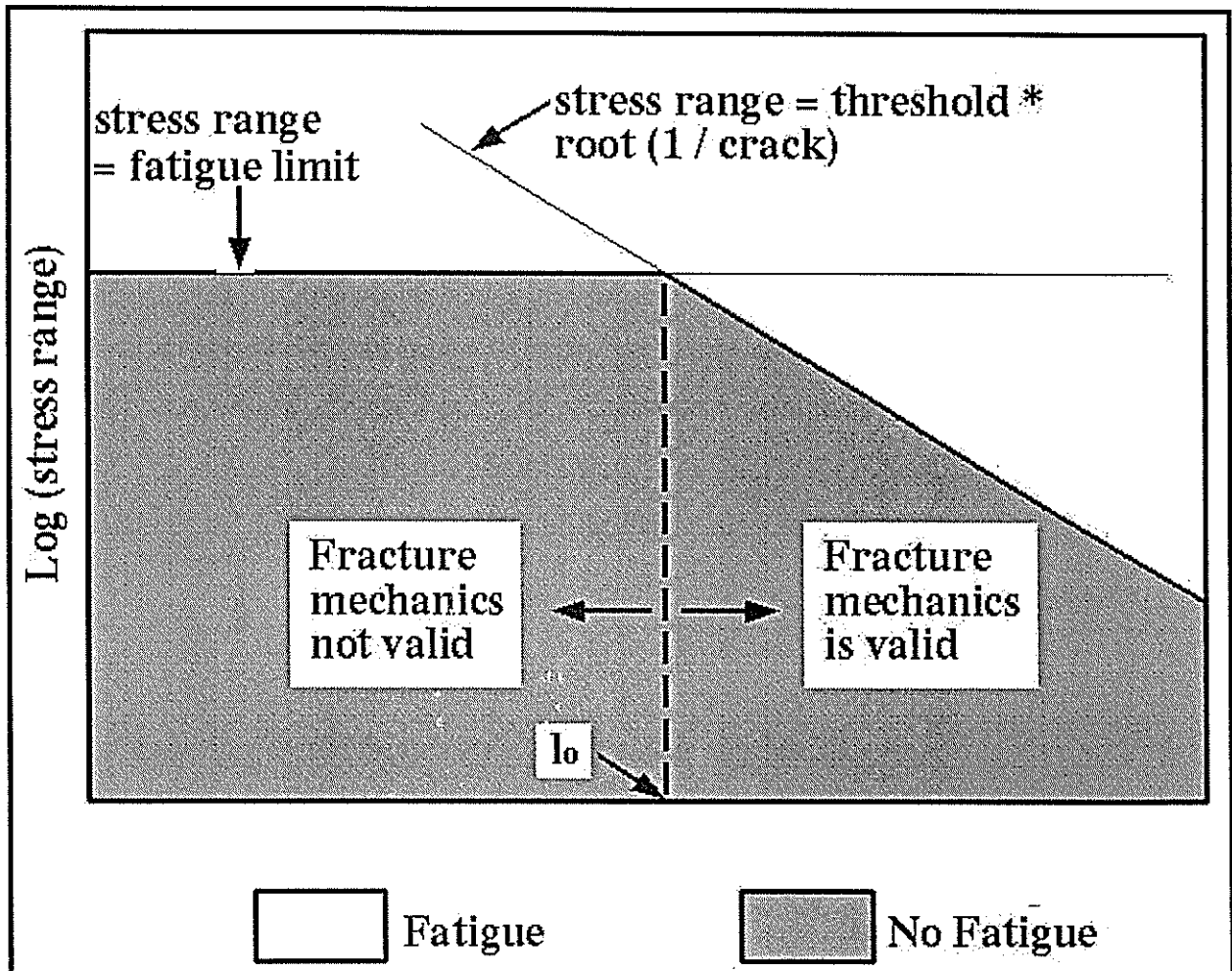


Figure 4.11 Example of 'Kitagawa Diagram' for fatigue.  
(after Anon., 1993)

In Figure 4.10, the cyclic stress intensity increases with time as one would expect as the crack length, and hence the geometry function parameter increase. Therefore, for a cracked specimen undergoing repeated constant load cycles, the rate of crack growth continually increases until the crack reaches the critical crack length, at which point the maximum stress intensity equals the fracture toughness and rapid failure occurs. A cycle by cycle fatigue crack propagation prediction code such as PFATIGUE calculates the crack extension for each load cycle in a load history and adds it to the current crack size. This process is repeated until the crack reaches the critical crack length. As previously mentioned, the driving force for crack propagation is the stress intensity

range ( $\Delta K$ ). For each load cycle the  $\Delta K$  calculated from the stress range, crack size and geometry function is known as the 'apparent or applied  $\Delta K$ '. To improve accuracy when using the Paris Law, this 'applied  $\Delta K$ ' is modified to obtain an 'effective  $\Delta K$ ' which accounts for the possible occurrence of crack closure, residual stresses, notch and environmental effects and negative loading ratios during each load cycle. Crack propagation life can therefore be accurately modelled but only on a cycle by cycle basis. Smith (1991) provides a simple method based on the Paris Law for estimating the propagation rate for a crack (equation 4.12) without the need for expensive computer codes.

$$N = \int_{a_i}^{a_f} \frac{1}{C(\Delta K)^m} da \quad (4.12)$$

where  $a_i$  = initial crack length  
 $a_f$  = final crack length

Rearranging equation 4.12, it becomes:

$$N = \frac{1}{C(\Delta\sigma\sqrt{\pi})^m} \int_{a_i}^{a_f} \frac{1}{\beta^m a^{m/2}} da \quad (4.13)$$

Assuming  $\beta$  does not change considerably (feasible for small crack extensions) and  $m$  does not equal 2, then equation 4.13 becomes:

$$N = \frac{1}{C(\beta\Delta\sigma\sqrt{\pi})^m} \left[ \frac{a_i^{1-m/2} - a_f^{1-m/2}}{m/2 - 1} \right] \quad (4.14)$$

Accuracy for calculating the number of cycles required for a crack to extend from  $a_i$  to  $a_f$  can be achieved by applying equation 4.14 to several crack extension increments between the initial and final crack lengths and summing the resultant load cycle numbers. This method adopts the updated geometry function values for each increment and hence provides a more realistic cycle estimation.

## 4.2 Stress intensity prediction - 3D finite element modelling

This section reports on the analysis results of two cracked roller shafts using a combination of finite element methods and basic fracture mechanics theory. An estimation of crack propagation rates for each roller under nominal operating loads is included.

### 4.2.1 Model parameters and techniques

The modelling singularity at a crack tip cannot be modelled accurately using conventional finite elements (Goldthorpe, 1992). Nevertheless, it is desirable to model the rapid rise in stress in this region. A more accurate solution for the overall behaviour of the structure and stress intensity at the crack tip is possible using 'quarter-point' elements around the included crack. In 3D fracture analyses, a ring of 20-node isoparametric brick elements surrounding the crack tip is required. One face from each element at the crack tip is degenerated onto the crack front and the mid-side nodes connected to the crack tip are positioned one quarter of the way along the edge from the tip. 'Quarter-point' elements are beneficial as they reduce the need for excessive mesh refinement at the crack tip. Goldthorpe (1992) suggests that the radial extent of the crack tip elements should be no less than 2 per cent and no more than 10 per cent of the crack length.

Two cracked mill rollers were analysed. To avoid complete rebuilding of the roller model to include the circumferential cracks and the associated elements (20-node brick elements), simple modifications to the model (8-node brick elements) used throughout Chapter 2 analyses were made. The 'fillet crack' model (Figure 4.12) has a 50 mm crack located at the transition of the drive-end inboard fillet. The 'landing crack' model (Figure 4.16) has a 50 mm crack located 50 mm in from the shell-end on the drive-end of the roller shaft. The modified sections for both rollers where 20-node elements replaced the existing 8-node elements are shown.

The transition surface between the 8 and 20-node elements will result in localised stress distribution errors. However, this transition is not anticipated to affect the J-integral calculations at the crack tips for either model. Loading used in Chapter 2 analyses (70 tonne/ft roll load and 931 kNm tailbar torque) was applied to both crack roller models. Misalignment loading (324 kN downward radial force and 425 kNm counter-clockwise moment) was applied to the shaft square to investigate the effect of roll lift on crack tip stress intensity factor. Figures 4.13 through 4.15 show the Von Mises stress distribution for the all loading cases applied to the 'fillet crack' model. Note, the yielding limit was set at 250 MPa for Von Mises plots. This value does not influence the J-integral values resulting from the analyses. Figures 4.17 through 4.19 show the Von Mises stress distribution for all loading cases applied to the 'landing crack' model.

J-integral values relating to a small crack advance perpendicular to the roller's axis were recorded for all loads applied to each model. Equation 4.8 relating to plane strain conditions was used to convert the J-integral values into an estimated mode I stress intensity factor (Table 4.1). Theoretical stress intensity factors derived using equation 4.3 corresponding to the bending moment loads (Appendix A5) are also listed in Table 4.1 for comparison.

Table 4.1 Plane strain stress intensity factors for the cracked roller models (fillet and landing).

Model	Loading case.	FEA stress intensity factor. [MPa.m <sup>0.5</sup> ]	Theoretical stress intensity factor. [MPa.m <sup>0.5</sup> ]
fillet	roll load only	48.3	40.7
fillet	roll and torsional loads	49.8	40.7
fillet	roll, torsional and misalignment loads	95.1	86.0
landing	roll load only	53.9	49.9
landing	roll and torsional loads	53.9	49.9
landing	roll, torsional and misalignment loads	82.7	78.9

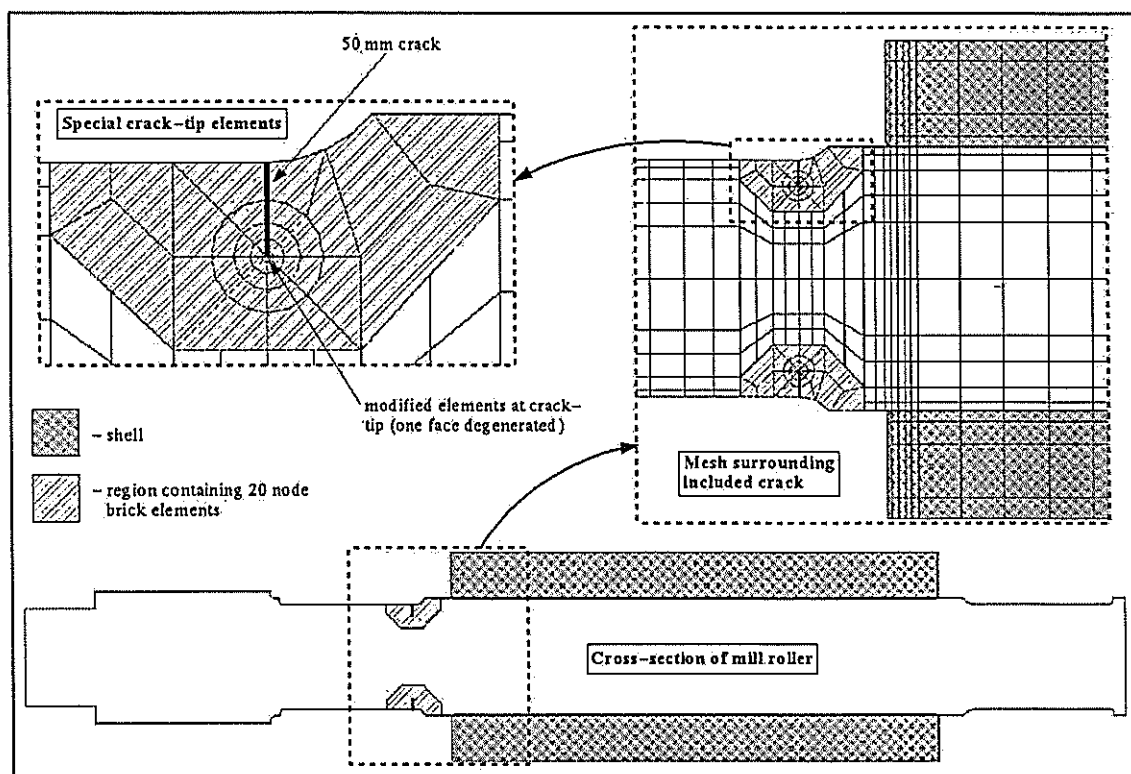


Figure 4.12 Sectioned view of the 'fillet crack' roller model.

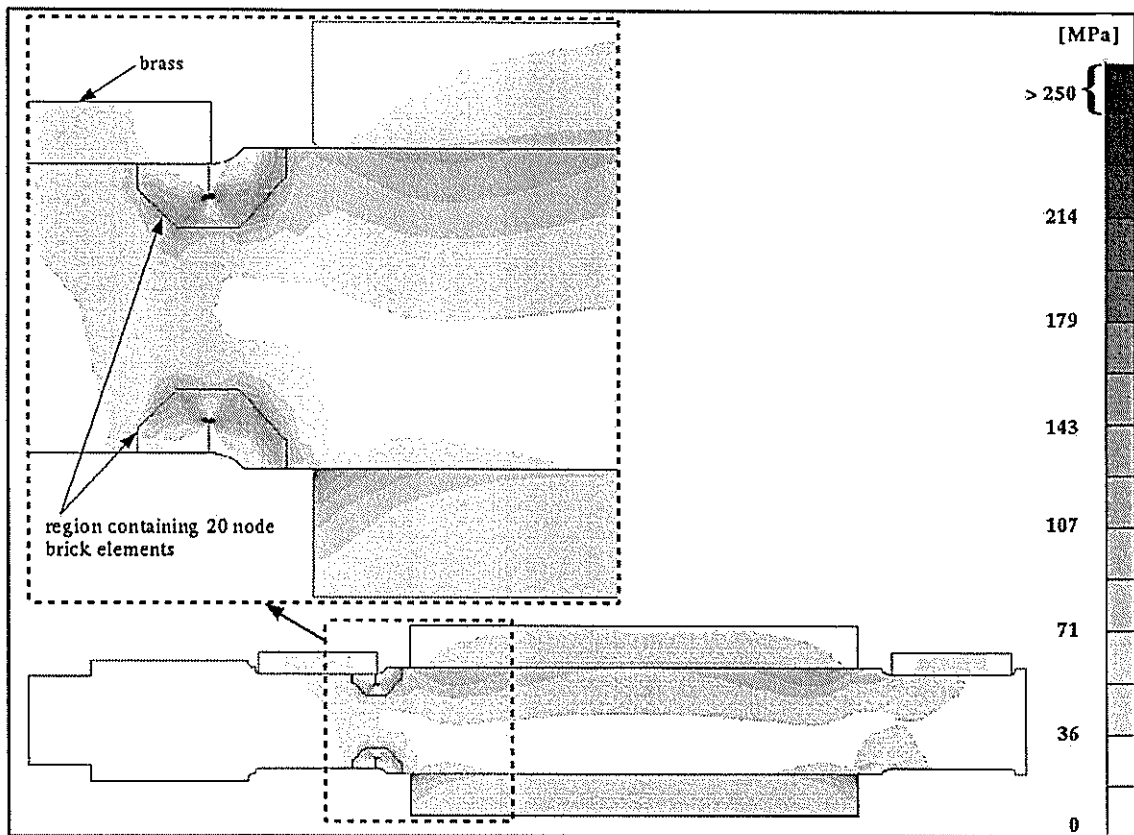


Figure 4.13 Von Mises stress plot ('fillet crack' - roll load only).

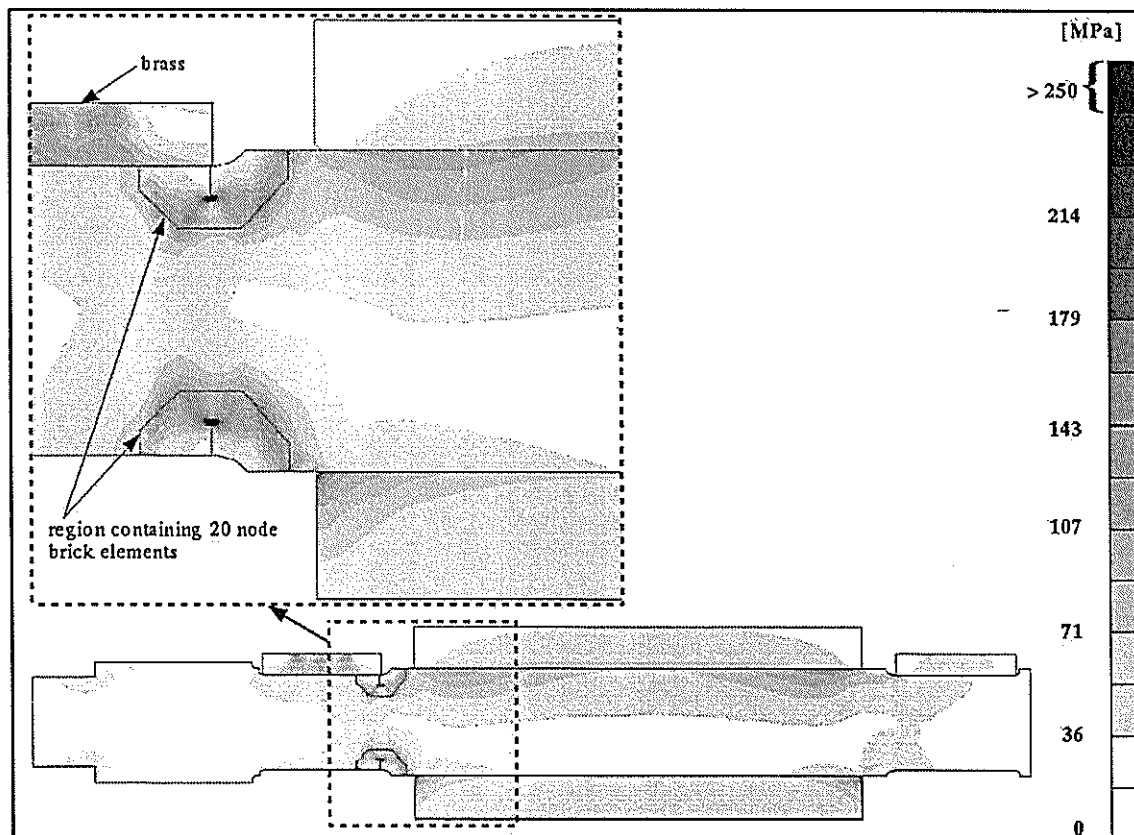


Figure 4.14 Von Mises stress plot ('fillet crack' - roll and torsional loads).

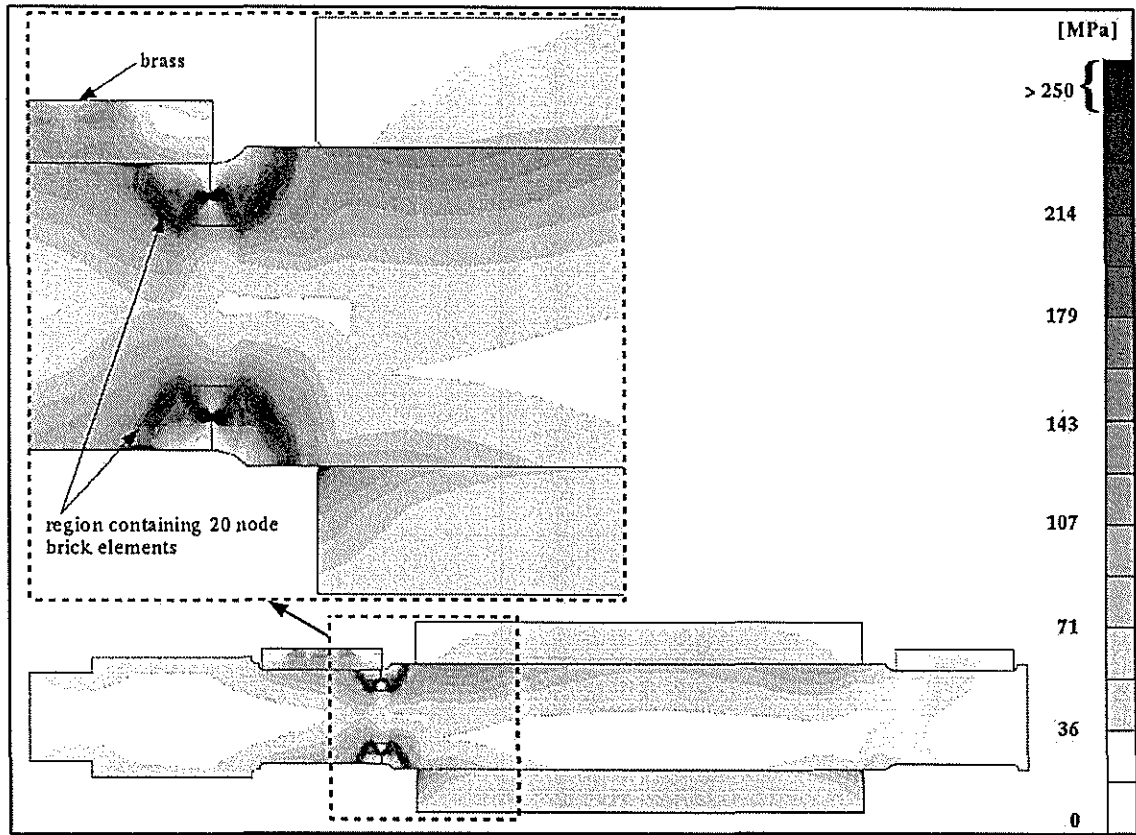


Figure 4.15 Von Mises stress plot ('fillet crack' - roll, torsional and misalignment loads).

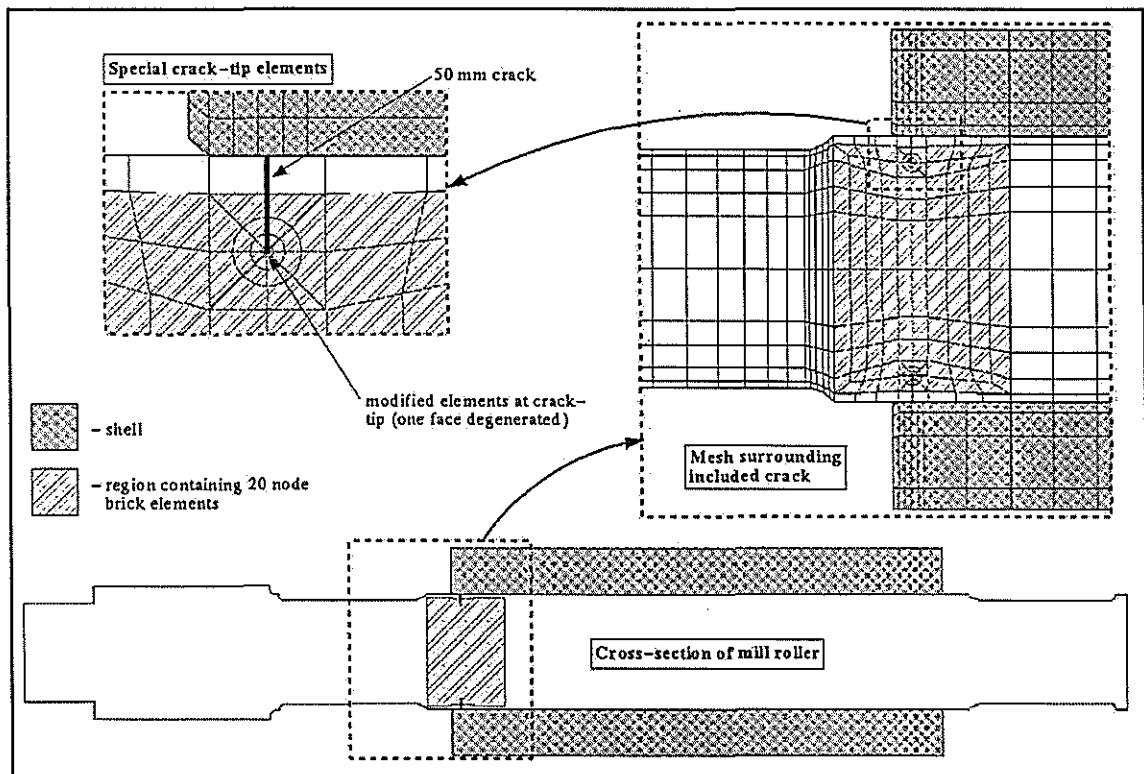


Figure 4.16 Sectioned view of the 'landing crack' roller model.

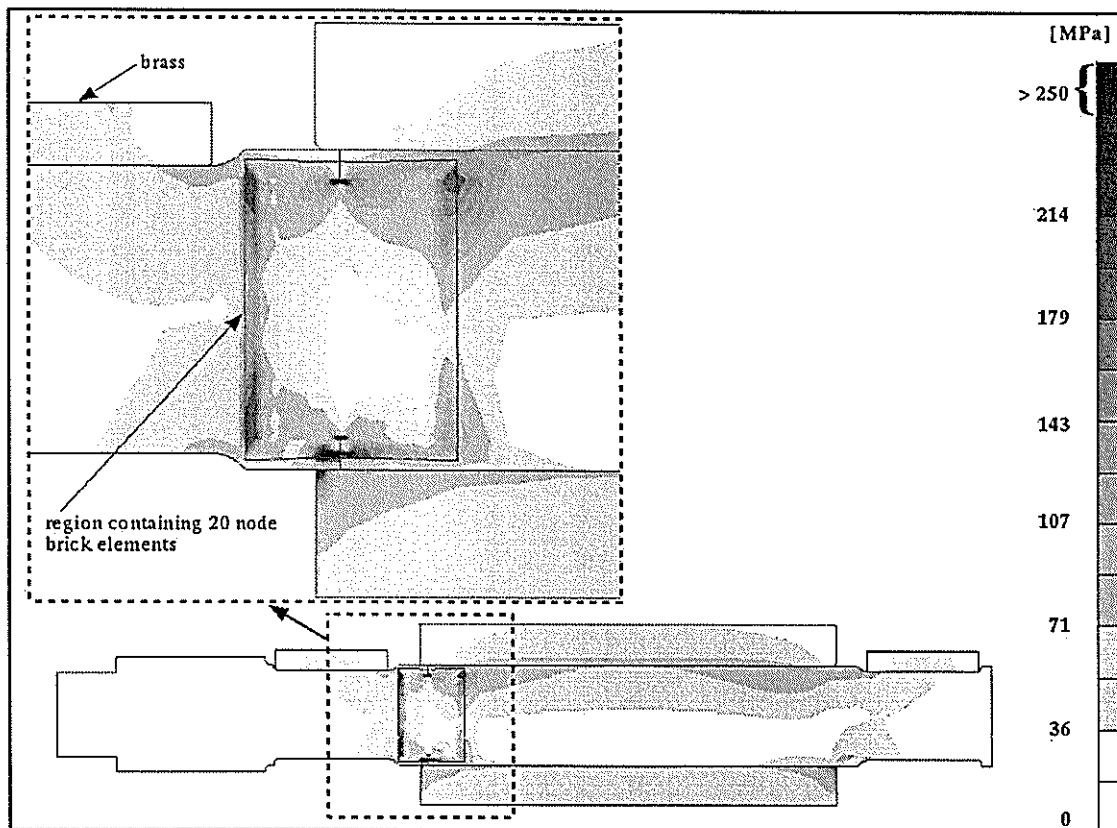


Figure 4.17 Von Mises stress plot ('landing crack' - roll load only).

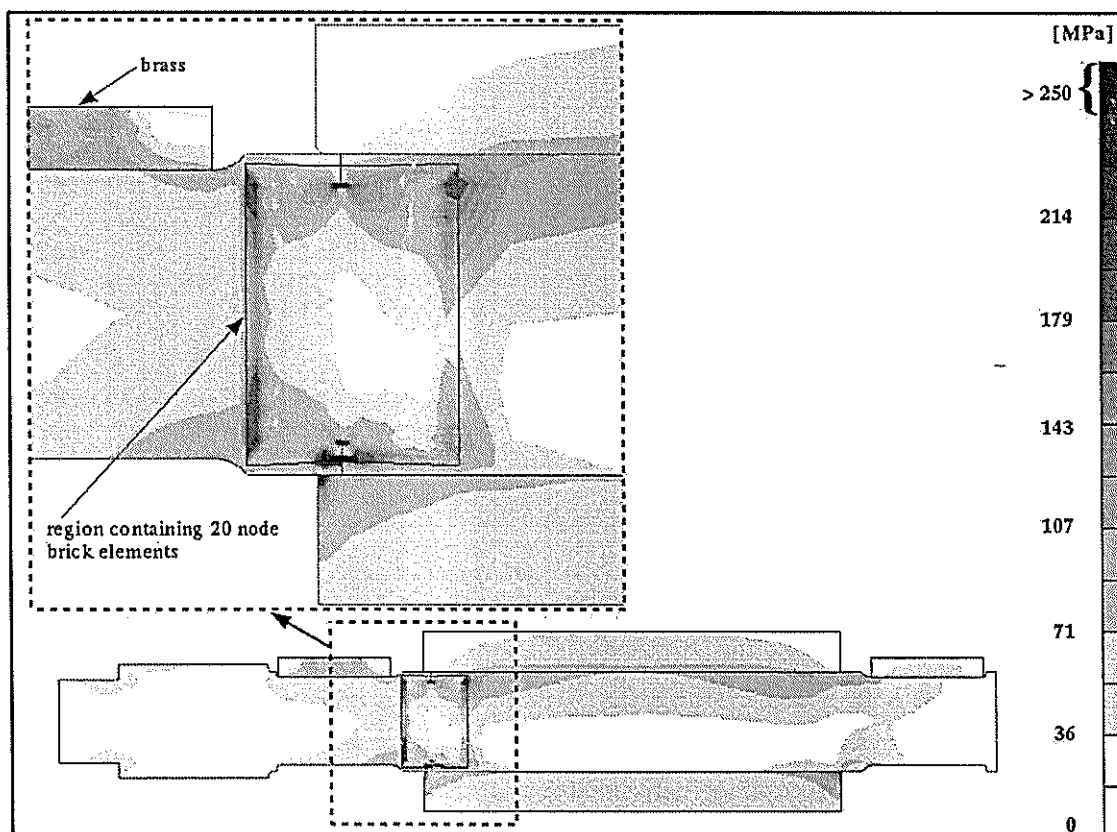


Figure 4.18 Von Mises stress plot ('landing crack' - roll and torsional loads).

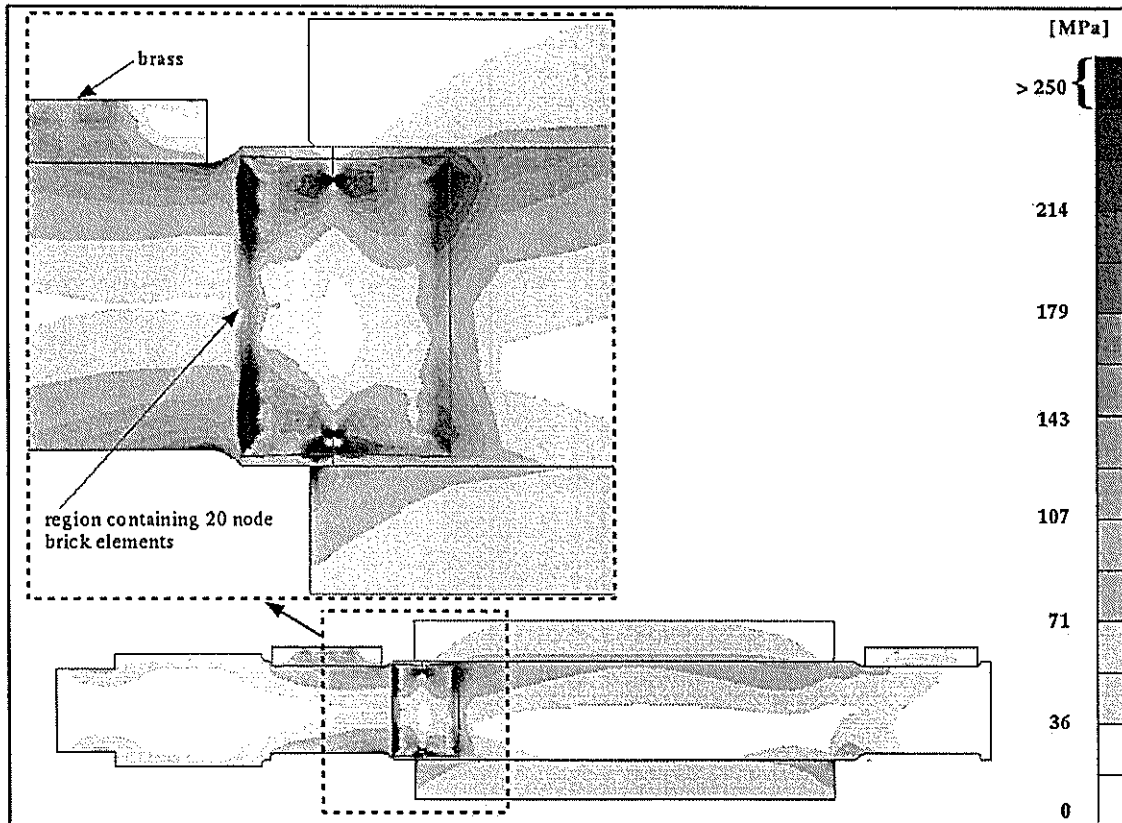


Figure 4.19 Von Mises stress plot ('landing crack' - roll, torsional and misalignment loads).

#### 4.2.2 Discussion

Two cracked mill rollers were analysed to predict the stress intensity factors for several loading conditions. These results compared favourably with the theoretical values calculated using only the bending moments at the axial location of the cracks as shown in Table 4.1. FEA stress intensity factors were on average 17 per cent higher than the theoretical values for a 50 mm circumferential crack located in the drive-end fillet. FEA stress intensity factors were on average 7 per cent higher than the theoretical values for a 50 mm circumferential crack located under the shell at the drive-end. The difference between FEA and theoretical predictions may be attributed to either; the theoretical assumption that the geometry function for a continuous cylinder can be applied to the roller's geometry; modelling simplifications which neglect crack surface interaction on the compressive side of the roller; load application; no consideration of torsional load effects in the theoretical calculations or mesh related inadequacies.

Misalignment loads did result in a significant increase in the stress intensity factor at the crack tip for both models. This suggests that misalignment loads need to be considered if an adequate evaluation of the structural integrity of a cracked mill roller is to be made. However, torsional loads had little effect on the mode I stress intensity factor predictions. Chapter 4.4 will summarise the crack modelling results.

### 4.3 Evaluation of a cracked mill roller

This section reports on the results from a spreadsheet developed to predict the critical crack size and estimate propagation times for roller shaft cracks using the equations listed throughout Chapter 4.1.

#### 4.3.1 Case study

A spreadsheet was constructed to apply fracture mechanics theory to predict the critical crack size and estimate propagation times for a cracked roller shaft. Prediction of the structural integrity of a roller using the spreadsheet is presented below.

Inputs required for the spreadsheet (Figure 4.20) include: diameter of shaft at the crack location; current crack depth; bending moment from roll loading at the crack location; and the fracture properties ( $K_{Ic}$ ,  $C$ ,  $m$ ,  $K_{th}$ ) for the shaft material. Equations 4.3 (modified for the bending moment case) and 4.14 are used to predict: the stress intensity for the current crack size; critical crack size; and remaining life for the cracked roller (assuming at operational speed of 4 rpm).

At the time of writing this report the fracture properties for a typical roller shaft material were unavailable so two candidate materials (Table 4.2) were chosen to demonstrate the capabilities of the spreadsheet. MANTEN and A533B are two gear steels listed in PATRAN's material database whose fracture toughness is expected to be similar to that of roller shaft steel (between 80 and 140  $\text{MPa}\cdot\text{m}^{0.5}$ ). Table 4.3 lists the critical crack size and time to failure estimations for several loading conditions and shaft materials for a fillet and shell-end crack. Note: the spreadsheet calculations do not account for torsional loads, possible crack closure and corrosion effects. Figure 4.21 shows the predicted growth of a 10 mm fillet crack under a 70 tonne/ft roll load for both candidate materials.

Table 4.2 Fracture properties for two candidate materials.

Material	A533B	MANTEN
Ultimate tensile strength [MPa]	552	552
Yielding limit [MPa]	345	324
Elastic modulus [GPa]	200	203
Paris Law coefficient, $C$	4.77E-13	3.00E-12
Paris Law exponent, $m$ [m/cycle]	3.73	3.43
Fracture toughness, $K_{Ic}$ [ $\text{MPa}\cdot\text{m}^{0.5}$ ]	100	121
Threshold stress intensity, $\Delta k_{th}$ [ $\text{MPa}\cdot\text{m}^{0.5}$ ]	4.65	8.00



Figure 4.20 Spreadsheet used to predict critical crack size and estimate time to failure.

Table 4.3 Critical crack size and time to failure estimations for several loading conditions.

Crack location at drive-end	Roll load description, Bending moment (from Appendix A5)	A533B		MANTEN	
		Critical crack size [mm]	Days to failure	Critical crack size [mm]	Days to failure
fillet	50 [tonne/ft], 488600 [Nm]	117.2	409.4	125.4	148.0
fillet	60 [tonne/ft], 586300 [Nm]	108.8	207.9	117.6	79.4
fillet	70 [tonne/ft], 684000 [Nm]	101.2	117.2	110.5	46.8
fillet	70 [tonne/ft]+misalignment, 1446000 [Nm]	58.9	7.1	70.3	3.6
shell-end	50 [tonne/ft], 861400 [Nm]	115.3	175.7	125.5	68.3
shell-end	60 [tonne/ft], 1033700 [Nm]	104.8	89.1	115.7	36.6
shell-end	70 [tonne/ft], 1206000 [Nm]	95.4	50.2	106.9	21.6
shell-end	70 [tonne/ft]+misalignment, 1907000 [Nm]	65.5	9.0	78.6	4.5

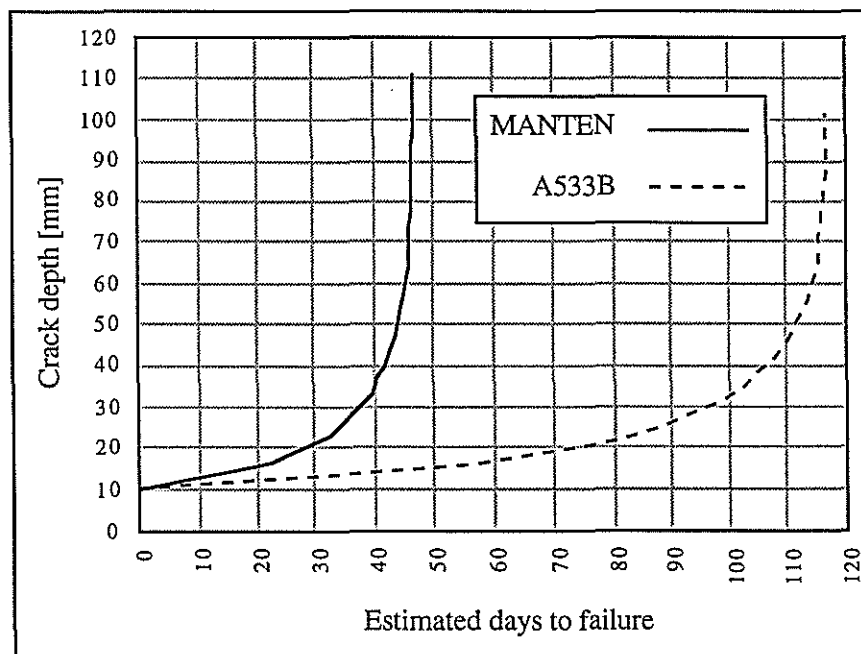


Figure 4.21 Crack depth versus estimated days to failure, (location :- drive-end inboard fillet, roll load:- 70 tonne/ft).

### 4.3.2 Discussion

A spreadsheet was constructed to predict the critical crack size and estimate propagation times for a cracked roller shaft based on equations 4.3 and 4.14. Results indicate that an estimation of remaining life for a cracked roller is highly sensitive to all fracture properties used and loading conditions. However, an accurate prediction of the critical crack size is only dependent on the fracture toughness and loading conditions.

#### 4.4 Durability modelling summary

This chapter has gone some way towards proving a procedure for estimating the structural integrity of a cracked mill roller. Prediction of critical crack sizes and the remaining life of a cracked shaft for known loading conditions are possible.

Finite element analysis of two cracked mill rollers was used to determine the suitability of applying fracture mechanics theory for cracked cylinders to mill roller geometry and loading. The modelling results compared favourably with the theoretical values calculated using only the bending moments at the axial location of the cracks. The difference between FEA and theoretical predictions may be attributed to either; the theoretical geometry function used; modelling simplifications which neglect crack surface interaction on the compressive side of the roller; load application; no consideration of torsional load effects in the theoretical calculations or mesh related inadequacies.

The two cracked roller models were modified versions of the 8-node brick element model used throughout Chapter 2. Sections of 20-node brick elements were used to model region associated with the included crack. The transition surface between the 8 and 20-node elements resulted in localised stress distribution errors, but this transition did not appear to affect the J-integral calculations at the crack tips for either model. However, it is suggested that the future modelling of crack mill rollers should be made using only 20-node elements to reduce uncertainty in stress intensity calculations.

A spreadsheet was constructed to predict the critical crack size and estimate propagation times for a cracked roller shaft based on equations 4.3 and 4.14. Results indicated that an estimation of remaining life for a cracked roller is highly sensitive to all fracture properties used and loading conditions. However, an accurate prediction of the critical crack size is only dependent on the fracture toughness and loading conditions. In all analyses, misalignment loads did result in a significant increase of crack growth rates and the associated reduction in critical crack sizes and remaining shaft life. This suggests that misalignment loads need to be considered if an adequate evaluation of the structural integrity of a cracked mill roller is to be made.

Fracture properties for a typical roller shaft material were unavailable at the time of this investigation so two candidate materials were chosen to demonstrate the capabilities of the spreadsheet. Critical crack size and time to failure estimations for several loading conditions and shaft materials for a fillet and shell-end crack were made. It should be remembered that the spreadsheet calculations do not account for torsional loads, possible crack closure and corrosion effects. Overall, the spreadsheet results offer conservative estimations regarding the structural integrity of a cracked roller.

# *Chapter 5*

*Conclusions and Recommendations*

## 5.0 Conclusions and recommendations

Reid's (1988) survey of mill roller failures in South African factories found that 50 per cent of failures occur at the inboard fillet regions and a further 40 per cent of failures occur at or just under the shell-ends. Detailed finite element analyses, both 2D and 3D, were applied to a seven foot mill roller to investigate the complex stress state and deflections induced by interference fits, nominal roll and torsional loads. The effect of roll lift and associated misalignment loads on roller stress was also analysed.

Simple beam theory combined with S-N fatigue theory is currently used by factory engineers to determine the maximum roll loads permitted. This method provides stress values comparable to those obtained during finite element analysis for the fillet regions. However, simple beam theory is inadequate in describing the stress state at the shell-end regions as the effect of interference loads are ignored.

The following conclusions and observations are made from this investigation:

1. Tailbar misalignment results in additional loads being applied to roller shafts. These loads are transmitted through the roller and superimpose with bending, torsional and interference loads. The resulting stress levels can be significantly above that predicted using conventional formulae (based on conventional endurance limits). Loads caused through misalignment are currently ignored in mill setting guidelines.
2. Under normal operating conditions a "gap" develops between the roller shell/shaft interface at the shell-ends. This gap forms a path for juice ingress which promotes stress corrosion fatigue.
3. The tapered shaft design which has been adopted widely by the Australian sugar industry, as a geometry to relieve shell-end stress, is shown to be ineffective under operational conditions.
4. The modelling has confirmed that the fillet and shell-end regions are the most highly stressed regions of a roller.
5. Alternative roller designs have been explored and are reported in detail. These included variations in shaft geometry, shell material and shell attachment methods. Of these, the ones which show the greatest potential for improved durability are: large inboard fillets; raised landing at shell-ends; shell-end recesses; and the application of surface treatments to high stress regions during manufacture. Reference is made to Figure 3.56 for a geometry which should be trialled by the Australian industry as soon as possible.
6. Non destructive testing of mill rollers to locate fatigue cracks in shafts takes place as a matter of course in factories. Based on the skill of the operator this procedure can locate and size cracks in critical locations. However, no procedure is available to assess the structural integrity of a cracked roller. In fact, it has been standard procedure in some factories to remove cracked

---

rollers when first observed. This report gives the industry a simple spread-sheet based method to assess the structural integrity of damaged rollers. Fracture mechanics is applied to estimate the critical crack size and crack propagation rates for known operating conditions. The method has been verified by finite element analysis.

# *References*

## References

- Adams, R.D. and Wake, W.C. (1984). *Structural adhesive joints in engineering*. Elsevier Applied Science Publishers.
- Anand, M. (1983). *Milling system 2001 - a concept of the future mill*. Proc. Hun. Conv. Sugar Technol. Assoc. (India), 16: E1-E9.
- Anderson, S.I. and Loughran, J.G. (1995). *Crack detection and durability assessment of low speed gears - Section B*. SRDC Project JCU2S.
- Anon. (1993). *PATRAN 3 - P3 / Fatigue user's manual*. PDA Engineering.
- Ashby, M.F. and Jones, D.R.H. (1982). *Engineering materials - an introduction to their properties and applications*. Pergamon Press.
- Broek, D. (1974). *Elementary Engineering Fracture Mechanics*. Martinus Nijhoff Publishers.
- Browne, R, O'M. (1949). *Bearing metals and their lubrication*. Proc. Qld. Society Sugar Cane Technol., 16: 51-57.
- Cessford, H. (1956). *Metallizing*. Proc. Qld. Society Sugar Cane Technol., 23: 99-106.
- Clarke, S.G. (1958). *A new design of crushing mill for the Queensland sugar industry*. Proc. Qld. Society Sugar Cane Technol., 25: 59-65.
- Clarke, S.G. (1977). *Thrust free tailbars for mill drive*. Proc. Qld. Society Sugar Cane Technol., 44: 247-249.
- Clarke, S.G. (1981). *Mill pinions and their associated problems*. Proc. Aust. Society Sugar Cane Technol., 3: 249-254.
- Coates, W.S. (1947). *Spotting mill rollers*. Proc. Qld. Society Sugar Cane Technol., 14: 81-85.
- Crawford, W.R. (1970). *Roller shells and the shrink fit*. Proc. Qld. Society Sugar Cane Technol., 37: 323-339.
- Cullen, R.N. (1968). *Influences of operating conditions on the stresses in a sugar mill roller shaft*. Proc. Qld. Society Sugar Cane Technol., 35: 281-287.

- Dalziel, H.R. (1953). *The failure of metals under repeated loading*. Proc. Qld. Society Sugar Cane Technol., 20: 65-75.
- Dillion, B. and Millett, A.R. (1984). *Number one mill low speed gearbox failure at Pioneer mill*. Proc. Aust. Society Sugar Cane Technol., 6: 187-190.
- Gatley, T.W. and Pearce, R.K. (1979). *Mill hydraulics - a new approach*. Proc. Aust. Society Sugar Cane Technol., 1: 243-248.
- George, R.L and Reid, J.M. (1951). *The sugar mill roller*. Proc. Qld. Society Sugar Cane Technol., 18: 75-83.
- Goldthorpe, M.R. (1992). *Finite elements, linear elastic fracture mechanics and structural integrity*. nCode International Ltd.
- Hill, J.W. and McGinn, J.A. (1965). *Ultrasonic inspection in Queensland sugar mills*. Proc. Qld. Society Sugar Cane Technol., 32: 269-275.
- Holt, J.E. (1963). *Empirical estimation of roll load and roll torque*. Proc. Qld. Society Sugar Cane Technol., 30: 111-116.
- Jacklin, G.D., Doolan, B.J. and Gatley, T.W. (1975). *The spheroidal roller bearing mill*. Proc. Qld. Society Sugar Cane Technol., 42: 161-165.
- Jorgensen, G.M., Johnstone, J.A. and Cant, C.A. (1986). *The application of high torque - low speed hydraulic motors in the sugar industry*. Proc. Aust. Society Sugar Cane Technol., 8: 269-278.
- Joyce, K.N. and Garson, C.A. (1996). *Whole-of-life costs for current roll shell materials*. Proc. Aust. Society Sugar Cane Technol., 18: 249-254.
- Kirkness, D.K. (1965). *The production of the sugar mill roller shaft*. Proc. Qld. Society Sugar Cane Technol., 32: 277-289.
- Kirkness, D.K. (1977). *Recent developments in the production of the sugar mill shaft*. Proc. Qld. Society Sugar Cane Technol., 44: 345-352.
- Loughran, J.G. and Henderson, I. (1992). *A prototype automated roll arcing machine*. Proc. Aust. Society Sugar Cane Technol., 14: 246-253.

- Loughran, J.G., Ritchie, W.H. and Refalo, B. (1995). *Stress and durability of sugar mill rolls*. Proc. Aust. Society Sugar Cane Technol., 17: 352-357.
- Macey, D. and McGinn, J.A. (1975). *Torque requirements of a roller-bearing mill*. Proc. Qld. Society Sugar Cane Technol., 42: 167-170.
- McGinn, J.A. and Mason, V. (1982). *Design aspects of roller bearing mills*. Proc. Aust. Society Sugar Cane Technol., 4: 213-220.
- Mostert, D.R. (1969). *Thrust generation in sugar mill drive*. Proc. South African Sugar Technol. Assoc., January: 221-224.
- Munro, B.M. (1964). *An investigation into crushing bagasse and the influence of imbibition on extraction*. Univ. of Qld., PhD Thesis.
- Murry, C.R. (1960). *A theoretical and experimental investigation into the mechanics of crushing prepared sugar cane*. Univ. of Qld., PhD Thesis.
- Okamura, H., Tanaka, H. and Terao, M. (1972). *Square box couplings in cane mill drives - Parts 1 and 2*. Proc. Intern. Sug. Journal. p291-293, 323-327.
- Parmley, R.O. (1989). *Standard handbook of fastening and joining*. 2nd Edition. McGraw-Hill.
- Pattenden, J. and Walker, R. (1980). *The application of special steels in the sugar industry*. Proc. Aust. Society Sugar Cane Technol., 2: 147-158.
- Peterson, R.E. (1974). *Stress concentration factors*. John Wiley and Sons.
- Pihl, G.T. (1954). *Roller bearings in cane crushing mills*. Proc. Qld. Society Sugar Cane Technol., 21: 241-245.
- Power, C. and Clarke, S.G. (1977). *Cane mill tailbar and couplings*. Proc. Qld. Society Sugar Cane Technol., 44: 243-245.
- Refalo, B. (1993). *Finite element modelling of sugar mill rollers*. James Cook University, Undergraduate Thesis.
- Reid, M.J. (1988). *Analysis of the causes of recent roll shaft failures in Natal sugar mills*. Proc. South African Sugar Technol. Assoc., June: 74-78.

- Rhydderch, A. (1934). *The recent development in foundry ferrous alloys*. Proc. Qld. Society Sugar Cane Technol., 5: 161-173.
- Ritchie, W.H. (1994). *Finite element modelling of roller shaft transition fillets*. James Cook University, Undergraduate Thesis.
- Russell, G.E. (1968). *An investigation of the extraction performance of sugar cane crushing trains*. Univ. of Qld., PhD Thesis.
- Russell, G.E. and Murry, C.R. (1968). *A method of determining settings for three-roll mills*. Proc. Qld. Society Sugar Cane Technol., 35: 81-93.
- Scott, W. (1986). *Reducing failures and wear of mill plant by effective lubrication*. Proc. Aust. Society Sugar Cane Technol., 8: 279-284.
- Scriven, H.E.B. (1962). *Developments in the design of sugar mills with floating rollers*. Proc. Qld. Society Sugar Cane Technol., 29: 249-252.
- Shann, D.S. (1959). *The corrosion fatigue of metals and its effect on the sugar industry*. Proc. Qld. Society Sugar Cane Technol., 26: 73-79.
- Shield, A.G. and Cant, C.C. (1995). *A new hydraulic drive unit for a 2.13 m crushing mill*. Proc. Aust. Society Sugar Cane Technol., 17: 332-338.
- Smith, R.N.L. (1991). *Basic fracture mechanics*. Butterworth Heinemann.
- Solomon, T.J. (1967). *Theoretical and experimental investigation into the mechanics of crushing prepared sugar cane*. Univ. of Qld., PhD Thesis.
- Suresh, S. (1991). *Fatigue of materials*. Cambridge Solid State Science Series.
- Tada, H., Paris, P.C. and Irwin, G.R. (1985). *The stress analysis of cracks handbook. Second edition*. Paris Productions Incorporated.
- Thistlethwaite, B.W. (1949). *Arc weld surfacing*. Proc. Qld. Society Sugar Cane Technol., 16: 59-67.
- Tosio, C.T. (1988). *A new sugar mill drive coupling*. Proc. South African Sugar Technol. Assoc., June: 74-78.

Tyson, K.B., Curran, P.T. and Ziebrath, D.K. (1991). *Solid film lubrication of mill brasses*. Proc. Aust. Society Sugar Cane Technol., 13: 252-260.

Tyzack, H.E.M. (1977). *Fatigue failure in mill pinions*. Proc. Qld. Society Sugar Cane Technol., 44: 261-270.

Tyzack, H.E.M. and Gatley, T.W. (1980). *Corrosion fatigue in mill roller shafts*. Proc. Aust. Society Sugar Cane Technol., 2: 155-158.

Williams, R.J. (1931). *The heat treatment of steel with the special reference to various types of steel*. Proc. Qld. Society Sugar Cane Technol., 2: 125-149.

# *Appendices*

A.1 Mill roller geometry

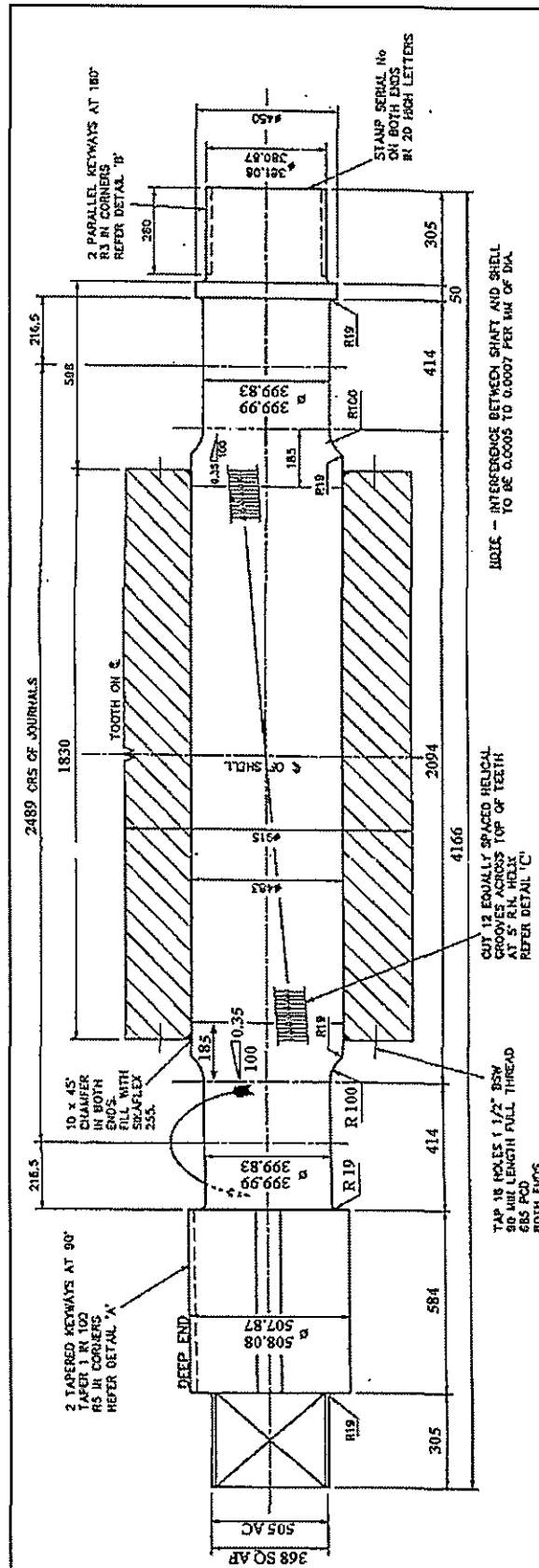


Figure A.1.1 Six foot top roller - part 1. (Bundaberg Foundry drawing no. A2-79-3025)

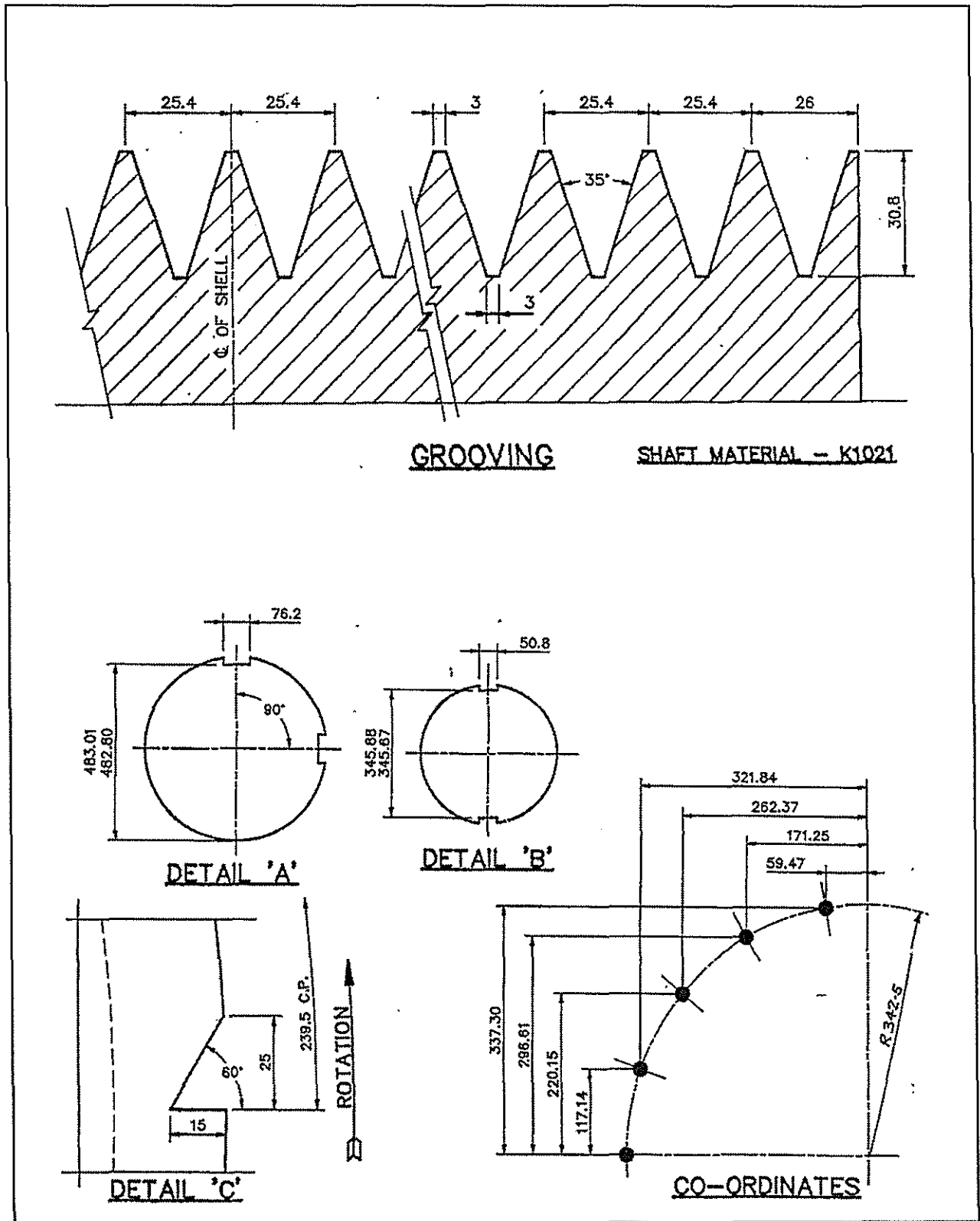


Figure A.1.2 Six foot top roller - part 2. (Bundaberg Foundry drawing no. A2-79-3025)



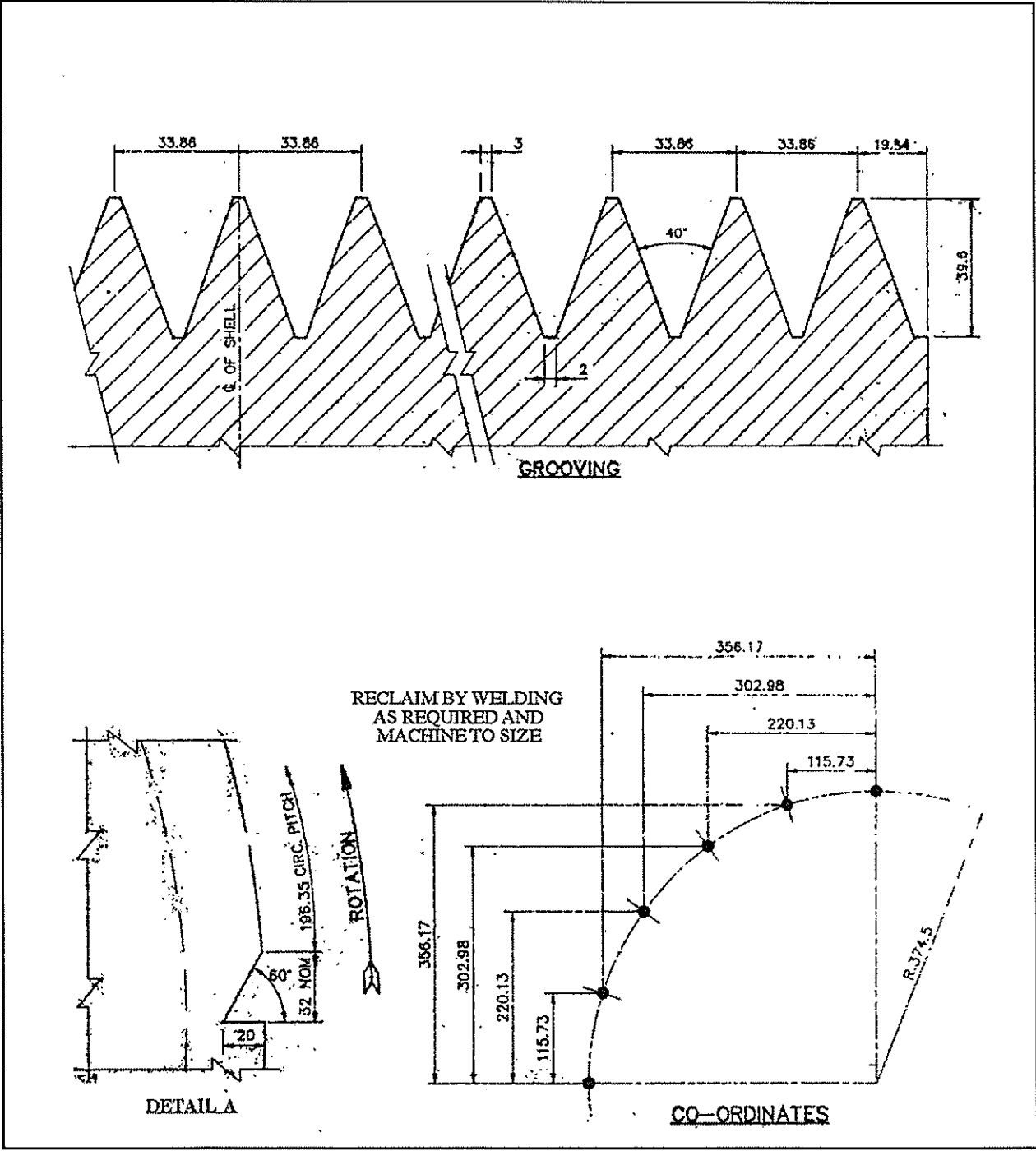


Figure A.1.4 Seven foot top roller - part 2. (Bundaberg Foundry drawing no. A2-79-3013)

A.2 Mill brass geometry

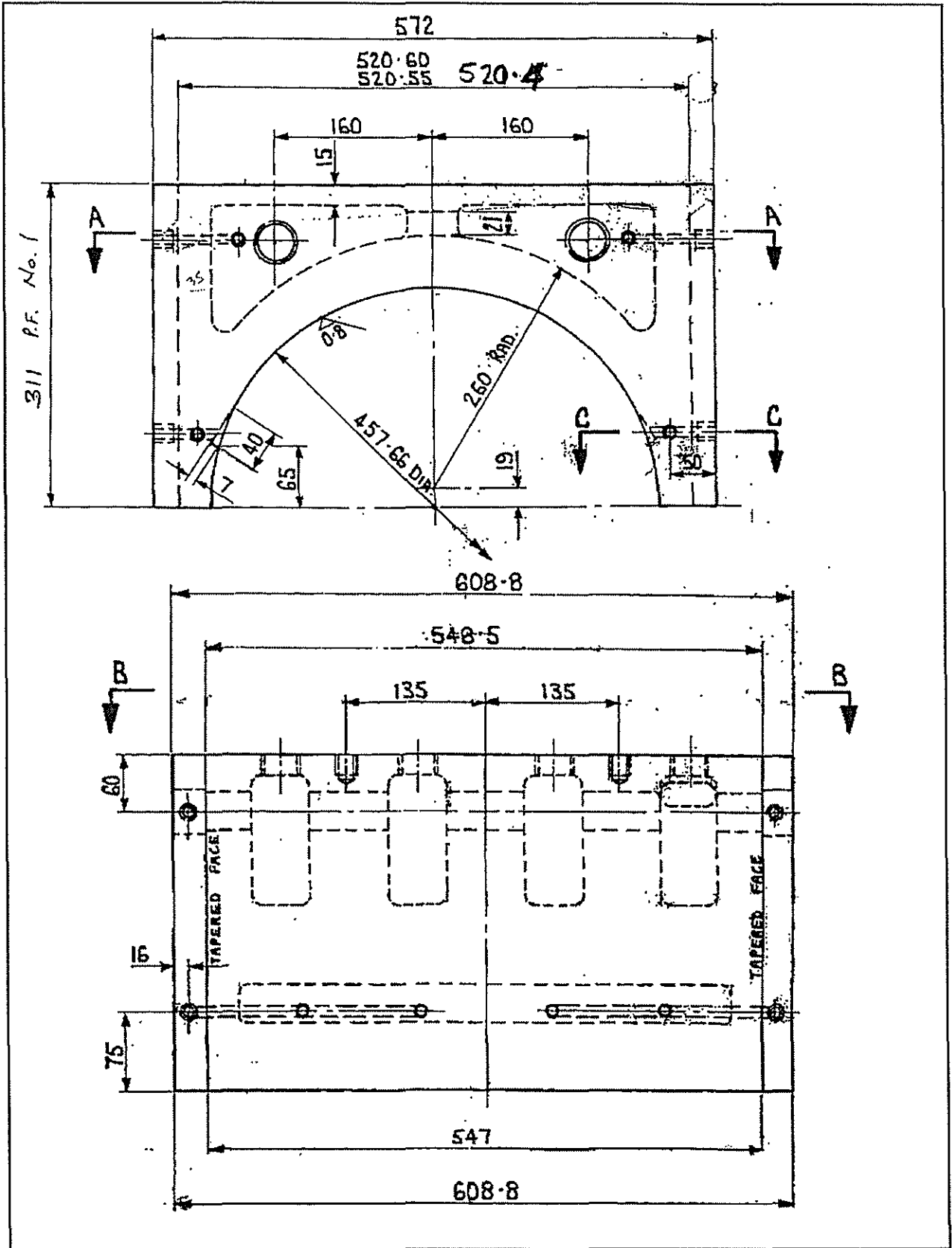


Figure A.2.1 18 inch top brass - part 1. (© Babinda Sugar Ltd)

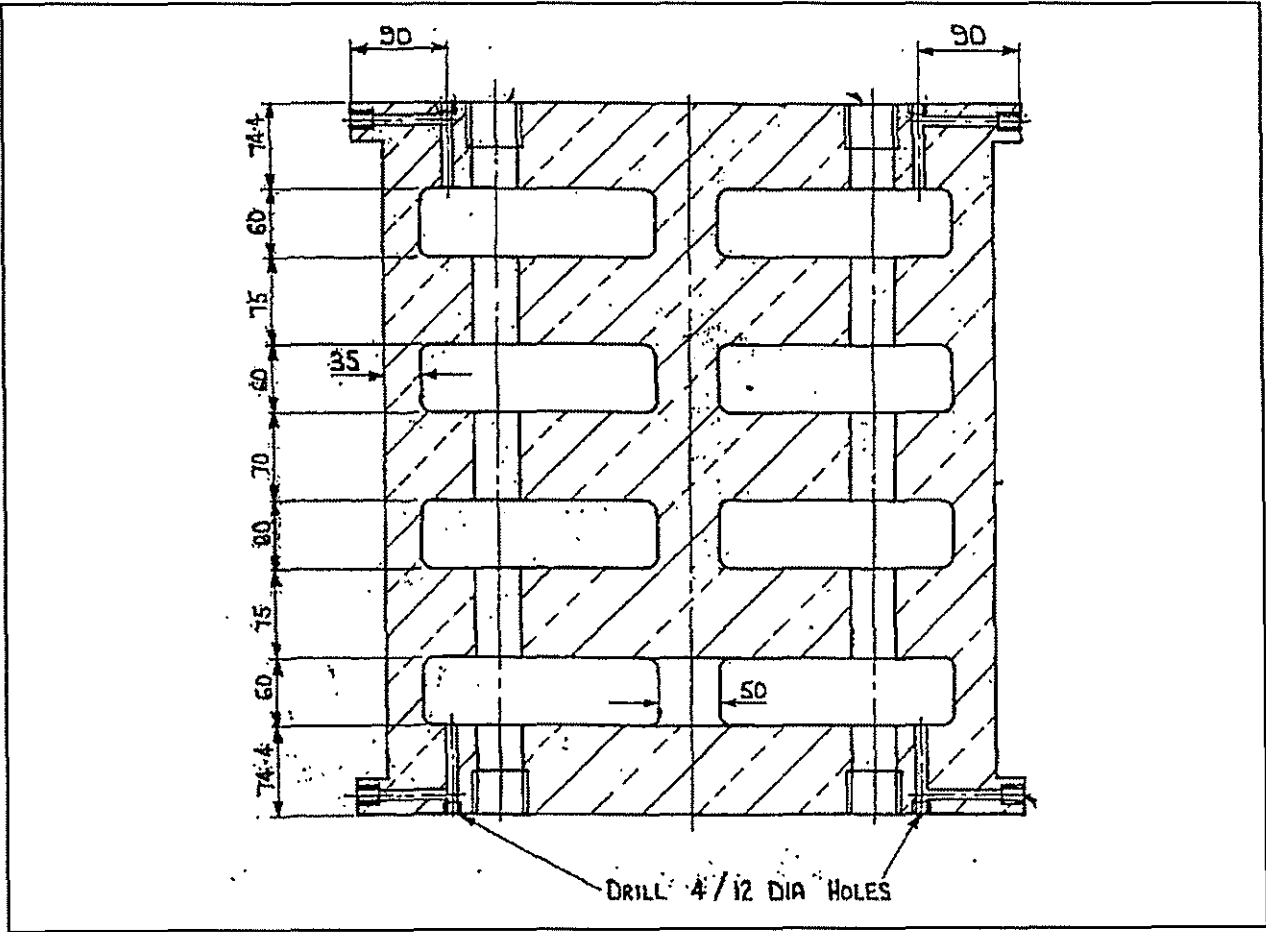


Figure A.2.2 18 inch top brass - part 2. (©/- Babinda Sugar Ltd)

### A.3 Roll load calculations

Calculating roll load from typical mill parameters

The following design parameters were taken from technical drawings of the seven foot roller (Appendix A1) and the operational parameters were estimated.

$$\begin{array}{ll}
 \text{Deff} = 0.96 \text{ m} & ; \quad \text{Ff} = 13.7 \% ; \\
 \text{L} = 2.134 \text{ m} & ; \quad \text{m} = 0.9 ; \\
 \Psi = 72^\circ & ; \quad \text{TCH} = 400 \text{ tonnes / hr} ; \\
 \text{W}_{\text{of}} = 100 \text{ mm} & ; \quad \text{N} = 4 \text{ rev / min} ; \\
 \text{W}_{\text{od}} = 63 \text{ mm} & ; \quad \text{P}_R = 6.21 \text{ MPa} .
 \end{array}$$

Using equation 1.17, 
$$C_F = \frac{\gamma}{1530} = \frac{\text{TCH F}_f / (3.6 \text{ L W}_o \text{ S})}{1530} ,$$

and equation 1.16, 
$$R_x = P_R \text{LD}(C_F - 0.1) ,$$

we get :-

Table A.3.1      Compaction, filling ratio and roll load for the feed and delivery nips.

Nip	Work Opening W <sub>o</sub> (mm)	Compaction γ (kg fibre / kg)	Filling Ratio C <sub>F</sub>	Roll Load R <sub>x</sub> (MN)
Feed	100	355	0.232	1.678
Delivery	63	563	0.368	3.410

Using equation 1.19, 
$$m R_{TV} = (R_F + R_D) \cos\left(\frac{\Psi}{2}\right) ,$$

we get :-

$$\begin{aligned}
 R_{TV} &= 4.574 \text{ MN (vertical)} \\
 &= 467 \text{ tonnes} \\
 &= 66.7 \text{ tonnes / ft}
 \end{aligned}$$

∴ Vertical roll load = 66.7 tonnes / ft

## Calculating torsional loads

Using equation 1.19, 
$$N_x = \left( \frac{P_N}{D} \right) \left( \frac{W_{ox}}{D} \right)^{0.5} C_{Fx}^{0.21} ,$$

where  $P_N$  is proportionality factor ( $\approx 0.656m$ , for mill set number 1),

and equation 1.20, 
$$G_x = N_x R_x D ,$$

we get :-

Table A.3.2 Torque load number and required torsional load for the feed and delivery nips.

Nip	Work Opening, $W_o$ (mm)	Filling Ratio $C_F$	Torque Load Number, $N_F$ (MNm) <sup>-1</sup>	Roll Load $R_x$ (MN)	Torsional Load, $G_x$ (MNm)
Feed	100	0.232	0.162	1.678	0.261
Delivery	63	63	0.142	3.410	0.465

Using equation 1.21, 
$$G_p = \mu (1-m) R_T \left( \frac{D}{2} + W_{op} \right) ,$$

where  $\mu = 0.3$ ,

and  $W_{op} = 140$  mm,

we get :- 
$$G_p = 0.085 \text{ MNm}$$

$\therefore$  Trash plate torque = 0.085 MNm

\*\* Neglecting brass friction at this stage.

Using equation 1.22, 
$$T_{DRIVE} = G_T = G_F + G_p + G_D ,$$

we get :- 
$$G_T = 0.811 \text{ MNm}$$

$\therefore$  Drive torque = 0.811 MNm

Using equation 1.23, 
$$T_{PINION} = \frac{G_F}{2} + \frac{G_D}{2} ,$$

we get :- 
$$G_{PINION} = 0.363 \text{ MNm}$$

Using equation 1.24,  $T_{\text{TRACTION}} = \frac{G_F}{2} + \frac{G_D}{2} + G_P$  ,

we get :-  $G_{\text{TRACTION}} = 0.448 \text{ MNm}$

∴ Shell traction torque = 0.448 MNm

Calculating reaction loads for pinion gearing

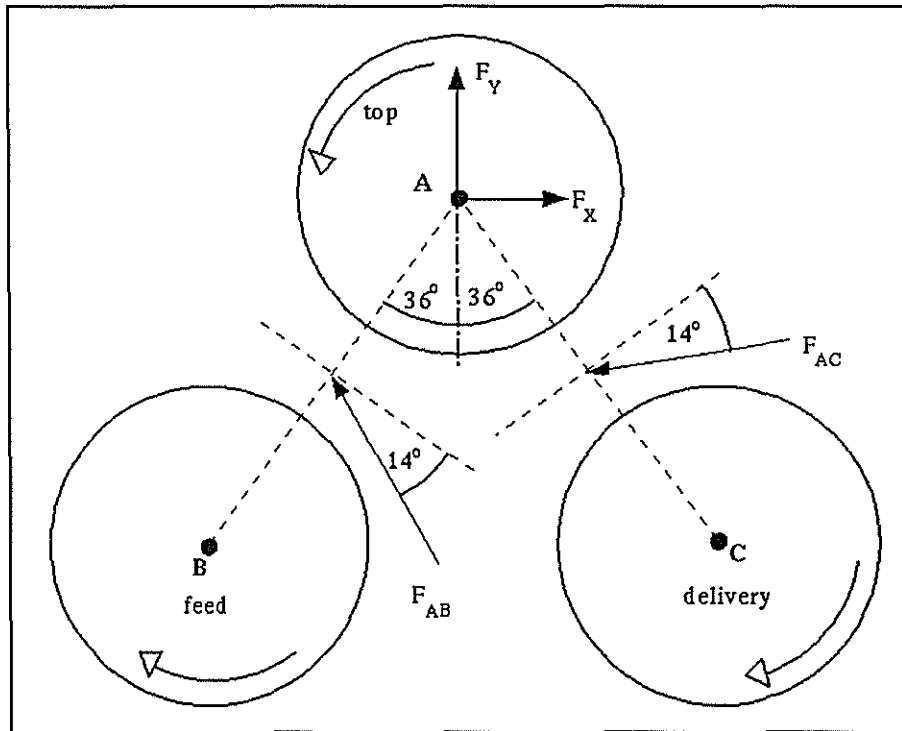


Figure A.3.1 Force interactions on the top pinion.

The pressure angle was set at  $14^\circ$  (typical value for mill pinion design).

Pitch diameter =  $D + \frac{W_o}{2} \approx 1.0 \text{ m}$  ∴  $r_p = 0.5 \text{ m}$

The pressure angle of mill pinions is typically  $14^\circ$

$$F_{ABt} = \frac{0.261/2}{0.5} = 0.261 \text{ MN}$$

∴  $F_{ABr} = F_{ABt} \tan(14^\circ) = 0.065 \text{ MN}$

$$F_{ACt} = \frac{0.465/2}{0.5} = 0.465 \text{ MN}$$

∴  $F_{ACr} = F_{ACt} \tan(14^\circ) = 0.116 \text{ MN}$

Summing the forces in the 'X' direction, we get :-

$$F_X = -F_{ABt} \cos(36^\circ) + F_{ABr} \sin(36^\circ) - F_{ACt} \cos(36^\circ) - F_{ACr} \sin(36^\circ)$$

$$\therefore \underline{F_X = -0.617 \text{ MN}}$$

Summing the forces in the 'Y' direction, we get :-

$$F_Y = F_{ABt} \sin(36^\circ) + F_{ABr} \cos(36^\circ) - F_{ACt} \sin(36^\circ) + F_{ACr} \cos(36^\circ)$$

$$\therefore \underline{F_Y = 0.027 \text{ MN}}$$

Calculating pressure loading for FEA model

To simplify the load application for the FEA roller model, constant pressures to simulate the feed, trash plate and delivery loads will be applied over corresponding regions on the shell mesh. The circumference of the roller model was divided up into 32 (11.25°) segments. Figure A.3.2 highlights the positioning of the pressure loading.

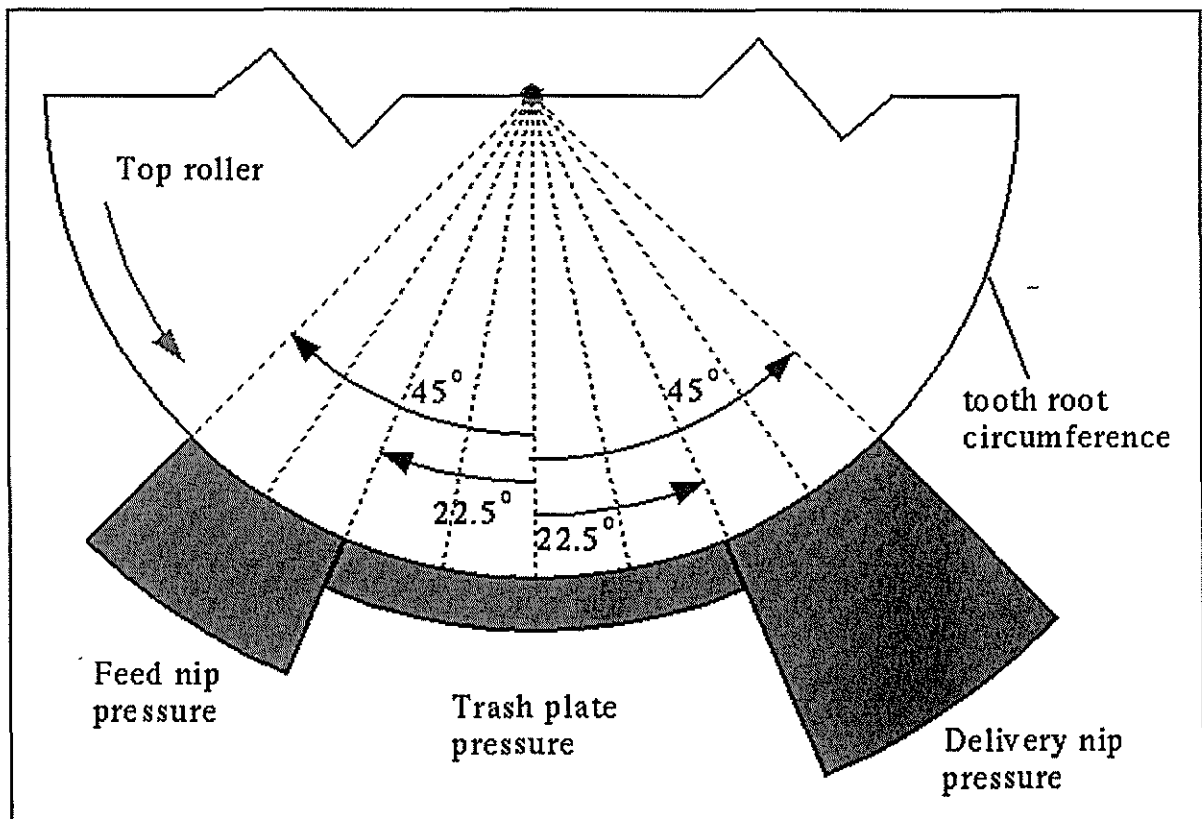


Figure A.3.2 Pressure loading for the FEA roller model.

Using a modified version of equation,  $R_{trash} = (1-m) R_{TV}$   
 we get :-  $= 0.457 \text{ MN}$

The diameter of the FEA roller model,  $D$ , is 0.92 m (tooth root diameter) and the length over which the trash plate pressure loading,  $P_{trash}$ , will be applied,  $L$ , is 2.138 m.

$$\therefore 0.457 = \frac{P_{trash}LD}{2} [\sin \Phi]_{-22.5}^{+22.5}$$

$$P_{trash} = 0.608 \text{ MPa}$$

Similarly for the feed and delivery nips where  $R_f = 1.678 \text{ MN}$  and  $R_d = 3.410 \text{ MN}$ , we get :-

$$1.678 = \frac{P_f LD}{2} [\sin \Phi]_{-45.0}^{-22.5}$$

$$P_f = 5.259 \text{ MPa}$$

$$3.410 = \frac{P_d LD}{2} [\sin \Phi]_{+22.5}^{+45.0}$$

$$P_d = 10.688 \text{ MPa}$$

Figure A.3.3 shows the load balance on the roller shell resulting from the applied pressure distribution used in the FEA modelling.

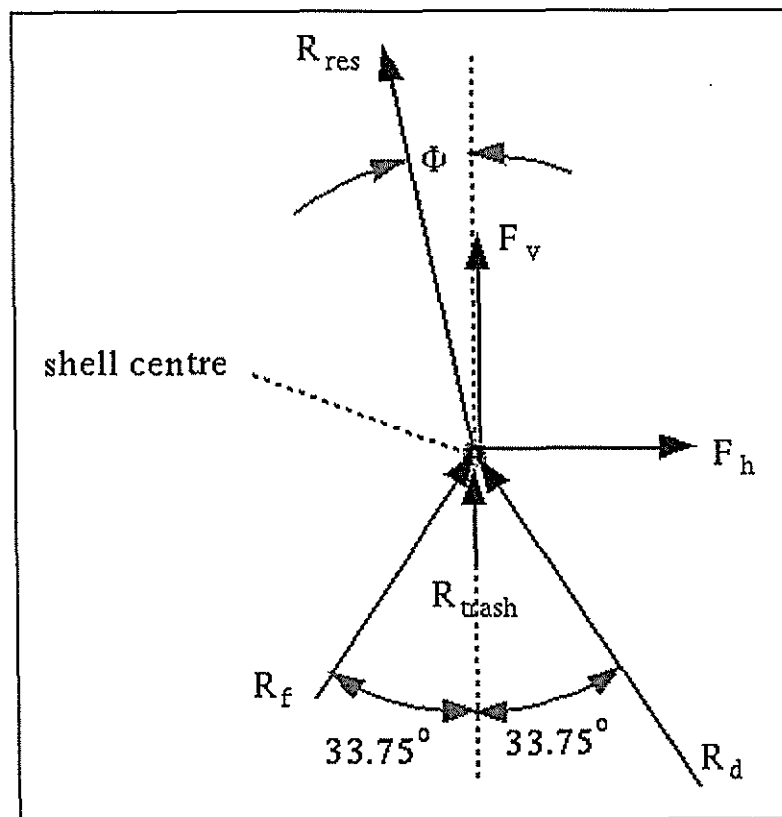


Figure A.3.3 Pressure load balance for the roller shell.

Summing the forces in the vertical direction, we get :-

$$F_v = (R_f + R_d) \cos(33.75^\circ) + R_{trash}$$

$$F_v = 4.688 \text{ MN} \quad (68.3 \text{ tonnes / ft})$$

Summing the forces in the horizontal direction, we get :-

$$F_h = (R_d - R_f) \sin(33.75^\circ)$$

$$F_h = -0.962 \text{ MN}$$

∴  $R_{res} = 4.786 \text{ MN}$  (69.8 tonnes / ft) at  $11.6^\circ$  from the vertical towards the feed roller. This value does not incorporate the effect of brass friction on the mill cheeks and may differ slightly from the roll load definition used by mill engineers.

Calculating bearing reactions

Figure A.3.4 layouts the forces and moments acting on the FEA mill roller model. Several unknowns still exist at this stage, including the reactions and the corresponding torque loss at the both the drive and pintle ends. The friction coefficient ( $\mu$ ) for the brass bearings was set at 0.1.

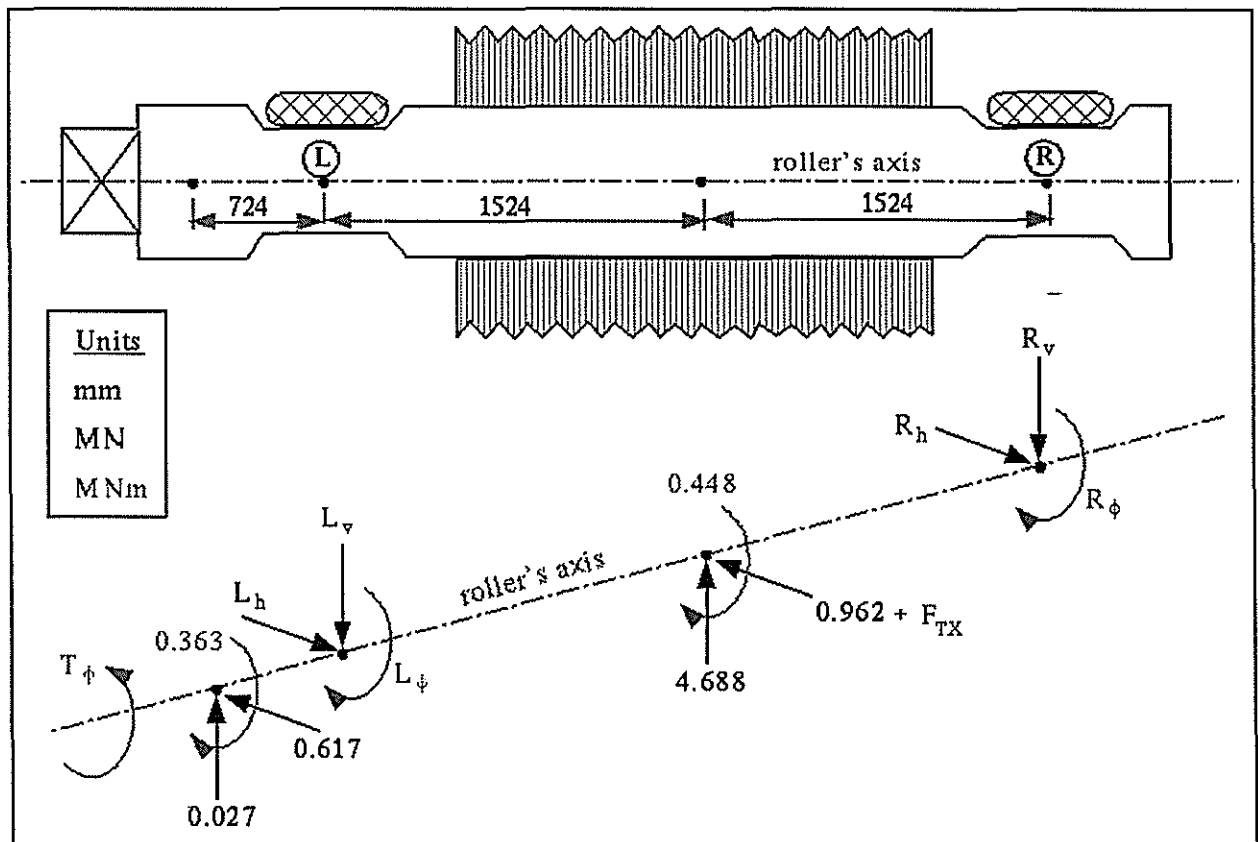


Figure A.3.4 Force and moment diagram of FEA mill foller model.

The shell traction torque, 0.448 MNm, was simulated by applying a constant value force to each surface node in the 90° segment acted upon by the feed nip, trash plate and delivery nip. As a result, a horizontal force,  $F_{TX}$ , effectively acts on the shell. A correction factor,  $C_{factor}$ , of 1.12 was required to account for the curvature of shell when transforming the shell tractive torque to an equivalent horizontal force.

$$F_{TX} = \frac{G_{TRACTION}}{C_{factor} D / 2}$$

$$F_{TX} = 0.870 \text{ MN}$$

Summing the moments about point R contained in the axial vertical plane, we get :-

$$L_v = 2.377 \text{ MN} \quad (\text{horizontal reaction force plus friction component})$$

Summing the vertical forces, we get :-

$$R_v = 2.338 \text{ MN} \quad (\text{vertical reaction force plus friction component})$$

Summing the moments about point R contained in the axial horizontal plane, we get :-

$$L_h = 1.442 \text{ MN} \quad (\text{horizontal reaction force plus friction component})$$

Summing the horizontal forces, we get :-

$$R_h = 0.769 \text{ MN} \quad (\text{horizontal reaction force plus friction component})$$

The corresponding torque loss due to friction between the shaft and drive end brass is :

$$L_\phi = \mu \sqrt{L_v^2 + L_h^2} \frac{D_s}{2} \quad \text{where } D_s \text{ is the journal diameter (0.4572 m)}$$

$$L_\phi = 0.064 \text{ MNm}$$

The corresponding torque loss due to friction between the shaft and pintle end brass is :

$$R_\phi = \mu \sqrt{R_v^2 + R_h^2} \frac{D_s}{2}$$

$$R_\phi = 0.056 \text{ MNm}$$

Summing the torsional moments about the roller axis, we get :-

$$T_\phi = 0.931 \text{ MNm} \quad (\text{total drive torque required to operate the three-roller unit})$$

Calculating torque related loading for FEA model
--

To simplify the load application for the FEA roller model, a constant value tangential force to simulate the shell traction and pinion torques will be applied over corresponding regions on the model.

Shell traction : 0.448 MNm at 0.46 m (shell radius) was applied over 9 rows of 25 nodes

$$\therefore \text{Force / node} = \underline{4329 \text{ N}} \quad (\text{tangential})$$

Pinion torque : 0.363 MNm at 0.292 m (pinion landing radius) was applied over 33 rows of 7 nodes

$$\therefore \text{Force / node} = \underline{5382 \text{ N}} \quad (\text{tangential})$$

Pinion reaction : 0.621 MN (horizontal component) was applied over 5 rows of 7 nodes. A correction factor of 1.04 was required to account for the curvature of pinion landing surface.

$$\therefore \text{Force / node} = \underline{16951 \text{ N}} \quad (\text{normal})$$

Tailbar torque : 0.931 MNm at an average of 0.2448m (distance from shaft axis) was applied over 3 rows of 5 nodes in each corner of the shaft square.

$$\therefore \text{Force / node} = \underline{63385 \text{ N}} \quad (\text{tangential})$$

### A.4 Misalignment load calculations

The following calculations are for a mill roller which has risen 10 mm above and parallel to the gear shaft axis during operation. Figure A.4.1 illustrates the radial and thrust forces and bending moment produced under such conditions. The following parameters were used :

- $L = 2.0 \text{ m}$  (effective length of tailbar) ;  $h = 0.01 \text{ m}$  (roll lift);
- $l_3 = 0.423 \text{ m}$  (tailbar width) ;  $T = 0.930 \text{ MNm}$  (transmitted torque);
- $l_{cb} = 0.6 \text{ m}$  (length of coupling box) ; and  $\mu \approx 0.3$  (friction coefficient).

Using equation 1.28, 
$$l_1 = 6.5 \frac{h}{L} l_{cb}$$

we get :- 
$$l_1 = 0.0195 \text{ m}$$

∴ 
$$l_2 = 1.961 \text{ m}$$

Using equation 1.25, 
$$F_r = \frac{4}{l_3} \left( \frac{l_1 \pm \mu l_3}{L + l_2} \right) T$$
 ,

we get :- 
$$F_r = 0.324 \text{ MN}$$

∴ Radial force = 0.324 MN

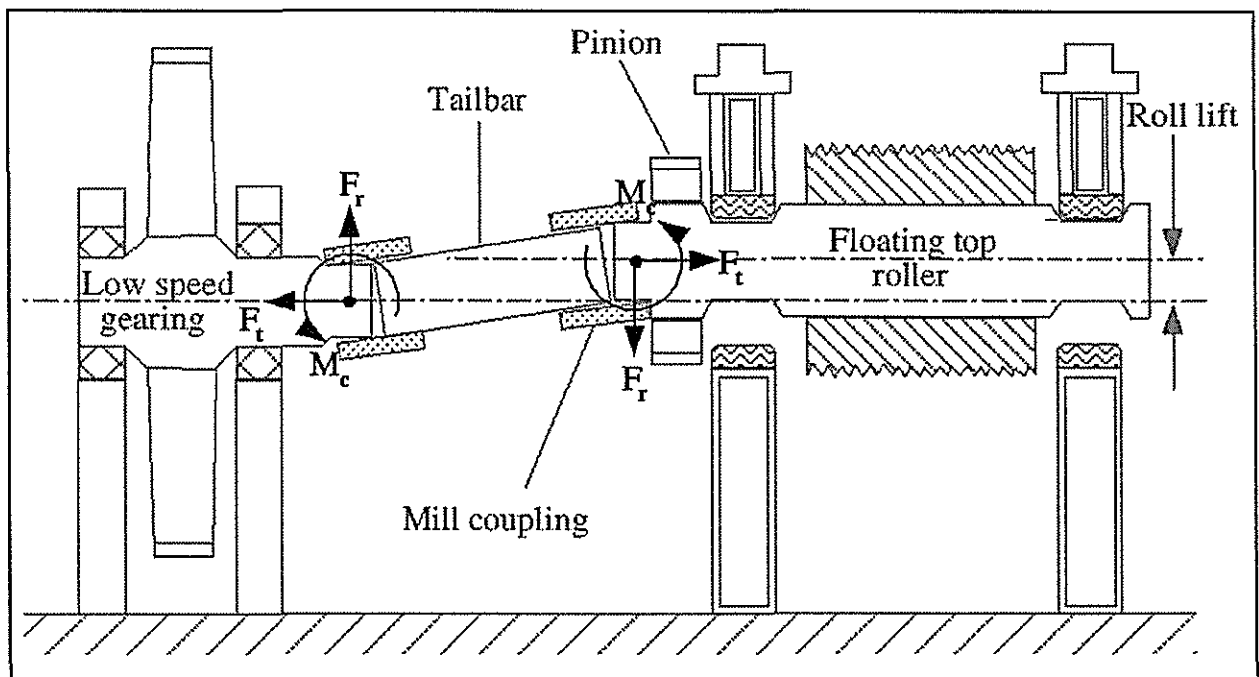


Figure A.4.1 Misalignment induced loads acting on roller shaft and final motion gear shaft.

Using equation 1.26, 
$$F_t = \frac{4}{l_3} \mu \left( \frac{l_1 \pm \mu l_3}{L + l_2} \right) T$$
,

we get :- 
$$F_t = 0.097 \text{ MN}$$

∴ Thrust force = 0.097 MN

Using equation 1.27, 
$$M_c = \frac{T}{l_3} \sqrt{(l_1 + \mu l_3)^2 + (\mu l_3)^2}$$
,

we get :- 
$$M_c = 0.425 \text{ MNm}$$

∴ Bending moment = 0.425 MNm

The radial force and the bending moment were applied to the FEA roller model as depicted in Figure A.4.2. The load application point was a node contained on the roller's axis, central to contact points on the shaft's. The thrust force was not applied to the FEA model as it would have no real effect on the stress state in critical regions on the mill roller. Such thrust forces are absorbed by the pintle end brass.

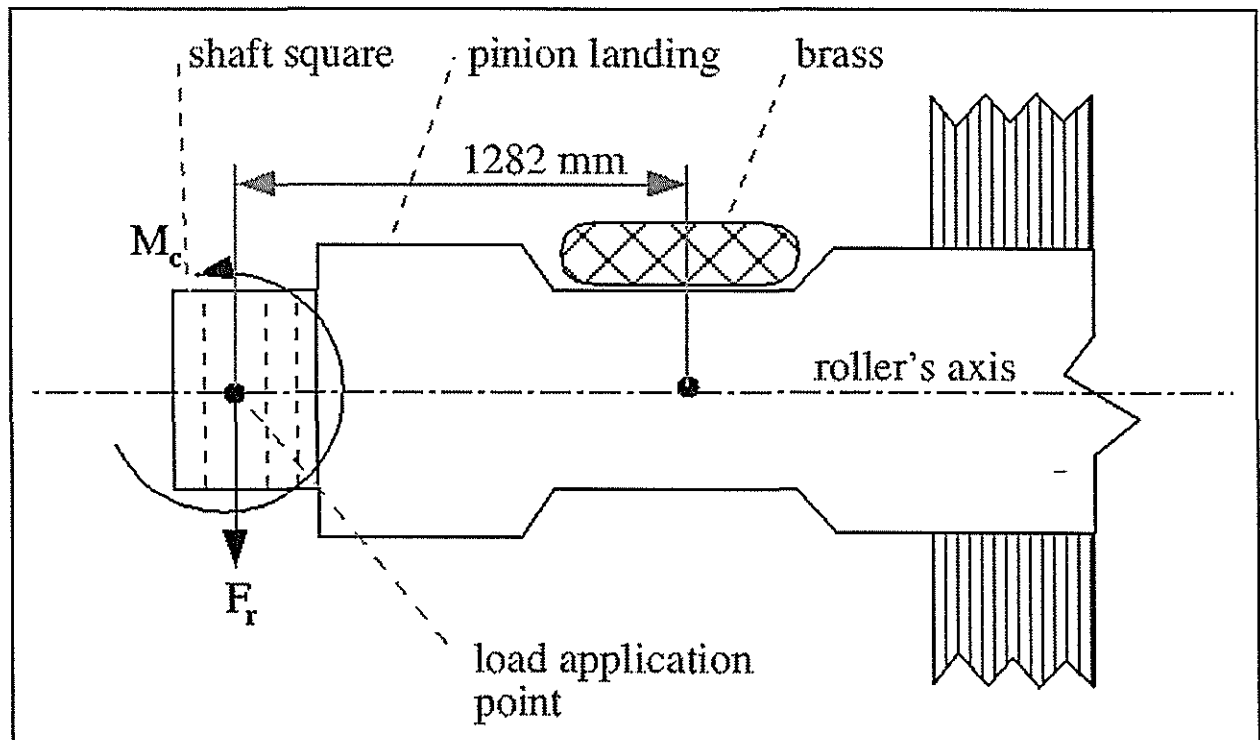


Figure A.4.2 Application of the roller misalignment induced radial force and bending moment to FEA roller model.

### A.5 Roller stress calculations

The following calculations, based on simple beam theory were used to estimate bending and torsional shear stress levels developed in a mill roller for comparison with finite element predictions. Several assumptions were made to simplify the calculations, including:

- roll loading (4.786 MN or 69.8 tonnes /ft ) is uniform across shell length ;
- pinion reaction and brass guide friction effects are negligible ;
- the centre of bearing pressure coincides with the journal centre ; and
- misalignment induced loads act in the same plane as the resultant roll load.

Calculating bending stress

Figure A.5.1 depicts the cross-section of the seven foot mill roller, showing the dimensions and loads which contribute to bending stress levels.

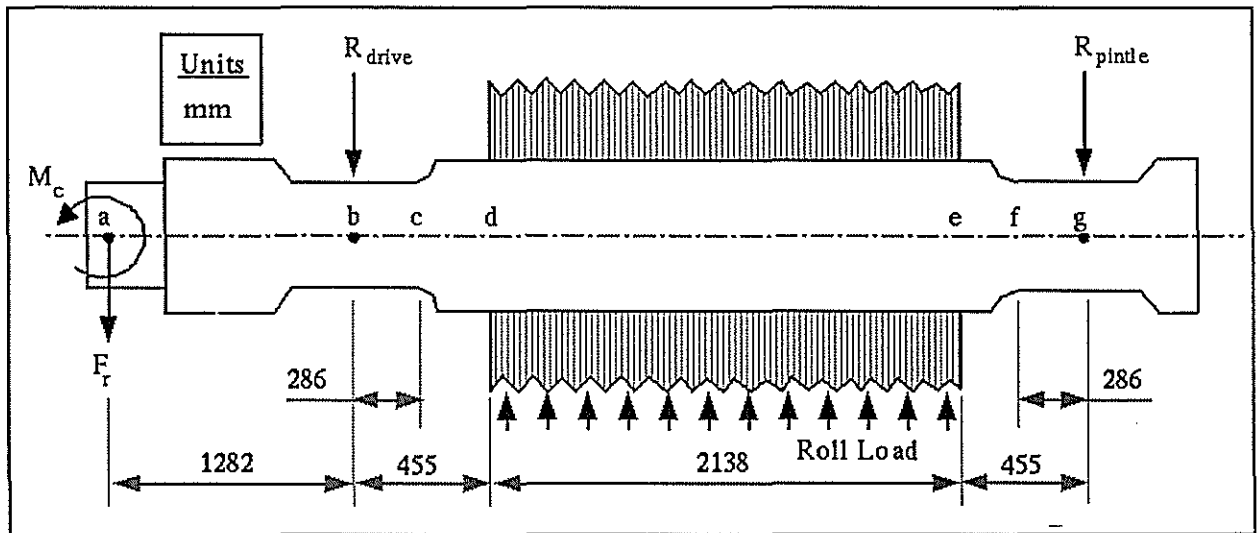


Figure A.5.1 Cross-section of mill roller highlighting bending loads and dimensions.

Two cases are analysed. Case 1 assumes uniform roll load with no additional loading applied. Case 2 assumes uniform roll load with additional misalignment loading applied being representative of a 10 mm parallel roll lift (Appendix A4). The equation shown below is used to calculate bending stress,  $\sigma_{bend}$ .

$$\sigma_{bend} = K_t \frac{My}{I}$$

where  $K_t$  is the stress concentration ;  $M$  is the bending moment ;  
 $y$  is the distance from the neutral axis ; and  $I$  is the second moment of area.

Figure A.5.2 shows the shear and bending moment diagrams relating to Case 1. Figure A.5.3 shows the shear and bending moment diagrams relating to Case 2.

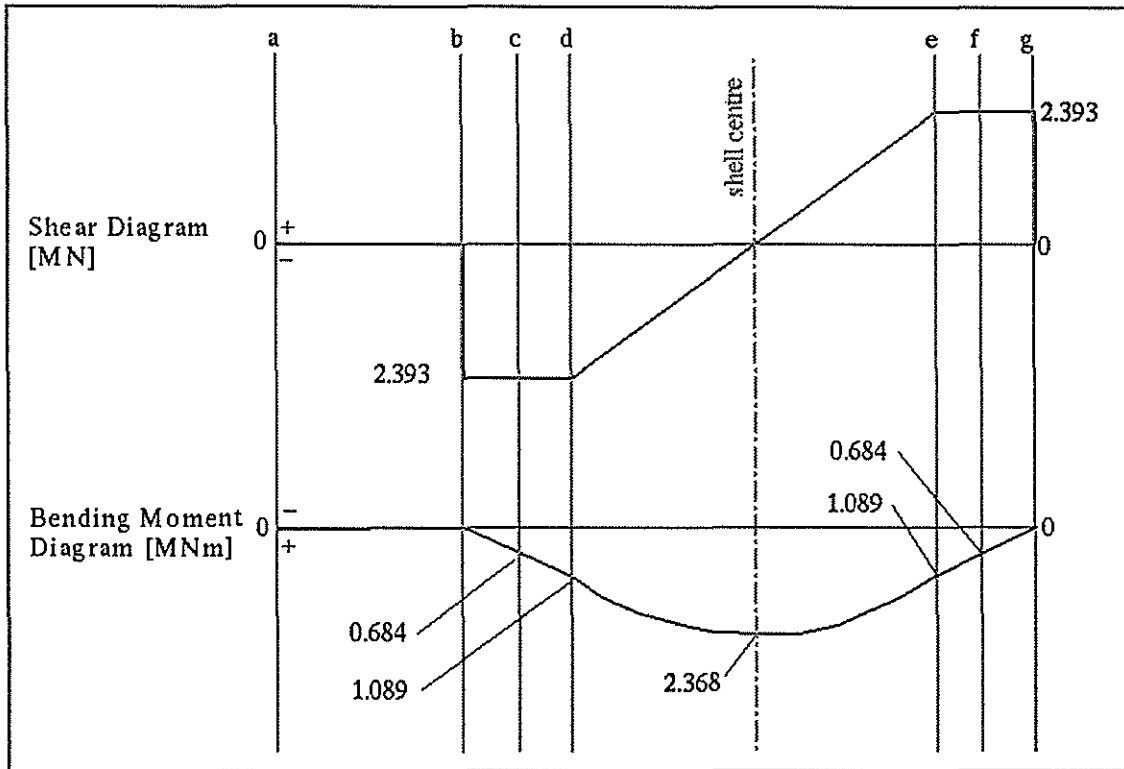


Figure A.5.2 Shear and bending moment diagrams relating to Case 1.

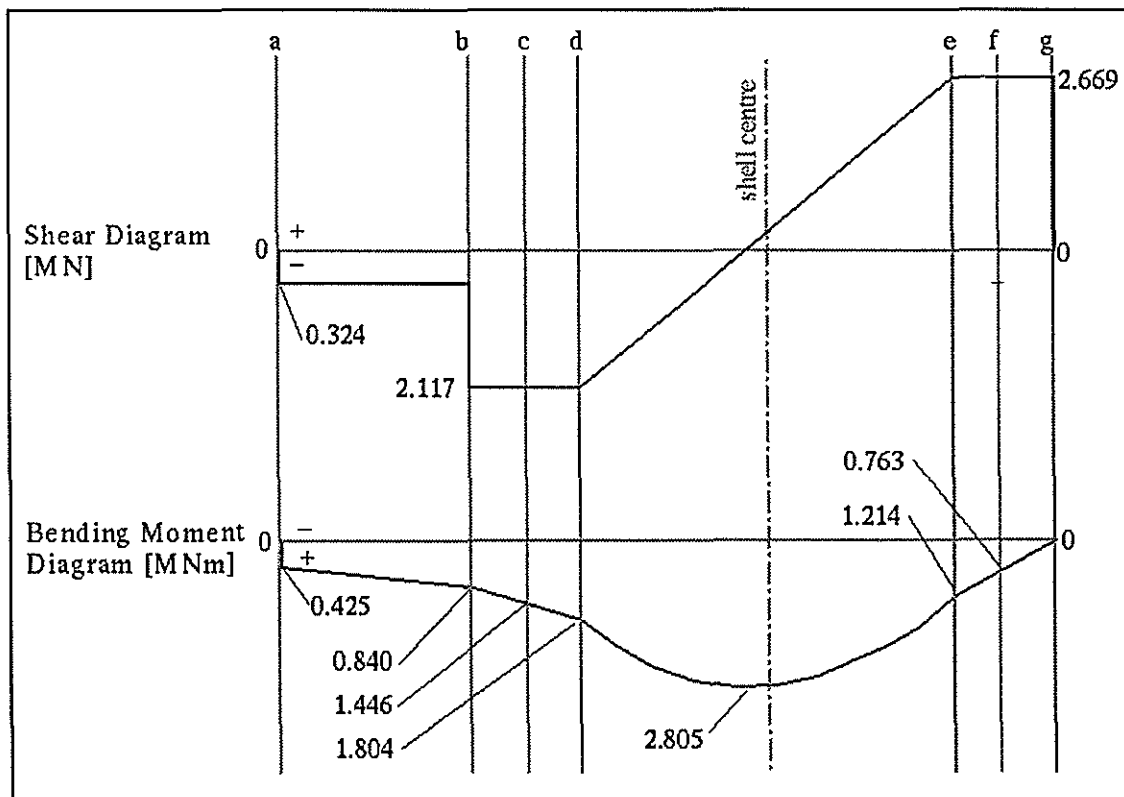


Figure A.5.3 Shear and bending moment diagrams relating to Case 2.

In Figures A.5.1 through A.5.3, labels were used to locate salient positions on the mill roller. Of importance, 'c' refers to the drive-end fillet, 'd' refers to the shell-end position on the drive-end of the shaft, 'e' refers to the shell-end position on the pintle-end of the shaft and 'f' refers to the pintle-end fillet. Point 'a' locates the position where the misalignment induced load and bending moment are applied in Case 2, 'b' is the centre of the drive-end journal and 'g' is the centre of the pintle-end journal.

### Fillet transition

From Petersen (1974), the theoretical stress concentration factor,  $K_t$ , for the bending of a stepped round bar with a shoulder fillet was approximated. Knowing the physical dimensions of the journal diameter (0.4572 m), shoulder diameter (0.510 m) and fillet radius (0.075 m) a value of 1.47 for the stress concentration of the fillet transition was obtained.

For case 1:

$$\sigma_{\text{bend}} = K_t \frac{My}{I} = 1.47 \times \frac{0.684 \times 0.4572/2}{\pi/64 \times 0.4572^4}$$

$$\therefore \sigma_{\text{bend}} = 107 \text{ MPa} \quad (\text{at both drive-end and pintle-end fillets})$$

For case 2:

$$\sigma_{\text{bend}} = K_t \frac{My}{I} = 1.47 \times \frac{1.446 \times 0.4572/2}{\pi/64 \times 0.4572^4}$$

$$\therefore \sigma_{\text{bend}} = 227 \text{ MPa} \quad (\text{at drive-end fillet})$$

$$\sigma_{\text{bend}} = K_t \frac{My}{I} = 1.47 \times \frac{0.763 \times 0.4572/2}{\pi/64 \times 0.4572^4}$$

$$\therefore \sigma_{\text{bend}} = 120 \text{ MPa} \quad (\text{at pintle-end fillet})$$

### Shell-end region

Petersen (1974), discussed the scenario where an outer collar is pressed or shrunk onto a shaft. Selecting a stress concentration factor,  $K_t$ , for this case is not straight forward as many factors are involved. These factors include; the physical dimensions of the shaft (diameter) and collar (diameter, length); the average interaction pressure due to the shrink fit; the stiffness characteristics of the shaft and collar (elastic modulus) and the level of bending stress in relation to the interaction

pressure. Unfortunately, fatigue related tests were only carried out on shaft and collars with diameters of 50 mm and 100 mm respectively, too remote from that of a typical mill roller (500 mm and 1000 mm) to allow an accurate estimate of stress concentration factors. These tests indicated that the fatigue-notch factor,  $K_f$ , was in the order of two. As a general rule, stress concentration factors are greater than fatigue-notch factors suggesting  $K_t$  is higher than two for the shaft specimens tested. However, fretting corrosion for pressed-on collars further weakens the transition zone, which concludes that  $K_t$  and  $K_f$  would be similar in this case. Tests were carried out on similar materials whereas the cast iron in a mill roller shell is less stiff than that of shaft steel, further complicating the situation. For the following analysis, the stress concentration factor was chosen at 1.75. Note this value will vary depending on the loading conditions as separation of the shell end from the shaft is possible above a certain roll load.

For case 1:

$$\sigma_{\text{bend}} = K_t \frac{My}{I} = 1.75 \times \frac{1.089 \times 0.510/2}{\pi/64 \times 0.510^4}$$

$$\therefore \sigma_{\text{bend}} = 146 \text{ MPa} \quad (\text{at both drive-end and pintle-end shell-end regions})$$

For case 2:

$$\sigma_{\text{bend}} = K_t \frac{My}{I} = 1.75 \times \frac{1.804 \times 0.510/2}{\pi/64 \times 0.510^4}$$

$$\therefore \sigma_{\text{bend}} = 242 \text{ MPa} \quad (\text{at drive-end shell-end region})$$

$$\sigma_{\text{bend}} = K_t \frac{My}{I} = 1.75 \times \frac{1.214 \times 0.510/2}{\pi/64 \times 0.510^4}$$

$$\therefore \sigma_{\text{bend}} = 163 \text{ MPa} \quad (\text{at pintle-end fillet shell-end region})$$

### Roller centre

Crawford (1970), derived an equation, shown below, for approximating the bending stress for any diameter,  $d$ , on the centre plane of the roller shell assuming zero slip at the pressure joint. The effective shell diameter,  $D_1$ , was set to the tooth root diameter of 920 mm for the following calculations.

For case 1:

$$\sigma_{\text{bend}} = \pm \frac{32}{\pi} \frac{M \frac{E_1}{E_2} d}{\left( \frac{E_1}{E_2} (D_1^4 - D_2^4) + D_2^4 \right)} = \frac{32}{\pi} \times \frac{2.368 \times \frac{120}{207} \times 0.920}{\frac{120}{207} \times (0.920^4 - 0.510^4) + 0.510^4}$$

$\therefore \sigma_{\text{bend}} = 29 \text{ MPa}$  (at outside centre of shell, \*\* the stress concentration of the grooves is not included)

$$\sigma_{\text{bend}} = \pm \frac{32}{\pi} \frac{M \frac{E_1}{E_2} d}{\left( \frac{E_1}{E_2} (D_1^4 - D_2^4) + D_2^4 \right)} = \frac{32}{\pi} \times \frac{2.368 \times \frac{120}{207} \times 0.510}{\frac{120}{207} \times (0.920^4 - 0.510^4) + 0.510^4}$$

$\therefore \sigma_{\text{bend}} = 16 \text{ MPa}$  (at inside centre of shell)

As the strain of the inside shell surface and the strain of the outside shaft surface can be presumed equal, then the stress at the shaft surface can be found as below.

$$\sigma_{\text{bend}} = \pm \frac{32}{\pi} \frac{M d}{\left( \frac{E_1}{E_2} (D_1^4 - D_2^4) + D_2^4 \right)} = \frac{32}{\pi} \times \frac{2.368 \times 0.510}{\frac{120}{207} \times (0.920^4 - 0.510^4) + 0.510^4}$$

$\therefore \sigma_{\text{bend}} = 28 \text{ MPa}$  (at shaft surface in the roller centre)

For case 2:

The maximum bending moment, 2.805 MNm, occurs approximately 120 mm towards the drive-end from the shell's centre line. Adopting the procedure used above for Case1, we get:

$\sigma_{\text{bend}} = 34 \text{ MPa}$  (at outside centre of shell, \*\* the stress concentration of the grooves is not included)

$\sigma_{\text{bend}} = 19 \text{ MPa}$  (at inside centre of shell)

$\sigma_{\text{bend}} = 33 \text{ MPa}$  (at shaft surface in the roller centre)

### Calculating torsional shear stress

For the following calculations, the torsional moments,  $T$ , along the roller are assumed to be unaffected by misalignment. The values for torsional moments can be found in Appendix A3.

The equation shown below is used to calculate torsional shear stress,  $\tau_{tors}$ .

$$\tau_{tors} = K_{ts} \frac{TR}{J}$$

where  $K_{ts}$  is the stress concentration ;  $T$  is the torsional moment ;  
 $R$  is radius ; and  $J$  is the polar area moment of inertia.

#### Fillet transition

From Petersen (1974), the theoretical stress concentration factor,  $K_t$ , for the torsion of a stepped round bar with a shoulder fillet was approximated. Knowing the physical dimensions of the journal diameter (0.4572 m), shoulder diameter (0.510 m) and fillet radius (0.075 m) a value of 1.205 for the stress concentration of the fillet transition was obtained.

For case 1 and 2:

$$\tau_{tors} = K_{ts} \frac{TR}{J} = 1.205 \times \frac{(0.448 + 0.056) \times 0.4572/2}{\pi/32 \times 0.4572^4}$$

$$\therefore \tau_{tors} = 32 \text{ MPa} \quad (\text{at drive-end fillet})$$

#### Shell-end region

As for the bending stress concentration for press-fit collars, the torsional stress concentration is not well documented. For the lack of a better value, 1.5 for chosen for the torsional stress concentration factor to allow further calculation.

For case 1:

$$\tau_{tors} = K_{ts} \frac{TR}{J} = 1.5 \times \frac{(0.448 + 0.056) \times 0.510/2}{\pi/32 \times 0.510^4}$$

$$\therefore \tau_{tors} = 29 \text{ MPa} \quad (\text{at drive-end shell-end region})$$

## Calculating the combined stress state

Adopting the distortion-energy failure theory, Shigley (1986) combined the bending ( $\sigma_{\text{bend}}$ ) and torsional shear stress ( $\tau_{\text{tors}}$ ) developed in a biaxially loaded shaft to produce a value for Von Mises stress,  $\sigma_{\text{vm}}$ , as shown below :

$$\sigma_{\text{vm}} = \sqrt{\sigma_{\text{bend}}^2 + 3 \times \tau_{\text{tors}}^2}$$

For case 1:

$$\sigma_{\text{vm}} = \sqrt{\sigma_{\text{bend}}^2 + 3 \times \tau_{\text{tors}}^2} = \sqrt{107^2 + 3 \times 32^2}$$

$$\therefore \sigma_{\text{vm}} = 121 \text{ MPa} \quad (\text{at drive-end fillet})$$

For case 2:

$$\sigma_{\text{vm}} = \sqrt{\sigma_{\text{bend}}^2 + 3 \times \tau_{\text{tors}}^2} = \sqrt{227^2 + 3 \times 32^2}$$

$$\therefore \sigma_{\text{vm}} = 234 \text{ MPa} \quad (\text{at drive-end fillet})$$

### Shell-end region

For case 1:

$$\sigma_{\text{vm}} = \sqrt{\sigma_{\text{bend}}^2 + 3 \times \tau_{\text{tors}}^2} = \sqrt{146^2 + 3 \times 29^2}$$

$$\therefore \sigma_{\text{vm}} = 154 \text{ MPa} \quad (\text{at drive-end shell-end region})$$

For case 2:

$$\sigma_{\text{vm}} = \sqrt{\sigma_{\text{bend}}^2 + 3 \times \tau_{\text{tors}}^2} = \sqrt{242^2 + 3 \times 32^2}$$

$$\therefore \sigma_{\text{vm}} = 247 \text{ MPa} \quad (\text{at drive-end shell-end region})$$